Laser-Driven Proton Acceleration with Two Ultrashort Laser Pulses

Inaugural-Dissertation

zur Erlangung des Doktorgrades
der Mathematisch-Naturwissenschaftlichen Fakultät
der Heinrich-Heine-Universität Düsseldorf

vorgelegt von

Jürgen Böker

aus Bünde

Köln, Januar 2015

Aus dem Institut für Laser- und Plasmaphysik

der Heinrich-Heine-Universität Düsseldorf

Gedruckt mit der Genehmigung der

Mathematisch-Naturwissenschaftlichen Fakultät der

Heinrich-Heine-Universität Düsseldorf

Referent: Prof. Dr. Oswald Willi

Koreferent: Prof. Dr. Dr. Carsten Müller

Tag der mündlichen Prüfung: 24.04.2015

Abstract

This thesis describes a laser ion acceleration scheme where two ultrashort, high intensity laser pulses are used. The scalability of the TNSA acceleration mechanism with multiple beams and the transition beyond TNSA is examined experimentally and analyzed with the aid of simulations.
The Arcturus laser facility at the Heinrich Heine University in Düsseldorf provides two <30fs short pulses, so that the intensity of both beams was in the order of 10^{20}W/cm^2. The target was a 5μm thick titanium foil, that the beams irradiated with an angle of incidence of 0° and 40°, respectively. The delay between the two pulses was varied in a first shot series in a range of ±200fs and in a further shot series in a range of 10s of picoseconds.
Three regimes were observed in dependence on the delay between the two pulses. If both pulses are synchronized and the beams are defocused, the resulting proton cut-off energy is lower compared to pulses that are delayed on a few 10s of femtoseconds. The remarkable result is confirmed by PIC simulations. As the delay is increased, the plasma and therewith the contamination layer thermally expands and gains some kinetic energy. Moreover, the duration of the appearance of the ambipolar electrical field is also increased by the delay. The heavy ions get more time for the acceleration. This result is consistent with the typically observed phenomenon with TNSA, that long pulses are more advantageous than short pulses with the same intensity for ion acceleration.
The second regime is observed for focused beams and pulses, that are delayed by a few 10s of femtoseconds. An enhancement in the proton cut-off energy is found compared to single beam shots. The highest proton cut-off energy is observed for synchronized laser pulses and decreases for longer delays. The same behavior is confirmed by PIC simulations. The ambipolar electrical field for synchronized pulses is longer lasting. This is caused by a resonantly enhanced $\vec{j} \times \vec{B}$ heating. The resonance leads to more hot electrons, that contribute to the ambipolar electrical field.
The last regime appears for delays in the range of 10s of picoseconds and only for shots where beam I - with normal incidence - is the later pulse. The plasma can expand for several 10s of picoseconds before the second pulse interacts with the plasma. An enhancement in the proton cut-off energy >5MeV is found. The second pulse propagates through a self-formed waveguide and breaks through the former target into free-space. Two magnetic vortices appear. Electrons circulate around the vortices and support with their current the magnetic field. Ions are accelerated by these strong magnetic vortices. The effects are described by an analytic ansatz that is based on a PIC simulation. The model predicts the proton cut-off energy in very good agreement with the PIC simulation and the experiment.

Zusammenfassung

Diese Arbeit beschreibt ein Laser-Teilchen-Beschleunigungs-Schema für Ionen, bei dem zwei ultrakurze Laserpulse mit sehr hoher Intensität benutzt werden. Die Skalierbarkeit des TNSA Mechanismus bei Einsatz von mehreren Strahlen und der Übergang des TNSA Mechanismus hin zu anderen Beschleunigungsmechanismen wird im Experiment und mit Hilfe von Simulationen untersucht.
Die Arcturus Laser Anlage an der Heinrich Heine Universität Düsseldorf stellt zwei Laserpulse mit Pulslängen <30fs bereit und erreichten so Intensitäten von 10^{20}W/cm^2. Als Target wurde eine 5μm dicke Titanfolie verwendet, auf die die Strahlen unter einem Winkel von 0° bzw. 40° fokussiert wurden. Der Delay zwischen den beiden Pulsen wurde in einer ersten Schußserie in einem Bereich von ±200 fs verändert und in einer weiteren Serie in einem Bereich von einigen 10 Pikosekunden.
Drei Regime wurden in Abhängigkeit des Delays zwischen den Pulsen beobachtet. Wenn beide Pulse synchron sind und die beiden Strahlen defokussiert sind, ergibt siche eine geringerer Protonenenergie im Vergleich zu Pulsen mit einem Delay von einigen 10 Femtosekunden. Das bemerkenswerte Ergebnis wird durch 2D PIC Simulationen bestätigt. Wenn der Delay vergrößert wird, erhält das Plasma und auch die Kontaminationsschicht Zeit sich thermisch auszudehnen und erhält bereits einen Impuls. Außerdem wird durch Vergrößerung des Delays auch das zeitliche Auftreten des ambiploaren Feldes vergrößert. Dadurch erhalten die schweren Ionen mehr Zeit zu beschleunigen. Das Ergebnis is konsistent mit dem Phänomen bei TNSA, dass längere Pulse gegenüber kürzeren Pulse vorteilhafter sind bei gleicher Intensität in Bezug auf die maximale Protonenenergie.
Das zweite beobachtete Regime tritt auf bei fokussierten Strahlen und Pulsen mit einer zeitlichen Distanz von einigen 10 Femtosekunden. Eine Erhöhung der Protonenenergie im Vergleich zu Einzelstrahlschüssen wurde bei synchronen Pulsen beobachtet. Bei einer Erhöhung des Delays sinkt auch die maximale Protonenenergie. Das gleiche Verhalten wurde auch in 2D PIC Simulationen festgestellt. Das ambilpolare elektrische Feld bei synchronen Pulsen exisitiert länger. Dies wird durch eine resonant gesteigerte $\vec{j} \times \vec{B}$ Heizung hervorgerufen. Die Resonanz führt zu mehr heißen Elektronen, die zu dem ambipolaren elektrischen Feld beitragen.
Das dritte Regime wurde für Delays von einigen 10 Pikosekunden beobachtet und zwar nur für Schüsse, bei denen Strahl I - mit senkrechtem Auftreffwinkel - der letzte Puls war. Das Plasma kann für einige 10 Pikosekunden expandieren bevor der zweite Puls mit dem Plasma wechselwirkt. Eine Erhöhung der maximalen Protonenenergie mit >5MeV wurde gefunden. Der zweite Puls bewegt

sich durch einen selbst erzeugten Hohlleiter und durchbricht schließlich die ursprünglich Folie in den freien Raum. Magnetische Wirbel treten auf. Elektronen bewegen sich um die Wirbel herum und unterstützen mit ihrem Strom die Magnetfelder. Ionen werden durch diese starken Magnetfelder beschleunigt. Auf Basis der PIC Simulationen werden die auftretenden Effekte durch einen analytischen Ansatz beschrieben. Das Modell gibt in sehr guter Übereinstimmung die maximale Protonenenergie der Simulationen und des Experiments wieder.

Contents

1. Introduction

The realization of the first optical laser by Theodore Maiman in 1960 is the starting point of an extensive development. During the last 50 years the laser has influenced various disciplines of science and it even has found its way into our daily life. Without semiconductor lasers our communication systems would not work. New generation of cars will use laser based range finder. STED (stimulated emission depletion) microscopes utilize a laser and have a spatial resolution beyond the defraction limit [29]. This new class of microscopes is widely used in biology.

All these lasers have a rather low power output and therewith the achieved intensities are limited. Higher peak powers for pulsed lasers were first reached with Q-switched laser. These nanosecond pulsed laser have proven their reliability in science and industry. The development of mode-locking realized pulses in the order of magnitude of picoseconds and femtoseconds.

In 1985 G. Mourou and D. Strickland [51] developed the chirped pulse amplification. The peak power enhancement achieved with this technique relies on the temporal pulse compression after amplification. Today, CPA based laser systems are found in science applications. The technique allows laser systems with a few hundred terawatt or even a petawatt at a larger room to be built. Which is in contrast to lasers used for inertial confinement research. These lasers are facilities with the size of a few football fields. In the early 2000s a beam of different ion species was detected after such a high power laser system was fired onto a few micrometer thick foil. The ions propagate perpendicular away from the target. Target normal sheath acceleration (TNSA) was identified as the driving mechanism. The tightly focused laser pulse accelerates electrons, that move through the foil. A cloud or a sheath of electrons accumulate at the rear side of the target. As every surface is contaminated with hydrocarbons and water, a quasi electro-static field builds up between the electron cloud and the ionized contamination constituents. Eventually, the ions are also accelerated in normal direction to the target by the strong electric field.

The ion beam has quite unique characteristics, that differ from ion beams generated by conventional rf accelerators [25]. The ions are accelerated in a bunch that last for a few picoseconds. Moreover, the particles originate from a point-

like source with the size of a few micrometer. Thus, the transverse emittance is smaller than[12] 0.004 mm rad and the longitudinal emittance is smaller than 10^{-4} eV. In the past decade the TNSA mechanism has been extensively investigated.
The unique particle beam characteristics make laser-driven accelerators an interesting complement technology to conventional accelerators. In particular it is proposed [34] to use the technology in the field of hadron cancer therapy. However, hadron therapy requires proton energies of up to 250 MeV at a dose rate of a few Gy per minute [66]. Schreiber et al. [48] developed a model for TNSA in accordance to several experiments. The cut-off energies of the ions scale in this model with $\sim \sqrt{P}$ the squareroot of the laser power. Thus, the effort to increase the ion cut-off energy includes a much higher effort for the increase of laser power. Today the maximum achieved proton energy by high-power laser systems is in the range of 60 MeV.
Other ion acceleration mechanism were proposed that may overcome these limitations. Most of these mechanisms rely on nanometer thick targets in combination with an ultra-high temporal contrast of the laser pulse, so that the target remains intact when the main part of the pulse approaches the target. Additionally, the power or more precisely the intensity has to be a few orders of magnitude larger than it has to be with TNSA. An increase of intensity can only be achieved by increasing the size of optics and crystals, because the limiting factor today is the damage threshold of the optics. Unfortunately the costs do not scale linearly with the size of the optics, but follow a power law. These limitations are the reason, why laser based ion accelerators have not found yet its way into hadron therapy or has become a common tool in material science.

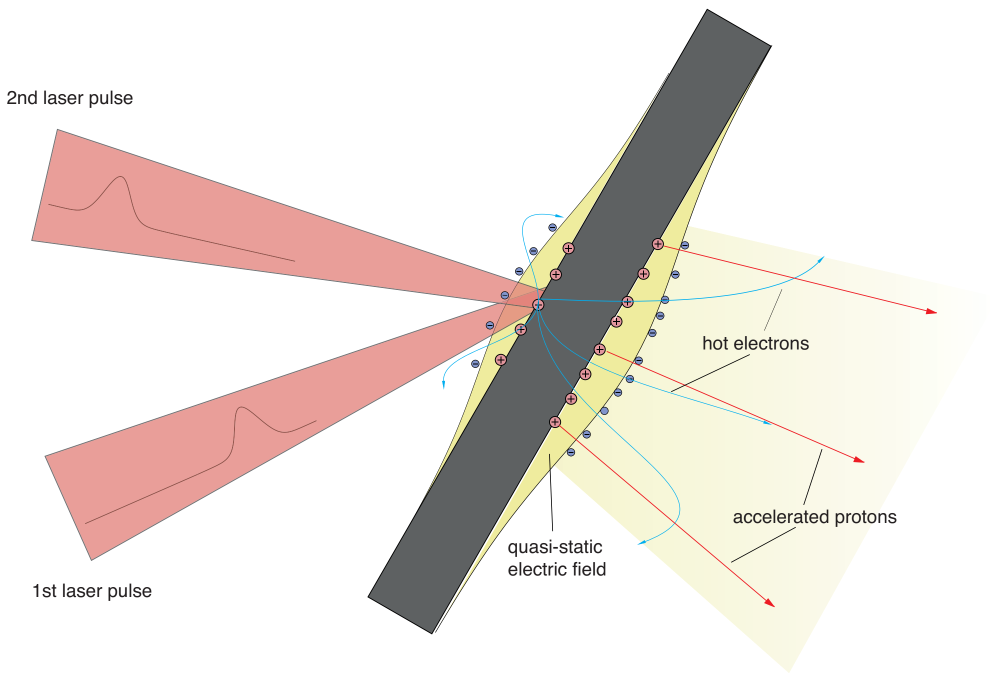

Figure 1.1.: TNSA with two ultrashort laser pulses.

The key question to be answered in this thesis is, if an enhancement in cut-off energies and in particle numbers could also be achieved with additional laser pulses. Two laser pulses with a somewhat lower intensity are used instead of a single laser with high intensity. A further question arises from the delay between the two pulses. The additional parameter is used to identify the limits of the TNSA mechanism. The experiment described and analyzed in this thesis utilized for the first time two close-to-synchronized, ultrashort, high intensity laser pulses for ion acceleration.

The Arcturus Laser Facility at the Heinrich Heine University in Düsseldorf has the unique feature of two main beams with 100 TW and 200 TW peak power, where the pulse length is below 30 fs for both beams. In preparation of the experiment the vacuum target chamber was redesigned and several components for the beam line were designed. The main diagnostic was a Thomson parabola spectrometer with a multi-channel plate as detector. The diagnostic was cross-calibrated with CR39 nuclear track detector in order to derive spectra from the MCP traces. The evaluation of the spectra was done by a self-written semi-automatic program. Particle-in-cell simulations were extensively carried out, in order to explain these spectra.

Overview of the Content of this Thesis

Chapter 2 describes the interaction between the electro-magnetic fields of the laser and matter. It begins with the interaction of a single, charged particle with electro-magnetic fields. A large number of charged particles is released due to ionization - a plasma is generated. Different ionization mechanisms in dependence on the laser intensity are shown. The collective behavior of the plasma can be described by a few parameters. Energy transfer from the laser to the plasma can occur in several ways that are briefly presented. Physical phenomena in the interaction process between laser and plasma are discussed that are relevant in the frame of this thesis. Beside the already mentioned TNSA mechanism further acceleration schemes were proposed. Relevant mechanisms are presented and discussed. As the interpretation of the experimental data is done with the particle-in-cell code EPOCH and the software CST, the basic underlying principles of the codes are shown.

Chapter 3 gives an overview of the Arcturus Laser Facility, the experimental setup and the applied diagnostics. The Thomson parabola spectrometer is explained and how the analysis was carried out. Moreover, the results of the cross-calibration of the TPS with CR39 nuclear track detectors are presented.

Chapter 4 presents the experimental results of the MCP. An analysis is done on basis of the MCP images and the varied parameters during the experiment. If the proton cut-off energy is drawn as a function of the delay between the two pulses, three regimes are identified. Defocused beams with a delay in the order of 10s of femtoseconds show a minimum for synchronized shots in the proton cut-off energy. Focused beams with a delay in the order of 10s of femtoseconds show a maximum for synchronized shots in the proton cut-off energy. Shots where the beam with normal angle of incidence is 50 picosecond later show also an enhancement, that must rely on a different acceleration mechanism than TNSA.

Chapter 5 begins with the analysis of the influence of the prepulse. The 2D PIC simulation modeled 10ps of the prepulse. The results are used in the subsequent simulations of the main pulses. First, the single beam interactions are simulated for focused and defocused beams. The computational results are compared with the experimental spectra. The next section presents the results of 2D PIC simulations of close-to-synchronized shots, i.e. the delay was in the range of 10s of femtoseconds. Again, the results are compared with the experimental spectra. Physical mechanisms are given that explain the results.

Chapter 6 interprets shots where the delay was in the range of 10s of picoseconds. The plasma expansion after a first main pulse has exploded the target is modeled in a 1D PIC simulation. The results are used in a 2D simulation for the interaction of the subsequent laser pulse with the plasma. The computational results show a new acceleration mechanism, that is extensively studied. In an analytic approach the observed phenomenon is described. The results of model, simulation and experiment are consistent.

The last chapter summarizes and concludes the thesis and gives an outlook for upcoming experiments.

2. Relativistic Laser-Matter Interaction

2.1. Introduction

This chapter discusses the interaction between the electro-magnetic fields of the laser and matter. In a simple approach the interaction can be divided into the following steps. A high intensity laser pulse ionizes atoms. The laser pulse transfers energy to electrons. A plasma is generated. Plasma and laser interact with each other and modify each other.
Different physical processes appear that depend on the laser intensity. The section starts with the interaction of a single atom with electro-magnetic fields. Afterwards absorption and ionization mechanisms are discussed. Physical phenomena in the interaction process between laser pulse and plasma are discussed that are relevant in the frame of this thesis. Several laser ion acceleration mechanisms have been theoretical proposed and experimental discovered in recent years. The different acceleration mechanisms are presented and discussed. Textbooks are used from Gibbon [19], Kruer [30] and Eliezer [16] and can give further details.
The interpretation of the experimental results can only be done with the aid of computational simulations. The basic properties of the particle-in-cell (PIC) code EPOCH are shown, which is extensively used for the simulation of the experiment. The evaluation of the experimental data and partly also for the interpretation of the PIC simulations, the software *CST* is used. The basis of the calculation method of the software is briefly presented.

2.2. Single Atom Interaction

In vacuum the electric and magnetic fields of a linearly polarized wave are given by

$$\vec{E}(\vec{r},t) = E_0(\vec{r},t)\vec{e_x}\exp[i(\omega t - \vec{k}\vec{z})] \tag{2.1}$$

$$\vec{B}(\vec{r},t) = \frac{1}{c}E_0(\vec{r},t)\vec{e_y}\exp[i(\omega t - \vec{k}\vec{z})], \tag{2.2}$$

where c is the speed of light, ω is the angular frequency, $\vec{k}$ the wave vector and $\vec{e_z}$ is the propagation direction.
The time averaged Poynting vector of these fields gives the energy flux density, which corresponds to the intensity

$$I = \frac{1}{\mu_0}\left\langle\left|\vec{E}\times\vec{B}\right|\right\rangle = \frac{\varepsilon_0 c}{2}E_0^2, \tag{2.3}$$

where μ_0 is the vacuum permeability and ε_0 is the vacuum permittivity.

Ionization

In order to estimate ionization a simple approach is made. The electrostatic field of a hydrogen atom is given by

$$E_H = \frac{e}{4\pi\varepsilon_0 a_B^2}, \tag{2.4}$$

where e is the electron's charge and a_B the mean distance from the proton - the Bohr radius. It is assumed for ionization, that the electrostatic field of the hydrogen atom becomes equal to the electric field of the laser at an intensity of

$$I = \frac{e^2 c}{32\pi^2\epsilon_0 a_B^4} \approx 3.5\times 10^{20}\frac{W}{m^2} = 3.5\times 10^{16}\frac{\mathrm{W}}{\mathrm{cm}^2}. \tag{2.5}$$

The very simple, classic approach suggests, that any material ionizes only at this intensity. Fortunately, ionization occurs already at lower intensities. Some of the most relevant ionization mechanism are explained in the following.

Multi Photon Ionization

Two-photon ionization was first described theoretically by Göppert-Mayer in 1931. In the early 1960s the first lasers provided photon energies high enough, so that the phenomena could be observed in experiments.
Multi-photon absorption describes the simultaneous event of absorption of N-photons by an atom, by with the atom is ionized. During the multi-photon ionization the atom passes through several intermediate and virtual states with increasing energy. If the absorbed photon-energy leads to an eigenstate, the process is called resonance enhanced multi-photon ionization [55]. Usually the intermediate states are no eigenstates, as the photon-energy is too small. Therefore these states are called virtual states. The lifetime of such a state is in the order of magnitude of femtoseconds. The photons needs to be absorbed quasi-simultaneously in order to reach the continuum. This process is called non-resonant multi-photon ionization. For non-resonant N-photon ionization the ionization rate is [15]

$$R_I = \sigma_N \Phi^N. \tag{2.6}$$

The probability of capturing N photons is given by the generalized cross-section σ_n, which has the unit of $cm^{2N}s^{N-1}$. The photon flux Φ is given by the laser intensity I divided by the photon energy E_{phot}. The probability of ionization is then [15]

$$P_I = \int R_I(t)dt = \tau_L \sigma_N \Phi^N, \tag{2.7}$$

where τ_L is laser pulse width. The necessary laser intensity for multi-photon ionization is then

$$I_{MPI} = \Phi E_{Phot} = \left(\frac{P_I}{\tau_L \sigma_N}\right)^{1/N} E_{phot}. \tag{2.8}$$

In order to estimate the necessary laser intensity, the generalized cross-section is needed.
For instance the ionization energy for copper is 7.726 eV for the first electron. The photon energy for radiation with a wavelength of 800 nm is 1.55 eV. Therefore five photons are needed for ionization. Lambropoulos et al. [32] developed a formula for hydrogen-like atoms to calculate the generalized cross-section. Hydrogen-like atoms are comparable with regard to the ionization energy U_{ion} and the radius R. For a rough estimate the use of this approach is adequate. Thus the cross-section is given by

$$\sigma_N(Cu) = \sigma_N(H)\left(\frac{R(Cu)^2 U_{ion}(H)}{R(H)^2 U_{ion}(Cu)}\right)^N \quad . \tag{2.9}$$

The hydrogen's generalized cross-section $\sigma_5(H)$ for five photon ionization is in the order of magnitude of $\sim 10^{-148} cm^{10} s^4$ taken from [8]. The cross-section for copper is then $\sigma_5(Cu) \sim 3.5 \times 10^{-140} cm^{10} s^4$, where values for R and U_{ion} are taken from [58]. It follows that the intensity for multi-photon ionization I_{MPI} (eq. 2.8) with a 100 fs laser pulse is

$$I_{MPI} = (10 \times 10^{-13} s 10^{-140} cm^{10} s^4)^{-1/5} 10^{-19} J = 10^{11} W cm^{-2} \quad , \tag{2.10}$$

where the probability P_I for ionization is set to one and $10^{-19} J$ scales the photon-energy from electron-volts to Joule.

Tunnel Ionization

For higher intensities the strength of the electromagnetic field of the laser becomes comparable to the atomic fields and the laser directly influences the atomic structure. The Coulomb potential of the atom is distorted by the laser fields. The probability for an electron to tunnel through the potential barrier is increased by the distortion. Therefore the ionization process is called tunnel ionization (TI). If the potential barrier is suppressed below the ionization potential of an ion, the electron escapes spontaneously. In this case the process is called barrier suppression ionization (BSI).
In order to separate the MPI regime from the TI regime, the Keldysh parameter is introduced

$$\gamma_K = \omega_L \sqrt{\frac{2E_{ion}}{I_L}}, \tag{2.11}$$

where E_{ion} is the ionization potential of an ion and ω_L is the angular frequency of the laser. For $\gamma_K \ll 1$ the probability for the tunneling of an electron is high. For $\gamma_K \gg 1$ MPI will dominate.
Again, in a simple, classical picture the distorted Coulomb potential is given by

$$U(x) = -\frac{Ze^2}{4\pi\varepsilon_o|x|} - eE_{cr}x, \tag{2.12}$$

where E_{cr} is the critical field strength where the ionization potential of the ion is equal to the threshold field strength. For BSI an threshold intensity is derived

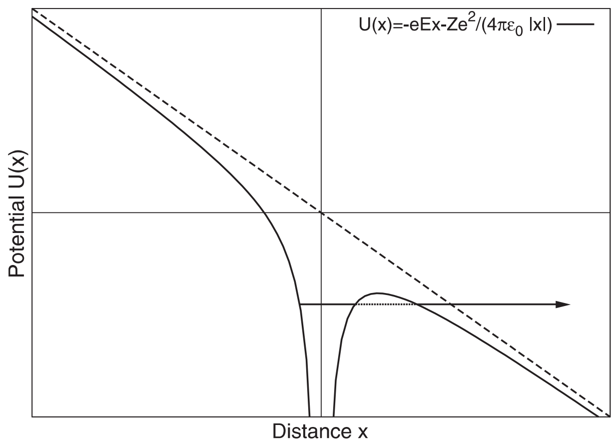

Figure 2.1.: Coulomb potential deformed by a static electric field. The arrow denotes the possibility for an electron to tunnel through the potential barrier.

by determining the position of the peak on the right hand side of the graph in figure 2.1, which is the position of the critical field strength E_{cr}. The effective appearance intensity is then given by

$$I_{BSI} = 4 \times 10^9 \left(\frac{E_{bind}}{\mathrm{eV}}\right)^4 Z^{-2} \frac{\mathrm{W}}{\mathrm{cm}^2} \tag{2.13}$$

For the ionization of titanium to the first ionization stage 6.8eV are necessary. The ionization appears already at an intensity of about $8.5 \times 10^{12} \frac{\mathrm{W}}{\mathrm{cm}^2}$

Ammosov-Delone-Krainov Ionization

A common tool in the validation of experiments in the field of laser particle acceleration are particle-in-cell (PIC) codes. These codes simulate the interaction between an intense laser pulse and a dense plasma. A brief overview of a PIC code is given in section 2.8. These codes also model the ionization of initially neutral matter. An algorithm widely used for ionization in PIC codes is based on the ionization model from Ammosov, Delone and Krainov (ADK) [4], [6]. The ADK model determines the probability for ionization in an alternating electric field of an atom or ion, where the oscillations of the electric field are averaged over one period.
For the PIC code a ionization rate is needed. The probability for ionization in the vicinity of a certain electric field is calculated from the ionization rate via

a Monte-Carlo simulation. The ionization rate for a hydrogen atom in a static electric field E is given by [33]

$$W_{DC} = 4\left(\frac{2E_{ion}}{E}\right)^{5/2} \exp\left(-\frac{2E_{ion}^{3/2}}{3E}\right) \tag{2.14}$$

The ionization rate in the vicinity of an alternating electric field is then given by

$$W_{AC} = \left(\frac{3}{\pi}\right)^{1/2}\left(\frac{E}{2E_{ion}}\right)^{1/2} W_{DC} \tag{2.15}$$

Some of the terms from equation 2.15 and 2.14 are also found in the ionization rate equation of the ADK model [6]

$$W_{ADK} = C_{n^*l}^2\left(\frac{3E}{\pi(2E_{ion})^{3/2}}\right)^{1/2} E_{ion} f(l,m)\left(\frac{2}{E}(2E_{ion})^{3/2}\right)^{2n^*-|m|-1} \times \exp\left(-\frac{2(2E_{ion})^{3/2}}{3E}\right) \tag{2.16}$$

with

$$\begin{aligned} C_{n^*l} &= \left(\frac{2e}{n^*}\right)^{n^*}\frac{1}{(2\pi n^*)^{1/2}} \\ f(l,m) &= \frac{(2l+1)(l+|m|)!}{2^{|m|}|m|!(l-|m|)!}, \end{aligned} \tag{2.17}$$

where n^* is the effective principal quantum number, l is the angular quantum number and m is the magnetic quantum number.
In order to account for ionization that occurs already at lower intensities, usually PIC codes have also an algorithm for multiphoton ionization.
In early versions of the PIC code EPOCH (cf. sec. 2.8) there was no ionization routine implemented. Due to the modular framework of the code, it was possible to implement the ADK routine. A draft of the routine was taken from the PIC code PSC.

2.3. Single Electron Interaction

The simplest case is the interaction of the laser with a single, charged particle - like an electron. A particle with the charge q and the velocity $\dot{\vec{r}} = \vec{v}$ in the vicinity of an electromagnetic field experiences the Lorentz-force in broader sense

$$\vec{F}_L = e[\vec{E}(\vec{r},t) + \vec{v}\times\vec{B}(\vec{r},t)] \quad , \tag{2.18}$$

where $\vec{E}$ and $\vec{B}$ are electric field and magnetic field of the laser

$$\begin{aligned} \vec{E}(\vec{r},t) &= \vec{E}_0(\vec{r})\cos\omega t \\ \vec{B}(\vec{r},t) &= \vec{B}_0(\vec{r})\sin\omega t = -\frac{c}{\omega}\vec{\nabla}\times\vec{E}_0(\vec{r})\sin\omega t \end{aligned} \tag{2.19}$$

For velocities $v \ll c$ the second term $\dot{\vec{r_1}} \times \vec{B}$ in equation 2.18 can be neglected. For this first order approach ($\vec{v} = \vec{v}_1$, $\vec{r} = \vec{r}_1$) the electron oscillates in the direction of the electric field

$$m_e \dot{\vec{v}}_1 + e\vec{E}_0(\vec{r}_0)\cos\omega t = 0 \tag{2.20}$$

The solution of the equation of motion is [16]

$$\vec{v}_1 = -\frac{e}{m_e\omega}\vec{E}_0(\vec{r}_0)\sin\omega t, \qquad \vec{r}_1 = \frac{e}{m_e\omega^2}\vec{E}_0(\vec{r}_0)\cos\omega t \tag{2.21}$$

If the next higher term is taken into account,

$$\vec{v} = \vec{v}_1 + \vec{v}_2, \qquad \vec{E}_0 = \vec{E}_0(\vec{r}_0) + (\vec{r}_1 \cdot \vec{\nabla})\vec{E}_0(\vec{r}_0), \qquad \vec{B}_0 = \vec{B}_0(\vec{r}_0) \tag{2.22}$$

the equation of motion becomes

$$m_e \dot{\vec{v_2}} = -e\left[\left(\vec{r_1} \cdot \vec{\nabla}\right)\vec{E}_0(\vec{r_0}, t) + \frac{1}{c}\vec{v_1} \times \vec{B}_0(\vec{r_0}, t)\right] \qquad , \tag{2.23}$$

One get the ponderomotive force by averaging over time [16]

$$\vec{F_P} = m_e\overline{\ddot{\vec{r_2}}} = -\frac{e^2}{4m_e\omega^2}\vec{\nabla}|\vec{E}_0(\vec{r_0}, t)|^2 \tag{2.24}$$

which is the gradient of the cycle-averaged electric field. The integration of equation 2.24 leads to the ponderomotive potential

$$\Phi(\vec{r}, t) = \frac{e^2}{4m_e\omega^2}|\vec{E}_0(\vec{r}, t)|^2 \tag{2.25}$$

The force and potential are not seen for plane waves, because the gradient in the x-direction would be zero. During a pulse of a plane wave the motion of an electron can be described as an harmonic oscillator. The laser beam is focused, so that the electrical field varies along the transverse direction. A charged particle will be pushed during the first laser-cycle to regions with a lower intensity. During the subsequent laser-cycle the electron experiences a lower restoring force, so that the particle does not return to its initial position. Moreover, the particle acquired energy from the laser field.
From the negative sign of equation 2.24 and the square of the charge follow, that charged particles are pushed away from regions with higher intensity - regardless of positive or negative charge. As the mass is in the denominator, the influence on light electrons is larger compared to heavy ions.

In order to differentiate the electron motion, if the motion is non-relativistic, relativistic or even ultra-relativistic, the dimensionless electric field amplitude a_0 is introduced

$$a_0 = \frac{eE_0}{m_e\omega_L c}. \tag{2.26}$$

The motion is classical for $a_0 \ll 1$. The electron oscillates in the direction of the electric field. As the laser pulse moves forward and the amplitude of the electric field decreases, the amplitude of the oscillation of the electron also decreases. Eventually, the electron's velocity is zero, when the laser pulse is away. The motion is relativistical for $a_0 \sim 1$. Already during a half cycle of the laser the electron approaches the speed of light. Effects like the ponderomotive force have to be considered. The motion is ultra-relativistic for $a_0 \gg 1$. Today the available laser systems do not approach ultra-relativistic intensities, but a lot of exciting theoretical work is done in this field [27, 28, 65]
With the dimensionless electric field amplitude a_0 several identities are rewritten [54]

$$
\begin{aligned}
E_0 &= a_0 \frac{2\pi m_e c^2}{e\lambda} = a_0 \left(\frac{\lambda}{\mu\mathrm{m}}\right)^{-1} 3.2 \times 10^{12}\mathrm{V/m} \\
B_0 &= a_0 \frac{2\pi m_e c}{e\lambda} = a_0 \left(\frac{\lambda}{\mu\mathrm{m}}\right)^{-1} 1.07 \times 10^{4}\mathrm{T} \\
I &= a_0^2 2\varepsilon_0 c \left(\frac{2\pi m_e c^2}{e\lambda}\right) = a_0^2 \left(\frac{\lambda}{\mu\mathrm{m}}\right)^{-2} 1.37 \times 10^{18}\mathrm{W/cm^2} \\
\Phi_P &= \frac{m_e c^2}{4\sqrt{1+a_0^2/2}} a_0^2 = \frac{m_e c^2}{4\bar{\gamma}} a_0^2,
\end{aligned}
\tag{2.27}
$$

where the cycle-averaged γ factor is introduced. From this follows that a laser with a wavelength of about 1μm will approach the relativistic regime with an intensity of $10^{18}\mathrm{W/cm^2}$. The electric field of the laser has then a strength in the order of TV/m and the magnitude of the magnetic field is in the order of 10kT.

2.4. Laser-Induced Plasmas

In general the laser does not interact with a single particle, but with a plasma that consists out of a large number of different kind of particles. The particles may differ in their charge and mass, but in general the plasma is described by a few parameters that include the collective behavior of the particles.
On a femtosecond timescale the ultra-short laser pulse has mainly an impact on the electrons in the plasma. Thus, the electron density plays an important role in the interaction process. The laser energy is absorbed by the electrons of the initially neutral atoms. Electrons are released from the electron shell - the atom is ionized. Several different ionization processes might appear, that are described in the previous sections. From the ionization stage the electron density can be estimated

$$
n_e = Z^* n_i = \frac{Z^* N_A \rho}{A}, \tag{2.28}
$$

where Z^* is effective ion charge, N_A is the Avogadro number, A is the atomic mass number and ρ is the density.

An electromagnetic wave, that propagates in an unmagnetized plasma, is described by the dispersion relation

$$\omega^2 = \omega_P^2 + k^2c^2, \text{ or}$$
$$k^2 = \frac{\omega^2}{c^2}\left(1 - \frac{\omega_P^2}{\omega^2}\right) \tag{2.29}$$

where ω is the angular laser frequency, k the wave number and ω_P the plasma frequency.

$$\omega_P = \sqrt{\frac{n_e e^2}{\varepsilon_0 m_e}}, \tag{2.30}$$

where e is the electron charge and m_e is the electron mass.
From the dispersion relation eq. 2.29 follows, that an electromagnetic wave can propagate in a plasma, as long the angular frequency of the laser is larger than the plasma frequency. The relation can be also expressed in terms of a critical electron density

$$n_{cr} = \frac{m_e \varepsilon_0 \omega_L^2}{e^2} \simeq 1.1 \times 10^{21} \left(\frac{\lambda}{\mu\mathrm{m}}\right) \mathrm{cm}^{-3}, \tag{2.31}$$

where ω_L is the angular frequency of the laser and ε_0 is the vacuum permittivity. If the electron density in a plasma exceeds the critical density for a given laser wavelength, the plasma is overdense.
Whatever laser absorption mechanism applies (cf. sec. 2.5.1 and sec. 2.5.2), in general the laser heats the plasma. Similar to a neutral gas that is heated, the plasma pressure

$$P_e = n_e k_B T_e, \tag{2.32}$$

where T_e is the electrons temperature and k_B is the Boltzmann constant, increases with a rising temperature. As the heating appears very rapidly, the plasma expands roughly with the speed of sound of the ions [19]

$$c_s = \sqrt{\frac{Z^* k_B T_e}{m_i}} \simeq 3.1 \times 10^5 \left(\frac{T_e}{\mathrm{keV}}\right)^{1/2} \left(\frac{Z^*}{A}\right)^{1/2} \frac{\mathrm{m}}{\mathrm{s}} \tag{2.33}$$

If the plasma isothermally expands, the density profile takes an exponentially shape. Thus, the electron density profile is described by

$$n_e(z) = n_{e,0} \exp\left(-\frac{z}{L}\right), \tag{2.34}$$

where L is the scale length. The scale length can be deduced from the ion speed of sound and the expansion time [19]

$$L = c_s \tau \simeq 3 \left(\frac{T_e}{\mathrm{keV}}\right)^{1/2} \left(\frac{Z^*}{A}\right)^{1/2} \tau_{\mathrm{fs}} \text{Å} \tag{2.35}$$

A plasma with Ti^{5+} ions and an electron temperature of 1 keV expands for 2ps. The scale length is then 0.3μm or $L/\lambda = 0.375$, which is a typical value for the expansion of a preplasma.

2.5. Heating Processes - Absorption

The transfer of energy from the laser to the plasma depends on the density profile, the angle of incidence of the laser, the laser intensity and the pulse length. Different absorption mechanisms apply in dependence on those parameters. There is no sharp boundary that defines an absorption regime. Thus, different absorption mechanisms might occur simultaneously [19].
Nevertheless, the different absorption mechanisms are attributed to collisional and collisionless absorption. The driving parameter is the intensity.

2.5.1. Collisonal Absorption

Collisional absorption is the dominating heating process mainly for longer laser pulses with intensities up to $\sim 10^{15}\mathrm{W/cm^2}$. The particles in the plasma collide during the interaction of the laser pulse with the plasma. The electron-ion collision frequency is given by [30]

$$\nu_{ei} = \frac{4\sqrt{2\pi}}{3}\frac{n_e Z e^4}{m^2 v_{te}^3}\ln\Lambda \sim 2.91\times 10^{-6} Z n_e T_e{-}3/3\ln\Lambda \mathrm{s}^{-1}, \tag{2.36}$$

where Z is the ionization state, T_e the electron temperature, v_{te} the thermal electron velocity and $\ln\Lambda$ is the Coulomb logarithm, whereas the Coulomb logarithm is connected with the Debye length λ_D by [19]

$$\Lambda = \lambda_D \frac{k_B T_e}{Ze^2} \tag{2.37}$$

As the electron velocity or the electron temperature are in the denominator in equation 2.36 the collision frequency decreases with increasing temperature. Thus, the energy transfer from electrons to ions decreases with higher temperature.

Inverse Bremsstrahlung

Due to the collisions of the electrons with the ions in the plasma, bremsstrahlung is emitted. The inverse effect occurs in the vicinity of the oscillating laser field. An electron oscillates in the electric field of the laser. During this oscillation the electron collides with an ion, so that energy is transferred from the laser to the ion. Inverse bremsstrahlung occurs predominantly for scale lengths in the order of $L/\lambda \sim 100$ and pulse lengths in the order of nanoseconds.

Skin Effect

For a perfect density step, so that the scale length $L/\lambda \to 0$, the absorption occurs similarly to the Drude model. The plasma behaves like a metal surface with a finite conductivity. In the overdense region the electric field becomes evanescent [19]

$$E(z) = E_0 \exp(-x/l_s), \tag{2.38}$$

where the decay length l_s is [19]

$$l_s = \frac{c}{\omega_P}\left(1 - \frac{\omega^2}{\omega_P^2}\cos^2\Theta\right)^{-1/2} \tag{2.39}$$

In case of $n_e/n_{cr} \gg 1$ the decay length l_s is the collisionless skin depth. The energy of the laser field in the overdense region is again transferred by collisions of oscillating electrons with ions. Thus, radiation is absorbed.
The reflection at the plasma-vacuum interface is described by Fresnel's equations

$$R_S = \left|\frac{\sin(\Theta-\Theta_t)}{\sin(\Theta-\Theta_t)}\right|^2, \qquad \text{for s-polarized light and} \tag{2.40}$$

$$R_P = \left|\frac{\tan(\Theta-\Theta_t)}{\tan(\Theta-\Theta_t)}\right|^2, \qquad \text{for p-polarized light,} \tag{2.41}$$

$$\tag{2.42}$$

where Θ is the angle of incidence and Θ_t is given by [19]

$$\Theta_t = \sin^{-1}\left(\frac{\sin\Theta}{n}\right) \tag{2.43}$$

with n as the refractive index.

2.5.2. Collisionless Absorption

In the previous section (sec.2.5.1) it was mentioned that with a higher temperature, the energy transfer decreases from the laser field to the ions. The electron-ion collisions appear less often. Thus, the fast heating of an ultra-short laser pulse with intensities larger than $\sim 10^{16}\mathrm{W/cm^2}$ comes along with a decrease in collisional absorption.
Collisionless processes become dominant for coupling energy from the laser to the plasma.

Resonant absorption

A plasma is considered that has a density gradient only in one direction - the z-direction. A polarized wave hits the plasma with an angle of incidence different from zero. The electric field oscillates in the y-z plane for a s-polarized wave and in the x-z plane for a p-polarized wave, as depicted in figure 2.2. The dispersion relation is then given by [16]

$$\omega^2 = \omega_P^2 + (k_y^2 + k_z^2)c^2 \tag{2.44}$$

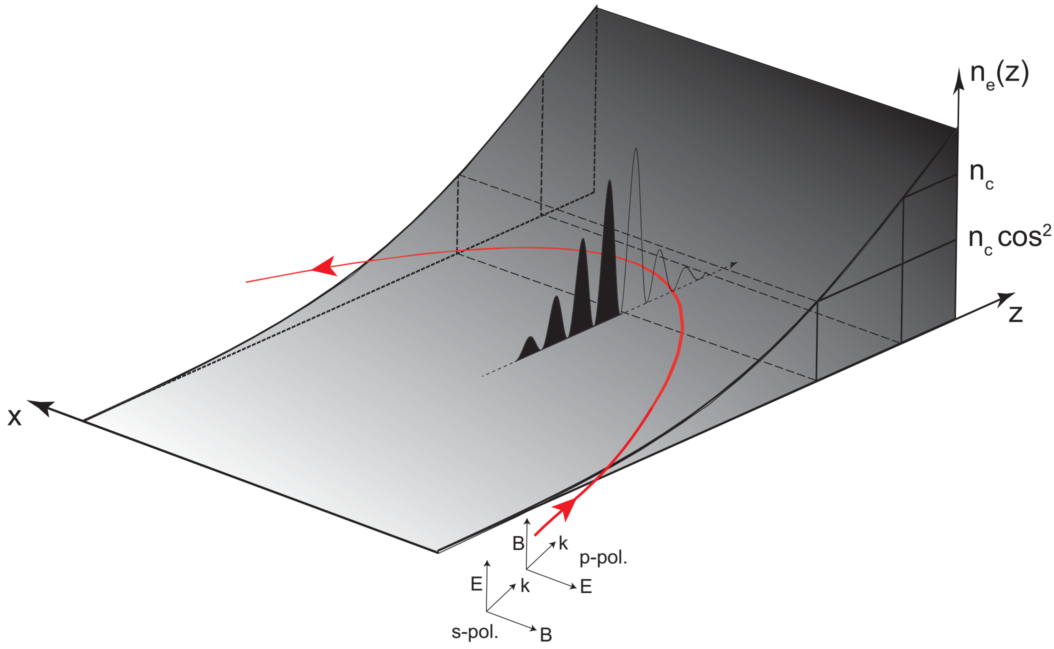

Figure 2.2.: Resonant absorption. [19]

The density depends on the z-direction, so that k_z is a function of z. On the contrary k_y is constant

$$k_y = \frac{\omega}{c} \sin \Theta \tag{2.45}$$

The solution of the wave equations for the electromagnetic fields shows that the wave is reflected at [19]

$$n_{refl} = n_{cr} \cos^2 \Theta \tag{2.46}$$

and the field amplitudes exponentially decay at n_{refl} into the plasma. The fields tunnel to n_{cr}. For a p-polarized wave the electric field component is parallel to the density gradient. At $n_e = c_{cr}$ electrons are excited to oscillate resonantly with the p-polarized electric field. An electrostatic plasma wave - a Langmuir wave - is initiated. The plasma wave propagates longitudinal through the plasma and dissipates its energy by particle trapping and wave breaking [19]. At lower laser intensities the plasma wave dissipates its energy by collisions.
Resonance absorption appears only for p-polarized waves. The electric field of a s-polarized wave does trigger a plasma wave, because the field is perpendicular to the density gradient. A further feature of the absorption mechanism is the strong dependence on the angle of incidence. If Θ is large, reflection occurs already at relatively low densities. Thus, the electric field has to tunnel a larger distance till the critical density, where the plasma wave is excited. If Θ is close to zero, there is no electric field component parallel to the density gradient, so that no plasma wave is excited. A further characteristic of resonant absorption is the generation of hot (fast) electrons. Only a small fraction of electrons absorb a large amount of energy in contrast to inverse bremsstrahlung where all electrons are heated [16].

Vacuum Heating

An absorption process that is highly efficient for p-polarized waves with an angle of incidence different from zero is vacuum heating. For steep density profiles resonant absorption becomes inefficient and vacuum heating dominates the absorption. A plasma wave cannot be generated, if the amplitude of the resonantly oscillating electrons exceeds the scale length.
An electron at the boundary layer between plasma and vacuum is rapidly accelerated into the vacuum during the first cycle of a laser. The field reverses its direction and the electron is accelerated back into the plasma. But as the plasma is overdense, the electric field amplitude decays exponentially. If the mean free path of the electrons in the plasma is larger than the skin depth for the laser, the returning electron propagates beyond the skin depth and dissipates its energy via collisions[19].
This so-called Brunel effect appears for scale lengths $L/\lambda < 0.1$ and intensities in the range of 10^{14} - $10^{18}\mathrm{W/cm}^2$. The effect plays an important role in the generation of high harmonics with wavelengths in the extreme ultraviolet range.

$\vec{j} \times \vec{B}$-heating

A further absorption mechanisms, which has similarities to vacuum heating, is $\vec{j} \times \vec{B}$-heating. The effect occurs for even higher intensities. Vacuum heating is driven by the acceleration of electrons by the electric field. Here the driving mechanism is the fast oscillating $\vec{v} \times \vec{B}$ part of the Lorentz force, which oscillates twice the laser frequency. For a linear polarized wave of the form $E_y = E_0(x)\sin(\omega t)$ the ponderomotive force in the x-direction becomes [31]

$$F_{P,x} = -\frac{m}{4}\frac{\partial v_{os}^2(x)}{\partial x}(1 - \cos 2\omega t) \tag{2.47}$$

The electrostatic part of the ponderomotive force forms a bow in the electron density. The second part of equation 2.47 accelerates an electron out into the vacuum. As the field direction changes again, the electron is accelerated back into the plasma, where the electron dissipates its energy via collisions. In contrast to vacuum heating, $\vec{j} \times \vec{B}$ heating works for s- and p-polarization and is most efficient for normal incidence.

2.6. Laser Interaction with Plasmas

The interaction between laser and plasma is not limited to the heating of the plasma by the laser. Several other effects can occur in dependence on laser intensity and plasma density. Some for this thesis relevant effects are discussed in the following.

2.6.1. Relativistic Transparency

The plasma frequency from section 2.4

$$\omega_P = \sqrt{\frac{n_e e^2}{\varepsilon_0 m_e}}, \tag{2.48}$$

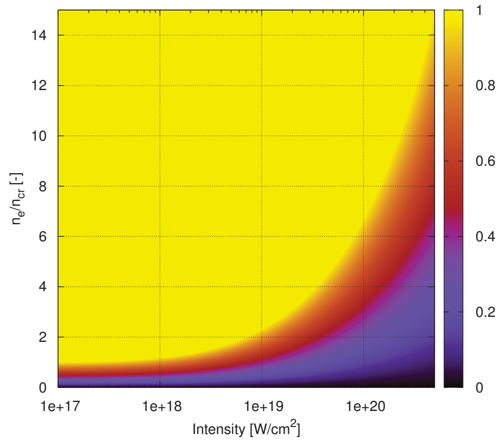

Figure 2.3.: Fraction of electron density and critical density over intensity.

shows, that it is proportional to the fraction of electron density and electron mass. An electromagnetic wave cannot propagate through the plasma, if the angular laser frequency is smaller than the plasma frequency $\omega_L < \omega_P$. For relativistic intensities, i.e. $a_0 > 1$, the motion of the electrons becomes relativistic. Due to the relativistic mass increase of the electron, the plasma frequency has to be corrected by the Lorentz factor

$$\omega_P^2 = \frac{\omega_P'^2}{\gamma}. \tag{2.49}$$

Thus, the plasma frequency is effectively reduced by the cycle averaged γ factor

$$\gamma = \sqrt{1 + a_0^2/2} \tag{2.50}$$

If the electron density is normalized to the critical density

$$n' = \frac{n_e}{n_{cr}}, \tag{2.51}$$

the relativistic opacity of the plasma is determined by $n'/\gamma < 1 < n'$ [25]. Figure 2.3 shows in color the γ corrected electron density normalized to the critical density n'/γ. The ordinate shows the non-relativistic electron density normalized to the critical density n' and the abscissa shows the laser intensity. The relativistic transparency can appear in the preplasma or in already exploded targets for intensities $> 10^{19}\mathrm{W/cm}^2$. The effect in particular takes place for delays between the two pulses in the order of picoseconds, which is described in chapter 6.

2.6.2. Relativistic Self Focusing

As shown in the previous section the mass of an electron increases in the vicinity of a relativistic laser pulse. Therefore the laser interacts with a more inert particle. In a uniform, underdense plasma the laser interacts with numerous electrons, whose mass has relativistically increased, this effect has to be considered in the dispersion relation. The refractive index along the radius of a focused laser pulse is given by [19]

$$\eta(r) = \frac{ck}{\omega} = \sqrt{1 - \frac{\omega_P^2}{\omega^2[1 + a(r)^2/2]^{1/2}}} \tag{2.52}$$

Because the beam is focused, the profile $a(r)$ has its highest value at $r = 0$, so that $d\eta/dr < 0$. This corresponds to a positive lens. A power threshold is given

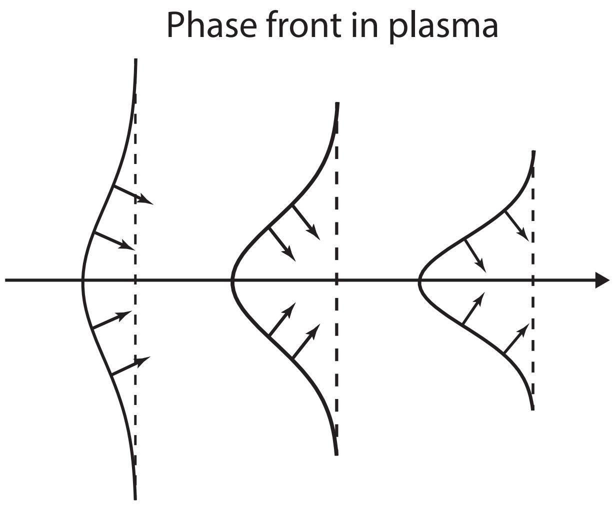

Figure 2.4.: The group velocity of a focused laser beam in a plasma is slower on axis, if the laser has relativistic intensities. The transverse intensity gradient causes different refractive indices and hence different group velocities.

for relativistic self-focusing from the requirement, that the beam's divergence is just balanced by the self-focusing

$$a_0^2\left(\frac{\omega_P \sigma_0}{c}\right) \geq 8, \tag{2.53}$$

where σ_0 is the radius of the focal spot.
The effect becomes significant in the interpretation of the experimental results, where a first laser pulse has expanded the target for 10s of picoseconds and a second laser interacts with the plasma (chapter 6). The expanded plasma is relativistically transparent to the laser, but as the plasma is not underdense, the conventional approach to describe the relativistic self-focusing is somewhat modified (cf. sec. 6.5.4).

2.6.3. Hole Boring

A further effect takes place with intensities of $> 10^{19}$W/cm^2 and plasma densities of several 10s of n_{cr}. The collective motion of ions starts, if the laser pressure P_L exceeds the plasma pressure P_e [18]

$$\frac{P_L}{P_e} = \frac{2I_0/c}{n_e k_B T_e} \gg 1. \tag{2.54}$$

Because the highest intensity is reached at the center of the focal spot, the plasma surface recess and a hole forms. In contrast to simple gas dynamics an electrostatic bow shock comes along with a density discontinuity. The shock can be modeled with one dimensional continuity and momentum conservation equations for the ions [18]

$$\frac{\partial \rho}{\partial t} + \frac{\partial}{\partial x}(\rho u) = 0 \tag{2.55}$$

$$\frac{\partial \rho u}{\partial t} + \frac{\partial}{\partial x} + \frac{\partial}{\partial x}(ZP_e + P_L) = 0, \tag{2.56}$$

where u is the velocity and ρ is the charge density of the ions.
The frame moves with the shock front, so that $\partial/\partial t = 0$. It follows for the integration over the density step

$$\rho u = \text{const.} \tag{2.57}$$

and

$$\rho u^2 = P_L = \frac{I_0}{c}(2 - \eta_a)\cos\Theta, \tag{2.58}$$

where η_a is the laser absorption and Θ the angle of incidence. The re-arrangement of the equation gives [18]

$$\begin{aligned} \frac{u}{c} &= \left(\frac{(2-\eta_a)I_0\cos\Theta}{2\rho c}\right)^{1/2} \\ &= \left(\frac{Zm}{M}\frac{n_{cr}}{n_e}\frac{(2-\eta_a)\cos\Theta}{4}\frac{I_{18}\lambda_\mu^2}{1.37}\right)^{1/2}. \end{aligned} \tag{2.59}$$

A Ti^{20+} plasma with a density of $10 \times n_{cr}$ is considered which does not absorb any laser radiation ($\eta_a = 0$). The laser with an intensity of $I_{18} = 100$ and a wavelength of $800nm$ has a normal angle of incidence. The resulting shock has a velocity of $0.023c$, so that a 5μm deep hole is formed after 720 fs.

2.6.4. Magnetic Field Generation

The interaction between laser and plasma mainly occurs on the level of laser and electrons. If the laser causes a collective motion of the electrons in a loop, magnetic fields are generated. Three different mechanisms where a laser creates current loops are described in the following.

Radial Thermal Transport

For situations, where the electron temperature gradient and the electron density gradient are not parallel, an electric current will start. This so-called thermo-electric source term is given by [19]

$$\frac{\partial \vec{B}}{\partial t} = \frac{\nabla \vec{T}_e \times \nabla \vec{n}_e}{e n_e} \tag{2.60}$$

Usually the density gradient is primarily oriented in the direction of the target normal and the temperature gradient is oriented parallel to the target's surface. If the temperature gradient is only considered to be parallel to the surface by $L_{\|}$ and the density gradient is only considered to be perpendicular to the surface by $L_{\perp}$, the magnitude of the magnetic field is estimated by [9]

$$B \sim 2\left(\frac{\tau}{\mathrm{ps}}\right)\left(\frac{k_B T_e}{\mathrm{keV}}\right)\left(\frac{L_{\perp}}{\mu\mathrm{m}}\right)^{-1}\left(\frac{L_{\|}}{\mu\mathrm{m}}\right)^{-1}\mathrm{MGauss} \tag{2.61}$$

The pressure driven by the magnetic field is in the order of the plasma pressure. If the magnetic pressure is larger than the plasma pressure, it leads to a pinching of the underdense plasma [19].

DC Currents in Steep Density Gradients

The derivation of the ponderomotive force showed that electrons are pushed out of the focal spot region of the laser. The electrons acquire a velocity from the ponderomotive force. A group of electrons gain the velocity [19]

$$\vec{v_P} \propto m_e^{-1}\vec{F_P} \sim \nabla E_L^2, \tag{2.62}$$

if the ponderomotive force $\vec{F_P}(t)$ increases in time. This leads to a current

$$\vec{J} = e n_e \vec{v_P} \sim n_e \nabla I_0 \tag{2.63}$$

With Ampere's law the magnetic field is given by

$$\begin{aligned}\nabla^2 \vec{B} &\sim \nabla \times \vec{J}\\ &\sim \nabla n_e \times I_0\end{aligned} \tag{2.64}$$

Thus, a focused laser that interacts with a density profile will generate a magnetic field in the plasma, due to accelerated electrons. The generated magnetic field is in the same order of magnitude as the magnetic field of the laser [52]. The direction of the generated magnetic field is inversely oriented compared to the magnetic field that occurs with radial thermal transport. Thus, from the magnetic field orientation in simulations one can decide which mechanism applies.

Fast Electron Currents

A further magnetic field generation can appear due to collisionless absorption. Fast electrons are generated during the absorption. These currents move either along the target surface or into the target. The charge imbalance caused by the accelerated electrons is eventually neutralized by a current of cold electrons. A current loop is formed and therewith a magnetic field. The magnitude of the magnetic field is in the region of 10kT for an intensity of $10^{20}\mathrm{W/cm}^2$.

A similar magnetic field pattern that occurs with *DC currents in steep density gradients* is observed in particle in cell (PIC) simulations (cf. sec. 2.8). These PIC simulations modeled the interaction of a laser pulse with an expanded plasma.

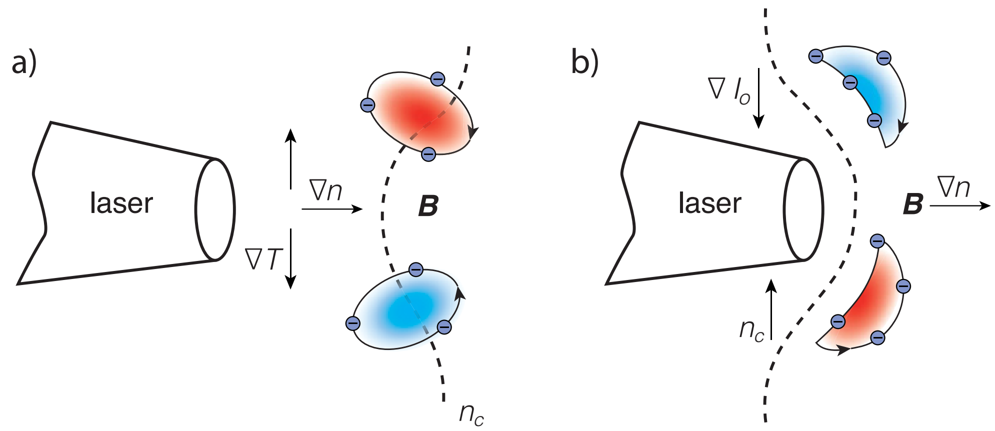

Figure 2.5.: a) Radial thermal transport: electron temperature and density gradients are not parallel. b) DC currents in steep density gradients: an electron current driven by the ponderomotive force. The orientation of thermoelectric driven magnetic field are the opposite to the ponderomotively driven magnetic field. [19]

2.6.5. Conclusion

In the experiment a first laser exploded a target. After 10s of picoseconds a second laser interacts with the expanded target. During the interaction process several effects occur. Some of these effects were described in this section. The plasma becomes relativistic transparent to the second high intensity laser pulse. Due to the thermal expansion of the plasma, the second laser experiences relativistic self-focusing. In the corresponding particle in cell simulation a hole is formed and strong magnetic fields evolve. The results of these simulations are presented in section 6.4.

2.7. Laser-Driven Ion Acceleration

This section will give an overview of the different ion-acceleration mechanism that can occur by todays laser technology. In general target thickness and laser intensity define which is the dominant acceleration mechanism.

2.7.1. Target Normal Sheath Acceleration (TNSA)

Hatchett and Brown [22] observed in the late 1990s for the first time the target normal sheath acceleration (TNSA) mechanism since lasers could exceed intensities of $10^{19} W cm^{-2}$. A detailed description of the mechanism was first given by Wilks et al. [60]. The characteristics are, that a several micrometer thick foil is illuminated by a relativistic laser pulse. The target surface is contaminated by water vapor and hydrocarbons from grease, i.e. finger prints, oil from workshop and so on. The prepulse ionizes the front of the target. This preplasma expands into the vacuum. The main pulse is partially reflected at the critical density of this expanding plasma. The absorbed fraction of the main pulse heats the plasma by $\vec{j} \times \vec{B}$ heating and resonance absorption. Hot electrons are generated which gain energy in the order of

$$E_{kin} = \gamma m_e c^2 = k_B T_{hot}, \tag{2.65}$$

where γ is the cycle averaged Lorentz factor. These hot electrons propagate through the target and form an electron cloud or electron sheath at the rear side of the target. The sheath has an extension in the order of the Debye length

$$\lambda_{D,h} = \sqrt{\frac{\varepsilon_0 k_B T_{hot}}{e^2 n_{e,h}}} \tag{2.66}$$

The contamination layer is also ionized. An ambipolar electric field builds up between the electron sheath and the ions from the contaminants. The electric field has a strength in the order of [24]

$$E \approx \frac{k_B T_{hot}}{e \lambda_{D,h}} \tag{2.67}$$

A laser with an $a_0 = 10$ generates hot electrons with a temperature of about 3.5MeV. The electron density in the electron sheath is in the region of $n_e \sim 10^{20}\mathrm{cm}^{-3}$. From this follows for the extension of the sheath 1.5μm and for the electric field strength $E > 2$TV/m. The ambipolar electric field causes eventually the acceleration of ions. In general the ions of water and grease are much lighter than the ions from the target material, which is usually made from metal.

The accelerated ions have a broad energy spectrum. As the acceleration mechanism originates from hot electrons, the thermal nature is also imprinted in the spectrum of the ions. An unique feature of the accelerated ions is a low transverse emittance. The reason is found in the point-like source of the ions. Instead of a source-size in the order of 100μm achieved with conventional accelerators, the source is in the order of magnitude of a few micrometer. A further feature that supports the low emittance is the charge neutrality of the ion beam. The accelerated ions co-propagate with cold electrons, so that the beam does not interact with the plasma.

2.7.2. Break-out Afterburner (BOA)

Yin et al. [63] identified from PIC simulations an ion acceleration mechanism which is similar to TNSA in the beginning. The linearly polarized laser rapidly ionizes a target. Hot electrons are generated that propagate through the target. An electron sheath builds up on the rear side of the target. Moreover, a return current of cold electrons is set up. Eventually, these cold electrons are also converted into hot electrons. As more and more electrons are accelerated, the electron density decreases in a layer with the thickness of the skin depth. Thus, the skin depth increases and the fields of the laser can penetrate deeper into the plasma. For sufficient thin targets the laser converts all electrons into hot electrons. The whole volume is heated. Eventually, the density of the plasma becomes relativistically transparent to the laser [23]. Two particle species with strongly different velocities now appear in the plasma, namely the relativistic electrons and the slow moving ions. A two-stream instability evolves [5]. The phase velocity of the instability is resonant with the ions, so that the energy is efficiently transferred from the electrons to the ions [62].
In contrast to TNSA, the break-out afterburner mechanism appears only for

ultra thin targets with thicknesses in the order of 10s of nanometer. Moreover, Yin et al.[64] describe that the protons from the contamination layer are fast removed from the target due to the volumetric heating and do not participate at the strong acceleration during the two-stream instability. The mechanism is more efficient for heavy ions, which is the opposite behavior to TNSA.

2.7.3. Radiation Pressure Acceleration (RPA)

Lightsail-regime

A further acceleration mechanism recently gained some interest which is called radiation pressure acceleration. As the name suggests the acceleration is driven by the light pressure of the laser $P_L = I_L/c$. The pressure is high enough to accelerate a whole block of plasma. Therefore the intensity has to be in the order of $> 10^{20}\mathrm{W/cm^2}$ and the target thickness has to be in the order of a few nanometer. In contrast to TNSA where the fast oscillating component of the ponderomotive force of a linear polarized laser strongly heats the electrons, Macci et al [36] describe a circular polarized laser that adiabatically compress the electrons. It evolves an electron depletion area at the plasma surface, which is followed by an electron compression area. Due to the charge separation an electrostatic field is set up. The highest field strength appears at the intersection of both layers. The compression phase stops until the electrostatic field balances the radiation pressure. In the next phase the ions are accelerated in the compression layer. In order to balance radiation pressure and electrostatic field, the electrons follow the ions. Thus, the compression layer moves through the plasma. During this phase further ions are caught up with the passing by compression layer. Eventually, a whole slab of plasma is accelerated to the same velocity. The acceleration is stable as long the electrons remain cold and do not start to expand.
The here described RPA mechanism is a subregime, that is called light sail. There are further subregimes which can be found in [45, 17, 46].

2.8. Particle-In-Cell Code EPOCH

The analytic description of phenomena in plasma physics usually shows that a phenomena has intensively be studied and is understood to a certain degree. In experiments only a limited number of parameters can be measured. In order to deduce from the measured data a consistent picture and description of an observed effect, simulation codes are needed. Particle in cell (PIC) codes are a common tool for the description of kinetic and nonlinear effects in high density plasma physics. Most of the here presented plasma mechanisms are at least validated by a PIC or even have been proposed from a PIC simulation. The basic approach of a PIC code is the simulation of the motion of a large number of charged particles in their own electric and magnetic fields and the laser fields.
In this thesis the PIC code EPOCH is intensively used. The code is freely available on the web [2] and its computational core is based on the PSC code by Hartmut Ruhl. The basic equations for a microscopic plasma description, that are evaluated by the PIC code, are derived in the following sections.

Vlasov Equation

The here presented derivation of the Vlasov equation refer to [26].
A large number N of similar systems is considered, where each system represents a point $\vec{X}_\nu$ ($\nu = 1...N$) in the phasespace. The distribution in the phase space is given by the probability (density) distribution function $f_N(\vec{q}_1, ..., \vec{q}_N, \vec{p}_1, ..., \vec{p}_N) = f_N(q_1, ..., q_{3N}, p_1, ..., p_{3N})$. This function gives the probability to find a particle in a given volume of the phase space. The points in the phase space move with the phase space velocity $\vec{v}(\dot{\vec{q}}, \dot{\vec{p}})$. Analogue to fluid mechanics a probability current

$$\vec{j} = f_N \vec{v} \tag{2.68}$$

is specified. As there are neither phase space points generated nor annihilated, i.e. there is no source or sink, the continuity equation is valid

$$\frac{df_N}{dt} = \frac{\partial f_N}{\partial t} + div\vec{j} = \frac{\partial f_N}{\partial t} + div(f_N \vec{v}) = 0 \tag{2.69}$$

where

$$div\vec{j} = div(f_N \vec{j}) = \sum_{i=1}^{N} \left(\frac{\partial}{\partial q_i}(f_N \vec{j}) + \frac{\partial}{\partial p_i}(f_N \vec{j}) \right) \tag{2.70}$$

From this follows

$$\frac{df_N}{dt} = \frac{\partial f_N}{\partial t} + \sum_{i=1}^{N} \left[\left(\frac{\partial f_N}{\partial q_i} \right) \dot{q}_i + \left(\frac{\partial f_N}{\partial p_i} \right) \dot{p}_i + f_N \frac{\partial \dot{q}_i}{\partial q_i} + f_N \frac{\partial \dot{p}_i}{\partial p_i} \right] \tag{2.71}$$

With Hamilton's equations $\dot{p}_i = -\frac{\partial H}{\partial q_i}$ and $\dot{q}_i = \frac{\partial H}{\partial p_i}$ the last two parts of the sum reduce to

$$\sum_{i=1}^{N} \left[f_N \frac{\partial \dot{q}_i}{\partial q_i} + f_N \frac{\partial \dot{p}_i}{\partial p_i} \right] = \sum_{i=1}^{N} f_N \left[\frac{\partial}{\partial q_i} \frac{\partial H}{\partial p_i} - \frac{\partial}{\partial p_i} \frac{\partial H}{\partial q_i} \right] = 0 \tag{2.72}$$

It remains the Liouville equation

$$\frac{df_N}{dt} = \frac{\partial f_N}{\partial t} + \sum_{i=1}^{N} \left(\frac{\partial f_N}{\partial q_i} \dot{q}_i + \frac{\partial f_N}{\partial p_i} \dot{p}_i \right) = 0 \tag{2.73}$$

The last sum in equation (2.73) is a force on the i-th particle. The force is determined by the position and velocity of all other particles and by external fields. The force term is now separated in a part which results from external fields and a part which originates from the interaction among the particles

$$\dot{\vec{p}_i} = \vec{\Phi}_{i,ex} + \sum_{j \neq i} \vec{\Phi}_{i,j} \qquad , \tag{2.74}$$

where it is switched back from coordinates to vectors.
The large number of independent variables in the Liouville equation makes the solution for practical problems unrealistic. In order to reduce the dimensionality

of the problem, a smaller number of particles s instead of N is considered. The probability density distribution f_s is derived by integrating f_N over the neglected particles $(N-s)$

$$f_s(\vec{q}_1,...,\vec{q}_s,\vec{p}_1,...,\vec{p}_s) = \int f_N(\vec{q}_1,...,\vec{q}_N,\vec{p}_1,...,\vec{p}_N)d^3q_{s+1}...d^3q_N d^3p_{s+1}...d^3p_N \tag{2.75}$$

A reduction of the $6N$ dimensionality of the Liouville equation is now achieved in a first step by connecting the one-particle probability density distribution with the two-particle probability density distribution. Therefore, equation 2.74 is put into the Liouville equation 2.73. Moreover, the relation of equation 2.75 has to be considered

$$\frac{\partial f_1}{\partial t} + \dot{\vec{q}}_1 \frac{\partial f_1}{\partial \vec{q}_1} + \vec{\Phi}_{1,ex} \frac{\partial f_1}{\partial \vec{p}_1} + (N-1)\int \vec{\Phi}_{1,2} \frac{\partial f_2}{\partial \vec{p}_1} d^3q_2 d^3p_2 = 0 \tag{2.76}$$

The general case is

$$\frac{\partial f_s}{\partial t} + \sum_{i=1}^{s} \dot{\vec{q}}_i \frac{\partial f_s}{\partial \vec{q}_i} + \sum_{i=1}^{s}\left(\vec{\Phi}_{i,ex} + \sum_{\substack{j=1\\ j\neq i}}^{s} \vec{k}_{i,j}\right)\frac{\partial f_s}{\partial \vec{p}_i} + \int \sum_{i=1}^{s} \vec{k}_{i,s+1} \frac{\partial f_{s+1}}{\partial \vec{p}_i} d^3q_{s+1} d^3p_{s+1} = 0 \tag{2.77}$$

where the factor $(N-s)$ is neglected, because it is not of interest to know the probability to find a special particle in a specific volume, but the probability to find any particle of a particle species in a specific volume. The full set of N equations of the so-called BBGKY hierarchy (Bogoliubov – Born – Green – Kirkwood – Yvon hierarchy) is equivalent to the Liouville equation, but with the aid of additional assumptions higher steps of the hierarchy can be neglected without loosing too much information. In plasma physics are the interaction between particles and electromagnetic fields of interest. Thus, the introduction of Maxwell's equations into the one-particle distribution 2.76 and the neglect of the interaction between the particles, i.e. collisions, leads to the Vlasov equation

$$\frac{\partial f_1^\mu}{\partial t} + \vec{u}_\mu \frac{\partial f_1^\mu}{\partial \vec{q}} + \frac{q_\mu}{m_\mu}\left(\vec{E} + \vec{u}_\mu \times \vec{B}\right)\frac{\partial f_1^\mu}{\partial \vec{u}_\mu} = 0 \tag{2.78}$$

$$\vec{\nabla}\cdot\vec{E} = 4\pi \sum_\mu \rho_\mu = 4\pi \sum_\mu q_\mu \int f_1^\mu d^3v \tag{2.79}$$

$$\vec{\nabla}\times\vec{B} - \frac{\partial \vec{E}}{\partial t} = \frac{4\pi}{c}\sum_\mu j_\mu = \frac{4\pi}{c}\sum_\mu q_\mu \int \vec{u} f_1^\mu d^3v \tag{2.80}$$

where ρ_μ is the charge density, j_μ is the current, q_μ is the charge, $\vec{v}_\mu$ is the velocity and $\vec{u}_\mu$ is the relativistic velocity of a particle species.

$$\vec{u}_\mu = \frac{\vec{v}_\mu}{\sqrt{1+|v_\mu|^2/c^2}} \tag{2.81}$$

Furthermore it is switched from momentum space to velocity space and μ indicates different particle species.
In the PSC code the right hand side of the Vlaslov equation is not zero, but binary collisions are considered via the Boltzmann collision operator. The equation 2.78 extends to [13]

$$\frac{\partial f_\mu}{\partial t}+\vec{u}_\mu\frac{\partial f_\mu}{\partial \vec{q}}+\frac{q_\mu}{m_\mu}\left(\vec{E}+\vec{u}_\mu\times\vec{B}\right)\frac{\partial f_\mu}{\partial \vec{u}_\mu}=\sum_\nu\int d^3p_\nu v_{\mu\nu}\int d\Omega\sigma_{\mu\nu}(f'_\mu f'_\nu-f_\mu f_\nu) \tag{2.82}$$

$v_{\mu\nu}$ is the relative velocity between the particle species μ and ν. $d\Omega$ is an element of the solid angle between the momentum before $\vec{p}_\mu$ and after $\vec{p}_\mu{}'$ the collision. The cross-section of the interaction is given by $\sigma_{\mu\nu}$. For further information reference [13] gives a comprehensive overview.
The solution of the coupled Maxwell-Boltzmann-Vlasov equations is carried out by the Monte-Carlo Particle-In-Cell method. An essential characteristic of PIC codes is the introduction of a macro particle. In real space the macro particle represents an ensemble of particles with the same mass and charge. This can be done, because these are the only physical constants of a particle appearing in equation 2.82. In phase space the macro particle can be seen as a finite volume of points which have (almost) the same trajectory.

2.8.1. Finite-Difference Time-Domain Method

Besides the description of the motion of the macro or pseudo particles, the electric and magnetic fields have to be described self-consistently. From this follows that Maxwell's equations

$$\begin{aligned}\frac{\partial}{\partial t}\vec{E}&=\vec{\nabla}\times\vec{B}\\ \frac{\partial}{\partial t}\vec{B}&=-\vec{\nabla}\times\vec{E}\end{aligned} \tag{2.83}$$

have to be solved in the time domain. A common approach for PIC codes to perform this task are Finite-Difference-Time-Domain solver. The fields are evaluated by the solver on a grid. The smallest element of this grid is a so-called Yee cell. In 3D the Yee cell is a cube (see figure 2.6). The electrical field components are placed at the cube edges and the magnetic field components are placed at the center of the cube surfaces. This approach takes advantage in the approximation of Maxwell's curl equations. As the abbreviation of FDTD suggests, the FDTD scheme solves Maxwell's equations in the time domain. Moreover, the differential operators are replaced by differences [53]

$$\begin{aligned}\frac{\partial}{\partial t}\vec{E}=\vec{\nabla}\times\vec{B}\quad&\rightarrow\quad\frac{\vec{E}(t+\Delta t)-\vec{E}(t)}{\Delta t}=\vec{\nabla}\times\vec{B}(t+\frac{\Delta t}{2})\\ \frac{\partial}{\partial t}\vec{B}=-\vec{\nabla}\times\vec{E}\quad&\rightarrow\quad\frac{\vec{B}(t+\frac{\Delta t}{2})-\vec{B}(t-\frac{\Delta t}{2})}{\Delta t}=-\vec{\nabla}\times\vec{E}(t)\end{aligned} \tag{2.84}$$

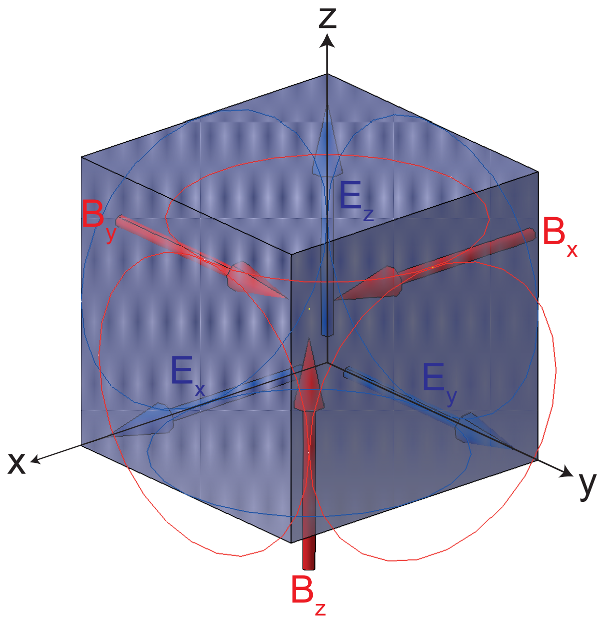

Figure 2.6.: Yee Cell.

An update is performed in the following manner [53]

$$\begin{aligned}
\frac{\vec{E}(t+\Delta t)-\vec{E}(t)}{\Delta t} &= \vec{\nabla}\times\vec{B}(t+\frac{\Delta t}{2}) \\
\rightarrow \qquad \vec{E}(t+\Delta t) &= \vec{E}(t)+\Delta t\vec{\nabla}\times\vec{B}(t+\frac{\Delta t}{2}) \\
\frac{\vec{B}(t+\frac{\Delta t}{2})-\vec{B}(t-\frac{\Delta t}{2})}{\Delta t} &= -\vec{\nabla}\times\vec{E}(t) \\
\rightarrow \qquad \vec{B}(t+\frac{\Delta t}{2}) &= \vec{B}(t-\frac{\Delta t}{2})-\Delta t\vec{\nabla}\times\vec{E}(t) \qquad (2.85)
\end{aligned}$$

With this set of equations 2.85 the solver scheme is as follows [53]

- Update $\vec{E}$ from $\vec{B}$: $\vec{E} \Leftarrow \vec{D}$
- Handle E field boundaries
- Handle E field source
- Update $\vec{B}$ from $\vec{E}$: $\vec{B} \Leftarrow \vec{E}$
- Handle B field boundaries
- Handle B field source

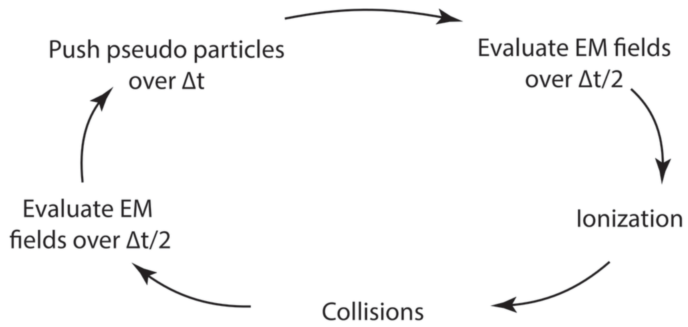

Figure 2.7.: Calculation scheme of the PIC code PSC [54]

2.8.2. EPOCH

The basic sets of equations that are used in a PIC code were presented. The PIC code preforms time steps in a calculation loop. In a first step the code checks via Monte-Carlo algorithm, if a particle is ionized or not. The ionization routines include Multi-Photon-Ionization and Barrier-Suppression-Ionization, whereas BSI is realized in an ADK routines (cf. 2.2). EPOCH has the capability to consider collisions based on a model from Sentoku and Kemp [49]. The collision evaluation routine would appear in the solver scheme after the ionization routine, but the routine is omitted in the here presented simulations (cf. 2.5.1). After the ionization the FDTD solver calculates the electromagnetic fields at the time $t+\Delta t/2$. The Vlasov equation is evaluated for the whole Δt, so that the particle positions are updated. Afterwards the Maxwell equations are calculated for the remaining half time step. The FDTD solver considers now the new positions of the particles. The loop is closed by the call of the ADK routine. The solver scheme is shown in figure 2.7.

The simulations were carried out on the cluster MOAC. The cluster is part of the Institute for Laser- and Plasma Physics at the Heinrich-Heine-University Düsseldorf. The cluster consists of 8 blades. The blades are connected via an InfiniBand interface. Each blade has four octo-core Intel Xeon E7-4820 working at 2GHz. In total the cluster has 256 cores, where two commands can be processed per cycle by hyper threading, so that 512 logic cores are available. The total memory of MOAC is 753GB. The local hard disk space of MOAC is 10TB. Additionally, two QNAP NAS systems with 15 TB each are accessible to the cluster.

The computational time for the simulations shown in chapter 4 was usually in the order of 15 hours. The size of the produced output was 1 TB. Some details of the simulation parameters are found in the appendix A.4.

2.9. CST

A further simulation tool that is used in the frame of this thesis is the software *CST*. The evaluation of the Thomson parabola spectrometer (cf. section 3.3.4) is made with the aid of the software module *Particle Studio*. In section 6.5.2 the module *Microwave Studio* is applied for the motivation of the use of transmission line theory for the description of the laser in a plasma channel.

The code originates from the software tool package *MAFIA* that was developed at the TU Darmstadt and is based on the Finite Integration Technique (FIT) that was developed by T. Weiland [56]. The fundamentals of the FIT are presented in this section.

Finite Integration Technique

The here presented basic constraints of FIT refer to [57] and [56]. The FIT discretizes the Maxwell equations in their integral notation

$$\oint\limits_{\partial A} \vec{E} \cdot d\vec{s} = -\int\limits_{A} \frac{\partial}{\partial t}\vec{B} \cdot d\vec{A} \tag{2.86}$$

$$\oint\limits_{\partial A} \vec{H} \cdot d\vec{s} = \int\limits_{A} \left(\frac{\partial}{\partial t}\vec{D} + \vec{J}\right) \cdot d\vec{A} \tag{2.87}$$

$$\oint\limits_{\partial V} \vec{D} \cdot d\vec{A} = \int\limits_{V} \rho dV \tag{2.88}$$

$$\oint\limits_{\partial V} \vec{B} \cdot d\vec{A} = 0 \tag{2.89}$$

to a staggered grid. The grid is similar to a Yee cell as shown in figure 2.6, but here are two grids. The so-called primary grid is assembled from cells with electric field components only. The so-called dual grid is shifted by half an edge length and is assembled only from cells with magnetic field components. Each cell of the grid is linked with the material properties ε_r, μ_r and κ. Faraday's

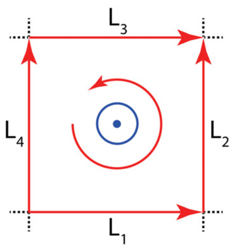

Figure 2.8.: Line integral for the electric field for one surface of the primary grid. [57]

law of induction for a surface of one mesh cell is shown in figure 2.8. The line integral of the electric field for this mesh cell is

$$\begin{aligned}\oint\limits_{\partial A} \vec{E} \cdot d\vec{s} &= \int\limits_{L_1} \vec{E} \cdot d\vec{s} + \int\limits_{L_2} \vec{E} \cdot d\vec{s} - \int\limits_{L_3} \vec{E} \cdot d\vec{s} - \int\limits_{L_4} \vec{E} \cdot d\vec{s} \\ &= e_1 + e_2 - e_3 - e_4 = \sum_{i=4}^{4} e_i,\end{aligned} \tag{2.90}$$

which is the sum of the edge voltages $e_i = E_i a$. The magnetic flux through the surface A for one mesh cell is given by $-\partial_t b_n$, so that Faraday's law of induction for one mesh cell is

$$e_1 + e_2 - e_3 - e_4 = -\frac{\partial}{\partial t} b_n, \tag{2.91}$$

which is exact. If several mesh cells are considered, one get a system of equations of the form

$$
\begin{pmatrix}
1 & 1 & -1 & -1 & & & & \\
 & -1 & & & 1 & 1 & -1 & \\
\vdots & & \ddots & & & & & \\
 & & & & & & & \\
 & & & & & & & \\
 & & & & & & & \\
 & & & & & & &
\end{pmatrix}
\cdot
\begin{pmatrix} e_1 \\ e_2 \\ e_3 \\ e_4 \\ e_5 \\ e_6 \\ e_7 \\ \vdots \end{pmatrix}
= -\frac{\partial}{\partial t}
\begin{pmatrix} b_1 \\ b_2 \\ \vdots \\ \\ \\ \\ \\ \\ \end{pmatrix}
$$

$$
\mathbf{C}\vec{e} = -\frac{\partial}{\partial t}\vec{b}, \tag{2.92}
$$

where the matrix $\mathbf{C}$ corresponds to the analytic curl operator and contains only $-1, 0, 1$. Similarly to Faraday's law of induction, the remaining Maxwell's equations are translated into a matrix equation. The total set of Maxwell equations in matrix notation is given by

$$
\begin{aligned}
\mathbf{C} \cdot \vec{e} &= -\frac{\partial}{\partial t}\vec{b} \\
\mathbf{C}_{dual} . \vec{h} &= \frac{\partial}{\partial t}\vec{d} + \vec{j} \\
\mathbf{S}_{dual} \cdot \vec{d} &= \vec{q} \\
\mathbf{S} \cdot \vec{b} &= 0,
\end{aligned} \tag{2.93}
$$

where $\mathbf{S}$ corresponds to the divergence operator. The material properties are also rewritten in matrix notation

$$
\begin{aligned}
\vec{d} &= \mathbf{M}_{\varepsilon} \cdot \vec{e} \\
\vec{b} &= \mathbf{M}_{\mu} \cdot \vec{h} \\
\vec{j} &= \mathbf{M}_{\kappa} \cdot \vec{e} + \vec{J}_S
\end{aligned} \tag{2.94}
$$

The solution of this set of matrix equations involves no approximation. Only during the discretization of space approximations are made in dependence on the grid resolution.

Particle Studio

The software module is used for the tracking of charged particles during their motion through a configuration of magnetic and electric fields. The setup of the Thomson parabola spectrometer (cf. 3.3.4) is modeled similar to a CAD software in 3D. Physical parameters are specified for the magnets as well as the voltage applied at the electrodes. In a first step the solver applies the finite integration method and solves Maxwell's equations. As the fields are known in 3D the different ion species are sent through the spectrometer with different velocities. Therefore the force acting on a charged particle is calculated. Then the particles are moved according to the calculated force. Eventually, a trajectory of a charged particle is determined.

The particle tracker has turned out to be highly reliable. The remanescent given from the manufacturer of the magnets is used for the calculation of the trajectories through the spectrometer, which corresponds exactly with the calibration of the spectrometer.

Microwave Studio

The *Microwave Studio* is a widely used tool in the development of communication devices. Electro-magnetic waves from a few Hz to PHz can be simulated in an arbitrary environment. Thus, the solver can also be applied for optical problems, with the restrictions that for those problems the spatial domain is usually limited by the available machine time.
In section 6.5 the software module is used for the motivation of the use of transmission line theory. The laser fields are described as modes in a hollow metallic conductor - in a waveguide.

2.10. Conclusion

The chapter begun with the interaction between a single atom and an EM wave. In dependence on the magnitude of the fields, different ionization mechanisms occur. But as there is no sharp boundary between the ionization regimes, they might appear simultaneously.
After the ionization of an atom the laser fields can interact with electrons. The behavior of a single electron in the vicinity of a (relativistic) laser field is described. But as there is usually more than one electron, the basic parameters that describe the collective behavior of a plasma are given.
Energy is transferred from the laser to the plasma by different absorption mechanisms. In dependence on the angle of incidence and the plasma density, the absorption mechanism differs. Collisionless absorption occurs during the experiment. In particular a combination of resonant absorption and $\vec{j} \times \vec{B}$ heating appears.
Not all of the laser energy is transferred to the plasma, so that the laser can strongly interact with the plasma in other ways. The described phenomena are relevant for observed effects in the experiment and in simulations or are at least similar to those effects. In dependence on the plasma density and the laser intensity the plasma becomes relativistically transparent to the laser, due to the relativistic mass increase of the electron [23]. Additionally the electrons in the plasma might cause a further focusing of the laser. The combination of these two effects play a role during hole boring and the generation of strong magnetic fields. The magnetic fields are caused by the acceleration of electrons and an evolving return current of cold electrons.
In the past decade several ion acceleration mechanisms have been proposed. The most relevant mechanism that might appear, due to the laser intensity or the combined intensity of two laser pulses, were presented. Moreover the different ion acceleration regimes depend on the target thickness.
The experimental results have been extensively interpreted by particle in cell simulations. The fundamentals of the code were briefly explained. The evaluation of the experimental results was done with the aid of the software package *CST*, due to its wide application in science and research the fundamentals of the code are also briefly presented.

3. Setup and Diagnostics

This chapter comprises the description of the experimental setup and the applied diagnostics. The Arcturus laser and its components are described in detail. Results are presented of the pulse's temporal and spatial shape.
The second section of this chapter presents the main diagnostics - a Thomson parabola spectrometer (TPS) - and their underlying physical mechanisms. The calibration results of the main diagnostic are shown. The calibration comprises the determination of the dispersion of the Thomson parabola and the cross-calibration of the Thomson parabola with CR39 nuclear track detectors.
The last part of this chapter introduces briefly radio-chromic-film detectors and its results.

3.1. The Arcturus Laser Facility

The Arcturus laser system is a commercially available table-top, high power laser system from the company *Amplitude Technologies*. The laser is based on the chirped pulse amplification scheme. The scheme is shown in figure 3.1. An

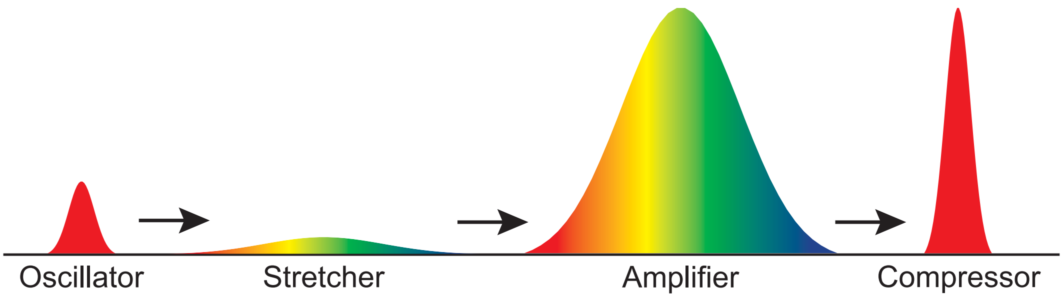

Figure 3.1.: Chirped Pulse Amplification

ultra-short laser pulse is stretched in time. The pulse has low energy and a large bandwidth. By stretching the pulse in time, the intensity of the pulse is even more reduced. This low intensity laser pulse can be amplified to high pulse energies. Because the pulse is stretched in time, the intensity is still below the

damage threshold of the optics. In a last step the pulse is again compressed in time. If the laser pulse is now focused, intensities in the order of 10^{20}W/cm^2 are reached.
The Arcturus laser has three beamlines: two main beamlines and a probe beamline. The pulse length's of each pulse can be smaller than 25fs. In beamline I the pulses reach energies of 3J before compression and in beamline II 4J before compression. The pulse energies of the probe beam are in the order of 100mJ. A few key components of the laser are described in the following similarly as in [20] and can be found in the schematic of 3.2.

3.1.1. Front-End

Oscillator

Both main pulses and the probe pulse originate from the same oscillator. The oscillator is a Ti:Sapphire laser system ($Ti^{3+}Al_2O_3$) from the company *Femto GmbH*. The titanium-doped sapphire crystal is pumped by a 5W laser diode at 532nm in cw. The laser pulses have a wavelength of roughly 800nm and a bandwidth of a 100nm. The pulses have a pulse length shorter than 25 fs and an energy of about 5nJ. The repetition rate is 75MHz.

Booster

As the energy of the oscillator's pulses are very low, the first device after the oscillator is the booster, that increases the energy from nJ to μJ. A Pockel's cell reduces the repetition rate from 75MHz to 10Hz. Thus, the cell picks 10 pulses per second from the 75MHz pulse train. A Ti:Sapphire crystal is pumped by the second harmonic of a Nd:YAG laser from *CFR Ultra*. The laser pulses pass several times through the crystal. Afterwards the temporal contrast is enhanced by a saturable absorber, i.e. the pulse is cleaned from the ASE (amplified spontaneous emission).

Stretcher

At this stage the laser pulse has still a length of several 10s of femtoseconds, which is far too short in order to apply chirped pulse amplification scheme. Therefore, the pulse is directed into a grating stretcher, which is a somewhat modified Offner spectrometer. The stretcher consists of two concentrically mounted spherical mirrors and a grating. The setup prevents chromatic aberration. The configuration of the spherical mirrors and the grating sorts the laser wavelength in time - a chirp is introduced. The pulse length is increased to roughly 500ps. A further device is installed in the stretcher module. The Dazzler is an acousto-optical filter that compensates group velocity dispersions and improves by this the contrast of the pulse after compression. The aim is to have a flat, minimum phase which results in a short pulse.

Regenerative Amplifier

Similar to the Booster, a Ti:Sapphire crystal is pumped by the *CFR Ultra* Nd:YAG laser in the regenerative amplifier. Two Pockel cells are used to control the seeding and outcoupling from the laser cavity. The pulses perform

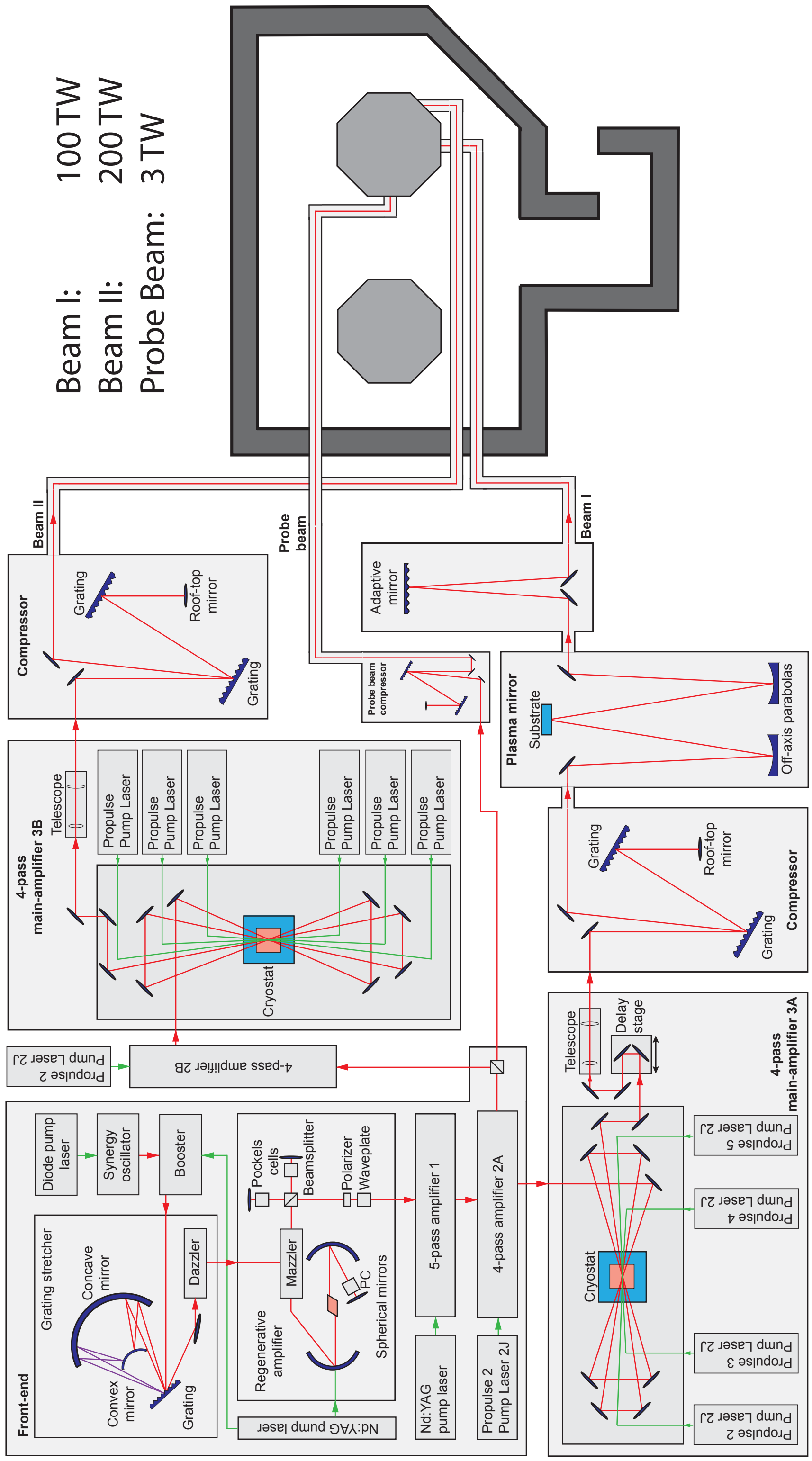

Figure 3.2.: The Arcturus Laser Facility in Düsseldorf.

several passes through the amplifying crystal and gain an energy of about 1mJ. The Pockel cell configuration also enhances the contrast of the pulses. An acousto-optical modulator is applied similar to the stretcher. The Mazzler filters unwanted spectral components. A gap is generated in the spectrum. This gain flattening increases the width of the spectrum.

Multipass 1 and Multipass 2A Amplifier

The first main amplifier crystal is pumped by the second harmonic of a *CFR 200* Nd:YAG laser. The pump laser has a pulse energy of 120mJ. Laser pulses are amplified to 23mJ. After amplification the laser beam is expanded by a telescope. The subsequent Multipass 2A amplifier is pumped by a *Propulse* 532nm Nd:YAG laser, which provides 2J of laser pulse energy. A laser pulse does four round trips in this amplifier through the Ti:Sa crystal. Afterwards it has an energy of about 600mJ.
The last element of the Multipass 2A Amplifier and therewith of the front-end is a 50:50 beam splitter. The pulse is directed into beamline I and beamline II, whereas in beamline II a second beam splitter separates 5% of the pulse energy into the probe beam line.

3.1.2. Beam I

Multipass 3A Main Amplifier

The last amplification stage for beam I is a 4-pass amplifier. The Ti:Sa crystal is pumped by four frequency doubled *Propulse* Nd:YAG lasers, where each Nd:YAG laser delivers 2J. The maximum pulse energy of beamline I is 3J. After four passes though the crystal a double pass delay stage is implemented for the experiment. The maximum travel distance of the linear stage is 5cm. Therefore the maximum delay range covered with the delay stage is ±166ps. The delay stage is moved by a micrometer screw. In combination with a *Heidenhain* glass scale, the delay is controlled with an accuracy of 5fs.
Due to the size of the Ti:Sa crystal of $5 \times 5 \times 3\text{cm}^3$, the diameter of the beam after amplification is limited to about 3cm. For the temporal compression and for reduction of damages to the optics, the beam is expanded by a telescope to 8cm.

Compressor

In the compressor are two gold coated gratings aligned parallel - with grating side to each other. The pulse enters the vacuum chamber through a window and is directed by the first grating to the second grating. This grating directs the pulse to a roof-top mirror, that reflects the pulse back onto a lower level of the second grating. By changing the level of the beam path, the gratings are used twice. Afterwards the pulse leaves the compressor.

Plasma Mirror

The plasma mirror is used to enhance the temporal contrast of the laser. The laser pulse is focused onto a dielectric substrate with an anti-reflecting coating, so that prepulse and ASE with a lower intensity compared to the main

pulse should be transmitted by the glass. If the a certain intensity threshold is reached, a plasma is ignited on the surface of the substrate. In dependence on the electrons' density in the plasma, the laser is reflected. Thus, the AR (anti-reflection) coated substrate acts as an ultrafast optical switch. A second off-axis parabolic mirror images the interaction, i.e. the parabola collects the laser light and directs the laser back into the beamline. The intensity of the pulse is tweaked by the focal position. In order to make the control of the focal position easier and more reliable, a large focal length 1524mm is chosen for the off-axis parabolic mirror.
A further advantage of a plasma mirror is the defect on the substrate generated by the rising flank of the main pulse. The defect prevents any larger laser energy reflected back into the beamline - in direction to the main amplifier and the compressor. The energy of those reflections can be high enough to destroy the sensitive optical components.
Additional information regarding the plasma mirror can be found in the PhD thesis by A.-L. Giesecke [20].

Adaptive Mirror

The adaptive mirror can modify the wavefront of the laser. The substrate surface is mechanically controlled by 32 Piezo-elements. The wavefront is measured by a Shack-Hartmann sensor. The sensor is installed right before the vacuum target chamber behind a mirror, that transmits enough radiation for the sensor. A computer program analyzes the wavefront and controls the Piezo elements of the adaptive mirror. The main aim of the adaptive mirror is to achieve a smooth gaussian shaped focal spot by modifying the wavefront.
The adaptive mirror was not used in the experiment.

Pulse Energy of Beam I on Target

After the main amplifier the laser pulse passes through compressor, plasma mirror and the beamline, where energy is lost due to absorption or imperfect beam alignment. The pulse energy that arrives on target was not measured. After the experiment beamline and compressor gratings were inspected. It is estimated from former experiments and from the inspection, that only 25% of the pulse energy after amplification arrive on target.

3.1.3. Beam II

Multipass 2B Amplifier

In contrast to beamline I, beamline II has a further amplification stage before the main amplifier. The 4-pass amplifier is pumped by a *Propulse* Nd:YAG laser with 1.2J pulses at 532nm. The pulse energy is increased from 300mJ to 600mJ

Multipass 3B Main Amplifier

The beam path difference of beam I and beam II was measured in advance. As the beam path of beam II was too short, a static delay stage was implemented in the multipass 3B main amplifier. Both beams are timed by this 5cm precise,

so that the delay stage in the multipass 3A main amplifier can overlap both main pulses in time.
The five *Propulse* Nd:YAG lasers of this main amplifier are equipped with LBO crystals instead KDP crystals for the generation of the second harmonic. The pulse energy of each laser is increased by this from 2J to roughly 2.5J. The pulses in the beamline II can reach before compression 4J.

Compressor

The setup of the compressor in beamline II is similar to the compressor in beamline I.

Plasma Mirror

At the time of the experiment the plasma mirror for the second beamline was in development, but not implemented. Thus, the contrast of beam I is better. A further consequence from this is, that during the experiment, it must be ensured that only radiation with a low intensity is reflected back into beamline II.

Adaptive Mirror

Similar to beamline I an adaptive mirror could have been used for the experiment, but this was not the case.

Pulse Energy of Beam II on Target

Similar as already described for beam I in section 3.1.2 pulse energy is lost at the gratings in the compressor and in the beamline, so that 4J cannot be expected on target. Again, the energy on target was not measured, but is estimated to be only 25% of the energy after amplification.

3.1.4. Probe Beam

Delay Stage

The probe beam neither have any further amplification stages nor other laser pulse enhancement devices. Therefore the beam path is much shorter compared to the main pulses. In order to have the probe beam temporally overlapping with the main pulses, several meter of beam path are implemented as well as a motorized delay stage.

Compressor

The probe beam has its own compressor. Instead of picking up some energy from a main pulse for a probe beam, where the probe pulse would have the same pulse length as a main pulse, the probe pulse length can be controlled independently from the main pulses. Thus, different processes can be probed, that might happen on different - longer - timescales than the main pulses.
The probe beam is used during the experiment for the TASRI diagnostic. This diagnostic is applied only a few times.

3.1.5. Bunker

A further important part of the Arcturus laser facility is the radiation safety bunker. Due to the high intensity that can be reached with the laser system, ionizing radiation is generated and particles are accelerated. The radiation safety regulations in germany require a radiation safety bunker in order to perform those experiments. The bunker walls consist out of rigid concrete, where small iron sphere are implemented in the bricks. The entrance into the bunker has a chicane. The beamlines are also entering the bunker via a chicane. Therefore, any straight propagating particle or photon is absorbed in the wall.

3.2. Experimental Setup

Two vacuum target chambers are installed in the bunker. The octogon-shaped chambers have an inner diameter of roughly 800mm and a usable height of 450mm. Chamber I is mainly used for experiments with gases. Chamber II is usually used for experiments with solid targets, as for this experiment. In preparation of this first two beam experiments, the chamber had to be redesigned. Two laser beams with a diameter of about 80-100mm have to be aligned, so that both beams interact with the target from the same side. For this purpose the roof of the chamber had to be replaced by a new, larger one, so that the useable height is increased by further 330mm.
One of the main advantages of the Arcturus Laser System is the relatively high repetition rate of 10 Hz for a high power system. A special target device is used, in order to utilize this advantage without venting the chamber after each shot. The device follows the principle of a magnetic tape recorder. A 5μm thin, 5mm high and 10m long titanium tape is spooled on a coil. A second coil is used as a spool for the used target. Four polished, round, thin bars made from brass are holding the tape in the focal position while the coils rotate.

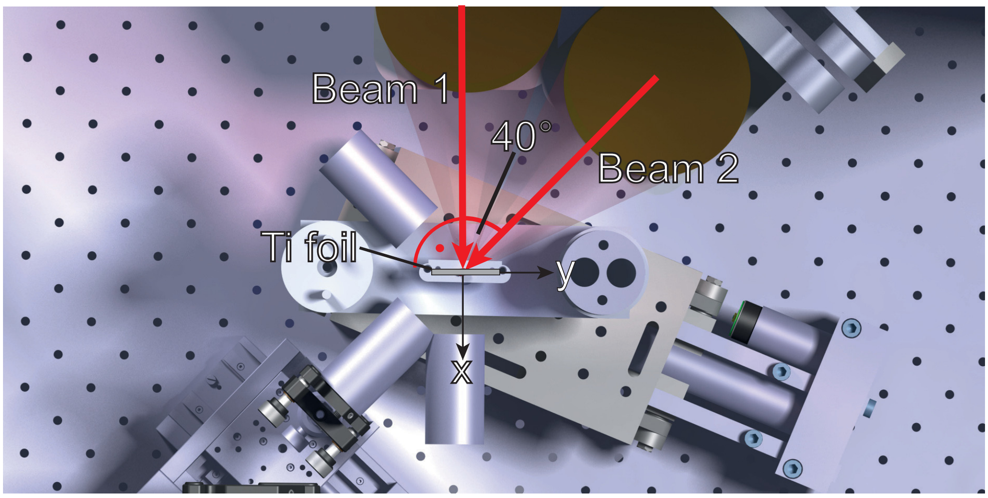

Figure 3.3.: Setup of the main diagnostic.

In figure 3.3 the setup of laser and target is shown. It shows in a top-view the tape target device with its two coils and the two 90° off-axis parabolas. The parabolas have a diameter of 101.6mm and an effective focal length of 152.4mm.

Beam I is perpendicular to the target - has an angle of incidence of 0°. Beam II has an oblique angle of incidence of about 40°. The probe beam illuminates the rear side of the target under an angle of roughly 45°. Three cylinders are located around the tape target. The cylinders are CAD dummy models for the focal diagnostic used microscopic objectives. The objectives are mounted on motorized linear stages.
The shown coordinate system in figure 3.3 is the same as it will be used in the PIC simulations.

3.2.1. Spatial and Temporal Laser Pulse Shape

Spatial Shape - Focus and Caustic

The measurements of the focal spots and their optimization is done with three *Mitutoyo* (10x Plan Apo Infinity-Corrected Long WD Objective) microscope objectives. The objectives are mounted onto motorized linear stages, so that the objectives can be moved within the vacuum. The light from the objectives is directed through windows out of the vacuum onto three *Basler scA640-74gm* CCD cameras.
The results of the caustic measurements can be found in the appendix A.2.1. The diameter of both focused main beams is roughly 5μm.

Temporal Shape

Introduction

The pulse length measurement is done with a device called Wizzler from the company *Fastlite*. The device utilizes Fourier-transform spectral interferometry (FTSI) and the cross-polarized wave effect (XPW-effect). The technique of self-referenced spectral interferometry (SRSI), which is applied in the Wizzler, uses FTSI and the XPW-effect for the pulse measurement. The effect and the basic principles are briefly explained in the following and refer to [14, 35, 3].

Fourier-Transform Spectral Interferometry

A spectrum in the frequency domain is considered. The spectrum is the interferogram of two delayed pulses. If the inverse Fourier transformation is taken, three peaks appear. The oscillating term in the time domain is centered between the delay of the two pulses. This peak is numerically filtered so that only the high frequency term remains. The result is again transformed into the frequency domain. Eventually, the result provides information about the phase difference of the two pulses and the product of the spectral intensities.
If the high frequency part is filtered instead of the continuos part, one gets information about the sum of the two spectral intensities. Thus, the two spectral amplitudes can be reconstructed.

XPW-Effect

Cross-polarized wave (XPW) generation is a third-order nonlinear effect. A linearly polarized wave is generated orthogonally from a high-intensity linearly polarized input wave. The amplitude of the cross-polarized wave in time depends on the input wave by

$$E_{XPW}(t) \propto | E_{in}(t) |^2 \cdot E_{in}(t) \tag{3.1}$$

The XPW-effect can be described as a temporal filter, because the generated pulse is just a copy of the initial pulse, where the pulse is filtered by its own temporal intensity. Hence, the XPW-pulse will have a broader spectrum and an even phase, as the pulse is shorter.

Self-Referenced Spectral Interferometry

The Wizzler summarizes these effects to a measurement technique called self-referenced spectral interferometry. A copy of the prepulse is made by a birefringent plate. The copy's polarization is perpendicular to the input's pulse. Moreover the copy is delayed in time. The XPW-effect is used in a second stage in order to generate from the main pulse a reference pulse with a broader spectrum and a flatter spectral phase, but with the same carrier frequency. The copied pulse from the birefringence plate and the reference pulse from the XPW filter now have the same polarization. Thus, the main pulse can be filtered by a polarizer and the two remaining delayed pulses can interfere in a spectrometer. The FTSI principle is applied to the spectrum from the two pulses and spectral phase and amplitude are reconstructed from the signal.

Conclusion

The *Wizzler* allows a robust and easy measurement of the pulse's temporal shape and it's phase. For the measurements two pick-off 1" mirrors are mounted on motorized linear stages in the vacuum chamber. The mirrors are moved into the beam path of beam I and beam II, respectively. Each mirror directs some radiation out of the vacuum through a 2mm thick BK7 window to the *Wizzler*. The detailed results of the measurements can be found in table A.2.2 in the appendix. *Mazzler* and *Dazzler* settings are optimized to have two short pulses. The pulse length in both beams is 23 fs during the shot series at the 15th and 16th of October 2012.

3.3. Main Diagnostic

Introduction

In this section the main diagnostic of the experiment is described in detail. In order to evaluate the measured data, it is necessary to understand the physical mechanisms that occur in the diagnostic and detector. Hence, the spectrometer - a Thomson parabola spectrometer (TPS) - is described in detail as well as the applied detector - a multi-channel-plate (MCP).
The magnetic field of the Thomson parabola has to be calibrated for a precise energy determination. The calibration with metallic filters and an image plate

is shown subsequently. In order to derive spectra from the MCP traces, the MCP is cross-calibrated with the nuclear track detector CR39. The intensity on the MCP image is correlated with a particle number on the CR39.
The electrodes of the TPS are hit by ions at each shot, so that the voltage of the electrodes drops with each shot. In addition the magnetic field showed inhomogeneities. In order to account for these effects, the TPS is extensively simulated with a 3D electromagnetic simulation program *CST*.
Finally, the results of the simulations and of cross-calibration are merged into a *C*-program. The program evaluates semi-automatically the MCP images and generates ion spectra and determines the cut-off energies.

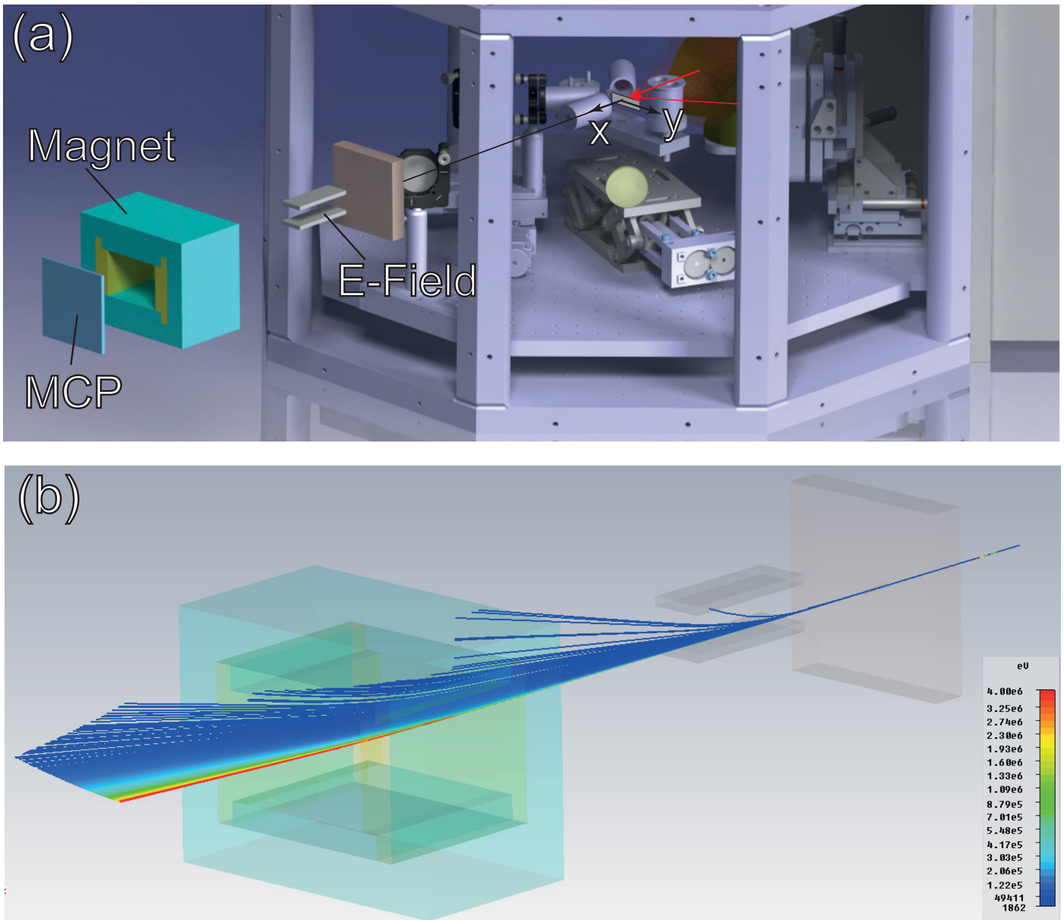

Figure 3.4.: a) Setup of the Thomson parabola spectrometer with the multi-channel-plate as detector. b) Proton trajectories for different kinetic energies through the E- and B-field of the Thomson parabola spectrometer.

3.3.1. Thomson Parabola Spectrometer

The Thomson parabola spectrometer (TPS) is a widely used detector in the field of laser particle acceleration. Its low sensitivity on radiation from the laser as well as from the laser plasma interaction are ideal for a robust and reliable detection of different ion species.
In a TPS are an electrical and a magnetic field parallel aligned to each other. The path of a positively charged particle is shown in figure 3.5. The electric field causes a deflection in the vertical direction. The deflection caused by the magnetic field is in the horizontal direction only. As the grade of deflection

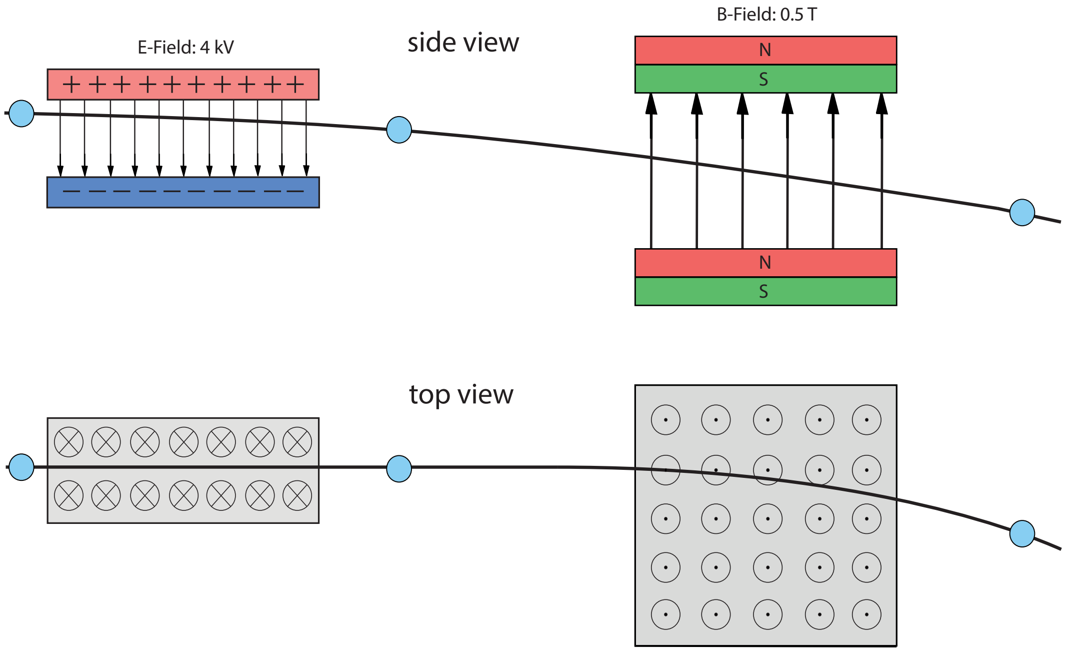

Figure 3.5.: Basic schematic of a Thomson parabola spectrometer. A positively charged particle moves through the configuration of the electric and magnetic field. The electric field causes a deflection downwards. Due to conservation of momentum, the particle continues its path in the downwards direction after leaving the area of the electric field. The deflection of the magnetic field is perpendicular to the particle's motion and to the magnetic field. Therefore the deflections is sidewards.

is dependent on the velocity, the ions are dispersed by their kinetic energy. Moreover the deflection depends on the charge-to-mass ratio of the ions. Thus, with a Thompson parabola spectrometer one can distinguish between the ion species and their energy. The deflection satisfies the following equations [11]

$$\begin{aligned} x &= \tfrac{qBL_{iB}}{mv}\left(\tfrac{L_{iB}}{2}+L_{fB}\right), \\ y &= \tfrac{qEL_{iE}}{mv^2}\left(\tfrac{L_{iE}}{2}+L_{fE}\right), \end{aligned} \tag{3.2}$$

where q is the particle's charge, m the particle's mass and v the particle's velocity. B and E are the electric and magnetic field components perpendicular to the velocity of the particle. L_i is the length of the electric and magnetic field, respectively. L_f is the distance where the particle moves in areas that are field-free. The lengths L_f and L_i used in the experiment are shown in figure 3.6. As the deflections in x and y are independently caused by the electric and magnetic field, the length factors in x direction belong to the magnetic field only and the length factors in the y direction belong to the electric field.
From equation 3.2 follows that the momentum per charge is constant for any vertical line with the same x values. Similarly, the energy per charge is constant for any horizontal line with the same y values [11]. The equations 3.2 can be reorganized to the following form

$$y = \frac{1}{v}\frac{EL_E}{BL_B}x \tag{3.3}$$

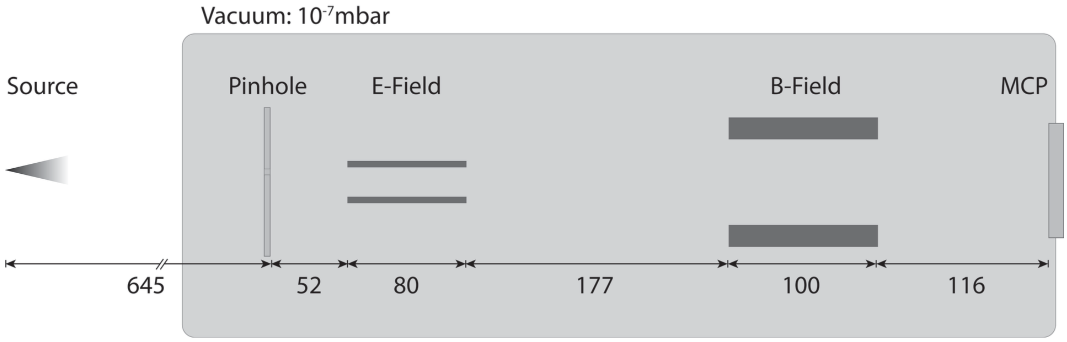

Figure 3.6.: Distances of the Thomson parabola spectrometer.

where L_B and L_E are the length factors $L = L_i(L_i/2 + L_f)$ for the E and B field. For any point on a straight line, that crosses the zero point - the 0th order - will have the same velocity independently from its charge-to-mass ratio. A further rearrangement of equation 3.2 gives [11]

$$y = \frac{m}{q}\frac{EL_E}{B^2 L_B^2}x^2, \tag{3.4}$$

The projected trajectory of a deflected particle describes a parabola. The parabolas depend on the charge-to-mass ratio of the ion. Unknown ion species can be deduced from the trace of known ion species. Thus, from the traces of a TPS it is possible to determine the cut-off energies of different ion species. Moreover, one can also get a hint for the acceleration mechanism that occurred, when using the constant momentum per charge, constant energy per charge or constant velocity line [11].

3.3.2. Multi-Channel-Plate

The particles are sorted by the Thomson parabola with respect to their charge-to-mass ratio and their energy. The detection of the ions is done with a multi-channel-plate.

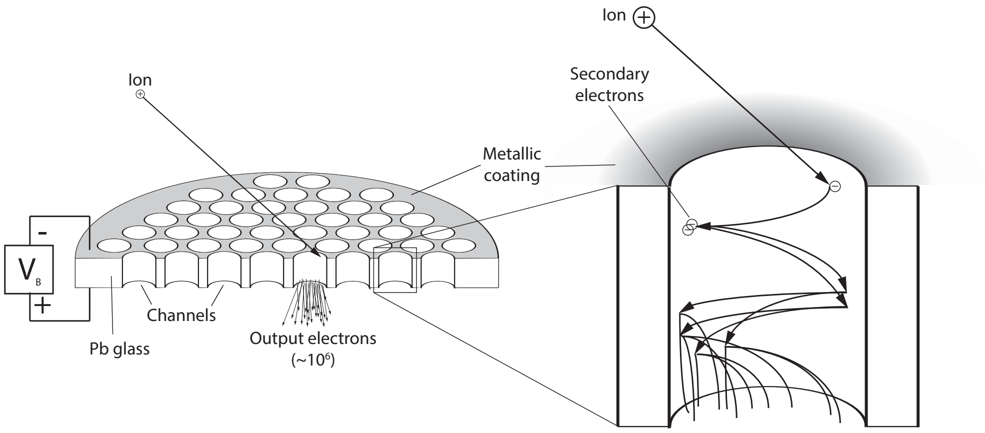

Figure 3.7.: Microchannel plate.[1]

Basically a microchannel plate is a photo multiplier tube. The central component of the MCP is a roughly 1mm thick Pb glass plate. The Pb glass has a

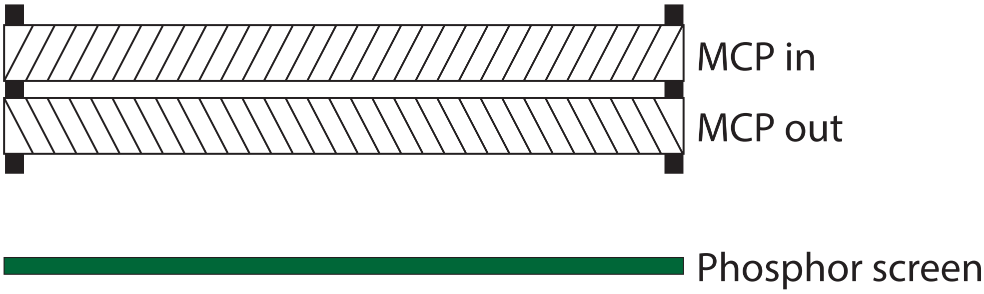

Figure 3.8.: Microchannel plate.[1]

low work of emission. The plate consists of a large number of channels [1], that are arranged in a honeycomb-like shape. The inner diameter of these channels is 20μm. The upper and lower side of the glass plate is coated with a metal - usually an NiCr alloy. A voltage is applied between the upper and lower side of the glass plate of typically 1 - 2 kV. An ion that impinges onto a channel's wall will release an electron. Due to the applied voltage, the electron is accelerated along the channel and will strike again onto the channel's wall and will release one or more secondary electrons. These electrons are also accelerated and the process repeats. Eventually several thousand electrons are accelerated. These electrons leave the channel and hit a phosphor screen. The glow of the phosphor screen is detected by a *Basler scA1400-17fm* CCD camera.
Technical details of the in the experiment used MCP are found in table A.1 in the appendix.

3.3.3. Dispersion of the Thomson Parabola

In order to determine the energy of the ions, the dispersion of the spectrometer is measured. The remanescent of the magnets is known with 1.055 T. But as the magnets are installed in a yoke, the magnetic field is difficult to calculate as the susceptibility of the yoke's iron depends on the local field. Thus, the dispersion is calibrated with the aid of an image plate (IP) and thin copper foils. The package of IP and foils is placed in front of the MCP, which is turned off for the calibration. Only charged particles with a characteristic kinetic energy threshold are able to pass through the foils. The threshold depends on the foil's material and thickness and is called Bragg peak.
The TPS sorts different ion species regarding their charge-to-mass ratio and disperses these ions regarding their kinetic energy. Hence, if certain areas of an image plate are shielded by thin copper foils, one is able to determine the position of an ion with a characteristic energy.
Figure 3.9 shows a scan of an illuminated image plate with the rough position of the copper foils. Several different ion species are visible. At some positions the parabolas are interrupted. At these positions the ions are stopped by the copper foils. The Bragg peak for 20μm Cu is 2.1 MeV and the Bragg peak for 5μm Cu is 0.8 MeV. The points on the IP, where the proton trace is interrupted behind the foils, correspond to these energies. The magnetic field can be calculated with the distance between the zeroth order and these interruption points. From this follows that the homogeneous magnetic field in the middle between the magnets must be 0.29T.
The TPS is modeled with the electromagnetic simulation program *CST*. The

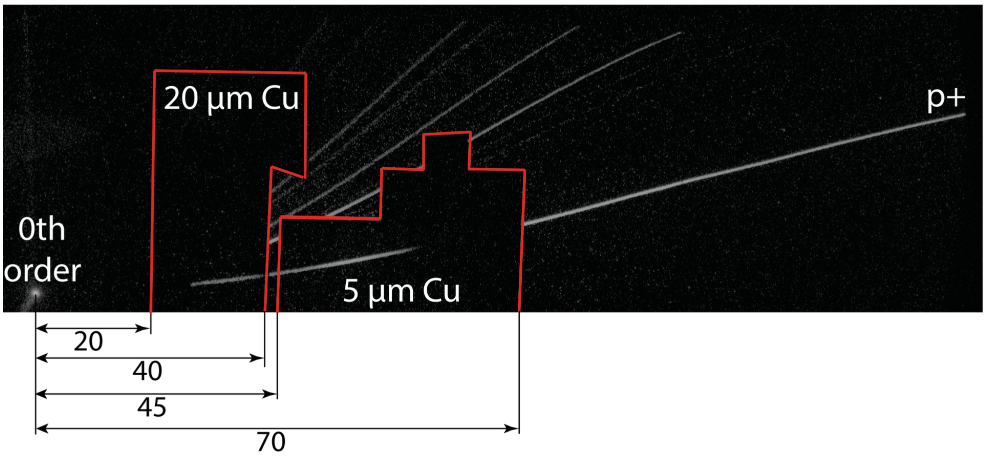

Figure 3.9.: Experiment. Scan of an image plate. Determination of the dispersion of the Thomson parabola.

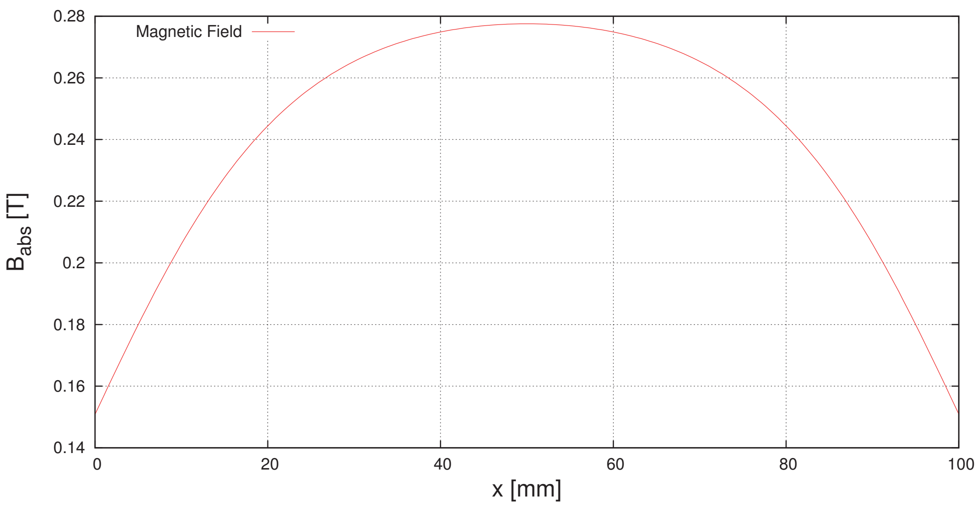

Figure 3.10.: Simulation of the magnetic field of the TPS. Line-out of the magnetic field in the yoke. The field distribution of the simulation agrees with former measurements of the yoke.

magnetic field along the designated particle path through the magnets is shown in figure 3.10. It is clear from the graph that the magnetic field is by no means homogeneous. The effect of this inhomogeneity on the ion parabolas is presented in the following section.
The dependence of the kinetic energy on the deflection of the ions in the x-direction is now determined for each ion species with the CST simulations. The energy and x-position value pairs at the MCP position are fitted by a power function $E(x) = ax^b$.

3.3.4. Evaluation of Thomson Parabola Spectrometer Images

Several steps and calculations are necessary in order to derive spectra from the MCP images. In the following these steps are briefly explained.

Deviations between Analytic and Experimental Parabolas

The inhomogeneities in the magnetic field cause especially for ions with low kinetic energy a deviation from the analytical parabolas. Figure 3.11 shows a

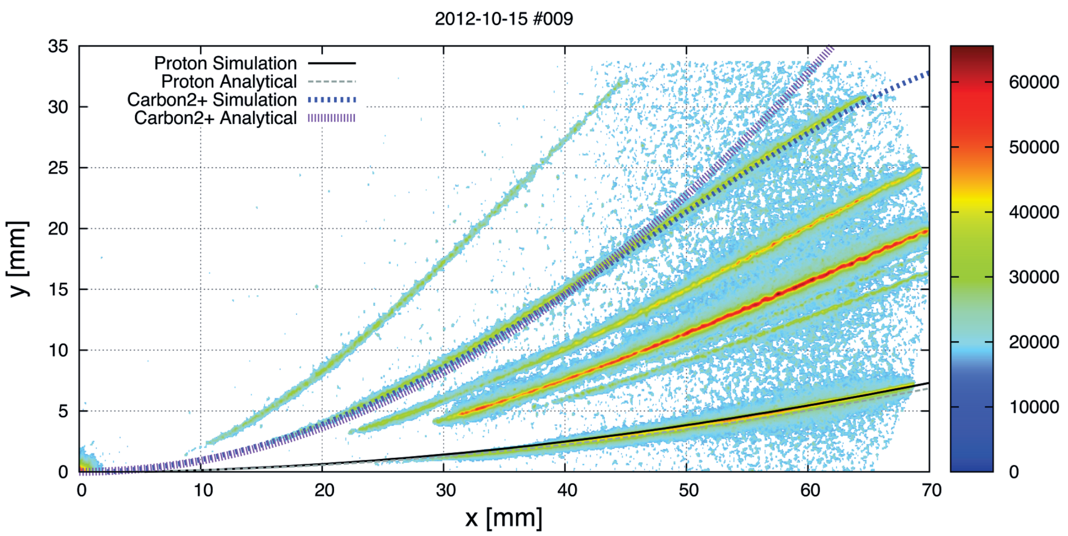

Figure 3.11.: MCP image of shot 9 2012-10-15.

typical result on the MCP. Several parabolas appear, that belong mainly to carbon ions and protons. The analytical parabolas are shown for protons and C^{2+}. Moreover, the parabolas calculated with CST are shown. Especially for low energies the distance increases between analytic parabola and experimental parabola. The CST solution follows the experimental parabolas even for low energies.
It is concluded from this deviation, that the parabolas are determined with the aid of CST. The use of the analytic parabolas would result in wrong spectra.

Voltage Drop with each Shot

A second effect that appeared during the experiment is shown in figure 3.12. The graph shows the voltage for each shot on two different days. The voltage of the electrodes of the TPS drops with every shot. It follows from this, that

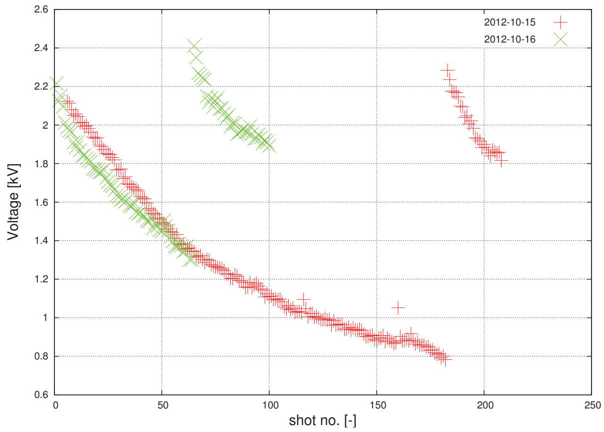

Figure 3.12.: The voltage of the electrodes of the TPS decreased with every shot .

charged particles with low kinetic energy must have hit the electrodes, so that the potential between the plates decreases each shot by a small amount. At a certain threshold the voltage supply triggers the voltage back to the preset value. One cannot deduce from this the particle number below a certain kinetic energy that have hit the electrodes, as a lot of different charged particles hit the electrodes.

Ion Traces on the MCP for Different Voltages

The distorted experimental parabolas, due to inhomogeneities of the magnetic field, and the change of voltage with each shot, made it necessary to use a more comprehensive approach than the simple analytic solution of the parabolas. Several CST simulations of the TPS with different voltages are made. The traces of the different ions are recorded at the MCP position. The traces for each ion for different voltages is collected into a single table, so that x and y are still spatial coordinates and z is the voltage. A surface is fitted to the 3D data set of each ion species with Matlab, where a polynomial is used. The fitted surfaces of the data sets of protons and C^{2+} are shown in figure 3.13. The surface of each ion species describes the position on the MCP for any voltage and not only for voltages where a CST simulation was made.

Semiautomatic Evaluation of the MCP Images

The large amount of shots necessitates a semiautomatic evaluation of the MCP images. In advance the 0th order, a point on the proton trace and a point on the trace of C^{4+} is marked by hand. A *C*-program was written, that determines the voltage of each shot from these positions on the MCP. As the voltage is determined, the parabolas of titanium-, nitrogen-, oxygen- and carbon-ions as well as the parabola for protons are calculated. Along these parabolas line-outs are made. The line-outs comprise a small stripe of 0.6mm width, where the background noise is ignored.
In order to derive a spectrum from these line-outs, the intensity of a pixel on an ion trace has to be related to the particle number of the ion. This correlation is presented in the next section. With the knowledge of the dispersion of the

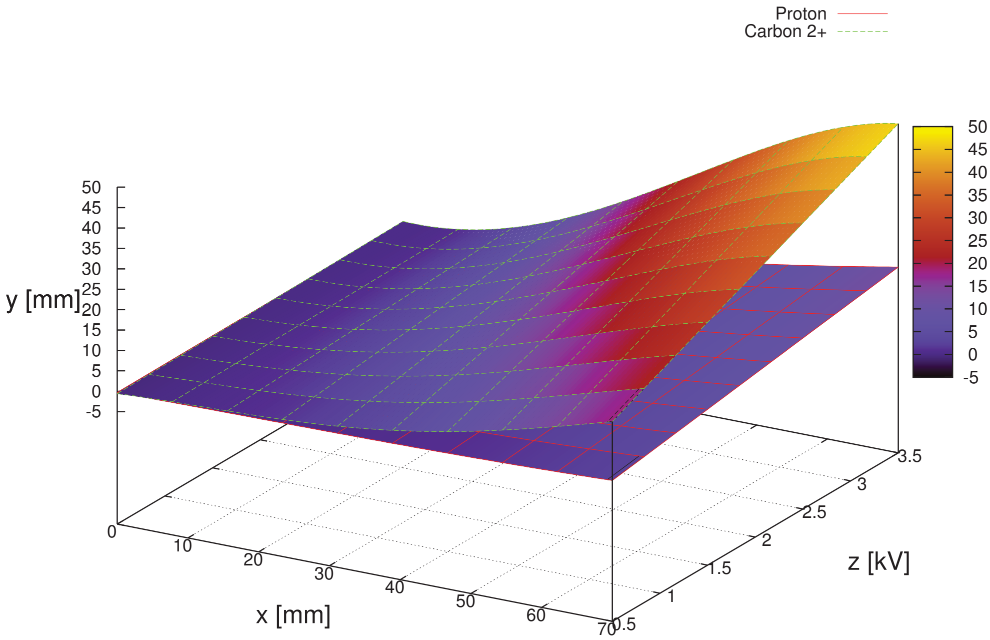

Figure 3.13.: Calculated proton and C^{2+} traces on the MCP for voltages from 0.5kV to 3.5kV. The x and y coordinate are spatial coordinates and z is the voltage.

TPS and the correlation between pixel intensity and particle number, spectra of each ion species are generated. Finally, the program determines the cut-off energies of each ion species.

3.3.5. Correlation between Particle Number and Counts on CCD Camera

In order to derive a spectrum from the recorded ion traces of the MCP, it is necessary to get a correlation between the measured intensity of the trace and the corresponding particle number. The here presented method adheres to a publication from Prasad et al. [41]. Solid state nuclear track materials are well suited for the detection of particle numbers - in particular the polymer CR-39 with the composition $C_{12}H_{18}O_7$. An array of small CR-39 stripes is placed in front of the MCP. Small gaps are between the stripes. Due to the gaps the CR-39 and the MCP are alternatingly irradiated by the deflected ions. Eventually, a particle number is correlated with counts on the CCD.

Setup of MCP and CR-39

CR-39 is a simple optically transparent plastic. CR-39 does not respond to X-rays and electrons, but it responds to heavily ionizing particles such as protons with a few MeV. This feature is the main advantage of CR-39. While a particle moves through the polymer, it destroys molecule chains and leaves behind free radicals.

After exposure to the radiation the CR39 is etched in an alkaline sodium hydroxide solution. As the molecule chains are broken along the trail of the charged

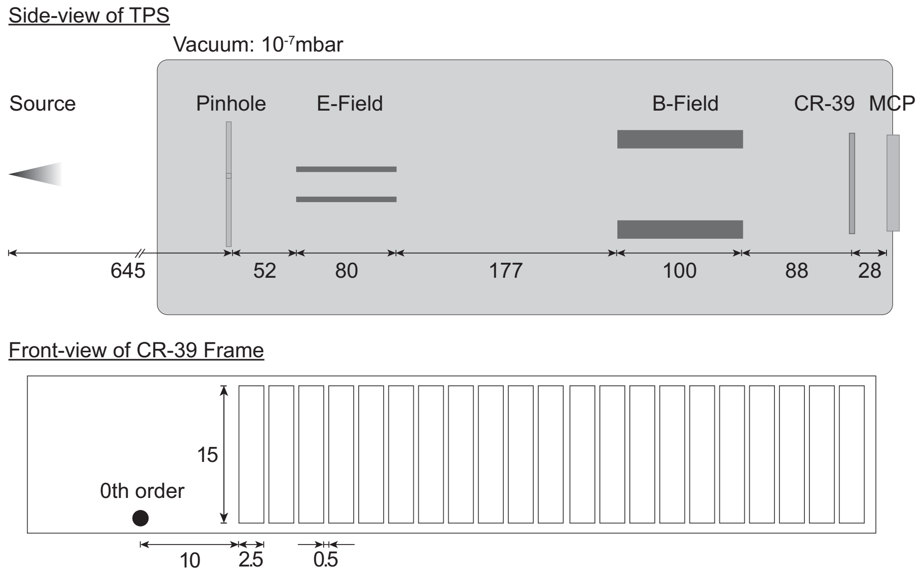

Figure 3.14.: Position of the CR39 stripes in the Thomson parabola spectrometer and setup of the frame with the CR39 stripes.

particle, the material is more easily etched away than the surrounding bulk material, which is depicted in figure 3.15 (a)-(c). The unequal etch-rate induces a small pit in the plastic after a couple of hours in the solution. The small pit can be measured with an optical microscope. An example of pits caused by protons is shown in figure 3.15 (d).
In the experiments a highly pure CR39 from *Track Analysis Systems Ltf* is used. It is delivered in 1mm thick sheets, which can easily be cut. The sheets are scribed with squares of $25 \times 25\text{mm}^2$. Small stripes are cut out of the sheets. These stripes are aligned on a frame next to each other. A small gap between the stripes is left out. The frame is placed in front of the MCP. The position of the frame and the arrangement of the CR-39 stripes is shown in figure 3.14. The small gaps between the CR-39 stripes allow some ions to hit the MCP, whereas a large fraction of the ions irradiate the CR-39.
The etching procedure is in detail as follows. The CR-39 stripe is placed in a 6N NaOH solution at 86°C. The CR-39 samples stay in the solution for 90 to 200 min. The etching time depends on the etch rate. Typically 10 to 20μm of the total stripe height is removed. After the bath in the NaOH solution the samples are neutralized in a 2% vinegar solution.
The evaluation is carried out with an optical microscope. The pits of the different ion species have made traces in the stripes. As the traces are larger than the field of view of the microscope, a series of images of each ion trace is made and stitched together by hand. The distances between traces on the stripes' long sides are carefully measured, in order to allocate the traces on the CR-39 to the traces on the MCP.
The images of the traces are further processed with the program *ImageJ*. The contrast and brightness levels of the images are adjusted and the images are transformed to binary images. Only the contours of the pits remain after the function *Skeletonize* is used. A procedure, that is used for cell counting, counts the pits and measures the position of each pit. An example of a stripe is shown in figure 3.15 e), where the measured positions of the pits are plotted and fitted

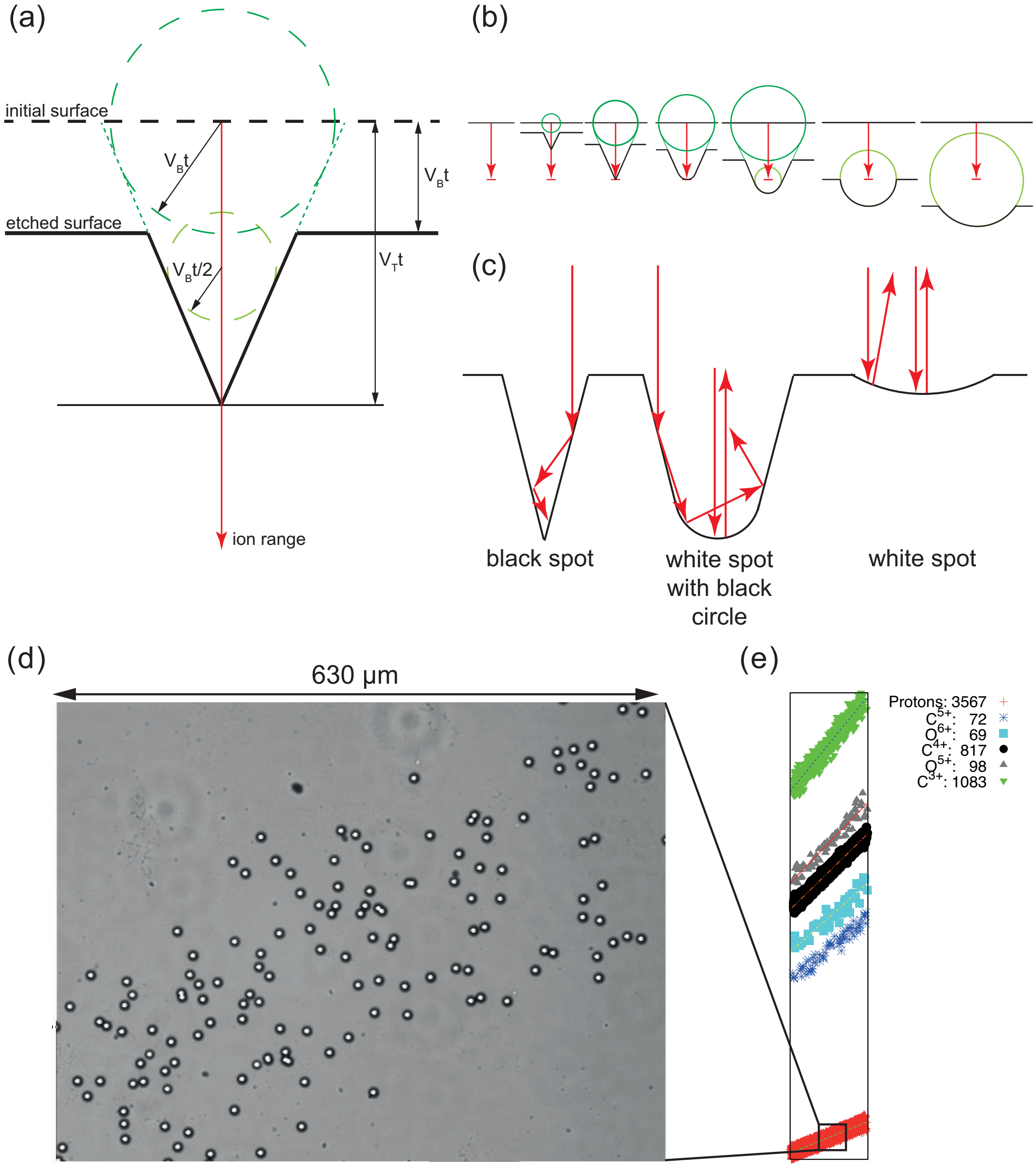

Figure 3.15.: a) Simplified etching profile of CR-39. v_B is the bulk etch rate and v_T is the track etch rate. The etch rate along the path of the ion is higher compared to the surrounding bulk material. b) Temporal evolution of a pit during the etching process. If the CR-39 is too long in the etchant, the pits disappear again. Schematics inspired by [42]. c) In dependence on the etching time, the shape of the pits differ. Ideally, a white spot with a black circle is seen with an optical microscope. d) Image made with an optical microscope. Small white spots with black circles, which are caused by protons. The field of view of the microscope is too small, in order to capture the whole trace on the CR-39. Thus, these images are stitched together by hand. e) The complete tracks of ions on the CR-39 stripe. The distances between the traces are measured, so that the traces with the pits can be aligned with the parabolas.

by linear functions.

Cross-Calibration of MCP and CR-39

Three frames with CR-39 stripes were irradiated. At the same time the MCP was in usage. The shots are single beam shots with beam I. The shot with the first frame did not have a strong signal on the MCP, so that these CR-39 stripes are not evaluated. The results of the second frame is found in the appendix A.2.3.

Figure 3.16 shows the MCP image as well as the CR-39 stripes. The pits on the

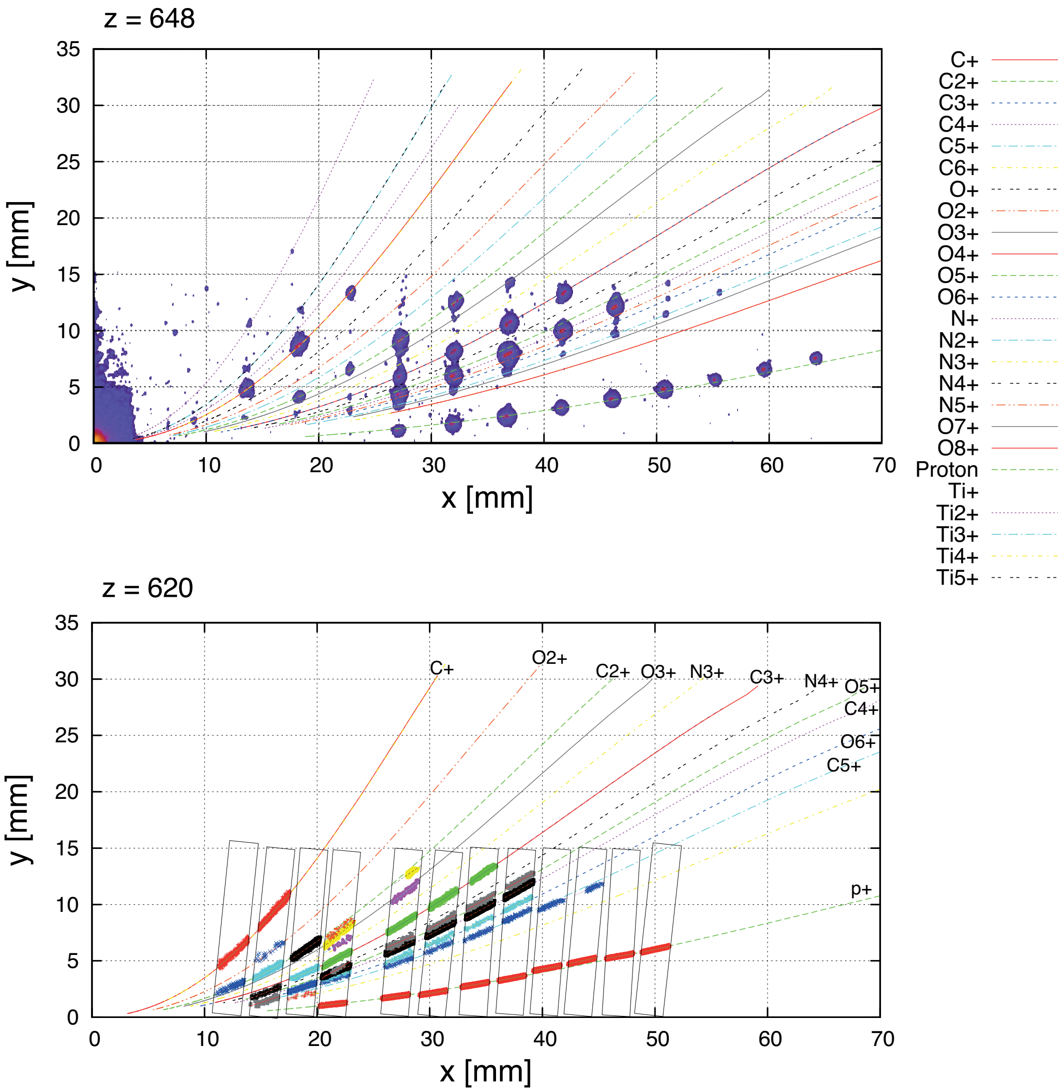

Figure 3.16.: Experiment. Third frame CR-39. The upper image shows the signal on the MCP. The gaps in the parabolas are caused by the CR-39 stripes, that are placed in front of the MCP. Due to the larger distance of the MCP to the magnetic and electric fields of the TPS, the ions are further dispersed on the MCP compared to the ions that irradiated the CR-39 stripes. Thus, the signal width along the parabolas on the MCP is larger than the gaps between the CR-39 stripes. For instance, the CR-39 stripe located at x=50mm belongs to the MCP signals at x=60mm and x=64mm, where the actual stripe width is 2.5mm.

CR-39 are counted and aligned with the corresponding parabola. The parabolas

are calculated for a different position compared to the MCP parabolas, because the frames were placed in front of the MCP and were therewith closer to the magnets and the electrodes. The difference is denoted in the figures with a different z value in the upper left corner. Some of the CR-39 stripes are somewhat tilted compared to the coordinate system, as these CR-39 were scanned while they were not aligned with the axes of the microscope.
The pits' distribution and the parabolas on the MCP have a certain width. In order to know how many particles are detected within a certain energy range, the pits are counted in 10μm intervals. Thus, a kind of particle density distribution is determined along the small side of the CR-39 stripe. The signal on the MCP is similarly evaluated, i.e. the signal's intensity is separated into 10μm intervals.

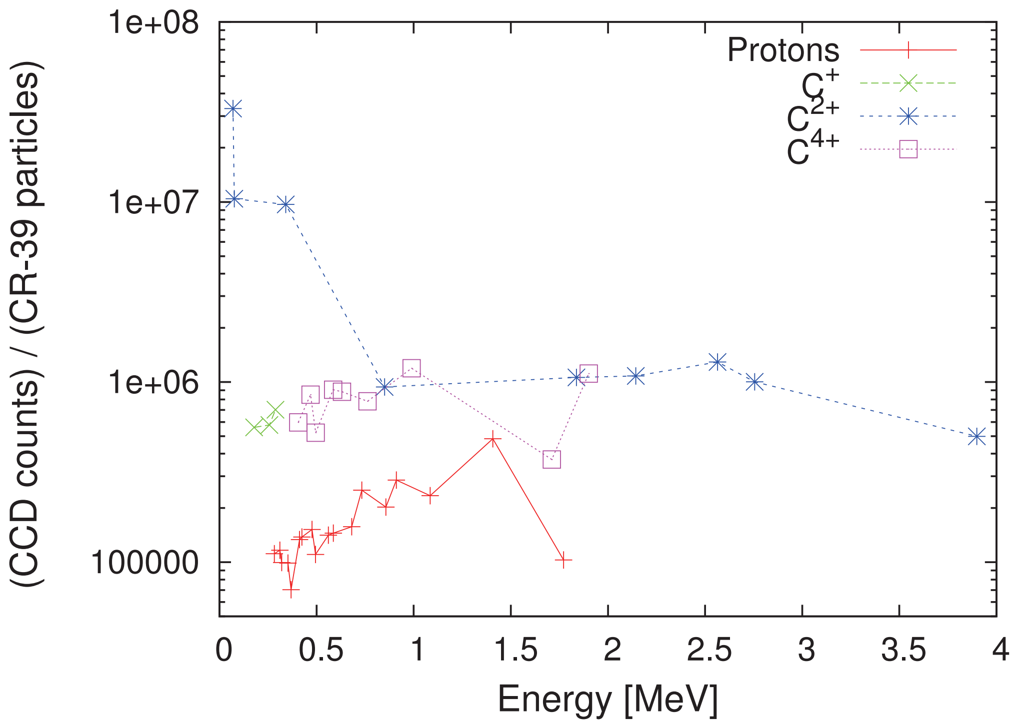

Figure 3.17.: Experiment. Response of MCP for protons and several carbon species.

Eventually, the signal's intensity distribution and the particle density distribution are correlated to each other. The results of the third frame for protons and several carbon ions is shown in figure 3.17. The response of the MCP is almost the same for different carbon ions. The response of the MCP on protons is partially an order of magnitude lower compared to the response on carbon ions. The decrease of response with increasing carbon ion energy is consistent with observations made by Harres et al. [21]. The results of the second frame are comparable to the third frame, but for the sake of clarity the results are not shown here.

3.4. Additional Diagnostics

3.4.1. Radiochromic Films

Radiochromic films (RCF) are a common diagnostic in laser particle acceleration. The detector resolves the spatial proton distribution. If a stack of RCFs is

Table 3.1.: Divergence angle. Error $\pm 2°$. 19 shots with beam II only on HD-RCFs. The RCF were scanned >4 weeks after the irradiation. As the RCFs had been irradiated by almost 20 shots and as there are shot to shot fluctuations, the divergence cone is blurred. It can be expected that a single shot has a smaller divergence angle.

RCF No.	**Diameter [mm]**	**Beam Divergence [°]**
HD 1	16.0	44
HD 2	10.5	30
HD 3	6.5	18

Table 3.2.: Divergence angle. Error $\pm 2°$. 5 shots with both beams on HD-RCFs. The RCF were scanned >4 weeks after the irradiation. No special features are observed, that may hint on double beam shots.

RCF No.	**Diameter [mm]**	**Beam Divergence [°]**
HD 1	12.5	35
HD 2	6	17
HD 3	2	6

used, information about the energy is obtained. In the experiment *Gafchromic* RCFs of the type HD-810 were used. The layer configuration of a single RCF as well as the stack configuration is shown in figure 3.18. In order to protect the RCFs from electrons and radiation, the RCFs are wrapped in aluminum foil. Bragg peak simulations are made of the RCF stack with the program *SRIM*. The program is based on a binary collision approximation [67], that calculates the stopping range of ions in matter. The results of the simulation are also shown in figure 3.18. Single protons with different energies are simulated. In dependence on their energy the protons stop at different positions of the RCF stack. The largest fraction of protons with the same kinetic energy are stopped at the so-called Bragg peak. In the lower graph the single particle interactions are smoothed by lines. Particles with an energy lower than 1MeV are stopped already in the aluminum foil. The highest proton energies are detected with 5.5MeV in the last RCF.

The protons are accelerated according to the TNSA mechanism due to an electron sheath. The sheath causes an energy dependent source sizes. The area from where protons are accelerated, increases with lower energies. The proton beam with a low kinetic energy has a larger divergence than the proton beam with higher kinetic energy. Thus, protons with the highest energy are emitted from a point-like source. Figure 3.19 summarizes this effect by the shown cones. Moreover, the effect causes different circle sizes on the HD-RCF, which is also shown in the figure.

Only two stacks of RCFs were irradiated. The effort to put the RCFs in place during the experiment is very high, but the information gained from the RCFs was not very high compared to the main diagnostic. In particular, it was necessary to have several consecutive shots on the RCFs, because the proton flux was relatively low. Thereby, shot to shot fluctuations are blurred out on the RCFs.

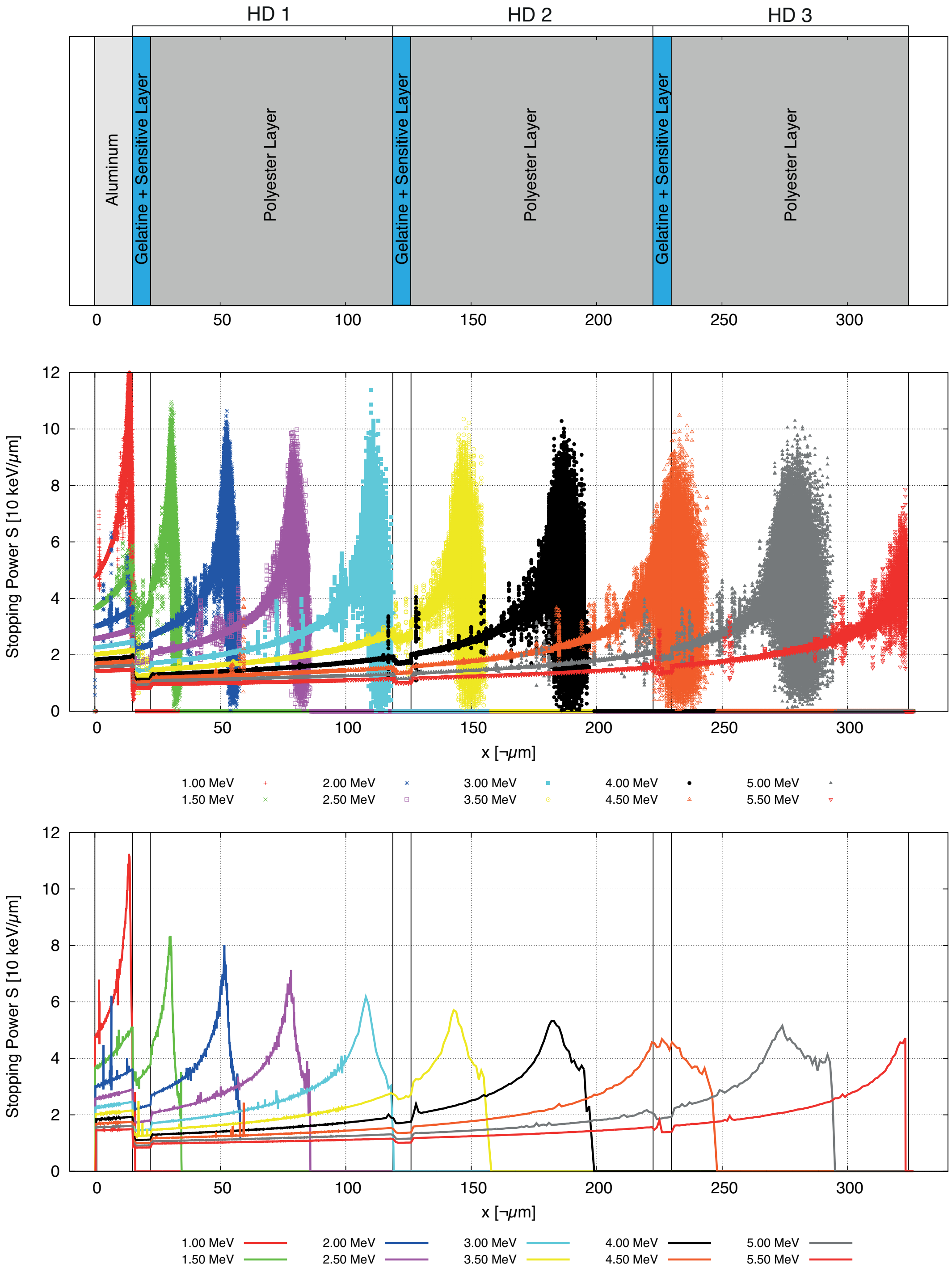

Figure 3.18.: The upper schematic shows the HD RCF stack that is used in the experiment. The stack is wrapped in aluminum foil. In order to determine the energy range that is covered by each RCF, SRIM simulations are made. The results are shown in the middle and lower graph. The stopping power over the position in the RCF stack is shown. In the lower graph, the single particle interactions of the middle graph are smoothed by lines. 1MeV protons are stopped already in the aluminum foil. 5.5MeV protons are stopped in a large fraction in the last RCF.

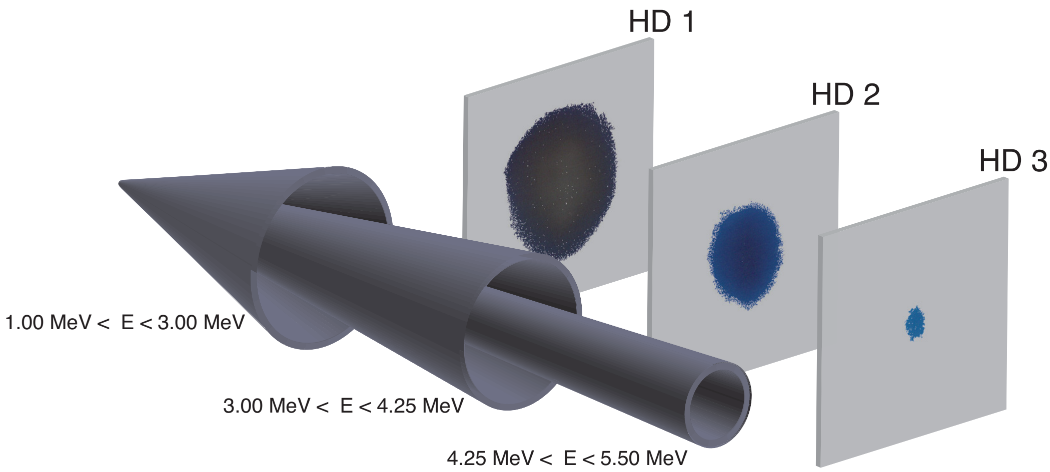

Figure 3.19.: Schematic of energy cones that are a consequence of the TNSA mechanism. On the RCF stack those energy cones cause different large color changes.

At first the RCF stack is irradiated by proton beams, that are generated by beam II only. The results of the divergence is shown in table 3.1. The RCF stack is irradiated by 20 shots of protons. Thus, the divergence is relatively high. The second RCF stack is irradiated by proton beams, that are generated by synchronized beam I and beam II shots. Five shots are made. Due to the lower shot number, the divergence is smaller compared to the previous RCF stack.
The RCF diagnostic did not reveal any special features of a double beam interaction. No special features of the double beam interaction are observed or are imprinted in the proton beams.

3.4.2. Spatial Overlap - Beam Pointing

PIC simulations were performed in advance in order to reveal critical parameters for the experiment. It turned out that the spatial overlap of both beams is crucial for enhanced maximum proton energies. Although the simulations were done with 10s of nanometer target thicknesses and therefore a different acceleration mechanism applies, this feature is also observed during the experiment. The focal spots of each beam moves rapidly in the target plane due to vibrations in the beamline and the building. During the day these vibrations are unavoidable. A better overlap is achieved by de-focussing the two beams, whereas a lower intensity has to be accepted.

3.4.3. Temporal Overlap - Timing

The most obvious and most important parameter that can be tweaked during the experiment is the delay between the two pulses. The delay is changed during the experiment via a double-pass delay stage that is implemented in the beamline of beam I. The rough delay was estimated via a fast photodiode and an oscilloscope. By doing this, the pulses are timed on several centimeters and nanoseconds, respectively. But as the aim is to time both beams several femtoseconds precise a different technique is necessary. The technique is described

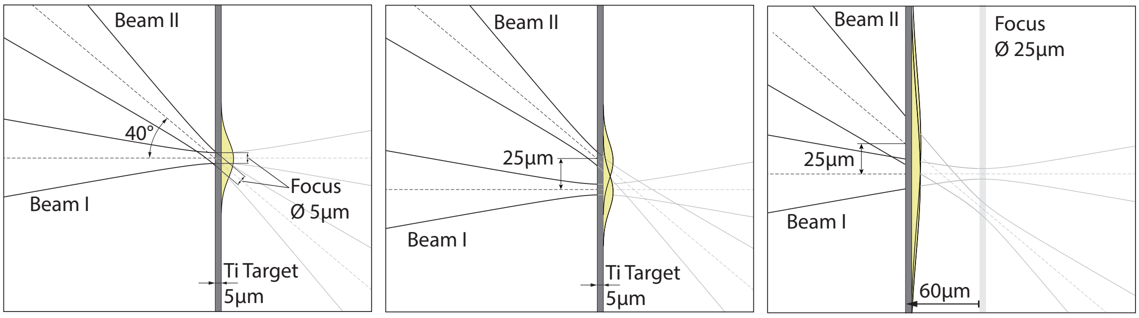

Figure 3.20.: Wizzler measurement. Measurement of phase, spectrum and temporal shape of beam II and I on two different days.

in the following.

Beam I is focused onto a thin glass plate with low energy. The pulse shall

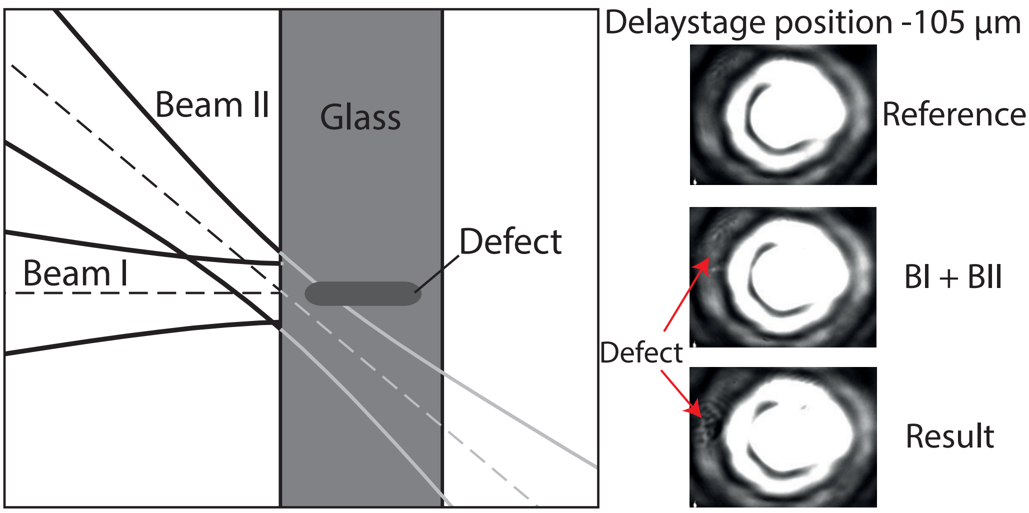

Figure 3.21.: Schemantic of the timing procedure. Beam I is focused onto a thin glass plate. The energy is chosen very low, in order only to generate a small change of the index of refraction. Beam II is probing the interaction of beam I with the glass. The focal diagnostic of beam II is used as imaging line.

change only in a small volume of the glass plate the index of refraction. Beam II is used to probe the interaction of beam I with the glass plate. The focal diagnostic of beam II is used as an imaging line. The schematic in figure 3.21 shows the basic principle. A first raw image is taken without beam I. The image is used as reference. The second image shows the interaction of beam I with the glass plate. In the upper left corner a small defect in the glass is visible. The last image shows again the image of beam II only, where still the defect is visible in the upper left corner. Now the delay stage of beam I has to be moved as long the defect disappears in the interaction image. Of course, the defect should still be visible in the resulting image after the interaction. Figure 3.22 shows the interaction of beam I with the glass plate and the resulting defect for three different delay positions. The pulse of beam I arrives later with an increasing delay. For a delay position of $5\mu m$ the defect is present in the interaction image and the result image. For a delay position of $200\mu m$ the defect completely disappeared in the interaction image. Thus beam II is too early to probe the interaction of beam I with the glass plate. For a delay position of $100\mu m$ the defect is al-

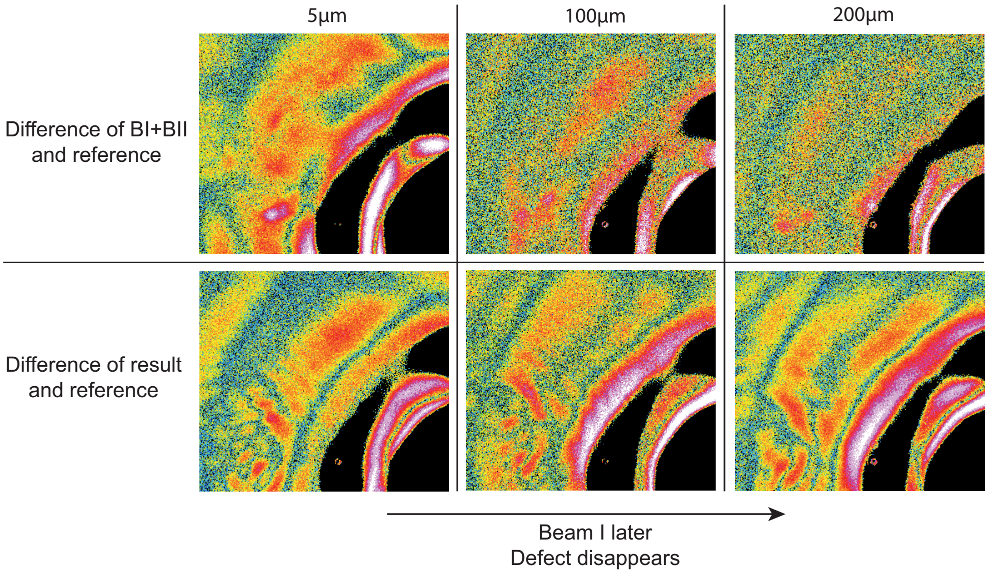

Figure 3.22.: The upper row shows the subtraction of the interaction image of BI and BII and the reference image. The lower row shows the subtraction of the result, i.e. the defect, and the reference image. The images were logarithmized, the contrast has been enhanced and the defect is zoomed in. Images at three delay position are shown. Beam I arrives later with an increasing delay position. For a delay position of 5μm the defect is clearly visible in the upper left region in the interaction image and the result image. For larger delays the defect disappears in the interaction images, but is still visible in the result image.

most disappeared. Hence, this delay position is a good starting point for delay scan with full power on titanium targets. The synchronized delay position is deduced from the ion signals on the MCP and the interference shift on the TASRI.

4. Experimental Results of Single and Double Beam Ion Acceleration

4.1. Introduction

In this section the experimental results are presented. The MCP traces are shown first. The dependence of the proton cut-off energies on the delay between the two pulses is derived from these traces. An analysis is conducted in combination with the three main parameters that could be varied during the experiment

- Position of the target with respect to the focus

- The delay between the two pulses

- The laser pulse energy

The delay dependence of the proton cut-off energy is derived from these shot series.

4.2. Examples of MCP Traces

Introduction

During the experimental campaign almost 1000 shots were made. But already from a few MCP images, one can get a good overview over this large amount of data. These characteristic images are presented in this section.

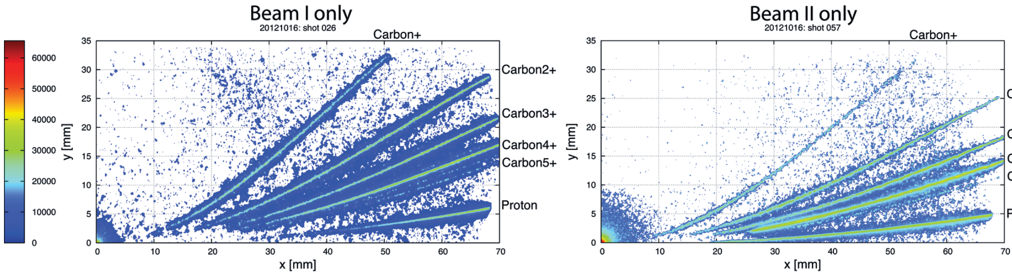

Figure 4.1.: Experiment. MCP measurements of single beam shots. The left images shows a beam I shot and the right image shows a beam II shot. Similar ion species appear for both shots. Only the cut-off energies are higher for the beam II shot. The main reason among others for this is found in the higher pulse energy of beam II.

Single Beam Shots

The single beam interaction is shown in figure 4.1 for beam I and beam II, respectively. Both beams accelerate several carbon ions and protons. The only difference between the two beams are the reached cut-off energies for the different ion species. If both beams interact with the target, the resulting images are for most shots a mixture of the two images in figure 4.1. The only noticeable difference is that the first pulse, that interacts with the foil, imprints its characteristic into the MCP images. Thus usually the first beam dominates the acceleration process. But with two specific sets of parameters, two MCP images were observed with complete different characteristics.

Double Beam Shots

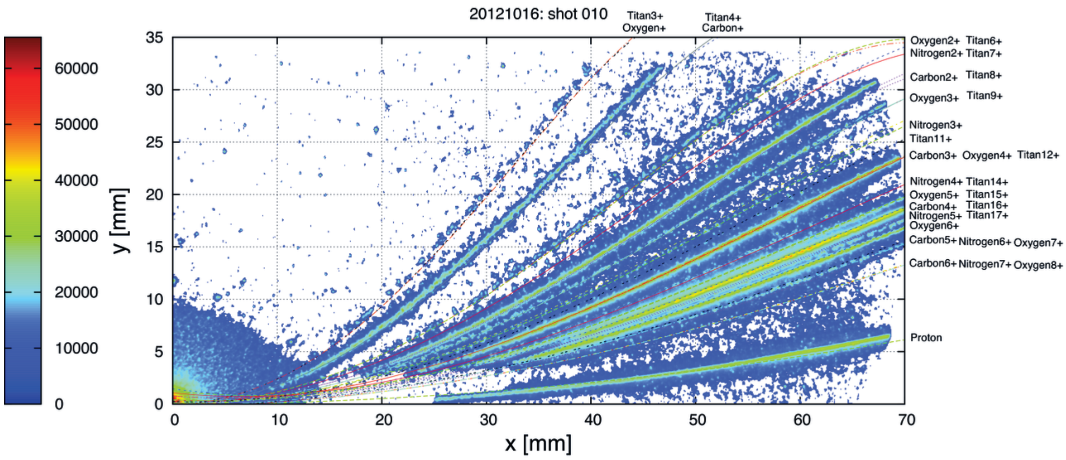

Figure 4.2.: Experiment. MCP measurements of a double beam shot. Appearance of these traces were detected only for defocused beams. Moreover these traces tended to appear for delayed pulses. Compared to the single beam shots, many more ion species appear. The Thomson parabola separates ions according to their charge-to-mass ratio. Thus, titanium ions are overlapping with ions from the contamination.

The MCP image shown in figure 4.2 appeared only for defocused beams. Moreover, the delay between the two pulses tend to be in the range of $90 \pm 20 fs$ and $-90 \pm 20 fs$, respectively. Thus, the beams shall not be synchronized. Obviously a large fraction of ions from the contamination is accelerated. If all ion energies are added up, the total energy belonging to these kinds of shots are the highest energies during the experimental campaign. Hence, these kinds of shots were the most efficient shots regarding the transfer of laser energy to the ion energy.

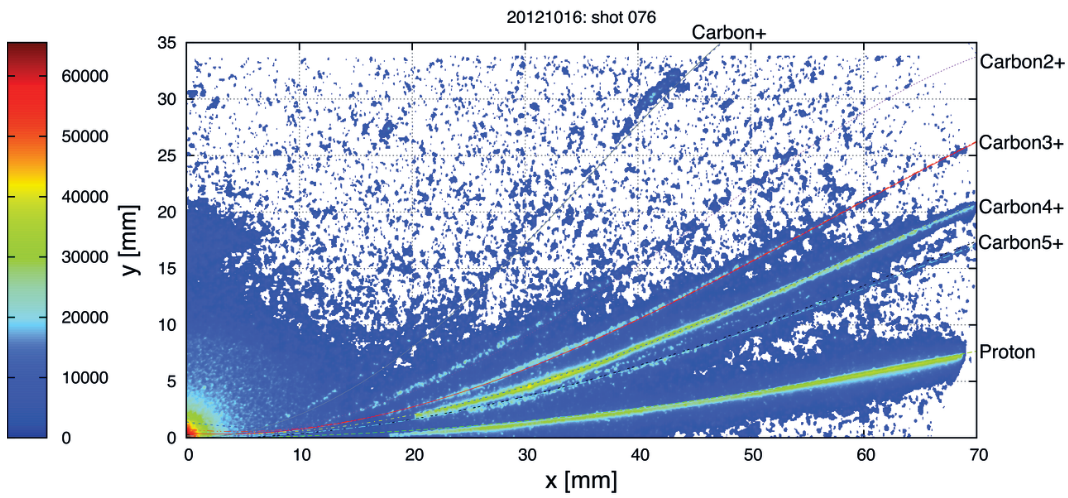

Figure 4.3.: Experiment. MCP measurements of a double beam shot. Both beams synchronized and focused. Compared to single beam shots, less pronounced ion species appeared. These shots were a rare event. The main reason for this rareness are vibrations in the beamlines, i.e. the spatial overlap of the focal spots is very critical.

The second remarkable shots are a rare event. Figure 4.3 shows the observed MCP ion trace. If both beams are perfectly overlapped in space and time, these kind of shots are observed. Only a few strong ion traces are visible. The proton energies achieved with these shots are the highest during the campaign.

Conclusion

These two characteristic shot pattern are of particular interest as these shots only occur with two beams. Therefore the focus is set on the explanation of these two shot pattern in the following sections and chapters.
The interaction of both laser pulses and the plasma are of main interest. The parameter with the largest effect on the interaction is the delay between the two laser pulses. The MCP images are evaluated regarding the proton cut-off energy in dependence to the delay between the two pulses, whereas a negative delay corresponds to a shot where beam II is the first pulse, that interacts with the target and vice versa.

4.3. Cut-off Energies over Delay between the two Beams

Introduction

This section presents the proton cut-off energies as a function of the delay between the two pulses. Moreover the impact of prepulse and the dependence on the pulse energy is discussed. From this first analysis constraints are derived for the PIC simulations.

Focused Shots - Close to Synchronized Shots

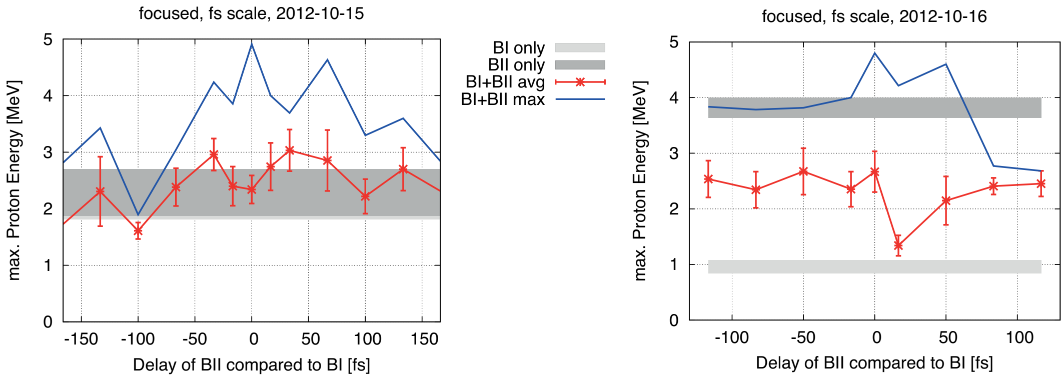

Figure 4.4.: Experiment. Proton cut-off energies over delay between the pulses. Delay in the range of femtoseconds. Negative values correspond to a shot where beam II was earlier than beam I. In grey bars the achieved proton cut-off energies for single beam interaction, in red the average achieved cut-off energy with error bars at that delay position, in blue the maximum cut-off energy achieved at that delay position are shown.
Both beams are focused. The difference between the left and the right shot series are the laser pulse energies. For both series the highest maximum cut-off energy is found for synchronized pulses, which is for the left graph 4.9 MeV and for the right graph 4.8 MeV. Beam II dominates the interaction for negative delays in the right graph with 4.7 MeV, as the maximum proton cut-off energy is the same as for a single beam interaction. The single beam cut-off energy is the same for both beams in the left shot series, i.e. 2.2 MeV. For the right shot series the cut-off energy for beam I only is 1.2 MeV, which is low compared to 4.7 MeV of beam II only. The maximum proton cut-off energy has the shape of a tilted triangle towards positive delays. The maximum proton cut-off energy for the synchronized pulses is simply the sum of cut-off energies of the single beam interaction.

The most promising regime for an enhanced proton cut-off energy is when both beams are focused and the timing of both beams is a few 10s of femtosecond. Figure 4.4 shows the maximum achieved proton energy over the delay between the two pulses. Both beams are focused onto target and the delay is varied from roughly -150 fs to +150 fs. Negative values mean that beam II is the first pulse before beam I. For positive values the situation is vice versa. Several shots are done at each delay position. The red line is the average cut-off energies reached at that position with the variance indicated by the error bars. The blue line shows the maximum cut-off energy achieved at that position, whereas the error is not shown. In light and dark grey bars are the cut-off energies for single beam interactions. Of course, there is no delay for a single beam interaction, but in order to guide the eye for a comparison between single and double beam interaction, the bars cover the whole delay range.

The main experimental difference of the left and right graph of figure 4.4 is the different energy in both beams. The different energy levels result in different single beam cut-off energies. The single beam cut-off energy in the left graph is roughly 2.5 MeV. The single beam cut-off energies in the right graph are 1 MeV and 4 MeV. The shape is completely different for the blue line, i.e. the maximum achieved cut-off energy, in these two graphs. Interestingly the synchronized shots - where the delay is zero - have in both cases the same value of about 5 MeV. The 5 MeV are just the sum of the single beam interactions, i.e. 2×2.5 MeV and $1 + 4$ MeV.
As already mentioned the shape of the maximum cut-off energies is completely different for the different laser energies, i.e. between the two graphs of figure 4.4. Especially in the right graph at negative delays the interaction is basically a single beam shot of beam II. The effect of the beam becomes only visible, if beam I follows beam II with a minimum delay of 20fs (-20fs in the graph). If beam I is earlier than beam II, the interaction is enhanced compared to a beam I only shot, but the cut-off energy is lower than a beam II only shot. Thus, if the absolute delay is too large, the effect is reduced for the second or following laser pulse that interacts with the target.
The interplay between the pulses is simpler for the left graph where the single beam cut-off energies are similar. The maximum cut-off energies rise with a smaller absolute delay. Thus no beam dominates the interaction.

From the comparison of the two graphs it is already possible to conclude that the electron distribution ”seen” by each pulse is important. As one laser ionizes the target to higher ionization stages, the electron density rises and the plasma expands due to the heat input. For a larger delay the electron distribution is extended to a larger distance compared to a small delay. The second laser might be absorbed and/or reflected by these electrons. If the pulse energies especially of the second laser pulse is increased, there is a higher laser energy in the prepulse. Hence, the initial plasma is already quite large before beam II irradiates the target and is further increased by the main pulse, so that beam I has no or no large influence on the acceleration mechanism.

Defocused Shots - Close to Synchronized Shots

In order to support the assumption that the prepulse has a significant influence on the acceleration mechanism, both beams are defocused by -60μm. This significantly reduces the intensity of the main pulses but also the intensity of the prepulses. The focal radius of both beams is increased from 2.5μm to 13μm, so that the intensity is reduced by a factor of 25. Figure 4.5 shows the proton cut-off energies over the delay between the two pulses. The left graph shows a local minimum for almost synchronized beams. This behavior somehow surprises as the sum of both intensities has here the highest value. An explanation might

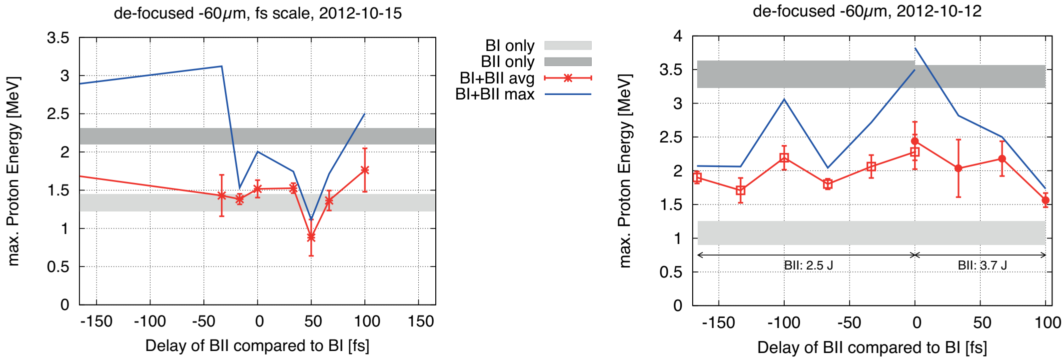

Figure 4.5.: Experiment. Proton cut-off energies over delay between the pulses. Delays are in the range of femtoseconds. Both beams are defocused by -60μm. The difference between the left and right shot series are again the laser pulse energies. Especially for the left shot series the intensity had been chosen very low in order to reduce also the intensity of the prepulse. For very low prepulses the highest cut-off energies are not found for synchronized shots. If the laser pulse energy is increased - especially for beam II - the shape of the blue curve is found to be similar to the focused shot series. From this follows the shape of the preplasma plays an important role in the interplay between the two laser pulses and the target.

be found in the reflection of the main pulses when they are synchronized. The intensity of both beams is in this case too low in order to accelerate electrons that could build up the quasi static electric field at the rear side of the target. If the beams have a delay the first pulse releases electrons from the titanium and these electrons can absorb the energy of the subsequent pulse.
If the pulse energy is increased for beam II and decreased for beam I, the shape of the curve of the maximum proton cut-off energy is the same as in figure 4.4. The cut-off energies increase with a smaller absolute delay. Furthermore after the synchronized shot position is found the pulse energy of beam II is increased for positive delays by 30%. According to the Schreiber model [48] the ion energy should raise with the square root of the laser power $\sqrt{P}$. At the synchronized position the cut-off energy is increased from 3.5 MeV to 3.8 MeV by the energy boost, which is in good agreement with the Schreiber model. Because the pulse energy of beam II is increased and therewith the intensity of the prepulse, the preplasma should be larger compared to the defocused shot series. It can be concluded from this, that the different ionization stages generated by the prepulse and the therewith released electrons, play an important role in the interplay between laser pulses and plasma.

Beyond TNSA Shots

For the last experimental shot series that is presented here, the delay timescale is increased from femtoseconds to picoseconds. The plasma has much more time to expand. The left graph of figure 4.6 shows the cut-off energies over the delay between the two pulses. Both beams are defocused by -60μm and the pulse energies are set to relatively low values. The experimental conditions are the same as for the left graph in figure 4.5. Thus the influence of the prepulse is thought to be very low. Close to a delay of "0" the results of the left graph of figure 4.5 are also shown, but they are just a vertical line.
For positive delays, i.e. beam I is the first pulse and beam II follows, there is no

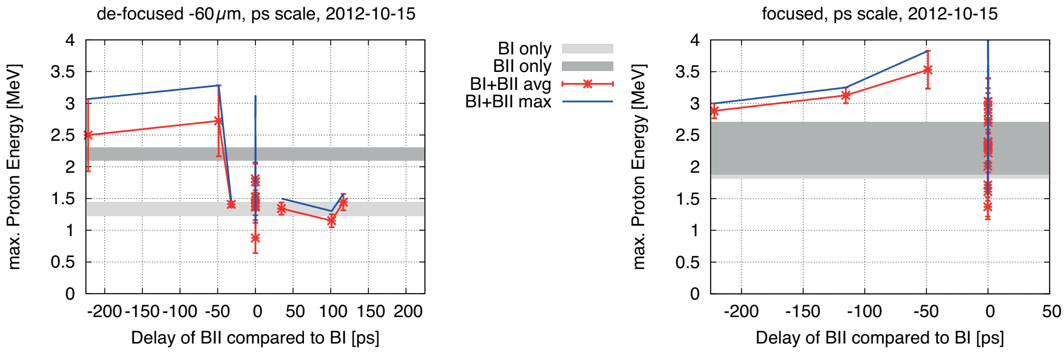

Figure 4.6.: Experiment. Proton cut-off energies over the delay between the pulses. Delay in the range of picoseconds. In the left shot series the beams were defocused. For the right case the target was in focus. The single beam cut-off energies are different for the different focal positions, but interestingly the combined laser pulses produce almost the same enhancement at a delay position of -50ps. For positive delays the cut-off energies correspond to a single beam shot of beam I.

difference to a beam I only shot, because the achieved maximum cut-off energies are the same. Thus beam II has no effect on the acceleration mechanism. For shots where beam II is earlier than beam I, it is observed that the maximum proton cut-off energy is enhanced. In a second series of shots with these long delays, the pulse energy of beam I is increased and the beams are focused again. The corresponding proton cut-off energies over the delay are shown in the right graph of figure 4.6. The maximum proton cut-off energy is slightly higher compared to the defocused series.
As the delay is in the order of magnitude of 10s of picoseconds, it is not possible for the subsequent pulse to effect the TNSA mechanism. The accelerated ions already moved a few millimeters away from the target, so that the quasi static electric field that might build up cannot contribute to the already accelerated particles. Thus the observed proton energy enhancement is believed to be a different acceleration mechanism.

Conclusion

The following regimes are identified from the analysis of the experimental results

- Close to Synchronized Shots, i.e. 10s of femtoseconds
  - Focused
  - Defocused
- Beyond TNSA, i.e. 10s of picoseconds

It is concluded that for two focused synchronized beams that have roughly the same pulse energy on target, the maximum cut-off energy constitutes from the maximum cut-off energy of the single beam interactions of each laser. Hence, the proton cut-off energy might be further increased by adding synchronal more laser pulses.
Additionally the analysis shows that the plasma distribution, that each pulse has to interact with, plays an important role. Especially for shots where beam II has a high pulse energy, beam I does not enhance the acceleration process, if

beam II is earlier than beam I. Beam II did not have a plasma mirror at that time, so that for higher pulse energy the energy in the prepulse is also increased. This assumption is supported by two following shot series, where at first the pulse energy of both beams is reduced. Moreover the two beams are defocused by -60μm.
In the last shot series presented in this section the delay between the two pulses is increased from 10s of femtoseconds to 10s of picoseconds. A local maximum is identified for -50ps, but not for +50ps. The interaction of a positive delay corresponds basically to a beam I only shot, i.e. there is no enhancement observed. But if beam II is roughly 50ps before beam I, the achieved energy is similar to a synchronized shot. Target normal sheath acceleration is taking place on 100s of femtoseconds. So, the beam I, which interacts after beam II with an expanding plasma can neither influence nor enhance the acceleration process regarding the TNSA mechanism. Thus beam I must trigger a different acceleration mechanism.

4.4. Conclusion

In this chapter, experimental results have been shown. MCP images reveal that different regimes occur that depend on the pulse energy and the delay between the two pulses. Most shots are a mixture that have either more the characteristic of beam I or of beam II. In particular two exceptional MCP images have been identified regarding the intensity and the delay between the two pulses.
In the subsequent section the MCP images have been evaluated regarding the proton cut-off energies. These results have been related to the delay between the two pulses. Moreover the results have been sorted regarding focused and defocused shots, the pulse energies as well as the delays.
From these graphs four regimes have been identified. Shots where the delay is varied in the range of 10s of femtoseconds showed different characteristics for focused and defocused beams. For defocused beams a minimum proton cut-off energy have been identified for synchronized shots. Although the total intensity and therewith the maximum field strength of the ambipolar electric field should be higher for a synchronized shot. For focused shots the maximum proton cut-off energy is observed for synchronized shots as one would expect.
If the delay is varied in the range of 10s of picoseconds, a local maximum of the maximum proton cut-off energy has been identified at -50 ps. For +50ps the cut-off energy corresponds basically to a beam I only shot. The influence of the focal position plays only a minor role. It is expected, that for a negative delay in the range of 10s of picoseconds the TNSA process is finished for the first interacting beam, which is in this case beam II. Thus, the enhancement in the proton energy is a different acceleration mechanism. As beam I is the subsequent laser pulse and this pulse cannot contribute the TNSA process of beam II, one can compare the enhancement for negative delays in the range of -50ps with the maximum proton cut-off energy of the single beam interaction. The maximum cut-off energy for beam I is for a defocused shot roughly 1.5 MeV and is increased in this shot series to 3.25 MeV, i.e. more than doubled.

5. Close to Synchronized Shots - Interpretation of Experimental Data

5.1. Introduction

The experimental results regarding this section are shown in figure 5.1 and 5.2. The delays between the two pulses are in the range of ±200fs. From this follows that the second laser pulse that interacts with the foil has an influence on the acceleration process - the TNSA mechanism. The experimental proton cut-off energies over the delay between the two pulses are shown again in figure 5.1a
In the first section of this chapter the prepulse - especially of beam II - is modeled via a PIC simulation. The results of these simulations are presented and used as initial conditions for the following simulation of the two beam interactions for delays of 10s of femtoseconds.

5.2. Prepulse

In order to have simulations that can be compared to the experimental results, it is necessary to model the influence of the prepulse properly. Beam II has no plasma mirror, so that at least the effect from the prepulse of this beam has to be considered.
Anna Lena Giesecke [20] has done extensive measurements of the laser contrast, as she set up the plasma mirror for beam I. There is no contrast measurement of beam II, but as both beams originate from the same front-end and the pulse energy is higher in the second beamline, the prepulse is most probable underestimated.
Figure 5.3 shows the contrast measurement for beam I. The intensity normalized to the maximum intensity over the time in picoseconds. The black line shows the contrast without any further optimizations. The second two lines show the contrast after the booster settings are optimized. These settings are

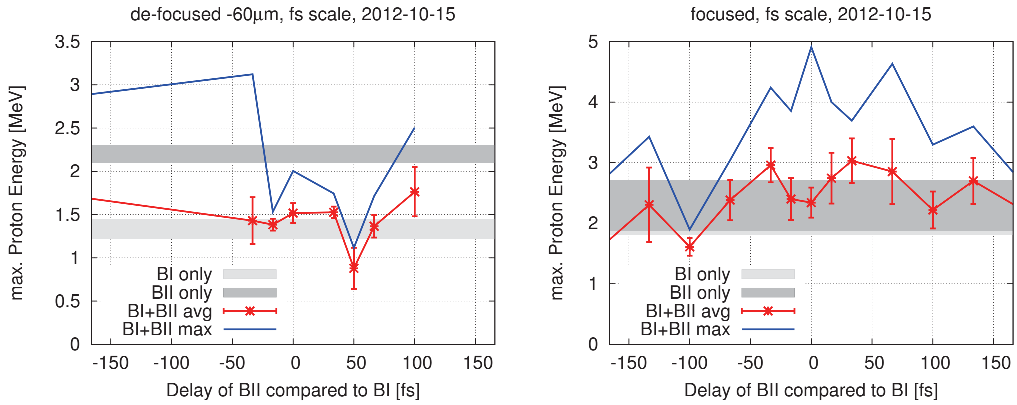

a Experiment. Proton cut-off energies over delay between the pulses. Both beams are defocused by -60μm, i.e. towards the OA parabolas.

b Experiment. Proton cut-off energies over delay between the pulses. Both beams are focused.

Figure 5.1.: The pulse energies are the same for the left and the right shot series. The pulse energy of beam II had been reduced in order not to have a dominance of beam II for negative delays. For the defocused shot series a local minimum is found for the maximum proton cut-off energy at synchronized laser pulses. For the focused shot series the highest cut-off energies are found for synchronized pulses.

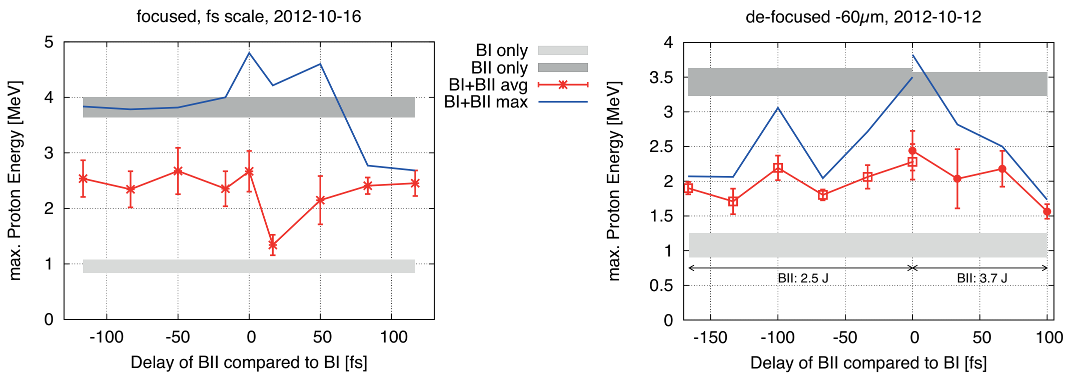

Figure 5.2.: Experiment. If the pulse energy of beam II is set to high values, the beam dominates the interaction, as can be seen for negative delays in the left graph. If the beams are defocused, as it has been done for the shot series corresponding to the right graph, the slope of the maximum proton cut-off energy is similar to the focused shot series of figure 5.1b.

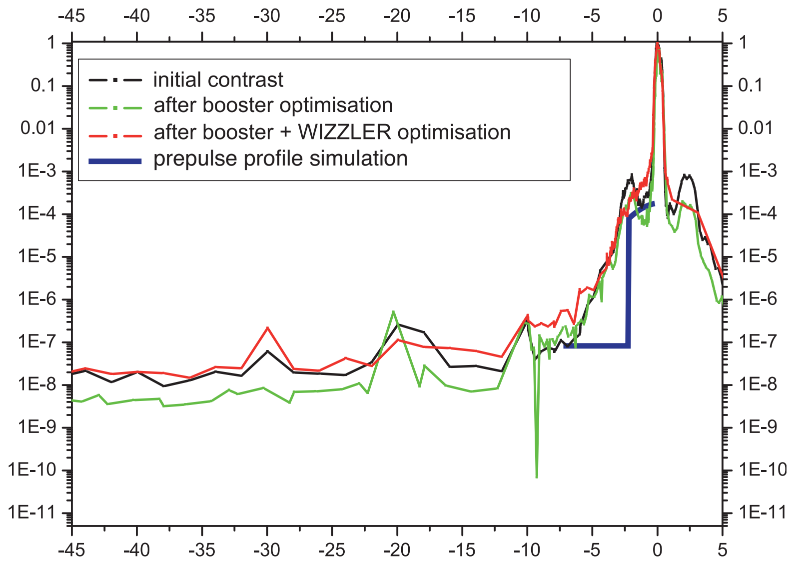

Figure 5.3.: Contrast measurement of beam I where no plasma mirror is used. In black the initial contrast of the laser. In green and red the contrast after optimizations of the booster and Wizzler. The optimizations are used in the experiment, because the optimization have been done under the conditions for two short pulses. An optimization for two short pulses and a high contrast for both pulses is not possible with the used setup. The blue line indicates the slope of the intensity, that is used in a PIC simulation in order to model the preplasma. Measurement by Anna Lena Giesecke [20].

not used in the experiment, because the settings are chosen for the shortest pulse length of both beams. The blue line shows the slope of the contrast for the prepulse simulation. At first the contrast is kept constant at 10^{-7} for 5 ps. A similar behavior is also found in the contrast measurement, where it starts at -12.5ps and ends at roughly -7.5ps. Then there is a steep rise of the contrast to 10^{-4}, followed by a slower rise to 2×10^{-4}.

The 5μm thick titanium target is not ionized. The beam has an angle of incidence of 40° similar to the experimental setup. The maximum intensity - where the contrast is 1 - is set to 6.5×10^{20}W/cm^2. The upper graph in figure 5.4 shows in red the evolution of the peak electron density. The green line shows the evolution of the contrast. Although the laser intensity is kept constant right before -2ps, the electron peak density already rises from -4ps slowly over $10n_{crit}$. This justifies the approach to simulate a constant laser intensity for several picoseconds. The steep rise in intensity causes also a steep rise in the electron peak density. Again a slower rise of the intensity is accompanied by a slower rise of the electron peak density.
The middle graph of figure 5.4 shows the evolution of the position where the electron density is equal to the critical density in the x-direction. The initial neutral titanium is distributed only in the range from ± 2.5 μm, so that a large fraction of the electrons is concentrated in this region. Especially the position in the negative x-direction remains basically constant.
The last graph of figure 5.4 shows three line-outs of the electron distribution at different time steps. It is obvious that for later times, the amount of electrons that have expanded away from the bulk target has increased. These electrons

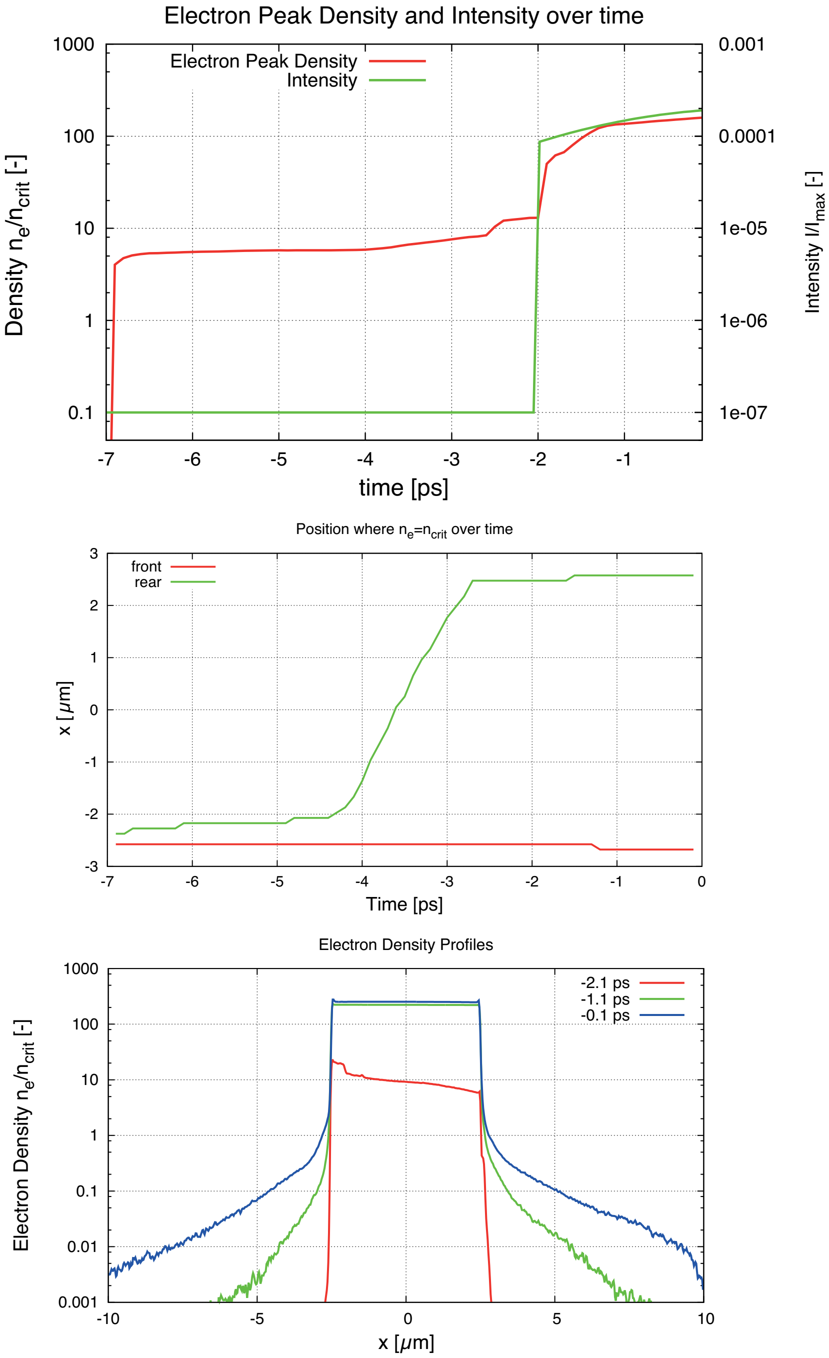

Figure 5.4.: Simulation. The prepulse of beam II is simulated over 10ps before the main pulse. The top graph shows the temporal evolution of the electron peak density. The green curve in the graph shows the contrast evolution, whereas the right y-axis belongs to the contrast. The peak electron density follows the evolution of the contrast. The middle graph shows in red the expansion of the electron density in front of the target and the position where the electron density is equal to the critical density, respectively. The green line shows the position of the critical density on the target's front and on the target's rear side, respectively. The bottom graph shows three cross sections of the electrons density at three different time steps. The density distributions at -0.1ps are taken for the focused and synchronized simulation. The distributions at -0.2fs are used for the simulations with -120fs and 120fs delay between the main pulses. The density distributions at -2.1ps are used for the low intensity, defocused simulations.

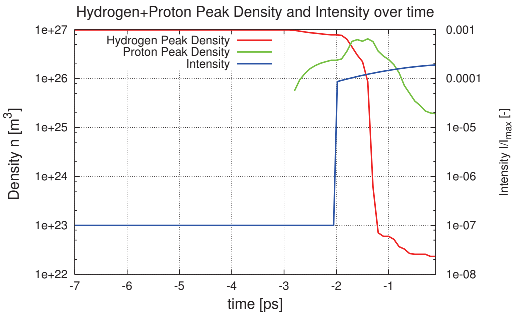

a Simulation. Temporal evolution of the peak densities of hydrogen (red) and protons (green). The evolution of the contrast is shown in blue. An increase in the peak proton density entails a decrease of the hydrogen density. For times >-1ps hydrogen has basically disappeared. The peak density of the protons also drops for times >-1.5ps as the protons expand.

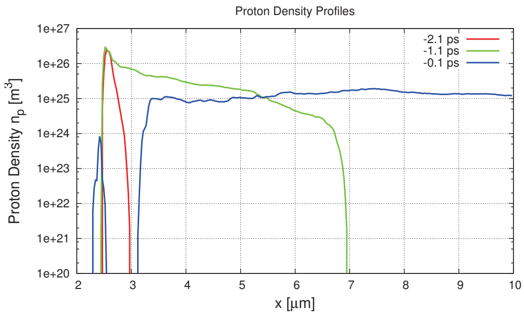

b Simulation. The graph shows three cross sections of the proton density at three different time steps. For low intensity, defocused shots (-2.1ps) the protons are still confined in a volume close to the target's rear side. For focused synchronized shots (-0.1ps) the protons have expanded already over an volume larger than 10μm behind the target.

Figure 5.5.: Simulation. Effect of the prepulse onto hydrogen and protons on the target's rear side.

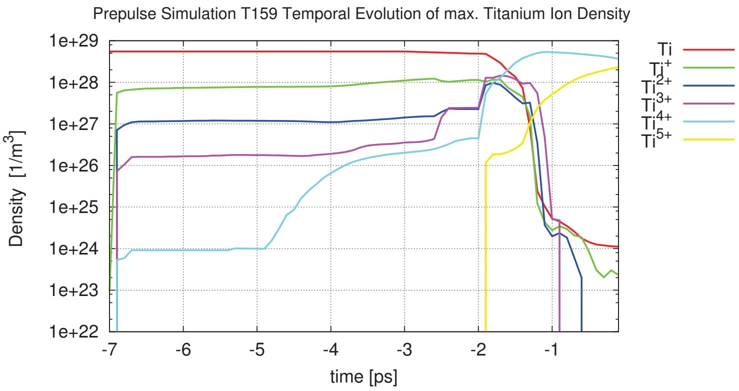

Figure 5.6.: Simulation. Temporal evolution of titanium ion densities during the prepulse. 1ps before the main pulse Ti^{4+} is the dominating titanium ion specie, but right before the main pulse is Ti^{5+} the dominating ion specie. Thus different ions have to be considered for low intensity, defocused simulations and for focused synchronized simulations.

will have a strong impact on the absorption of the main pulses and consequently on the TNSA acceleration.
Besides the expansion of the electrons, hydrogen and ionized hydrogen are also expanded. Figure 5.5a shows the hydrogen and proton peak density over time. Moreover the graph shows the laser contrast. The first hydrogen is ionized right after -3ps. The density of the hydrogen drops along with the increase of proton appearance. Due to the expansion of the protons, the peak density also drops after -1.5 ps. Figure 5.5b shows the proton distribution for three different times. 100 fs before the main pulse, the protons have extended already over 10 μm.
The interplay is as follows between delay and prepulses of both beams. If beam I is the first pulse that interacts with the target, the prepulse of the second laser - namely beam II - will be interrupted by the first beam. From this follows that the preplasma is smaller for a delay of -100 fs compared to a delay of e.g. 10fs. The situation is the same for the inverted case, because the contrast is the same on a timescale larger than -1ps and the main influence has already taken place, which is the prepulse of beam II below -1ps.
If both beams are synchronized the prepulses add up and the preplasma is much larger compared to the delayed situation.

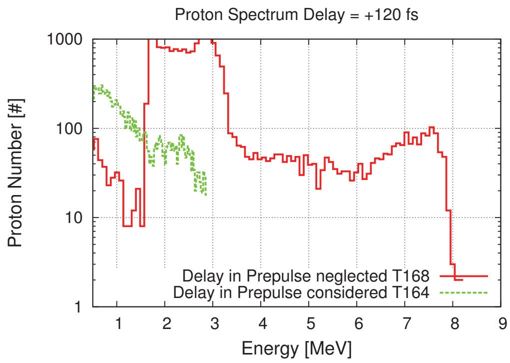

Figure 5.7.: Simulation. Comparison of proton spectra. If the influence of the delay between the pulses is neglected for the prepulses, the prepulse is overestimated. The result is a more than two times larger proton cut-off energy, compared to the case where the delay is considered.

If the delay in the prepulse is neglected, so that the second laser beam interacts with a much larger preplasma, the proton cut-off energies strongly change. Figure 5.7 shows in red the proton spectra where the delay in the prepulse is neglected. The green line shows the proton spectra where the effect is considered. For this case the cut-off energy is more than 2.5 times lower. From this follows, that the electron density distribution has a larger effect onto the cut-off energies than the difference in the pulse energies.
In the following this prepulse simulation gives the initial particle distributions for the defocused and focused shot series on a femtosecond timescale. Therefore line-outs are made at y=0 for the different particle species. These distributions are used as initial conditions for new PIC simulations, that simulated the interaction of the main pulses with these distributions. The simulations are in 2D, thus the 1D line-outs are expanded along the y-direction. By doing this, any deviations in the y-direction are neglected, but it is believed that these deviations would have only a minor effect on the results of interest. For example, the density distributions at -0.1ps are taken for the focused and synchronized shot

simulation. For delays of -120fs and 120 fs the density distributions at -0.2ps are taken as initial density distributions for the 2D simulations of the main pulses. This is not done for the defocused shot series. The particle distributions at -2.1ps before the main pulse are taken for the defocused shot series. As the intensity of the prepulse is thought to be very low for the defocused shots, the preplasma distribution is the same for all delays.

5.3. Single Beam Interaction

Before the double beam interaction is interpreted, the single beam interaction is briefly evaluated. The understanding of the single beam interaction plays an important role in the understanding of the double beam interaction - in particular the focused single beam interaction.
The evolution of the electric field at the rear side of the target, which is a result of the PIC simulation, shows counter intuitive behavior for the comparison of the focused and defocused shot series. The higher field strengths are achieved for the defocused shot simulations. The cut-off energy is higher in the focused shot simulation.
The explanation is found in the PIC simulation in particular in the different prepulses and therewith in the different preplasma conditions for the focused and defocused simulations.

5.3.1. Defocused - Single Beam Interaction

In the experiment the beams are both defocused by -60μm. The energy in both beams is set to 2.2 J before compression. It is reminded that only 25% of the pulse energy can be expected on target (cf. sec. 3.1.2 and 3.1.3). The intensity on target for the defocused beam II is 1.0×10^{19} W/cm^2 and for beam I 0.5×10^{19} W/cm^2. The intensities in the simulation is set to higher values compared to the experiment. Beam I has an intensity of 1×10^{20} W/cm^2 and beam II has an intensity of 3×10^{20} W/cm^2. As shown in the previous prepulse section, the influence of the prepulse is also reduced by the defocusing. Hence, the preplasma is the same for both single beam interaction simulations.

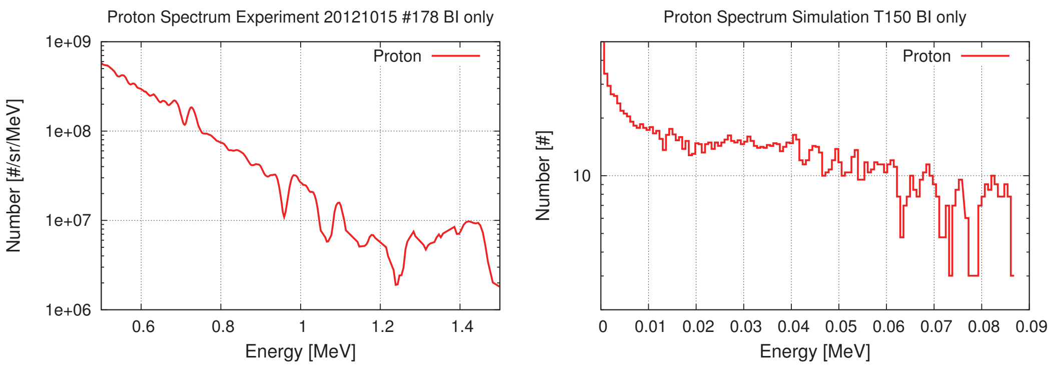

a Experiment. Proton spectrum from the experiment for a beam I only shot. It is a thermal spectrum with a small non-thermal part right before the cut-off energy.

b Simulation. Proton spectrum from the PIC simulation for a beam I only shot. The cut-off energy is not very clear.

Figure 5.8.: The beam I cut-off energies of the experiment strongly differ from the simulation. Both curves show a small bump right before the cut-off energy.

As the intensity is strongly reduced by the defocusing, the cut-off energies are also somewhat lower. Figure 5.8 and 5.9 show the spectra for the single beam shot of beam I and beam II, respectively. The left graphs are spectra of typical shots from the experiment. The right graphs are the spectra from the simulation. Although the cut-off energies of the simulations are considerably lower,

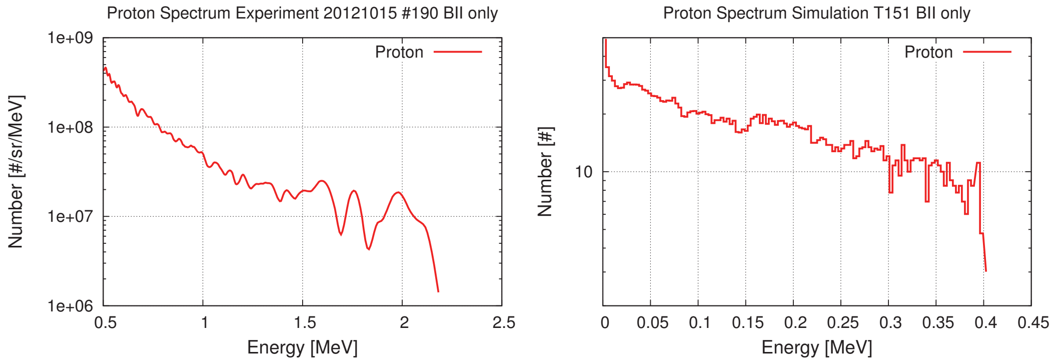

a Experiment. Proton spectrum from the experiment for a beam II only shot. The curve shows a clear cut-off.

b Simulation. Proton spectrum from the PIC simulation for a beam II only shot. The curve shows a clear cut-off.

Figure 5.9.: The BII cut-off energies of the experiment strongly differ from the simulation. Nevertheless, the curves of simulation and experiment both have a clear cut-off energy.

the simulations of the double beam shots reveal that the physical mechanisms must be the same. The next section compares experiment and simulation of double beam shots.
Especially the cut-off energies from the simulation show, that it is difficult to compare the cut-off energies of both beams with each other. The intensity of beam II is three times higher than of beam I in the simulation. The cut-off energy of beam II is five times higher compared to the cut-off energy of beam I. Thus, the Schreiber scaling does not apply, where the cut-off energy is proportional to the square root of the laser power. The main reason for this is the different angle of incidence for both beams. Therewith the absorption mechanisms are different. The temporal evolution of the electric field perpendicular to

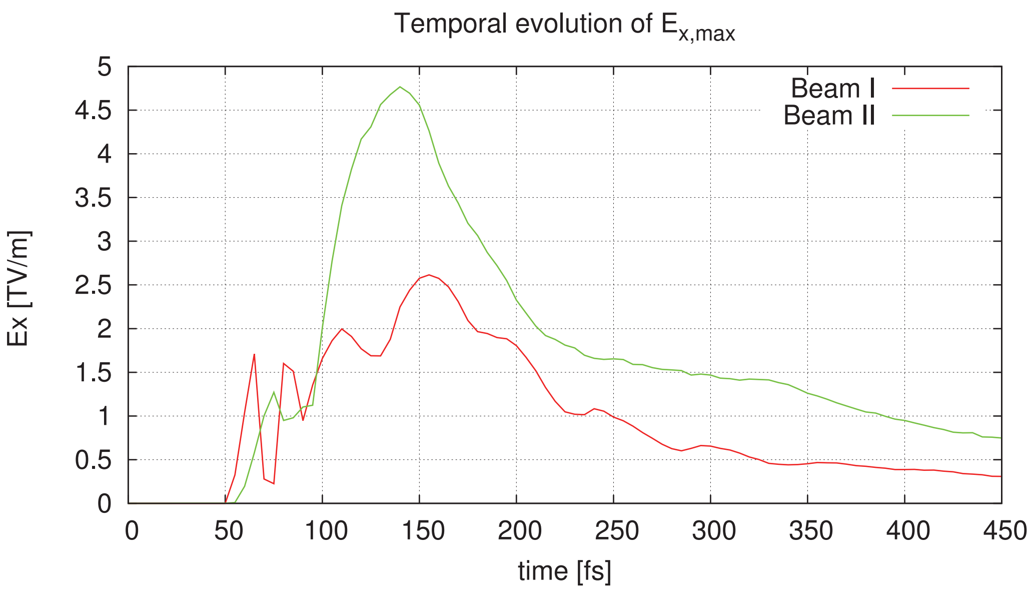

Figure 5.10.: Simulation. The temporal evolution of the maximum E-field in beam I direction on the rear side of the target.

the target gives a further explanation for the higher cut-off energy. The graph

in figure 5.10 shows the temporal evolution of this electric field. Both curves have roughly their maximum at around 150fs. Although the intensity of beam II in the simulation is three times larger than beam I, the maximum electric field strength is only doubled by the tripled intensity. Nevertheless, the electric field strength remains higher compared to the electric field strength caused by beam I for the whole period shown in the graph.
It can be concluded from this, that an increase in intensity not necessarily involves the same increase in the electric field strength. Moreover, the period where the electric field at the rear side of the target has a certain strength plays an important role. A similar effect is presented in the subsequent section.

5.3.2. Focused - Single Beam Interaction

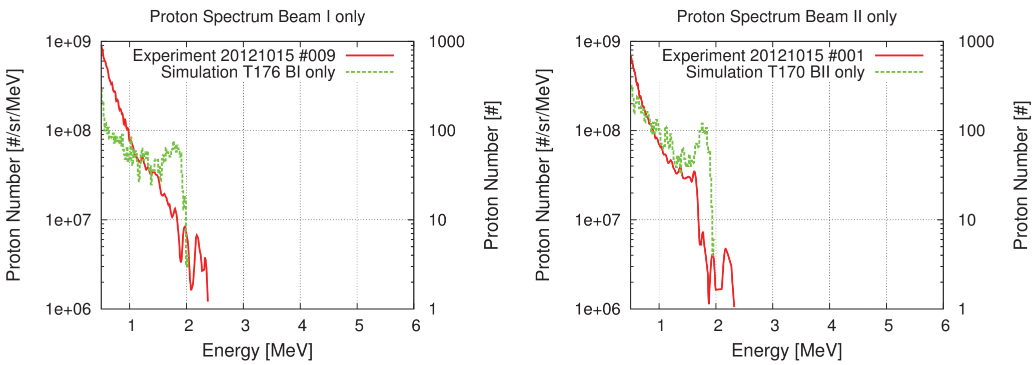

a Comparison of proton spectra from the experiment and from the simulation. Beam I only shot.

b Comparison of proton spectra from the experiment and from the simulation. Beam II only shot.

Figure 5.11.: Experimental results and simulation are in good agreement - especially the cut-off energies.

The same initial density distributions in both single beam simulations are used. The density distributions are taken from the prepulse simulation at -0.1ps. The pulse energy in the simulations is 2.8 J for beam II and 0.9 J for beam I. Figure 5.11 shows the single beam proton spectra in the experiment and the simulation. The shots of the experiment are average shots for the grey bars in figure 5.18. The cut-off energies are the same and in good agreement with the experimental results, whereas the proton number in the experiment for beam I decreases faster compared to the simulation as well as with the beam II spectrum. The pulse energy of beam II is three times larger compared to beam I and the cut-off energy of the protons should scale with square root of the laser power regarding the Schreiber model. But as already shown in section 5.3.1, due to the different angle of incidence the scaling model does not apply between the two beams.

The solution of the dilemma is again found in the temporal evolution of the electric field strength at the rear side of the target, which is shown in figure 5.12. Only a small stripe along the beam I direction is taken into account for the graph. The field field strength in this direction is for both beams almost the same with a peak value of about 3TV/m. Moreover the shape of the curves are almost the same. Eventually, the almost same field strength causes a similar spectrum, which is already shown in figure 5.11.

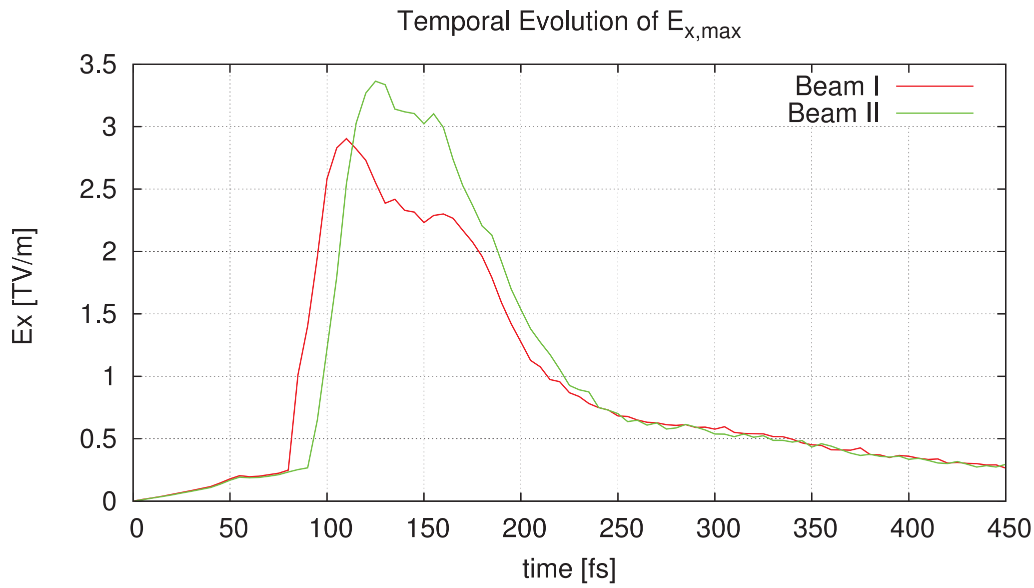

Figure 5.12.: Simulation. The temporal evolution of the maximum E-field in beam I direction at the rear side of the target.

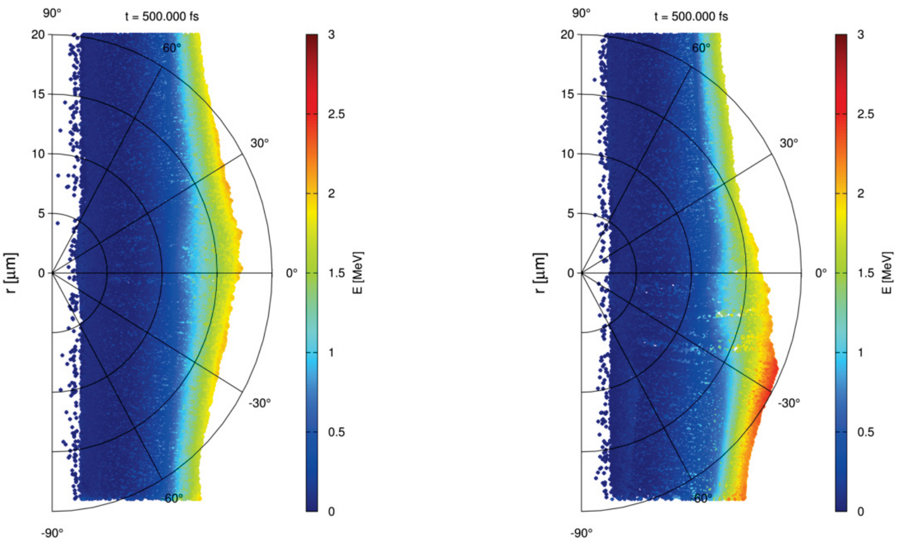

a Simulation. Polar plot of the proton energy distribution after 500fs. Beam I only shot. The distribution has a gaussian shape in the y-direction, centered at the focal position.

b Simulation. Polar plot of the proton energy distribution after 500fs. Beam II only shot. The distribution has a gaussian shape in the y-direction, centered somewhat below the focal position, but the temporal evolution is similar to the beam I distribution.

Figure 5.13.: The proton energy distributions comply with the expectations for TNSA.

A closer look of the spatial energy distribution of the protons is shown in figure 5.13 at 500fs. The proton energy is found to be the highest for the beam I interaction at an angle of 0°. In contrast the highest proton energy for beam II is found at an angle of 30°. Moreover the energy of the protons is more in the range of 3MeV instead of 2MeV as found in the spectrum. The velocity vectors of the protons for this interaction are basically perpendicular to the target surface. But as the Thomson parabola spectrometer only detects particles in the direction of beam I, i.e. at an angle of 0°, theses more energetic protons are not found in the experimental spectrum. In order to compare the experimental results with the results from the simulation, only a small stripe of $\pm 1\mu$m at an angle of 0° has been used for the generation of the spectra from the simulation. Thus the 3 MeV protons are also not found in the spectrum of the simulation.
The reason for the shape of the proton energy distribution is found for beam II in the motion of the fast electrons. The beam II hits the target at $y = 0$. The fastest electrons propagate in the beam direction and leave the target somewhat lower, namely by $t \tan \alpha$, where t is the target thickness and α the angle of incidence.
A second effect that has to be considered in order to explain the shape of the proton energy distribution of beam II. Beam II has a higher pulse energy and the oblique angle of incidence causes a better energy transfer from the laser into the plasma. Therefore beam II generates more fast electrons than beam I. Because the fastest electrons propagate in the beam direction, the protons also gain some momentum in the negative y-direction. Hence, the protons do not propagate in the beam II direction, but have a small angle in the order of magnitude of $-10°$.
The shape of these two energy distributions is also found in the next section for the double beam interaction.

5.4. Double Beam Interaction

This section compares the experimental results of double beam shots with simulations of double beam shots. The defocused shot series is interpreted first similar to section 5.3. Afterwards the focused shot series is discussed.
The dependence of the cut-off energy on the delay between the pulses is completely different between the defocused and focused shot series. The temporal evolution of the electric field at the rear side of the target shows for both shot series counter intuitive behavior. Higher field strength does not necessarily lead to higher proton energies.
In the defocused shot simulations the synchronized shot has the highest electric field strength at the rear side of the target compared to delayed shots, but the cut-off energy is higher for delayed pulses. In contrast the electric field strength caused by a synchronized and focused shot is only slightly higher than for delayed focused pulses. Nevertheless, the cut-off energy is distinctly higher for synchronized shots.
PIC simulations show the physical mechanisms behind this behavior.

5.4.1. Defocused - Double Beam Interaction

Introduction

The first experimental shot series presented in this section relates to defocused beams. The two beams are defocused by $-60\mu m$ in the laser beam directions, so that the intensity is reduced by a factor of 25. Moreover the energy in both beams is set to 2.2 J before compression and plasma mirror. The intensity on target for the defocused beam II is due to losses 1.0×10^{19} W/cm^2 and for beam I 0.5×10^{19} W/cm^2. In the simulations the intensity is set to 1×10^{20} W/cm^2 for beam I and to 3×10^{20} W/cm^2 for beam II. In the previous section it has been shown that the influence of the prepulse is reduced for defocused beams. Therefore the interaction of the two main pulses with the plasma is somewhat simpler and thus easier to model with a PIC simulation.

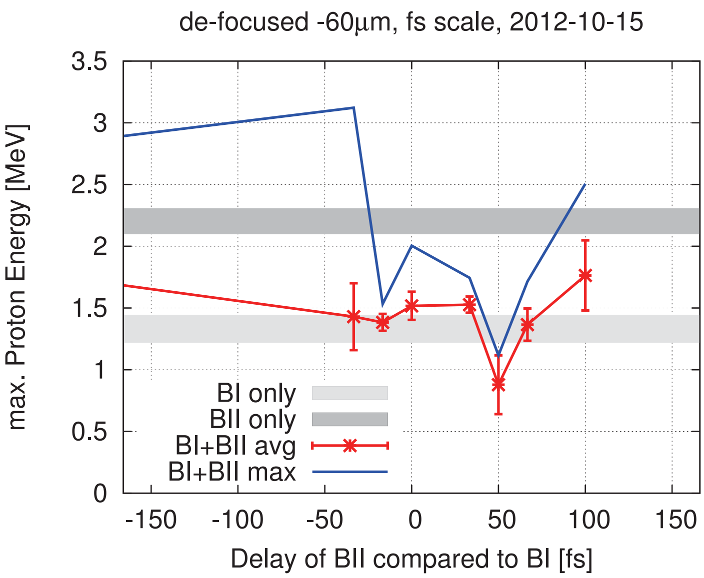

Figure 5.14.: Experiment. Maximum proton energies over delay between beam I and beam II. Both beams are defocused by -60μm, i.e. towards the OA parabolas. The highest maximum proton cut-off energies were achieved for delayed shots. At the synchronized delay position the maximum cut-off energy is just in between the cut-off energies of the single beam interactions. The maximum cut-off energy curve has the shape of a *w*.

Figure 5.14 shows the maximum reached proton energies over the delay between the two beams. The maximum proton energy increases with a larger delay. This behavior somewhat surprises, because the higher intensities are expected to be reached for smaller absolute delays. The characteristic is explained by PIC simulations. The configuration of laser and target in the simulation is the same as in the experiment. As described in the previous section the initial density distributions of these simulations are taken from the prepulse simulation at -2.1ps before the first main pulse. 1D line-outs at y=0 are expanded along the y-direction for the following 2D simulations. In contrast to the focused shot simulations the preplasma distribution is the same for all delays.

In the experiment the Thomson Parabola collects only ions that propagate in the direction of beam I. Therefore only protons in a small stripe of $\pm 1\mu m$ along the beam I axis are taken from the simulations to generate the proton spectra.

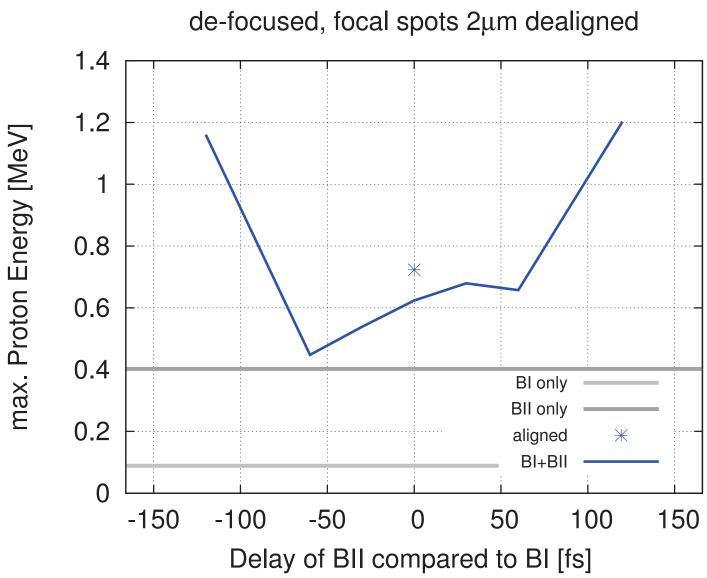

Figure 5.15.: Simulation. Maximum proton energies over delay between beam I and beam II. The shape of the curve is similar to the experimental result (cf. fig. 5.14, i.e. the characteristic w shape. Thus, the physical parameters are well reproduced by the simulation.

The proton cut-off energies are plotted as a function of the delay between the two pulses, which are shown in figure 5.15.
Although the energies are lower in the simulations compared to the experiment, it appears again the characteristic w structure. An electric field at the rear side of the target causes the ions to accelerate in the TNSA regime. The field evolves due to a separation of electrons from the target.

Temporal Evolution of the Electric Field Strength

The graph in 5.16 shows the maximum electric field strength in the x-direction - in beam I direction - over time. The highest strengths are achieved for the synchronized shot. Especially for a delay of $120fs$, the maximum field strength is almost one half compared to the maximum field strength for a delay of $0fs$. Moreover the influence of the two separated pulses are clearly visible in the shape of the red and blue curve.

Temporal Evolution of the Ion Momenta

Figure 5.17a shows the temporal evolution of the proton momentum for the three different delays, i.e. -120, 0 and 120 fs. The acceleration of the protons starts for all three cases 50 fs after the ambipolar electric fields build up. The velocity of the particles is the highest for the synchronized shot for a time period of 100 fs. This period corresponds with the rise and collapse time of the electric field for this delay. For times larger than 200 fs the acceleration of the protons is basically the same for all three delay scenarios. The shape of the red curve is somewhat smoother. This behavior is also found for the evolution of the maximum electric field strength, where the bump of beam I - the late beam - is relatively small. More importantly the velocity of the protons for

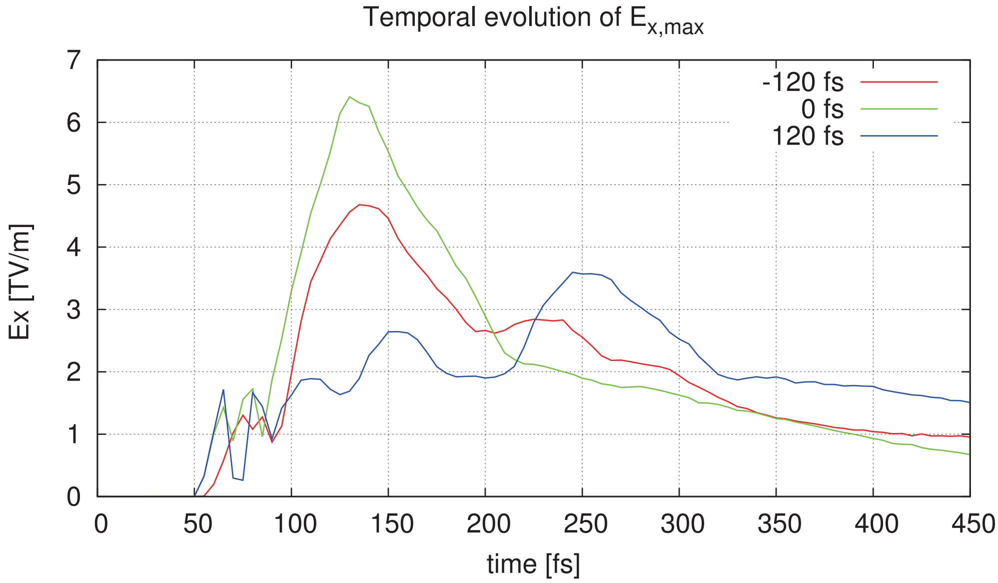

Figure 5.16.: Simulation. The temporal evolution of the maximum E-field in beam I direction at the rear side of the target. The synchronized case has the highest field strength, but it also drops faster. The blue curve, where beam II is late, has two bumps at 150 fs and 250 fs, which correspond to the fields driven by beam I and beam II, respectively.

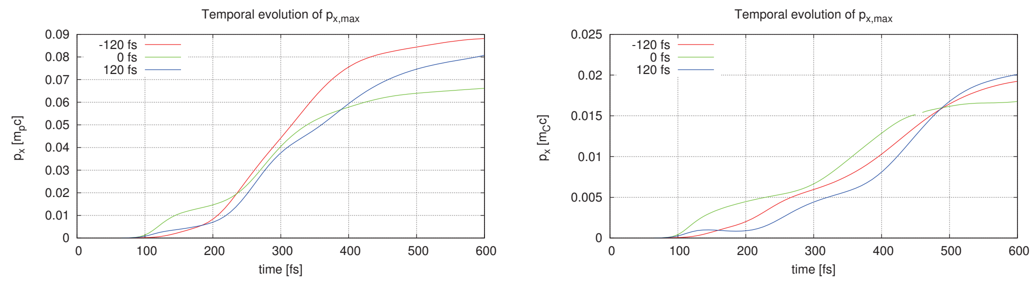

a Simulation. Temporal evolution of the proton momenta from different delay simulations.

b Simulation. Temporal evolution of the C^{4+} momenta from different delay simulations.

Figure 5.17.: The acceleration of the protons is higher for the synchronized pulses (green) over a time period between 100fs and 200fs compared to the delayed pulses. But the fast appearance and disappearance of the electric field causes also fast saturation of the proton momenta after 350fs. Eventually the proton momenta is higher for delayed shots. A further interesting feature is is seen for the delayed shots in the shape of the curve. The delayed pulse causes a bump in the shape of the curve. The temporal evolution of the C^{4+} momenta have the same features, but the curves are somewhat extended.

the synchronized shots saturates first. The velocity in the delayed simulations increases further. Finally the velocities of these simulations is almost the same, which is not shown in the graph.
The same behavior as for the protons is obtained for carbon 4+ ions in figure 5.17b. The temporal evolution is similar as for the protons, but due to the higher mass - higher inertia - the respond of the ions to the electric fields is somewhat attenuated.

Conclusion

The highest electric field strength is achieved for a synchronized shot, as one would expect. Furthermore, due to in the absolute terms lower prepulse intensity - compared to the focused shots - , fewer electrons and ions have expanded away from the bulk target before the main pulses arrive. Thus the ions are still relatively closely concentrated at the rear side of the target. It follows from the high concentration of the ions at the rear side of the target and the fast appearance and disappearance of the field, that the action between ions and electric field is lower for the synchronized case. In other words the ions cannot react fast enough on the appearance and disappearance of the electric field. By delaying the two pulses the lifetime of the electric field is artificially increased. The ions are getting more time to interact with the electric field.
The experimental shots, where a lot of ion species appeared, occurred only for the defocused shots. Moreover, the characteristic MCP images tended to appear more often for the delayed shots. Again, due to a lower thermal expansion of the ions due to a lower prepulse, the ions are more concentrated in a small volume close to the rear side of the target. Nitrogen and oxygen occur in a smaller number in the contaminants compared to carbon and hydrogen. Thus, at the time accelerated electrons generate the ambipolar electric field, a lot of nitrogen and oxygen is still located at the rear side of the target. This would not be the case for a more intense prepulse. Eventually, these less often occurring contaminants constituents are also accelerated. In order to resolve this feature in simulations, the total particle number has to be significant higher. This would drastically exceed the available machine time.

5.4.2. Focused - Double Beam Interaction

This section discusses double beam shots in experiment and simulation. For focused shot simulations the preplasma has a different shape compared to the defocused situation. As already described in section 5.2, the subsequent laser interrupts the prepulse of the first laser pulse by its strong main pulse. Thus the preplasma has a larger extension for synchronized shots compared to delayed shots. As the preplasma plays such an important role, only experimental shots will be compared to the PIC simulation where both single beams achieved a similar proton cut-off energy. Otherwise the beam II will dominate the acceleration mechanism with its strong prepulse for negative delays.

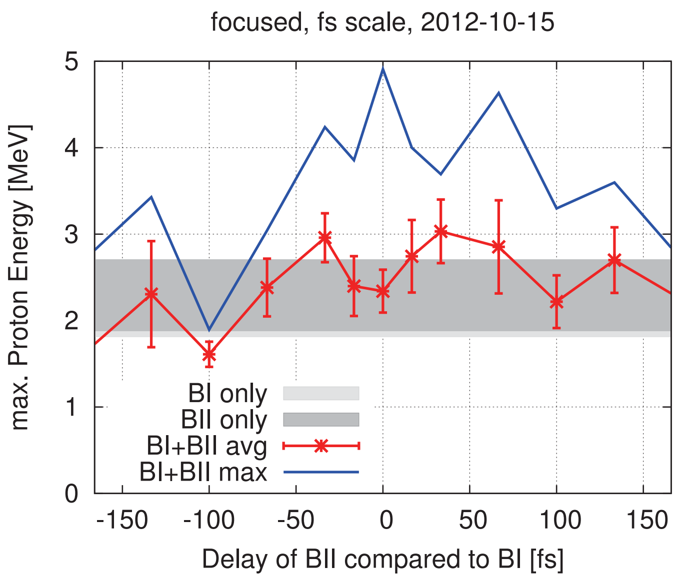

Figure 5.18.: Experiment. Maximum proton energies over delay between beam I and beam II. Both beams are focused. Highest proton energies are observed for synchronized shots. The sum of the cut-off energies from the single beam interaction corresponds to the maximum cut-off energy for synchronized pulses. The maximum cut-off energies for negative delays tends to be somewhat lower compared to positive delays.

The maximum proton cut-off energies over the delay between the two pulses are indicated by the blue line in figure 5.18. In average the cut-off energy rises with a smaller absolute delay.

As already shown in section 4.3, the experimental result of the cut-off energies over the delay between the two pulses is shown in figure 5.18. This graph is reproduced with PIC simulations as shown in figure 5.19. The maximum proton cut-off energy line of the experimental data has the shape of a triangle with its tip at a delay of 0 fs. Furthermore, the triangle is somewhat tilted to higher energies for a positive delay - where beam I is the first beam. The same trend is also found in the simulation. A positive delay tends to have a slightly higher proton cut-off energy compared to a negative delay, although the total laser energy involved in the interaction is the same for all cases.
In the following these characteristics are explained by PIC simulations. In

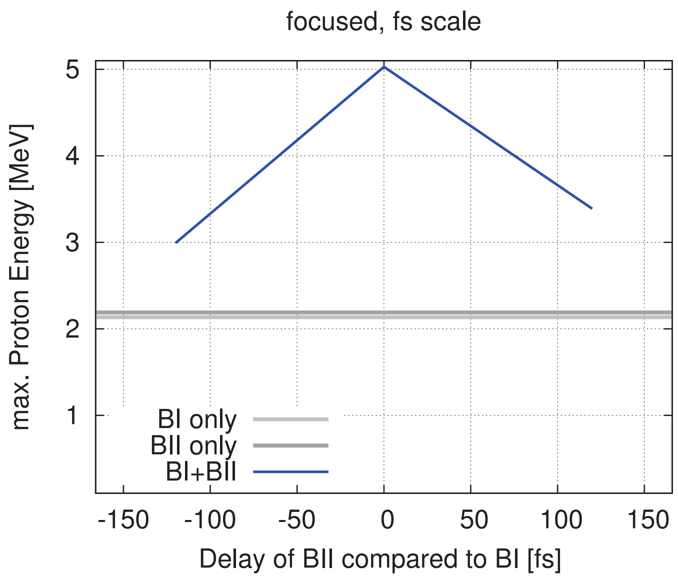

Figure 5.19.: Simulation. Maximum proton energies over delay between beam I and beam II. The shape of the curve is similar to the experimental result (cf. fig. 5.18) - especially the proton cut-off energy is somewhat lower for negative delays. In the experiment the maximum cut-off energy for synchronized pulses composed roughly from the cut-off energies from the single beam interaction. In the simulation the cut-off energy for synchronized pulses is even higher compared to the sum of the cut-off energies from the single beam interactions.

particular the reason for the highest proton energies for synchronized pulses and why the proton cut-off energy is higher for positive delays.

The three spectra of figure 5.20 show the proton spectra for delays of -120fs, 0fs and 120fs from the experiment in red and from the simulation in green. The agreement of experiment and simulation is remarkably. Only with the approach to consider the delay between the two pulses also for the prepulse, it is possible to reproduce the experimental spectra with the simulation. Therefore, the underlying physical mechanism of the acceleration that is found in the simulation represents with quite confidence the reality.
So, in contrast to the defocused shot series, the highest proton energies are found for synchronized pulses.

Figure 5.21 shows the evolution of the maximum electric field strength in x-direction from the simulation. Although the intensity of the two pulses are increased from $1.0 \times 10^{20}\mathrm{W/cm^2}$ and $3.3 \times 10^{20}\mathrm{W/cm^2}$ to $3.2 \times 10^{20}\mathrm{W/cm^2}$ and $6.5 \times 10^{20}\mathrm{W/cm^2}$, the maximum field strength is lower for all three delay cases compared to the three delay cases for the defocused simulation series (cf. fig. 5.16).
The reason for this is found again in the different density distributions of the preplasma. For defocused shots the preplasma is not as much extended as the preplasma during focused shots. Especially the ions from the contamination do not gain a lot of energy from the prepulse, but are still at rest in a confined volume close to the target's rear side. For focused shots the contamination's ions could gain some energy from the preplasma and expand thermally away from the target's rear side. Thus there is no need for high field strength caused by a large charge separation in order to accelerate the particles to high energy,

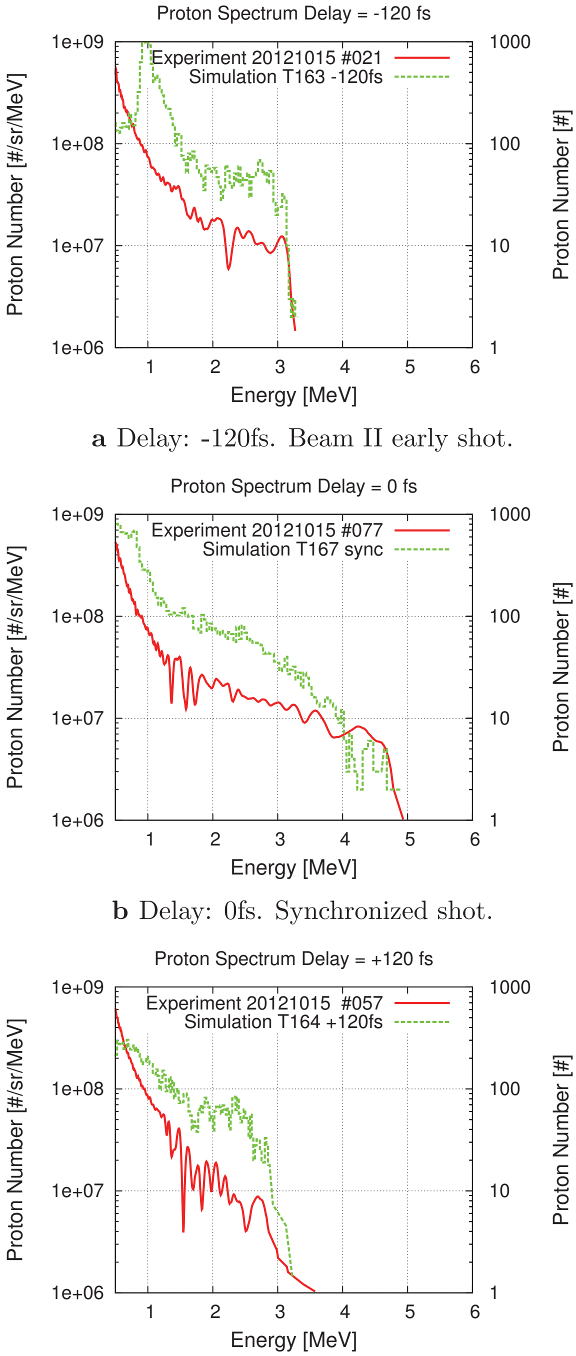

a Delay: -120fs. Beam II early shot.

b Delay: 0fs. Synchronized shot.

c Delay: 120fs. Beam I early.

Figure 5.20.: Comparison of proton spectra from the experiment and from the simulation. Experimental results and simulation are in good agreement - especially the cut-off energies.

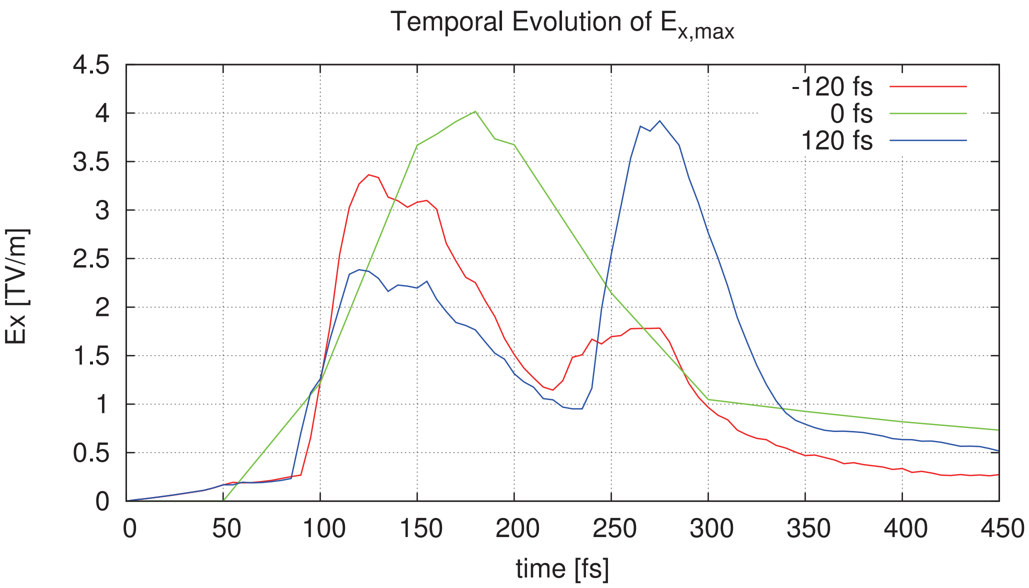

Figure 5.21.: Simulation. The temporal evolution of the maximum E-field in beam I direction at the rear side of the target. The maximum field strengths are almost the same for the three different delay shots. The electric fields strength remains on a relatively high level for a long time for the synchronized shot. The delayed shots clearly show the impact of the first and second pulse. In total the field strengths are lower compared to the defocused simulations (cf. 5.16)

because the prepulses assist the acceleration process in advance. One should keep in mind that this is valid for this specific case, where a rather thick target has been used. Nanometer thick targets would need of course a high laser contrast, otherwise the target would have been blown away by the prepulses.

A further remarkable feature is found in figure 5.21. The maximum field strength is almost the same for a synchronized shot and a delay of 120fs, but the synchronized shot has a significant higher proton cut-off energy. The reason for this is found in the energy distribution of the protons. Figure 5.22 shows the proton energy distributions for a delay of -120fs, 0fs and 120fs at the same simulation timestep namely 500fs. The color range is increased from 4 MeV to 6 MeV for the synchronized case. All three distributions have their own characteristic shape. For a delay of -120fs two peaks are visible. For synchronized pulses one large peak is observed. Moreover protons up to an energy of roughly 0.5 MeV are not present. In the proton spectrum this leads to a gap, which is seen in the simulation, but not in the spectrum from the experiment, because the Thomson parabola does not resolve those low energy protons. The last energy distribution, where beam II is late, shows no significant peak, but a rather large area that is accelerated to high energies. Thus, the higher proton energies tended to appear for shots where beam II is late, because a larger area is accelerated to high energies for those shots which can enter the Thomson parabola in beam I direction.
The shape of the energy distributions can easily be deduced from the single beam interaction. Figure 5.23 shows a schematic the evolution of the electron sheath. The first beam generates a sheath. The subsequent laser pulse mod-

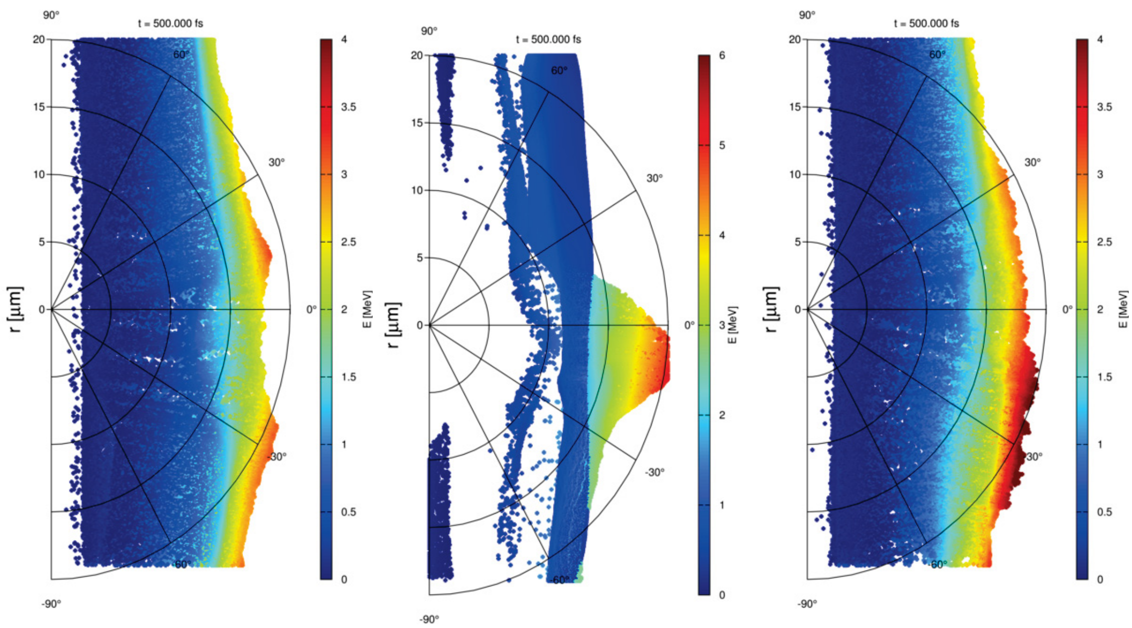

a Simulation. Delay: -120fs. Beam II is the first pulse. Two peaks are clearly visible in the proton energy distribution.

b Simulation. Delay: 0fs. Synchronized shot. The color range is increased from 4MeV to 6MeV compared to the delayed shots. The distribution of the highest energies have the shape of a top-hat. There are almost no protons with an energy below 0.5MeV.

c Simulation. Delay: 120fs. Beam I is the first pulse. A large area of protons is accelerated to high energies. The peak is somewhat located below the focus position in the y-direction.

Figure 5.22.: Polar plots of the proton energy distribution after 500fs. Every delay has its own characteristic shape in the proton energy distribution. The shapes for the delayed pulses can be deduced from the single beam interaction. The distribution of the synchronized shot is explained by a different mechanism.

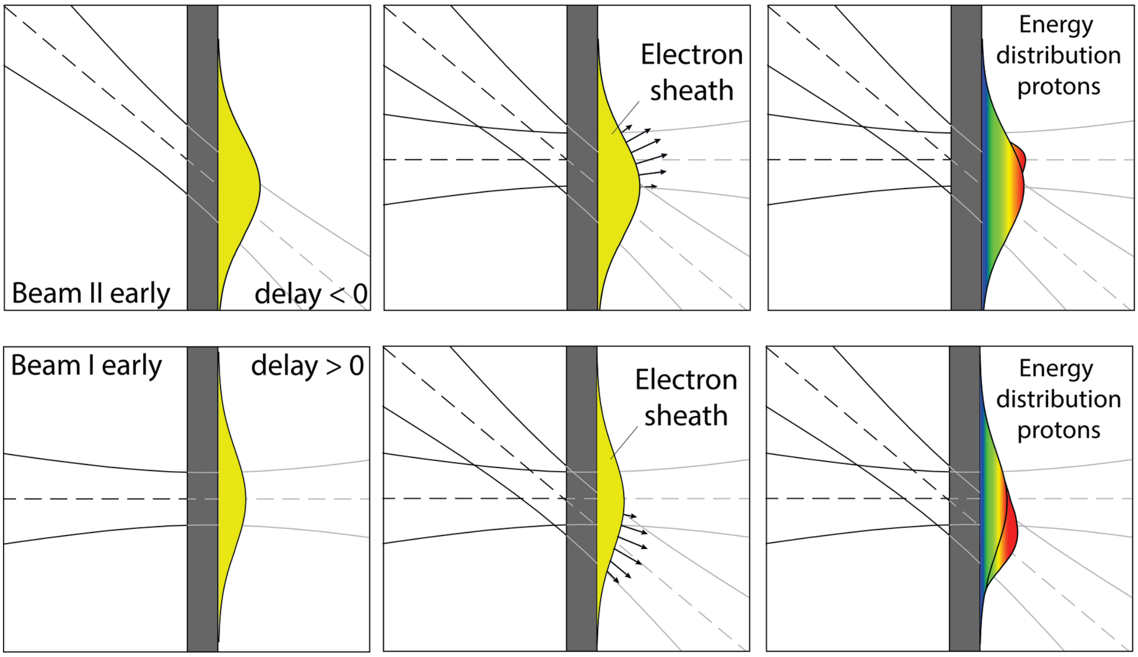

Figure 5.23.: The schematic shows how the electron sheath is affected by the subsequent laser pulse. The first pulse that interacts with the target imprints its own characteristic electron sheath into the plasma. The subsequent laser pulse only modifies the electron sheath with its own characteristic electron sheath shape. The level of magnitude of the modification depends on the pulse energy. Therefore beam II has usually more pulse energy than beam I and has a stronger influence onto the electron sheath. Thus, the electron sheath looks different for a negative and a positive delay. For a negative delay for example, beam II generates an electron sheath which is somewhat below the focal position in the y-direction. The weaker pulse of beam I modifies the electron sheath in the height of its focal position only by a small amount. Thus, a second small peak appears in the proton energy distribution.

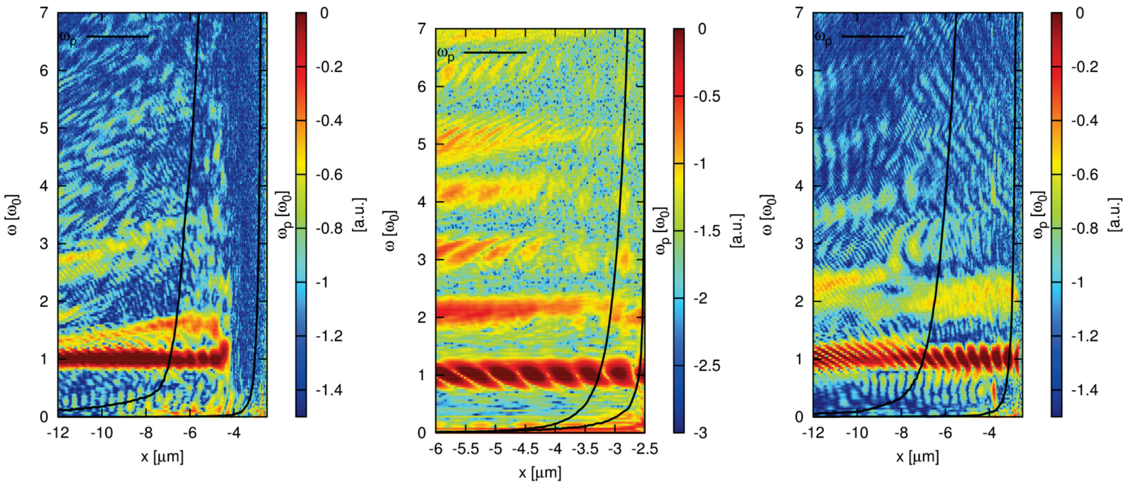

a Simulation. Delay: -120fs. Beam II is the first pulse.

b Simulation. Delay: 0fs. Synchronized shot. The color range is doubled, i.e. increased from 1.5 to 3 compared to the delayed shots.

c Simulation. Delay: 120fs. Beam I is the first pulse.

Figure 5.24.: Simulation. E_x in spatial and frequency space. The temporal window of the Fourier transformation covers 300fs, in order to have the effect of both beams. The black lines are the electron densities normalized to the critical density at the start and end of the temporal window, respectively. Resonant $\vec{j} \times \vec{B}$ heating is only observed for the synchronized shot. The resonances effectively transfer laser energy into electrons. These resonances are not found for the defocused simulations.

ifies the shape of the already present sheath. In particular as beam II has a higher pulse energy and an inclined angle of incidence, i.e. resonant absorption can take place, the electron sheath is dominated by beam II and therewith the proton energy distribution. From this follows, that for a shot where beam II is early, the weaker beam I generates only a further small bump in the electron sheath and therewith in the proton energy distribution. For the inverse case, beam II interacts with a larger plasma in front of the target and resonant absorption is more efficient. Eventually, the larger energy transfer to the plasma leads to a larger area of protons that are accelerated to high energies.
In order to understand the three very different proton energy distributions, the absorption mechanisms in the first place is investigated. Nuter et al. [38] describe a resonantly enhanced $\vec{j} \times \vec{B}$ heating. A preplasma is generated by a first low intensity laser pulse, which is followed by a high intensity laser pulse. Thus, the second laser interacts with a expanding electron distribution. The delay between the two pulses is varied. So, basically the electrons' scale length is varied. The authors refer to a publication of Andreev et al. [7]. If the electron density is in the order of magnitude of $4n_{crit}$, the $2\omega_L$-oscillating evanescent part of the Lorentz force can resonantly trigger an electrostatic wave [38]. An optimal preplasma scale length is derived where enhanced laser absorption occurs. For scale lengths larger than the optimal scale length, the evanescent part of the Lorentz force is unable to reach the plasma region where $n_e \approx 4n_{crit}$ [38]. If the scale length is too short, the plasma gradient is too steep so that no plasma wave develops.

In order to check whether such a resonant $\vec{j} \times \vec{B}$ heating occurs in the present double beam shots, the spectral power of the longitudinal field E_x is plotted in figure 5.24. The electron densities are shown as black lines for the corresponding times. The E_x spectra cover 300 fs in order to have the full influence of both beams. The delayed spectra show a small resonances at 2ω. For the synchronized case one observes resonances till 6ω. Furthermore the logarithmic intensity range has changed. Due to the larger preplasma the two laser pulses generate resonantly plasma waves and transfer laser pulse energy more effectively into the plasma. These resonances are not found for the defocused simulations.
For synchronized and focused beams the proton cut-off energy is higher compared to the delayed and focused beams. This is not the case for defocused beams. There the proton cut-off energies are lower for a synchronized case compared to the delayed shots. The driving mechanism for this behavior is the electron density distribution. For focused beams the prepulse intensity is also significantly higher. The largest electron expansion before the main pulses is observed only for the synchronized shots. Delayed main pulses interrupt the influence of the other beam, so that the electron expansion is lower compared to the synchronized case. The synchronized interaction of both beams leads to resonant $\vec{j} \times \vec{B}$ heating. This mechanism efficiently transfers the laser pulse energy to electrons. These electrons contribute to the ambipolar electric field at the rear side of the target. Eventually, this leads to higher proton cut-off energies as compared to the delayed case.
For defocused beams the intensity of the prepulse is also lower. Thus, the absolute contrast is higher. Therefore, the electron expansion for the synchronized shots is lower as for delayed shots.

5.5. Conclusion

In this chapter the experimental results were analyzed and interpreted by PIC simulations regarding delays in the order of magnitude of 10s of femtoseconds. The analysis of the MCP images already showed that the preplasma plays an important role. Thus, the prepulse of a single beam, in particular beam I, was modeled by a PIC simulation over 10ps before the main pulse. Contrast measurements of beam I were used as input. The results of the PIC simulation were used in turn as input for the subsequent interaction of the main pulses. It turned out that the delay between the two main pulses also has to be considered for the prepulse in order to explain the experimental results. The first main pulse that interacts with the target interrupts the prepulse of the subsequent main pulse. Hence, the largest preplasma is observed for synchronized laser pulses.
Simulations were performed for focused single beam interactions. The simulations showed characteristic features of the proton energy distribution. Beam I has a peak in the proton energy distribution, which is located at the same height on the target's rear side as the focus on the front side. Moreover the protons with the highest energy propagate in the direction of beam I, i.e. perpendicular to the target. Beam II has an angle of incidence of 40°. The peak in the proton energy distribution on the target's rear side was located somewhat below the focal position on the target's front side. Both features of the single beam interaction are observed for the double beam simulations.

The influence of the delay onto the prepulse has to be considered for high intensities, i.e. focused beams. If the influence is neglected, the proton cut-off energies from the simulation are the same for delayed pulses and synchronized pulses. If the influence of the delay onto the prepulses is considered, the proton spectra of experiment and simulation are in good agreement.
In the simulation the driving fields for the acceleration are lower for the focused shot series compared to the defocused shot series. Due to the higher intensity of the prepulses for focused shots the ions expand thermally away from the target's rear side before the main pulses arrive. Hence, the ions gain already some momentum from the prepulse. Eventually, the action between moving ions and electric field is larger for the focused shots compared to the defocused shots.
The comparison of the proton energy distribution for three different delays showed, that each distribution has its own characteristic shape. For negative delays, where beam II interacts first with the target, the proton energy distribution shows two peaks. For positive delays, where beam I interacts first with the target, the proton energy distribution shows a large area of protons that were accelerated to high energies. The shape of these distributions can be deduced from the single beam interactions. The subsequent laser pulse modifies the electron sheath of the first pulse and therewith the shape of proton energy distribution is modified. In the experiment only ions in beam I directions were detected by the Thomson parabola, thus the shape of the proton energy distribution could not be validated by the experiment yet.
Remarkable MCP traces were observed for synchronized shots in the experiment. The traces have a relatively low number of different ion species but a high proton cut-off energy. Similarly, simulations revealed also high proton cut-off energies for synchronized pulses. Moreover, the proton energy distribution shows that the highest energies are located in a small area. Nuter et al. as well as Andreev et al. describe a resonantly enhanced $\vec{j} \times \vec{B}$ heating. For electron densities close to $4n_{crit}$, the $2\omega_L$-oscillating evanescent part of the Lorentz force resonantly excites an electrostatic wave [38, 7]. The results of the PIC simulation of the electric field in x-direction have been Fourier transformed. Strong resonances are only observed for the synchronized case. Resonances are not observed for the delayed shots. The PIC simulations give a reasonable explanation for the rare MCP traces.
The influence of the delay onto the prepulse can be neglected for low intensities, i.e. for defocused shots with low pulse energies. The maximum cut-off energy is not observed for synchronized shots, but for delayed shots. The PIC simulations showed that although the electric field strength at the rear side of the target has the highest strength for synchronized pulses. However, during the time period the field is present is shorter compared to the delayed cases. Thus, the ions' inertia is too large so that the particles cannot *react* on the fast appearance and disappearance of the electric field. The effect can also explain experimental defocused shots where a large number of different ion species appeared. The relatively low prepulse of those shots does not thermally expand the dirt constituents, so that these ions are still confined in a small volume close to the target's rear side. As in the experiment these MCP traces tended to appear more often for delayed pulses, the effect of a longer lifetime of the ambipolar electric field causes a smooth acceleration of a large number of ions.

6. Magnetic Vortex Acceleration - Interpretation of Experimental Data

6.1. Introduction

In the previous chapter the laser pulses were delayed on a timescale of several 10s of femtoseconds. Because of target thickness and laser intensity ions are accelerated due to the TNSA mechanism. During the double beam interaction, the subsequent laser pulse enhances the TNSA mechanism.
This chapter concentrates on delays between the two pulses in the order of 10s of picoseconds. The maximum proton energies achieved with these long delays are shown in figure 6.1. When beam II was late, i.e. for positive delays, the cut-off energy is equal to a beam I only shot. For negative delays an enhancement appears in the cut-off energy. The subsequent laser pulse does not have an influence on the TNSA mechanism, as this process last only for several 10s of femtoseconds. Any enhancement in the proton's cut-off energy on a larger timescale must rely on a different acceleration mechanism. The chapter identifies for these relating experimental shots a acceleration mechanism called magnetic vortex acceleration. Bulanov et al. [10] describe a laser pulse that propagates through a relativistic transparent material. The laser pulse accelerates electrons. In combination with a return current, a self sustaining magnetic field is generated. The quasi static magnetic field efficiently accelerates ions to high energies.
The first section starts with the simulation of the plasma expansion after one main pulse has interacted with the target. In dependence on the initial conditions, two scenarios are possible for the particle distribution after several 50s of picoseconds. The scenarios belong either to a shot where beam I or a beam II is late.
Afterwards, these particle distributions are used for simulations where the subsequent laser pulse interacts with the expanded plasma. The interaction of beam II with the expanded plasma is shown first. Similar to the experimental

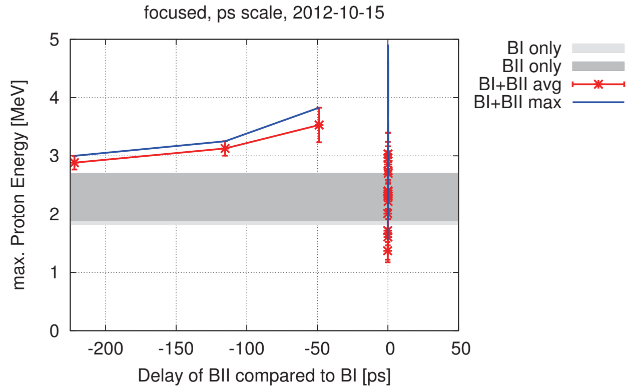

a Experiment. Proton cut-off energies over the delay between the two pulses. Focused shots. Negative delays correspond to shots, where beam II is early.

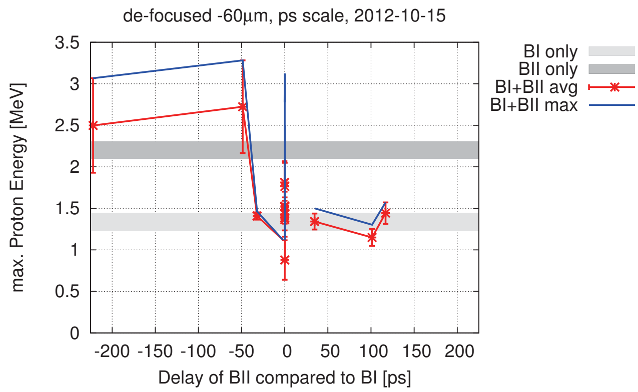

b Experiment. Proton cut-off energies over the delay between the two pulses. Defocused shots. Negative delays correspond to shots, where beam II is the first pulse .

Figure 6.1.: For long delays TNSA is not effective anymore and the later beam cannot influence the ions that were accelerated by the TNSA mechanism. The cut-off energies show an enhancement for shots, where beam II is the first pulse. Especially for shots where beam I is 50 ps later than beam II. Compared to a single beam shot of beam I, the cut-off energy has more than doubled.

shots, beam II does not show an enhancement in the proton cut-off energies. In contrast the interaction of beam I with the expanded plasma shows remarkably features. The appearing magnetic vortex acceleration is described in detail.
Due to the target thickness used in the experiment and in the simulations, the results are somewhat different to the publication of Bulanov et al. [10]. Therefore, an analytic description is developed for the observed phenomena. The effects of relativistic sef-focusing in an overdense plasma and the strengths of the accelerating fields are described. The results for the proton cut-off energy are in remarkably good agreement for experiment, simulation and analytic description.

6.2. Plasma Expansion

In order to explain the experimental results of the long delay shots, the expansion of the plasma has to be taken into account. The first laser accelerates particles according to the TNSA mechanism. After several picoseconds the plasma has expanded and especially the shape of the plasma has a strong effect on the second laser pulse. Therefore, the expansion of the plasma is analyzed in a first step.
An proton energy enhancement with a long delay is discovered only for the defocused beams. Hence, the computational results from these simulations are the starting point. The spatial size of the new simulation is estimated by considering that the expansion takes place with the speed of the ion acoustic wave

$$c_s = \sqrt{\frac{Zk_BT_e}{m_i}}, \tag{6.1}$$

where Z is the charge of the dominating ion species, k_B Boltzmann's constant, T_e electron temperature and m_i the mass of the dominant ion species. The electron temperature is taken from the last output file of the defocused beam II only simulation, so that the ion acoustic speed is $c_s = 1.2 \times 10^6 m/s$. As the delay is in the order of $100ps$ the spatial size of the simulation box needs to be in the order of $\pm 120\mu m$. The large size of the simulation box and the large time period that has to be covered make a 2D simulation not reasonable with the available system performance.
The following 1D simulations start after the last dump of the defocused BII-only simulation. The spatial size of the simulation is $\pm 200\mu$m with a spatial resolution of 12.5nm. The simulations covers a time period till 120 ps and 300 ps, whereas every 200 fs an output file is written. The density distributions are taken from a line-out of corresponding particles from the last dump of the simulation, whereas the line-out comprises a stripe of $y = \pm 1\mu$m. The momenta of the particles are fitted by a polynomial of 1st order in sections and a polynomial of 8th order, respectively. For the ion's momenta this is a reasonable approach, as the momenta have a line-like shape. But as the electrons already thermalize after 750fs the momenta is bulb shaped. Figure 6.2 shows the electron momenta from a stripe that comprises $y = \pm 1\mu$m of the 2D simulation with BII only at 750fs. A simple linear fit to these points clearly underestimates the momenta and represents the lowest expectable plasma expansion. The maximum kinetic

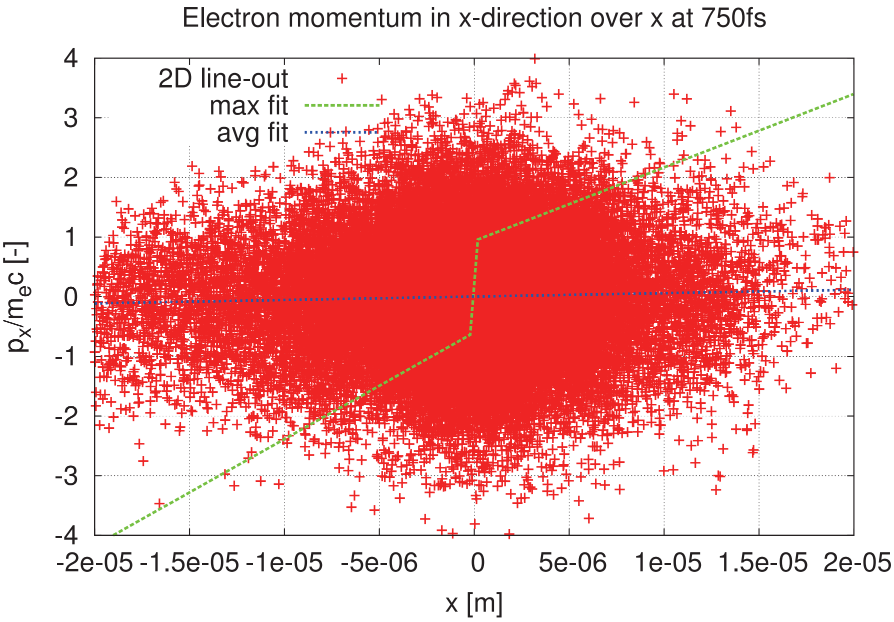

Figure 6.2.: Simulation. The crosses are the electron momenta in the x-direction from a stripe that comprises $y = \pm 1\mu$m of a 2D simulation with beam II only at 750fs. The blue line is an average fit to these crosses. For the green line the maximum kinetic energy of the electrons is taken and linearly fitted. Moreover, this fit is converted back to momenta and it is assumed, that for negative x-values the momenta should also be negative and vice versa.

energy of the electrons is taken in order to accommodate higher electron momenta. These energies are converted back to momenta and are fitted by straight lines. It is assumed that for negative x-values the momenta are also negative and vice versa. The result of this fit is shown by a green line in figure 6.2. The positive momenta on the front side and negative momenta at the rear side of the target is completely neglected with this approach. The plasma expansion is expected to be overestimated. In general a 1D PIC simulation overestimates the particle numbers as the degree of freedom is reduced. So, it is expected that the higher initial electron momenta, i.e. the green line in figure 6.2, results in a more realistic solution of the plasma expansion.

Figure 6.3 compares the three different cases till 3.4 ps, i.e. the 2D simulation is continued till 3.4 ps, whereas the 1D simulations used the density and momenta distributions as described above. The 1D simulations started at 0.75 ps and also stopped at 3.4 ps. The maximum momentum curve - indicated by the dashed green curve - has a five times lower peak density compared to the 2D simulation. Moreover the region where $n_e > n_{cr}$ is much larger. In contrast the average momentum curve - indicated by the dashed blue curve - overestimates the peak density compared to the 2D simulation by 20% and underestimates regions where $n_e > n_{nr}$.
For the later interaction of the second laser pulse with the expanded plasma the peak density and the region where $n_e > n_{cr}$ play a major role. If the peak density is still in the order of magnitude of a solid target, the acceleration proceed according to the TNSA mechanism. It is not expected that this is the case,

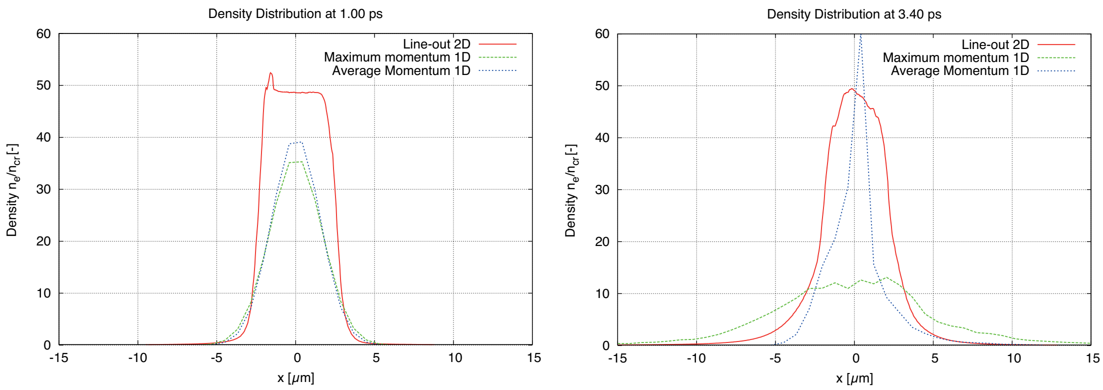

Figure 6.3.: Simulation. Line-outs of electron density distributions, that results from different initial electron momenta. The solid, red line is a line-out from the 2D PIC simulation. The dashed, green line is the electron density that results from the maximum momentum distribution and the dashed blue line is the electron density that results from the average momentum distribution. The dashed lines are results from 1D simulations. The left graphs is plotted at 1ps and the right graph is plotted at 3.4ps, because the 2D simulation was stopped there.
For the 1D simulations a gaussian fit was used for the initial electron densities. The comparison of left and right graph give a hint on the temporal evolution of the densities. The results from the maximum momentum simulation show, that the electron peak density is the lowest and the expansion is the farthest compared with the other simulations. The results from the average momentum simulation shows, that the electron peak density is even increased and the width of the density distribution is decreased. The results of the 2D simulation are right in the middle between these two extremes. Thus, it is reasonable to use both final 1D results as initial conditions for a 2D simulation of the subsequent main pulse.

because the enhancement occurred in the experiment only when BI was late, i.e. the weaker beam enhanced the acceleration. So the peak density must be significant lower compared to solid density, in order to have a strong effect by BI.
The second condition that follows from the experimental result is that the region where $n_e > n_{cr}$ should not be too large. If a large region has an overcritical density and a slow rising density slope, the laser is well absorbed. The absorbed energy heats only the electrons in a small region, where the electrons cannot interact with the protons at the rear side of the target.
The two different initial electron momentum distributions lead to different electron distributions. From the two different 1D simulations the peak density and the overcritical region are of main interest.

Average momentum distribution

The first graph of figure 6.4 shows that the region - which is overcritical - steadily rises till 140ps. After a rapid decrease of the peak density, a region of $\pm 20\mu$m remains overcritical. As the overcritical region gets larger, the peak densities drop, which is shown in the middle graph of figure 6.4. After 50 ps the peak densities are below $10n_{cr}$ and stay relatively constant till the end of the simulation. With a peak density below $10n_{cr}$ and a laser intensity of 10^{20}W/cm^2 the plasma becomes relativistically transparent; cf. figure 2.3. But as the laser pulse has to cross a large, overcritical region, it is expected that the laser will release a lot of its energy to heat electrons only in front of the target.
The plasma expansion and density distributions that result from this 1D simulation are expected to be the case for the beam II late shots in the experiment (figure 6.1b): The peak densities are sufficient low to be relativistically transparent for the laser, but the overcritical region is too large so that the laser cannot accelerate electrons in the forward direction, protons and other ions.

Maximum momentum distribution

Due to the higher electron momentum, the overcritical region reaches its maximum expansion much earlier, as can be seen in the first graph of figure 6.5. After 50 ps the overcritical region shrinks below $\pm 5\mu$m. The peak density of the bulk electrons drops after 20 ps to $6n_{cr}$ and remains relatively constant.
In the experiment the enhanced proton energies appeared with delays lower than -50ps, i.e. with a minimum of 50 ps after beam II (figure 6.1b). So, it is expected that this 1D simulation belongs to shots, where beam II is the first pulse: The peak densities are low enough to be relativistically transparent and the electron densities in front and rear side of the target are low enough, that the laser can interact with the bulk electrons.
In the next section the two different derived density distributions from the 1D simulation are used as initial conditions for 2D simulations. The density distributions that are derived from the 1D simulations are fitted by a Matlab program via a sum of gaussians. These functions are used for the 2D simulations, whereas the distributions in x direction are copied in the y direction in order to have a 2D map of the densities. Obviously any density deviations in the y direction are neglected by this approach.

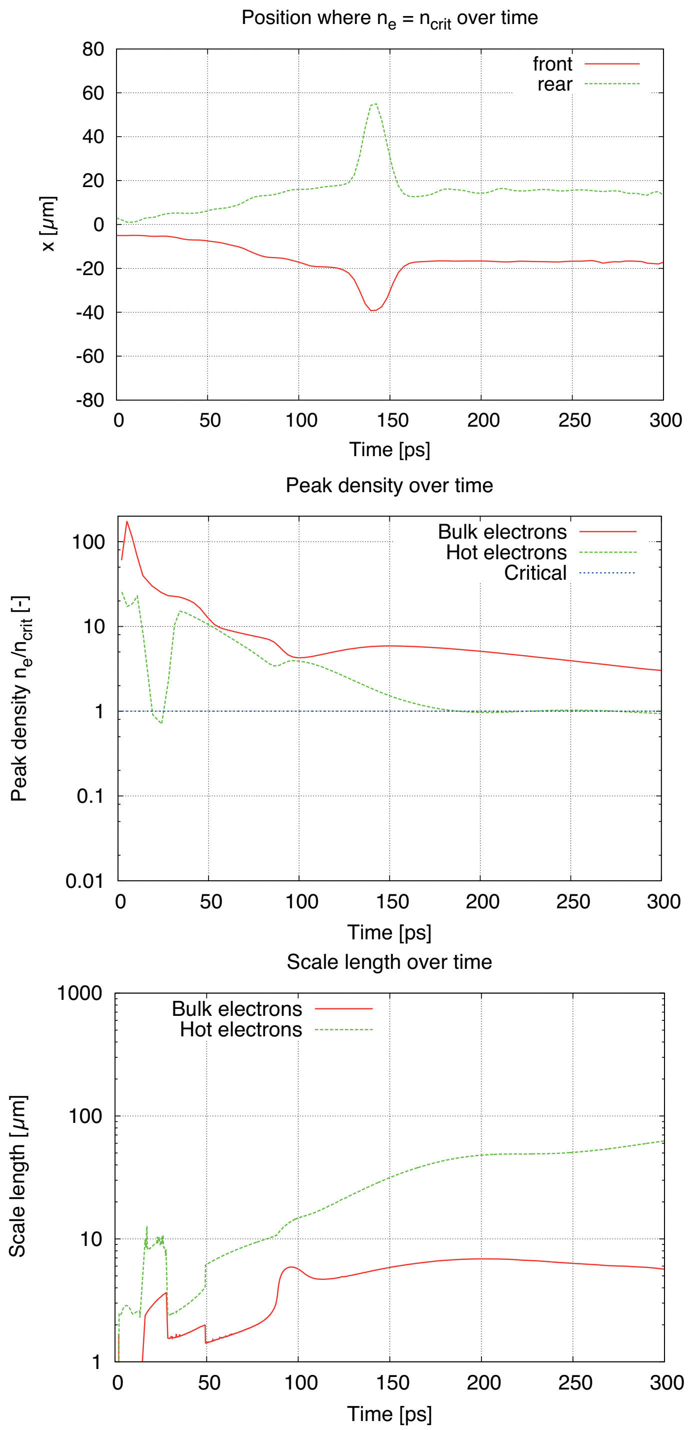

Figure 6.4.: 1D simulation with the average electron momentum distribution. The first graph shows the x position where the electron density is equal to critical density over time. The graph in the middle shows the peak density of the bulk and hot electrons over time. The electron distribution is automatically fitted via a bi-gaussian distribution by a Matlab program. Especially, during the first 50 ps the electron distribution tends to form spikes and bunches of electrons move apart from the bulk, respectively. So that the peak densities for hot and bulk electrons change somewhat abrupt. This behavior is also observed in the lower graph. The graph shows the scalelengths for the hot and bulk electrons over time.

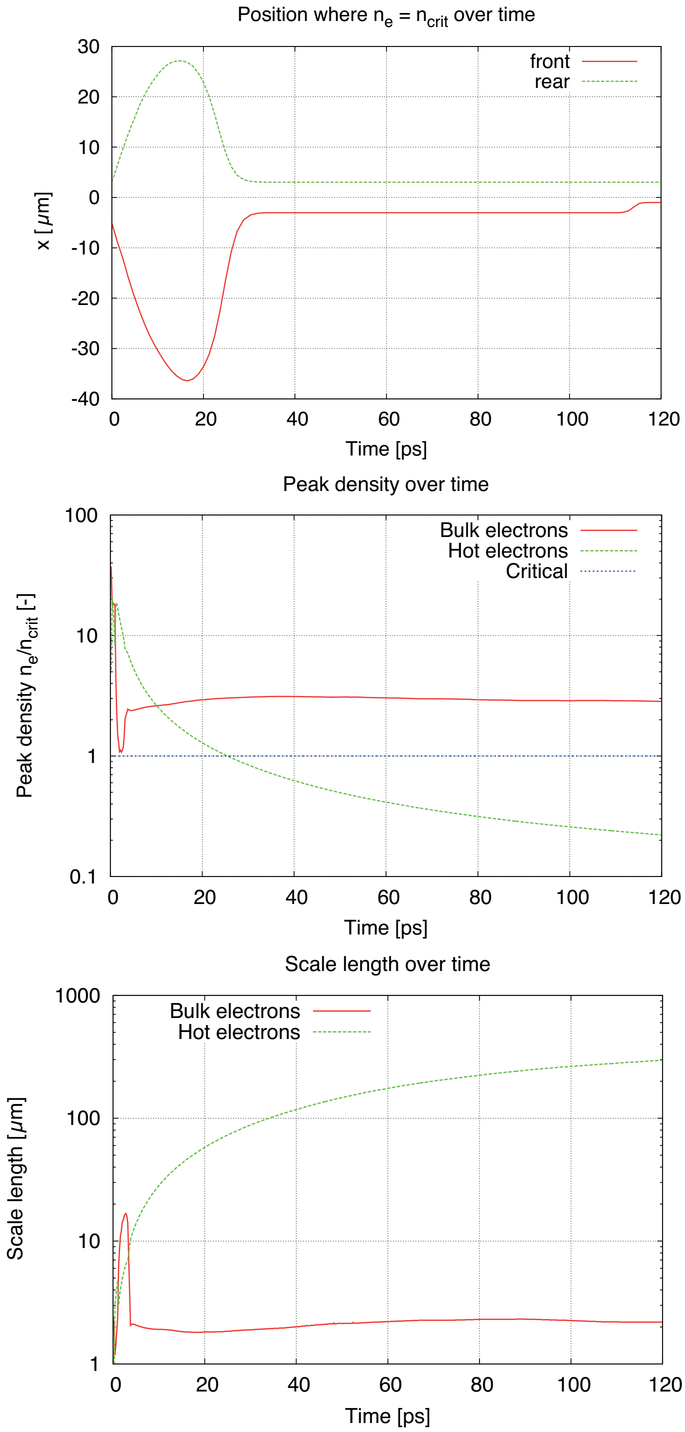

Figure 6.5.: 1D simulation with the maximum electron momentum distribution. The first graph shows the x position where the electron density is equal to critical density over time. The graph in the middle shows the peak density of the bulk and hot electrons over time. The electron distribution is automatically fitted via a bi-gaussian distribution by a Matlab program. Especially during the first 10 ps the electron distribution tends to form spikes and bunches of electrons move apart from the bulk, respectively. So that the peak densities for hot and bulk electrons change somewhat abrupt. This behavior is also observed in the lower graph. The graph shows the scalelengths for the hot and bulk electrons over time.

6.3. Beam II Late Shot

Before the 2D simulation is presented, the interaction of the laser with a rising electron density is analyzed. The laser pulse has to propagate for several micrometers through a near critical plasma, so that the laser is refracted with every step through the plasma. The plasma is unmagnetized and can therefore be described as an isotropic medium. Hence, the dielectric properties are described by a constant and not by a tensor [39]

$$\epsilon = 1 - \frac{\omega_{pe}^2}{\omega_L^2} \tag{6.2}$$

The refractive index is then

$$n = \sqrt{\epsilon(\lambda_L, n_e)} \tag{6.3}$$

only a function of the laser wavelength λ_L and the local electron density n_e. As the laser has relativistic intensities, the effect of relativistic transparency has to be considered $\omega_{pe}^2 = \omega_{pe}'^2/\gamma$. With every step in x direction the laser experiences a different electron density and therewith a different refractive index. Thus, the *bending* of the laser changes with every step.

The bi-gaussian electron distribution from figure 6.4 at 150 ps is being taken to

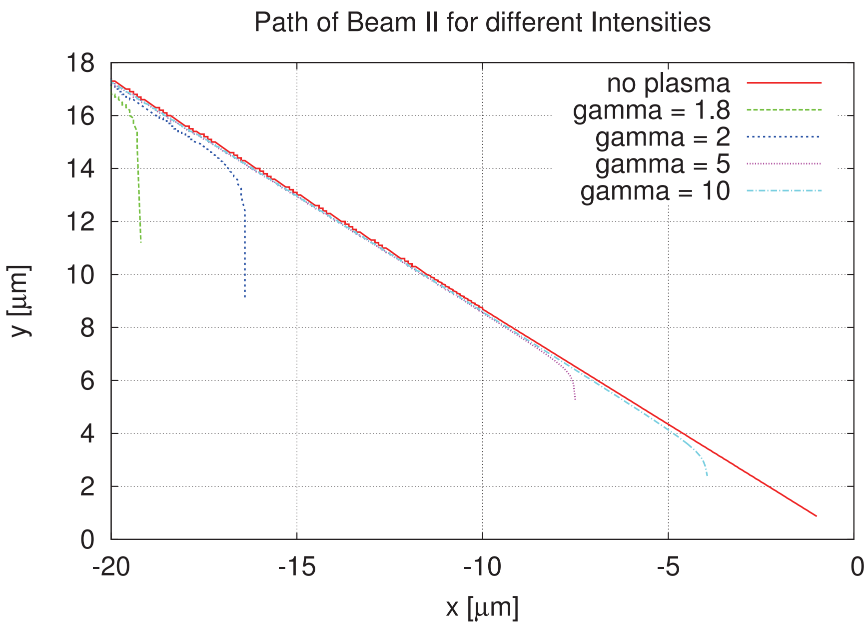

Figure 6.6.: Calculation. Path of a laser with different intensities through a plasma. The arrangement of laser and target is the same as it is in the 2D simulation. The electron density distribution is taken from the 1D simulation (fig.:6.4) at 150 ps. The red line indicates the path of a laser without a plasma. In dependence on the intensity of the laser the beam is refracted to $-90°$. The higher the γ-factor the further the laser can propagate through the plasma.

analyze the influence of refraction. The arrangement of target and laser is the same as it will be in the 2D simulation, i.e. the angle of incidence is $-40°$, the laser enters the simulation box at $x = -20\mu$m and the peak density of the bulk electrons is located at $x = 0$. Figure 6.6 shows the beam path for different intensities and γ factors, respectively. The red line indicates the beam path without a plasma. Without the relativistic correction the laser would not propagate into the plasma, because a laser pulse with a $\gamma = 1.8$ is already refracted to $-90°$ at -19μm. Even with a γ-factor of 10, which corresponds to an $a_0 = 14$, the laser pulse will most likely not propagate through the target, although the peak density of the bulk electrons is relativistically transparent to the laser.

The analysis shows that for a sufficient interaction of the laser with the bulk

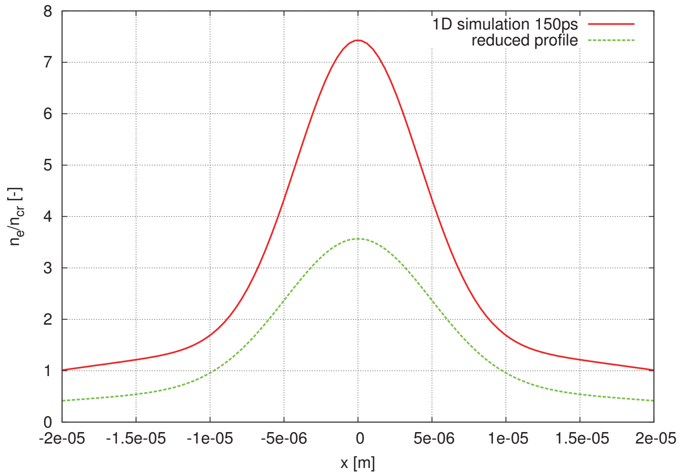

Figure 6.7.: Calculation. Electron density profiles. The red profile is taken from the 1D simulation (fig.:6.4) at 150 ps. For the green profile, the hot electron density at the boundaries has been halved. Moreover the peak density of the bulk electrons has been reduced to $3.5n_{cr}$.

electrons, either the laser intensity has to be high enough and/or the hot electron density has to be low enough. For the upcoming 2D simulation the density distribution of the electrons is further reduced, as it is shown in figure 6.7. The intensity is the same as it is used for the de-focused, fs-delay 2D simulations, i.e. $I = 3.3 \times 10^{20}$W/cm^2 corresponding to $a_0 = 12.3$. Figure 6.8 shows the electron distribution normalized to the critical density 120 fs after the peak of the laser pulse had entered the simulation box. A channel-like structure is visible, that is formed by the laser. The channel is a sign of the trajectory of the laser through the plasma. As the laser gets closer to the initial target position the laser is refracted by the plasma. Due to relativistic self-focusing the channel narrows down. Eventually the laser pulse stops in the plasma. The picture on the right is a close-up view of the region, where the laser stops. The black line indicates the beam path as it would be without a plasma. The bright line shows the calculated, refracted path with the same electron distributions as it is used for this 2D simulation and a γ-factor of 10. The sharp bend of this line is in good agreement with the sharp bend in the 2D simulation. Furthermore it has to be mentioned, that the entry point of the laser into the simulation box is shifted from $y = 18\mu$m to $y = 10\mu$m. While the laser enters the simulation box, the laser pulse has not a sufficient high intensity in order to propagate in a straight line, but is strongly refracted within a 1μm. As the intensity increases rapidly, the index of refraction also changes rapidly, so that the laser is refracted back in the shown manner.

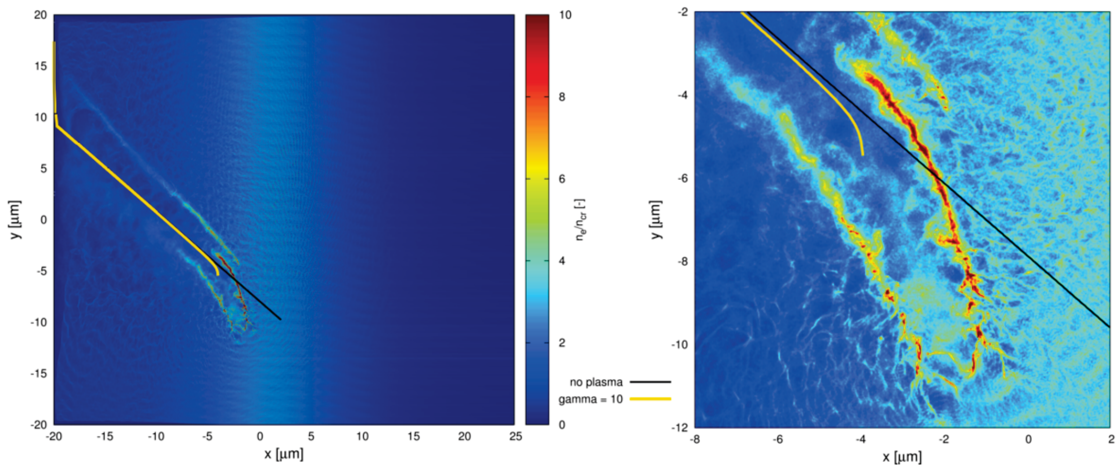

Figure 6.8.: Simulation. The right image is a zoom in of the left image. Electron densities normalized to the critical density 120 fs after the peak of the laser pulse has entered the simulation box. The pulse of beam II generates a channel. The pulse does not propagate along a straight line as indicated by the black line, but is refracted. The gold line indicates the path of the beam, if refraction is taken into account (cf. eq. 6.3) The curve is calculated by the use of the same electron density distribution as in the PIC simulation and a $\gamma = 10$, whereas γ was 8 in the PIC simulation. Although the plasma relativistically transparent to the laser, the laser stops in front of the former target.

6.4. Beam I Late Shot

Beam I is at normal angle of incidence to the target, so that there is no refraction. The beam is focused on the front side of the target. The minimum radius of the gaussian beam caustic is calculated to be $3\mu m$.

Magnetic Vortex Acceleration

The evolution of the electron density normalized to the critical density and the magnetic field in the z-direction is shown in figure 6.9. The laser propagates through the near critical plasma and expels electrons and ions from its path. Thus a channel is formed by the laser.
Moreover the laser experiences relativistic self-focusing. The channel diameter and the laser's diameter becomes smaller and smaller as the electron density increases. The smallest diameter of the laser is reached at the peak electron density. While the front part of the laser pulse breaks-out through the expanded target into the lower plasma density region and diverges, the later part of the laser propagates through the self-generated channel or waveguide. Due to the interplay between laser field, waveguide wall and accelerated electrons, the magnetic field in the z-direction starts from 125 fs to separate in a positive and a negative region. A torus like magnetic field evolves. As the later part of the laser approaches the lower plasma density region, the torus shaped magnetic field increases its size, i.e. the minor radius. Moreover electrons are trapped by the magnetic field and circulates around the vortices. Eventually the major radius of the torus also increases, namely with a velocity of $55 \times 10^6 m/s$.

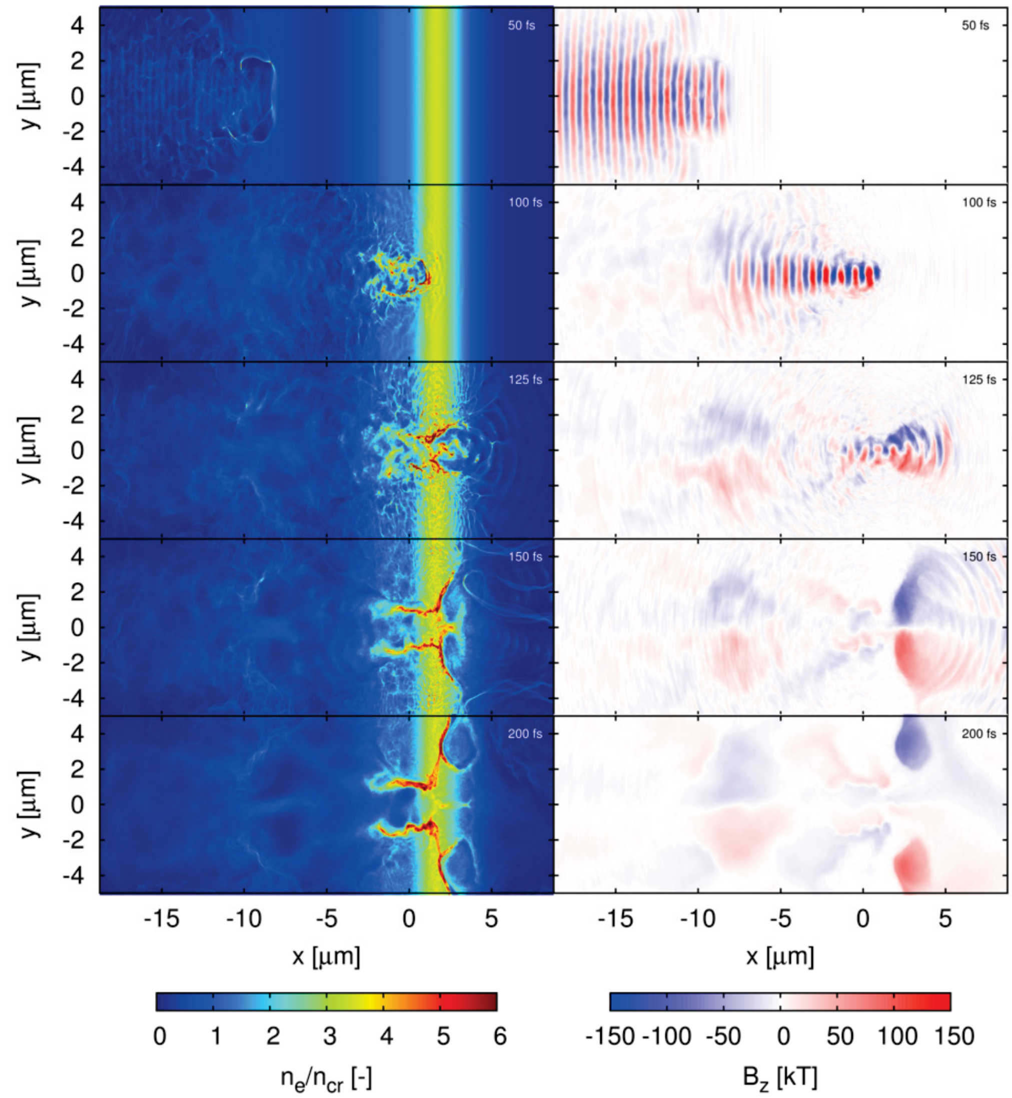

Figure 6.9.: Simulation. Electron density is normalized to the critical density, whereas the maximum is set to $6n_{cr}$. The magnetic field B_z in kT. The time increases with each row by 50fs, but a intermediate step is made at 125fs. While the laser pulse propagates through the plasma, a channel is generated. The feature becomes more evident as the pulse approaches the higher density parts of the plasma. Until 100fs the magnetic field pattern has the shape of a TEM wave. At around 125fs the front part of the pulse breaks through the target into free space with a large divergence. The magnetic field pattern has changed. A region with a positive B_z and a region with negative B_z is observed. The separation is also observed in the electron density map. The magnetic vortices leave the self-generated channel and move in different directions along the former target surface. Electrons circulate around these vortices and support with their current the vortices.

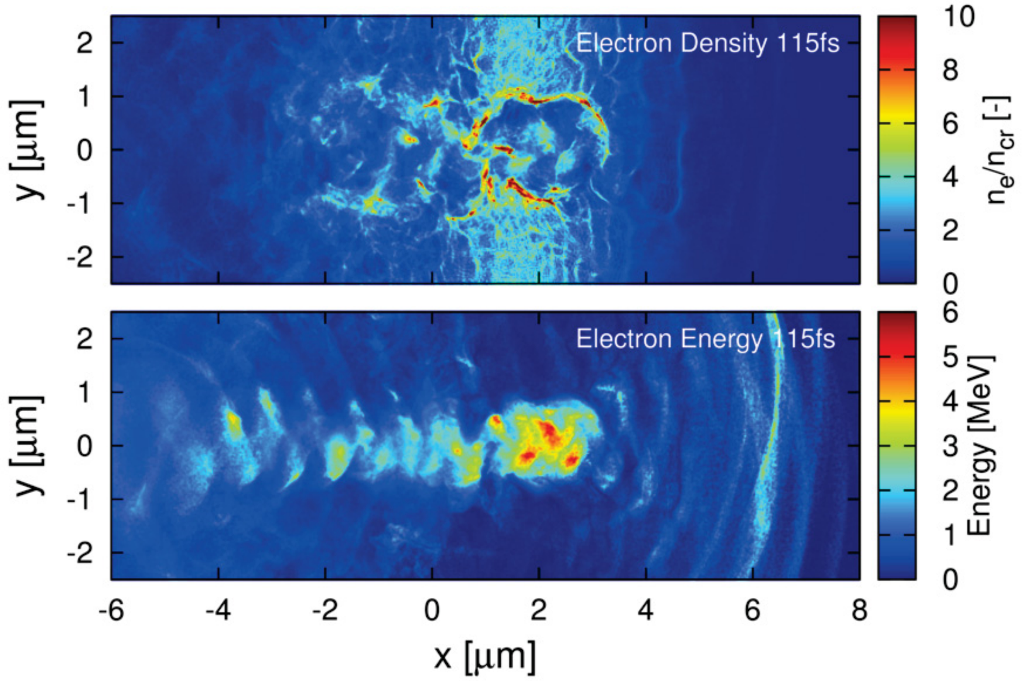

Figure 6.10.: Simulation. Electron density normalized to the critical density and the corresponding electron energies after 115 fs. The laser has formed a channel like structure. In the electron energy map a saw-tooth like structure is visible. Three of the saw-tooth peaks are also visible in the density map in the channel. The oscillating component of the ponderomotive force accelerates a group of electrons twice every laser cycle. Thus the saw-teeth are separated by $\lambda_L/2$.

The accelerated electrons play an important role in the formation of the magnetic vortices. Figure 6.10 shows a map of the electron density and the distribution of the kinetic energy of the electrons at 115 fs. The electrons form a sinuous line in the middle of the channel. In the interface between the front of the laser pulse and the plasma a strong, high-frequency electrostatic field appears [59]. The field is the oscillating component of the ponderomotive force [50] $f_P = \nabla(\gamma - 1)m_o c^2$, where $\gamma = \sqrt{1 + p^2/m_0^2}$ and p is the electron oscillatory momentum in the transverse and longitudinal direction. As the frequency of oscillating ponderomotive force is $2\omega_0$, twice every circle a group of electrons are accelerated [59]. The train of electrons is separated by a distance half of a laser wavelength.

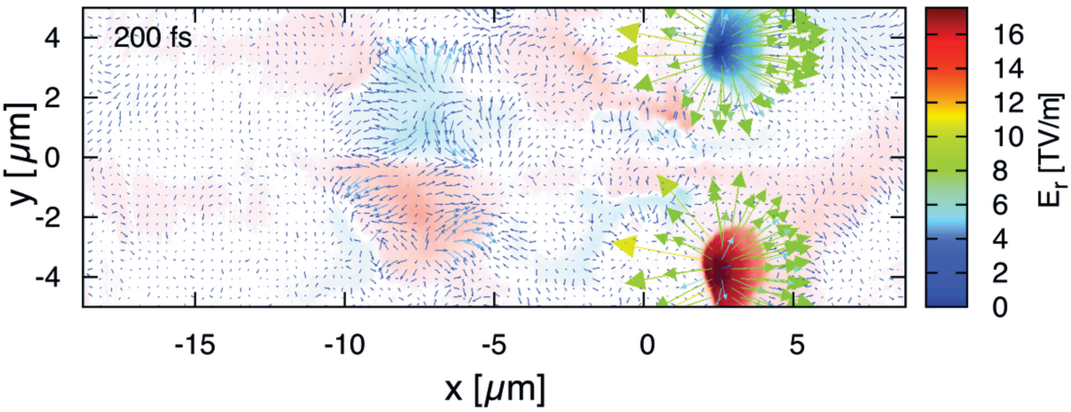

Figure 6.11.: Simulation. The electric field vectors at 200fs. Again, in a color map the magnetic field B_z kT at 200fs (c.f. figure 6.9). The highest electric field gradients are observed at the magnetic vortices. The electric field is circular arranged around the the vortices and the vectors point radial away from the vortex center. The field strength is at least doubled compared with the ambipolar electric field of TNSA achieved for a single beam shot.

Besides the magnetic fields and accelerated electrons, the electric fields are also involved in the acceleration mechanism. Figure 6.11 shows the electric field as vectors and the magnetic field in the z-direction as a color map. The magnetic vortices are associated with the electric field.

The schematic in figure 6.12 summarizes the acceleration mechanism. Due to the interplay between laser field, waveguide wall and accelerated electrons, two magnetic vortices appear. The magnetic vortices arise from the laser field, because the current of the accelerated electrons is too low for the appearing field strength. Eventually the accelerated electrons circulate around the vortices. Thus a self-sustaining electrical generator is formed by the electrons. Moreover an electric field is observed that points radial away from the vortex center. Due to the strong electric and magnetic fields the remaining protons, that have not been accelerated by TNSA mechanism from the first laser pulse, are eventually also accelerated by these fields.

Proton Acceleration

The angular distribution of the proton energies is shown in figure 6.13. The acceleration is already finished after 200 fs as the maximum energy does not

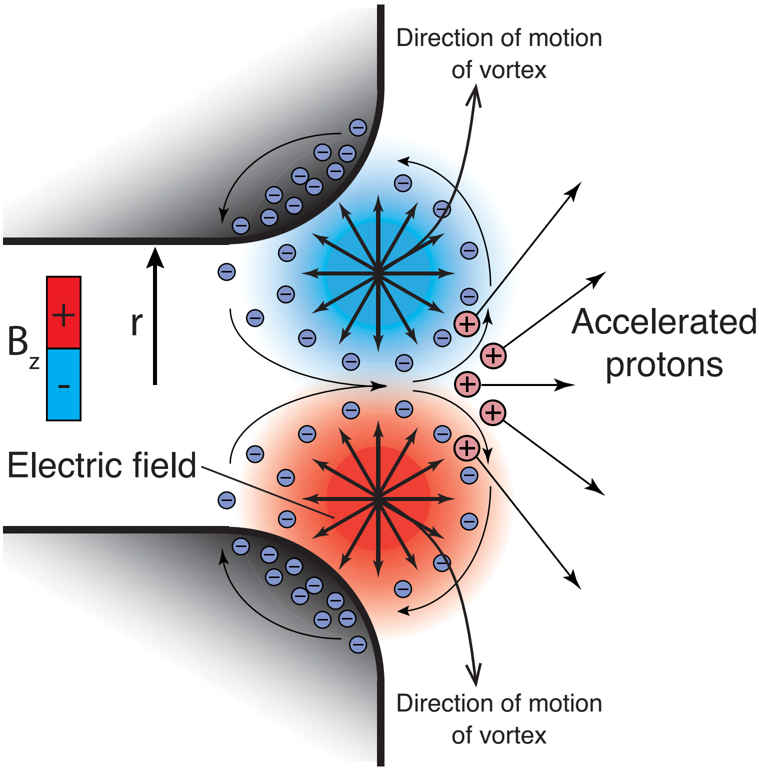

Figure 6.12.: Schematic of magnetic vortices, electric field and particles while the ions start to accelerate. The magnetic vortices start to leave the self-generated channel and move along the former target surface. The intensity of the magnetic field suggests, that the magnetic field arises from the laser rather than the current of the moving electrons. But as the electrons circulate around the vortices, the electrons form a self-sustaining electric generator. Along with the magnetic vortices and the moving electrons an electric field is produced that is circular arranged around the vortices. The field vectors point radial away from the vortex center. The acceleration of the ions is driven by these electric and magnetic fields.

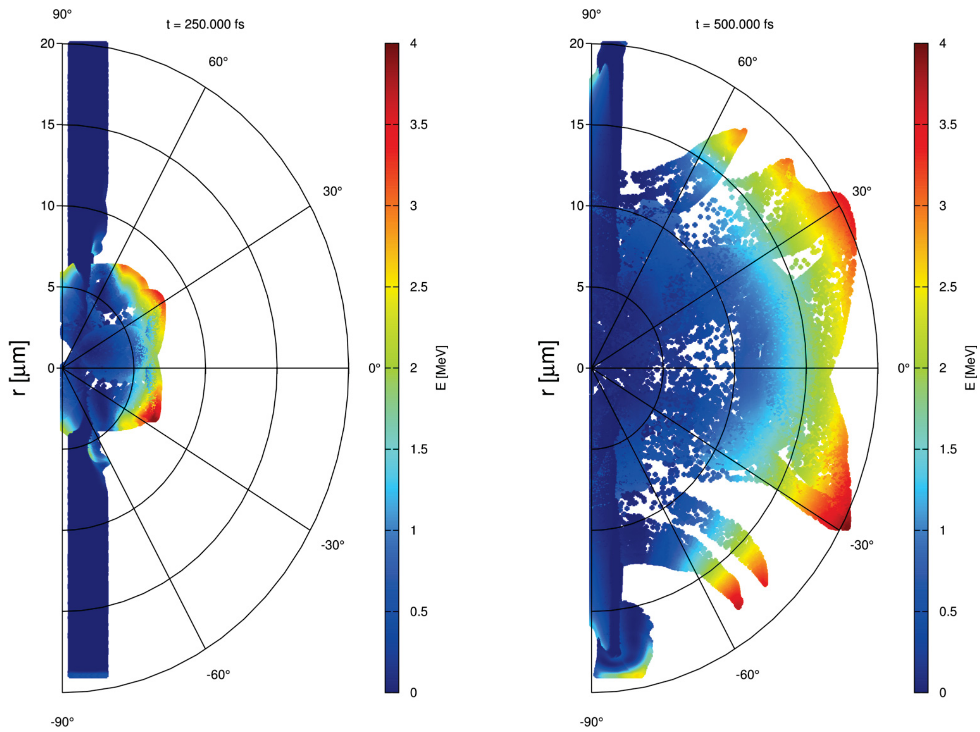

a Proton energies after 250 fs **b** Proton energies after 500 fs

Figure 6.13.: Simulation. Proton energies in a polar plot at different times. The protons reach their maximum kinetic energy already after 250 fs, as the maximum energy does not change till 500fs. The highest energies are found in two lobes at ±30°. The electric field connected to the magnetic vortices cannot contribute to the proton acceleration at an angle of 0°, because the electric field only acts in the y-direction at $r = 0$. Therefore the energy is somewhat lower.

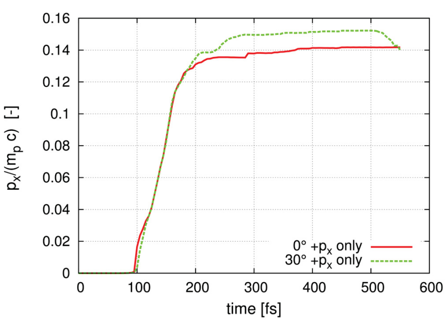

Figure 6.14.: Simulation. Proton momenta in the positive x direction along the declared angle. The acceleration starts at 100 fs. The momenta steeply rise till 200 fs and remains basically constant. Thus, the acceleration starts and ends at the same time.

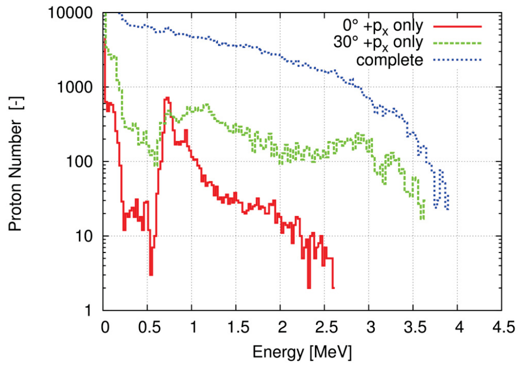

a Simulation. Proton spectra from the simulation. The different angle declaration comprise a stripe $\pm 2\mu m$ along that angle with momenta only in the positive x direction. The blue line comprises all momenta from the semi-circle in figure 6.13 and includes also momenta in the y-direction.

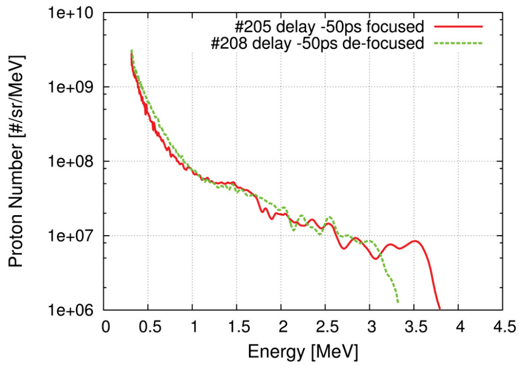

b Experiment. 20121015. Proton spectra. Shot #205 was focused and shot #208 was defocused by $-60\mu m$.

Figure 6.15.: Comparison of simulation and experiment. The Thomson parabola was placed in the direction of beam I, i.e. at an angle of 0°. Therefore the experimental results are only compared to the computational result for the 0° stripe. The simulation shows a gap in the spectrum from 0.2 MeV to 0.7 MeV which is not the case for the spectrum from the experiment. It has to be considered that the spectrum of the experiment is the integration of the accelerated protons from beam II according to the TNSA mechanism and the accelerated protons from beam I according to the magnetic vortex acceleration. The following slope of simulation and experiment are in good agreement, as slopes decrease constantly by an order of magnitude from 1 MeV to 2.5 MeV.

change anymore. A closer look to the evolution of the maximum proton momenta shows that the protons are accelerated from 100 fs to 200 fs as shown in figure 6.14. The highest proton energies are achieved in two lobes which are located around angles of +30° and −30°. The electric field acts at the line $y = 0$ in figure 6.11 only in the y direction, so that the electric field cannot contribute to the acceleration in the x direction. Therefore the energy is for an angle of 0° somewhat lower compared to the two lobes at ±30°. The proton spectra of the simulation is shown in figure 6.15a. Three spectra are shown. The blue line indicates the spectra of all momenta, i.e. energies, in the semi-circle from figure 6.13 in x- and y-direction. The cut-off energy is at 3.8 MeV. The two other spectra account only for protons with a momentum in the positive x-direction in a stripe of $\pm 2\mu m$ along the declared angle. The green line is the spectrum of the lobe at +30°. The proton numbers remains relatively high till the cut-off energy of 3.6 MeV. The spectrum along an angle of 0° has a cut-off energy of 2.5 MeV. In the experiment the spectrometer was positioned along the beam I direction, so that the spectrum from the simulation along an angle of 0° is compared to the experimental spectrum.
The spectra of two shots from the experiment that correspond to the simulation are shown in figure 6.15b. The proton number of the spectrum from the simulation drops from 0.2 MeV to 0.7 MeV, which is not the case in the experimental spectra. The experimental spectra accounts not only for the protons accelerated from beam I , i.e. the later pulse, but also for protons accelerated

from beam II, i.e. the first pulse, via TNSA. Hence, there is no decease in the proton number in the experimental spectra. For energies higher than 1 MeV the proton number from the simulation and from the experiment drop by an order of magnitude to 2.5 MeV. Thus the spectrum from the simulation is in very good agreement with the experiment.

Ion Acceleration

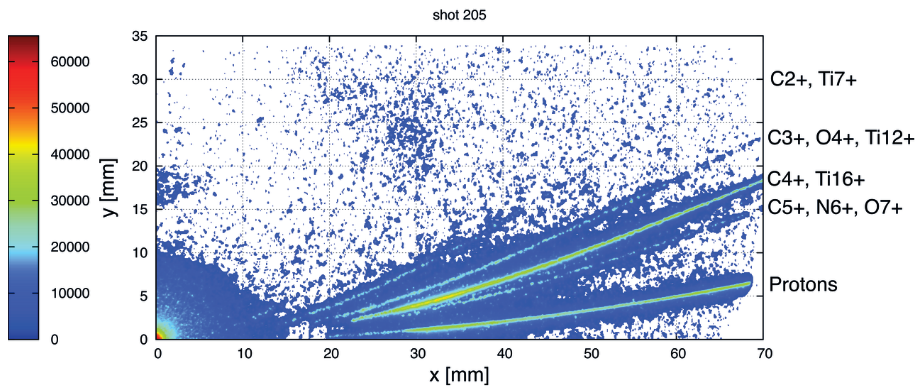

Figure 6.16.: Experiment. MCP measurement of shot # 205 2012-10-15. BI is delayed by 50ps. The bright trace above the proton trace corresponds to either C^{4+} or Ti^{16+}. Due to the same charge to mass ratio, the traces overlap.

The MCP image in figure 6.16 shows a strong C^{4+} trace or Ti^{16+} trace, respectively. Due to the same charge to mass ratio, the traces overlap. In the simulations only a few C^{4+} ions are accelerated, because the plasma is relativistically transparent and the laser intensity is still sufficient high at the rear side of the target to ionize a large fraction of carbon to C^{6+}. If the ionization is turned off for C^{4+}, a larger fraction of C^{4+} is accelerated.

The velocities of C^{4+} or Ti^{16+} from the PIC simulations are shown in figure

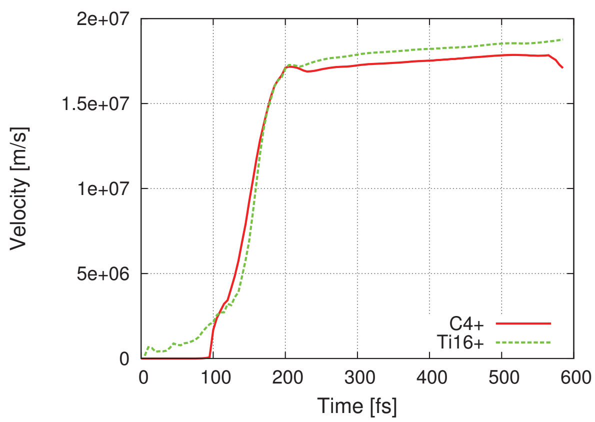

Figure 6.17.: Simulation. The temporal evolution of the velocity of C^{4+} and Ti^{16+}. As the acceleration of the ions occurs due to electric and magnetic fields, the velocity of the particles depends on the charge to mass ratio. Because C^{4+} and Ti^{16+} have the same charge to mass ratio, the velocity is the same.

6.17. It reveals that the acceleration mechanism depends strongly on the charge to mass ratio, because the velocity increase is the same for both ion species. It

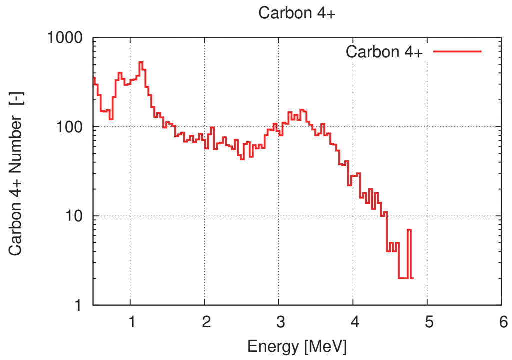

a Simulation. C^{4+} spectra from the simulation. The spectrum comprises a stripe $\pm 2\mu m$ along $0°$ with momenta only in the positive x direction.

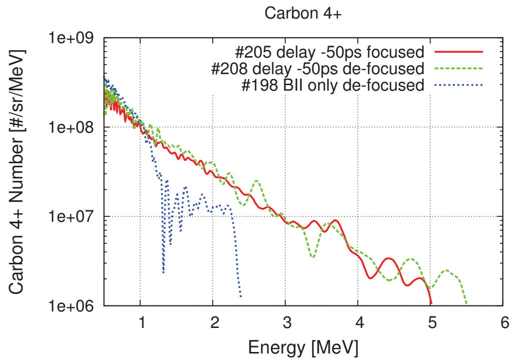

b Experiment. 20121015. The MCP traces of Ti^{16+} and C^{4+} overlap. Here, the trace is considered as C^{4+}. The blue line shows the spectrum of a beam II only shot. Shot #198 has relatively high C^{4+} energies. Shot #205 is focused and shot #208 is defocused by $-60\mu m$.

Figure 6.18.: Comparison of simulation and experiment. The simulation does not show an acceleration of a large number of C^{4+}, as most carbon ions are ionized to C^{6+}. Only if the ionization routines are turned off in the simulation for C^{4+}, a larger fraction of C^{4+} is accelerated. The experimental results showed a strong signal on the MCP for both C^{4+} or Ti^{16+}, but no C^{6+} signal.

follows from this, that it is plausible, that both ion species might have appeared in the experiment.

If the MPC trace is considered as C^{4+}, the resulting spectrum from the experiment is shown in figure 6.18b. The blue line shows a beam II only shot with a relatively high cut-off energy for C^{4+} at 2.3 MeV. The long delay shots have at the same energy a four times higher particle number. The cut-off energy for both long delay shots is 5 MeV, whereas the defocused shot has a slightly higher energy. The spectra do not have a sharp cut-off energy, but more a thermal spectrum. The spectrum from the PIC simulation as shown in figure 6.18a has a cut-off energy of 4.5 MeV, which would be in good agreement with the experiment, but the cut-off energy is more noticeable as in the experiment.

If the MCP traces from the long delay shots are considered as Ti^{16+} traces, the spectra have the same shape as for C^{4+}, but only a different particle number. The spectra are shown in figure 6.19b. Again the blue line is the spectrum from a C^{4+} trace from a single beam shot, but it is evaluated with the dispersion for Ti^{16+}. If Ti^{16+} was accelerated and belongs to the here shown spectra, then everything below 10 MeV is most probable a mixture of Ti^{16+} and C^{4+}. The cut-off energies for the long delay shots is 20 MeV, but again the spectra have a thermal shape. The spectrum of Ti^{16+} from the PIC simulation is more flat than the spectrum from the PIC simulation for C^{4+} (cf. 6.18a) So far it cannot be decided whether C^{4+} or Ti^{16+} are accelerated. The PIC simulations show C^{4+} ions only, if the ionization is turned off for C^{4+}, i.e. there are no further ionization stages.. The experiment does not show a strong C^{4+} signal on the MCP for a single beam interaction especially in terms of the particle number.
In the experiment the Thomson parabola cannot distinguish between ion species with the same charge to mass ratio. The maximum ion energies in the spec-

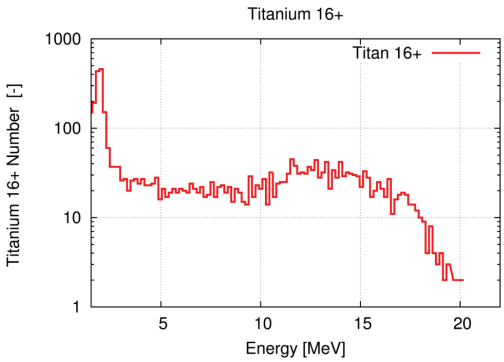

a Simulation. Ti^{16+} spectra from the simulation. The spectrum comprises a stripe $\pm 2\mu m$ along 0° with momenta only in the positive x direction.

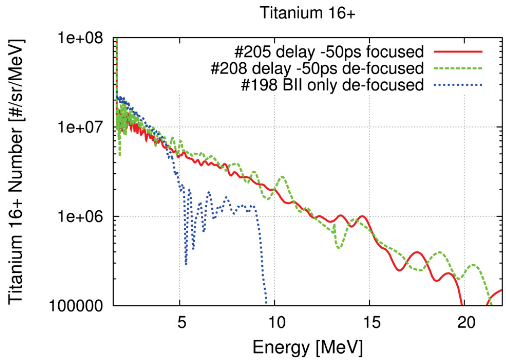

b Experiment. 20121015. The MCP traces of Ti^{16+} and C^{4+} overlap. Here the trace is considered as Ti^{16+}. The blue line shows the spectrum of a BII only shot. The spectrum is a C^{4+} spectrum evaluated with the dispersion for Ti^{16+}. As shot #198 has relatively high C^{4+} energies, everything below 10 MeV should be considered as C^{4+} for the other two spectra. Shot #205 is focused and shot #208 is defocused by $-60\mu m$.

Figure 6.19.: Comparison of the simulation and experiment. Due to the same charge to mass ratio of C^{4+} and Ti^{16+}, the traces of these ion species overlap on the MCP. The acceleration mechanism also depends on the charge to mass ratio. Therefore the evaluation of the MCP trace as a Ti^{16+} gives also a spectrum that is in agreement with the spectrum from the PIC simulation.

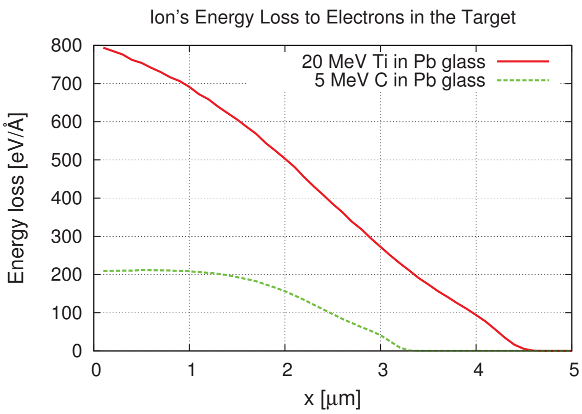

Figure 6.20.: Calculation SRIM. Ion's energy loss to electrons in the Pb glass of the MCP. 20 MeV titanium ions deposit four times more energy in the electrons of the Pb glass compared to 5 MeV carbon ions.

tra from the PIC simulation correspond to the maximum energy that might have appeared in the experiment for either C^{4+} or Ti^{16+}. There was no cross-calibration between MCP and CR39 for Ti^{16+} and therewith the exact response is uncertain of the MCP to titanium. The SRIM calculations in figure 6.20 suggest that titanium would release four times more electrons in the MCP glass plate than carbon. This will cause a much stronger signal on the MCP. If the relation is linear between energy loss of ions to electrons in the Pb-glass and the response of the MCP, the particle number of Ti^{16+} should also be four times higher. As discussed above for the C^{4+} spectra, the particle number was four times higher for a long delay shot compared to a single beam shot (cf. blue line in figure 6.18b and figure 6.19b).
But still, it cannot clearly be decided whether the ion trace on the MCP belongs to C^{4+} or Ti^{16+}. The bright signal on the MCP might also just be a result from the lower dispersion of the Thomson parabola for higher ion energies.

In summary, the shots in the experiment, where beam II is later than beam I, showed no enhancement in the proton energies. The simulation that based on a density distribution, that results from the averaged momentum distribution, shows also no enhancement in the proton energies. The reason is that the beam is strongly refracted in the plasma in front of the target. The laser stopped in that region and heated the electrons without having any effect on the protons. The simulation that based on a density distribution that results from the maximum momentum distribution shows an enhancement in the proton energy. The results correspond very well to the experimental shots where beam I is late. From this follows that the assumption made for these simulations are correct and that especially the initial density distribution is correct.
The observed acceleration mechanism is driven by two magnetic vortices. These vortices result from the interaction of the laser field with the self-formed waveguide and accelerated electrons. Electrons circulate around the magnetic fields and form a strong current that supports the magnetic field. Electric fields are radially arranged around the vortices. The electric and magnetic fields drive the acceleration of the ions.

6.5. Analytic Description of Magnetic Vortex Acceleration

6.5.1. Introduction

In order to get a better understanding of the magnetic vortex acceleration, the following section presents an analytic description of this acceleration mechanism. The aim is to estimate the maximum proton energy from basic parameters. As the acceleration mechanism relies on the electric and magnetic fields on the rear side of the target, the relation between the laser and these fields has to be found. At first the electric and magnetic fields in a circular waveguide are described. Before the circular waveguide theory is presented, a brief motivation for the use of transmission line theory is given. The approach to describe the fields within the self-generated channel as circular waveguide modes is similar

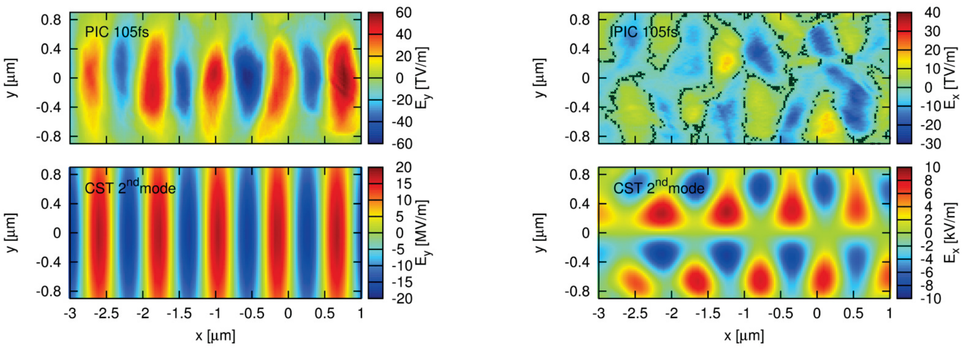

a Simulation. Electric field in the y-direction. Top graph PIC simulation.

b Simulation. Electric field in the x-direction. Top graph PIC simulation. Black crosses mark positions where the electric field is zero in the PIC simulation.

Figure 6.21.: Comparison of a PIC simulation and a CST simulation. The CST simulation shows the second mode of an electromagnetic wave in a circular waveguide. The diameter of the waveguide is 900 nm, which corresponds to the channel diameter in the PIC simulation. The frequency of the wave is 375 THz or 800 nm, respectively. The field pattern in the PIC simulation corresponds to the second lowest mode of an EM wave in a circular waveguide.

as it was done by Bulanov et al. [10], but the results are somewhat different. Furthermore relativistic self-focusing is derived so that it fulfills the requirements of the simulations and the experiments. With this knowledge the size of the circular waveguide is estimated. As energy is conserved and the size of the waveguide is known, the magnitude and extension of the electric and magnetic fields can be roughly estimated at the rear side of the target. The acceleration of ions is driven by the Lorentz force. Eventually, the kinetic energy of the protons is calculated

6.5.2. Motivation for Transmission Line Theory

In this section a brief motivation is given, why the laser is described as a wave in a circular waveguide. In general a circular waveguide is a hollow metal tube that supports TE and TM waveguide modes. TEM modes do not appear in a circular waveguides. The upper graphs in figure 6.21 show the electric field in x- and y-direction as it is found in the PIC simulation at 105 fs (cf. fig. 6.9). The lower graphs show the field pattern of a TM_{01} mode in a circular waveguide. The waveguide has a diameter of 900 nm and the frequency of the wave is 375 THz. The field pattern of the PIC simulation corresponds to the field pattern of the waveguide mode.
The interplay between the electric and magnetic fields and the electrons is shown in figure 6.22. The first part of the laser forms a channel and imprints its field pattern in the electron distribution as can be seen in figure 6.22a. More and more electrons are accelerated. The first part of the laser pulse approaches the lower density regions and expands like a point source into free space. The later part of the laser interacts with a current of electrons.

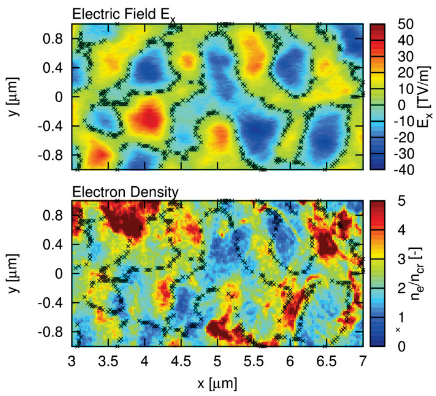

a Simulation. Electric field in the x-direction and electron density normalized to the critical density. Black crosses mark positions where the electric field is zero in the PIC simulation. There are similarities in the field pattern and electron distribution. For example the blue spot in the lower right corner in the electric field map also appears in the density map. The PIC simulation here is different simulation compared to the other simulation results presented in this section. The target density is similar, but the target thickness is 20μm and the pulse length is 100 fs in order to achieve a kind of steady state in the channel.

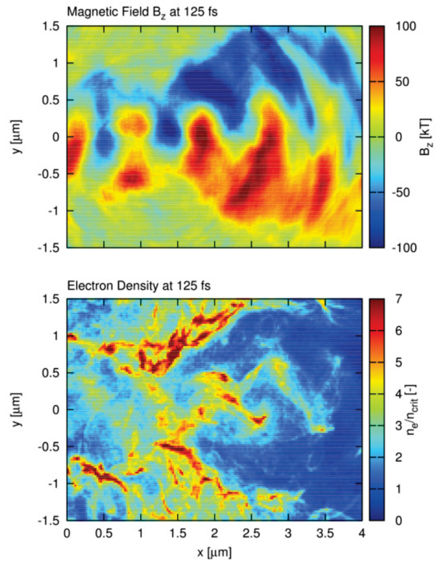

b Simulation. Magnetic field in the z-direction and electron density normalized to the critical density. The similarities between the magnetic field pattern in the z-direction and the electron distribution are quit obviously. The sinusoidal line in the magnetic field also appears in the electron distribution

Figure 6.22.: Comparison of field pattern and electron distribution in the PIC simulation. There is a strong interplay between electric and magnetic fields and the electrons.

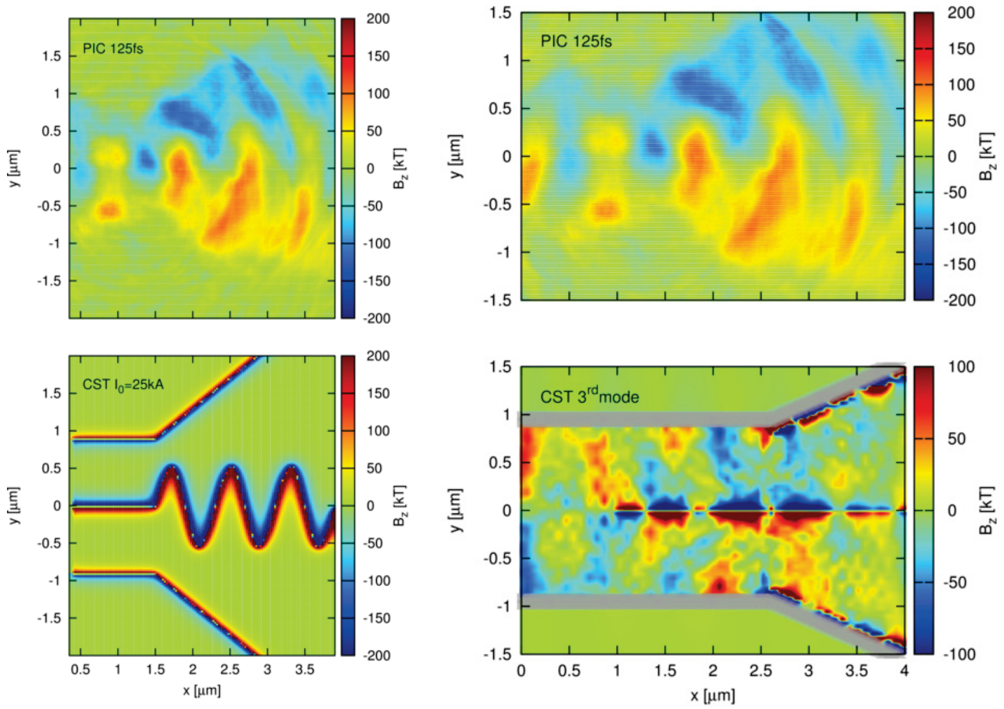

a Simulation. Magnetic field in the z-direction. Top graph PIC simulation. Bottom graph CST simulation of a wire with a current of 25 kA. Due to Biot-Savart's law the field strength is stronger closer to the wire.

b Simulation. Magnetic field in the z-direction. Top graph PIC simulation. Bottom graph CST simulation of an open circular waveguide. Along the tapered waveguide wall at the top and at the bottom, a current is applied, as well as along the symmetry axis starting from $x = 1\mu$m. The field pattern is similar to the PIC simulation.

Figure 6.23.: Comparison of PIC simulation and CST simulation. In the PIC simulation the magnetic field of the later part of the laser interacts with accelerated electrons. It appears a ring like magnetic field pattern. A simple wire simulated with CST does not reproduce this field pattern. The overlap of the magnetic field of an EM wave at 375 THz and the magnetic fields from currents can approximate the field pattern observed in the PIC simulation.

The striking feature of the magnetic field in the z-direction appears after 125 fs. A separation of the positive and negative magnetic field in the z-direction along the accelerated electrons. Figure 6.23 shows in the upper graphs the magnetic field of the PIC simulation and in the lower graphs two CST models. The left model is a simple wire with a current of 25 kA. The current strength corresponds to the current of the electrons in the PIC simulations. The lower graph of figure 6.23a shows the magnetic field in the z-direction from this current. From Biot-Savart's law follows, that the field strength of a magnetic field from a current in a wire is stronger closer to the wire. In the PIC simulation the field pattern is somewhat inverted compared to this behavior, i.e. the strongest magnetic field appears not close to the highest electron current, but right in the middle between the currents.
The second model in figure 6.23 shows an open circular waveguide. The open part is tapered. Moreover a current of 25 kA is placed along the tapered part at the top and at the bottom. A third current is placed along the symmetry axis starting from $x = 1\mu$m. An electromagnetic wave with a frequency of 375 THz enters the waveguide from the left. The graph shows the sum of the magnetic fields of the wave as well as the magnetic fields from the currents. The field pattern from the CST simulation has similarities to the magnetic field from the PIC simulation.
The separation of the magnetic field in the z-direction in positive and negative regions is a result of the interplay of currents and laser field. The energy for the magnetic field from the current is delivered by the laser, because the electrons are accelerated by the laser. As the magnetic field of the ensuing magnetic vortices is in the same order of magnitude as the magnetic field of the laser, it is reasonable to describe the electric and magnetic fields as fields in a circular waveguide.

6.5.3. Circular Waveguide

The detailed derivation of the electric and magnetic fields in a circular waveguide is found in the appendix A.3.1 and refers to the textbook from Pozar [40].

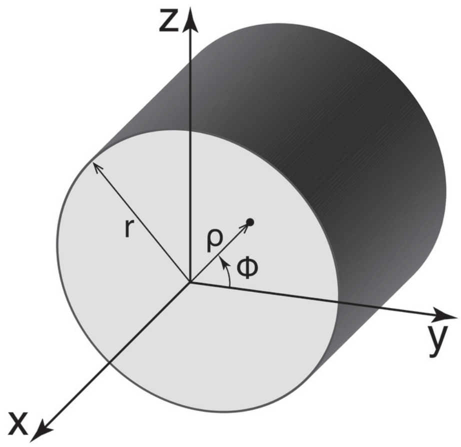

Figure 6.24.: Geometry of a circular waveguide.

The main focus in this section are the results that follow from this transmission

line theory and that are used in the following for the description of the magnetic vortex acceleration. These results are amplitudes of the electric and magnetic field, as well as the power flow in a circular waveguide.
The amplitude of magnetic field in the waveguide in the z-direction, i.e. $\rho = r$ and $\phi = \pi/2$ is given by (c.f. eq. A.26 and eq.A.30)

$$\hat{H}_\rho = \frac{\beta m_e c a_0 p'_{11} J'_1(p'_{11})}{e\mu} \tag{6.4}$$

and as $B = \mu H$

$$\hat{B}_\rho = \frac{\beta m_e c a_0 p'_{11} J'_1(p'_{11})}{e}, \tag{6.5}$$

where $\beta = \sqrt{k^2 - k_c^2}$ is the propagation constant, $k_c = p'_{11}/r$ and p'_{11} is the root of the Bessel function of the first kind so that $J'_1(p'_{11}) = 0$.
For an $a_0 = 7$, a frequency of 375 THz and by neglecting k_c in the propagation constant β, one gets

$$\hat{B}_z = 100\text{kT}$$

The value is roughly 10% higher compared to the value of a free space wave.

In a next step the energy of the laser pulse within the circular waveguide is estimated. The average power of the TE_{11} wave in the circular waveguide can be estimated from the Poynting vector and the integration over the area

$$\begin{aligned}
P_0 &= \frac{1}{2}\text{Re} \int\limits_{\rho=0}^{r} \int\limits_{\phi=0}^{2\pi} \bar{E} \times \bar{H}^* \hat{x} d\phi d\rho \\
&= \frac{1}{2}\text{Re} \int\limits_{\rho=0}^{r} \int\limits_{\phi=0}^{2\pi} \left[E_\rho H_\phi^* - E_\phi H_\rho^*\right] \rho d\phi d\rho \\
&= \frac{\omega\mu |A|^2 \text{Re}(\beta)}{2k_c^4} \int\limits_{\rho=0}^{r} \int\limits_{\phi=0}^{2\pi} \left[\frac{1}{\rho^2}\cos^2\phi J_1^2(k_c\rho) + k_c^2 \sin^2\phi J_1'^2(k_c\rho)\right] \rho d\phi d\rho \\
&= \frac{\pi\omega\mu |A|^2 \text{Re}(\beta)}{2k_c^4} \int\limits_{\rho=0}^{r} \left[\frac{1}{\rho} J_1^2(k_c\rho) + \rho k_c^2 J_1'^2(k_c\rho)\right] d\rho \\
&= \frac{\pi\omega\mu |A|^2 \text{Re}(\beta)}{4k_c^4} \left(p_{11}'^2 - 1\right) J_1^2(k_c r)
\end{aligned} \tag{6.6}$$

The same derivation for a TM_{01} wave results in

$$P_0 = \frac{\pi\omega\mu |A|^2 \text{Re}(\beta)}{4k_c^4} p_{01}^2 J_2^2(k_c r). \tag{6.7}$$

The propagation constant β reduces to

$$\begin{aligned}\beta &= \Bigg(k^2 - \underbrace{\left(\frac{p'_{11}}{r}\right)^2}_{\ll k^2}\Bigg)^{1/2} \\ &= k\end{aligned} \tag{6.8}$$

Equation (A.30) and equation (6.8) are inserted into equation (6.6), so that one gets

$$P_0 = \frac{\pi r^2}{4} n_{cr} m_e c^3 a_0^2 \left(p'^2_{11} - 1\right) J_1^2(p'_{11}). \tag{6.9}$$

The laser pulse has a finite duration and the shape of the pulse will be gaussian. The integration over time results in

$$\int\limits_{-\infty}^{+\infty} \left[\exp\left(-\frac{4t^2}{\tau_L^2}\right)\right]^2 dt = \sqrt{\frac{\pi}{8}}\tau_L \tag{6.10}$$

The result of laser pulse energy inside the self-generated plasma waveguide is

$$\mathcal{E}_L = r^2 n_{cr} m_e c^3 a_0^2 \tau_L K \tag{6.11}$$

with K for the dominating mode TE_{11}

$$K_{TE11} = \sqrt{\frac{\pi^3}{128}} \left(p'^2_{11} - 1\right) J_1^2(p'_{11}) = 0.40$$

and K for the TM_{01} mode

$$K_{TM01} = \sqrt{\frac{\pi^3}{128}} p_{01}^2 J_2^2(p_{01}) = 0.53$$

The numerical values for K_{TE11} and K_{TM01} do not differ very much. Because the transformation of the TEM mode to the TM mode is not complete and further assumptions are made in the following, the numerical value of K_{TE11} is used.

The length of the circular waveguide d can now be estimated from the energy acquired by an electron from the laser. The energy of an electron oscillating in the transverse field of the laser is [59]

$$\epsilon_e = a_0 m_0 c^2 \tag{6.12}$$

$$= 0.511 a_0 [\mathrm{MeV}] \tag{6.13}$$

The energy transferred to the electrons in the channel is then the number of electrons in the cylindrical volume times the energy of a single electron [61]

$$\mathcal{E}_{etot} = \epsilon_e n_e \pi r^2 d \tag{6.14}$$

By $\mathcal{E}_{etot} = \mathcal{E}_L$ from equation 6.14 and 6.11 the channel length is

$$d = c\tau_L K \frac{n_{cr}}{n_e}\frac{a_0}{2} \tag{6.15}$$

In the simulation the channel formed in a region where $n_e = 3.1 n_{cr}$. The laser had an a_0 of 7 and a pulse length of 30 fs. Thus, the channel length is 5.4 μm, which is in good agreement with the simulation (cf. fig 6.10). The channel diameter cannot be estimated from the circular waveguide theory, but from the effect of relativistic self-focusing. Relativistic self-focusing is presented in the next section.

6.5.4. Relativistic Self-Focusing

In the following the effect of relativistic self-focusing is described and adheres to [19]. The effort of derivation is done to show at what point the equations are modified and differ from the usually used solution.
In general relativistic self-focusing is an effect that is caused by the mass increase of electrons travelling close to the speed of light. Similar to section 6.3 the index of refraction has to be corrected by a γ factor. An EM wave that propagates in a uniform plasma with the vector potential A is described by

$$\frac{\partial^2 A}{\partial t^2} - c^2\nabla^2 A = -\omega_P^2 \frac{n_e A}{\gamma} \tag{6.16}$$

As the fast change of the field phase is not of interest, but only the laser's amplitude $a(\rho, x, t)$, the so-called slowly-varying envelope approximation is used

$$A = \frac{1}{2}\left(a e^{j\psi} + a^* e^{-j\psi}\right) \tag{6.17}$$

Further simplifications are made by neglecting 2nd derivatives of the envelope and using a linear dispersion relation $\omega^2 = \omega_P^2 + c^2 k^2$. The wave equation moving with the group velocity of the pulse reads with these simplifications as follows

$$j\omega\frac{\partial a}{\partial \tau} = c^2\nabla^2\frac{a}{2} + \omega_P^2\left(1 - \frac{n}{\gamma}\right)\frac{a}{2} \tag{6.18}$$

By expanding the γ factor in a series and using the normalizations $\tilde{t} = \frac{\omega_P^2}{\omega} t$ and $\tilde{\rho} = k_P \rho$ the paraxial equation becomes

$$\frac{\partial a}{\partial \tilde{t}} = -\frac{j}{2}\nabla^2 a - \frac{j}{2}|a|^2 a \tag{6.19}$$

which is the nonlinear Schrödinger equation with the Hamiltonian H

$$H = \int \left(\frac{1}{2}|\nabla a|^2 - \frac{1}{16}|a|^4\right) d^2\tilde{\rho} \tag{6.20}$$

and the normalized beam power P

$$P = \int |a|^2 d^2\tilde{\rho} \tag{6.21}$$

The variance or 2nd moment of equation 6.19 can be interpreted as focusing. The twice integration of this variance over time gives the beam equation

$$< \tilde{\rho}^2 >= \frac{2H}{P}\tilde{t}^2 + C\tilde{t} + D \tag{6.22}$$

A beam with the radial profile

$$a(\tilde{\rho}) = a_0 \exp\left(-\frac{\tilde{\rho}^2}{2\tilde{\sigma_0}^2}\right) \tag{6.23}$$

is considered. The normalized power P and the Hamiltonian H read with this beam profile as

$$\begin{aligned} P &= \int |a|^2 d^2\tilde{\rho} \\ &= \int_0^\infty 2\pi\tilde{\rho} \left| a_0 \exp\left(-\frac{\tilde{\rho}^2}{2\tilde{\sigma_0}^2}\right)\right|^2 d\tilde{\rho} \\ &= \pi a_0^2 \tilde{\sigma_0}^2 \end{aligned} \tag{6.24}$$

and

$$\begin{aligned} H &= \int \left(\frac{1}{2}|\nabla a|^2 - \frac{1}{16}|a|^4\right) d^2\tilde{\rho} \\ &= \frac{1}{2}\int_0^\infty 2\pi\tilde{\rho}\left| -\frac{a_0\tilde{\rho}}{\tilde{\sigma_0}^2}\exp\left(-\frac{\tilde{\rho}^2}{2\tilde{\sigma_0}^2}\right)\right|^2 d\tilde{\rho} - \frac{1}{16}\int_0^\infty 2\pi\tilde{\rho}\left| a_0 \exp\left(-\frac{\tilde{\rho}^2}{2\tilde{\sigma_0}^2}\right)\right|^4 d\tilde{\rho} \\ &= \frac{1}{2}\pi a_0^2 - \frac{\pi}{32}a_0^4\tilde{\sigma_0}^2 \\ &= \frac{\pi}{2}a_0^2\left(1 - \frac{a_0^2\tilde{\sigma_0}^2}{16}\right) \end{aligned} \tag{6.25}$$

The results of H (eq.6.25) and P (eq.6.24) are inserted into the beam equation 6.22

$$< \tilde{\rho}^2 >= \frac{\tilde{t}^2}{\tilde{\sigma_0}^2}\left(1 - \frac{1}{16}a_0^2\tilde{\sigma_0}^2\right) + \tilde{\sigma_0}^2 \tag{6.26}$$

The time and space coordinates are now substituted back from dimensionless units to physical units. But instead using the transformations

$$\begin{aligned}\tilde{t} &= \frac{\omega_P^2}{\omega} t \\ \tilde{\rho} &= \frac{\omega_P}{c} \rho \\ \tilde{\sigma_0} &= \frac{\omega_P}{c} \sigma_0\end{aligned} \tag{6.27}$$

the following transformations are used

$$\begin{aligned}\tilde{t} &= \frac{\omega_P^2}{\omega} t \\ \tilde{\rho} &= \frac{2\pi}{\sqrt{2}} \frac{\omega_P}{c} \rho \\ \tilde{\sigma_0} &= \frac{\lambda_L}{\sigma_0}\end{aligned} \tag{6.28}$$

A different substitution for $\tilde{\sigma}_0$ is chosen. This can be done, because $\tilde{\sigma}_0$ is basically just a constant. It is the variance or width of the gaussian distribution. With these substitutions the beam caustic in a plasma becomes

$$< \rho >= \frac{\sqrt{2}}{2\pi} \left[\frac{n_e}{n_{cr}} \frac{1}{\gamma} x^2 \frac{\sigma_0^2}{\lambda_L^2} \left(1 - \frac{1}{16} a_0^2 \frac{\lambda_L^2}{\sigma_0^2} \right) + \frac{\lambda_L^2}{\sigma_0^2} \frac{c^2}{\omega_P^2} \right]^{1/2} \tag{6.29}$$

For comparison the beam radius or caustic in an underdense plasma is

$$< \rho >= \sigma_0 \left[1 + \frac{x^2}{x_R^2} \left(1 - \frac{P}{P_C} \right) \right]^{1/2} \tag{6.30}$$

with the critical power $P_C = 17.5(\omega/\omega_P)^2[\mathrm{GW}]$ and the Rayleigh length x_R. In underdense plasmas the laser can propagate several millimeters, if the laser power is not too high. For plasmas with near critical densities and lasers with TW power the P_C term causes a fast collapse of the radius. In equation 6.29 this behavior is prevented by the different scaling of the beam radius, namely the scaling in laser wavelengths rather than plasma frequencies. Thus, the influence of the second term in the bracket in equation 6.26 is reduced. Thereby the early break down of the beam radius to zero is prevented. Moreover the influence of the electron density is increased, but remains relativistically transparent due to the γ factor. The density distribution is gaussian, so that for large x the density is very low. Because x decreases faster than the density increases with smaller x, the beam focuses as the laser approaches higher densities.
The caustic is now calculated for the density profile as it was used in the PIC simulation, i.e. a bi-gaussian distribution. The point where the beam radius becomes zero is set to the position of the highest density. The radius at the box entrance of the PIC simulation is used as σ_0.

Figure 6.25 shows the cycle averaged intensity of the PIC simulation. The caustic of the beam is initially designed as gaussian beam caustic in vacuum.

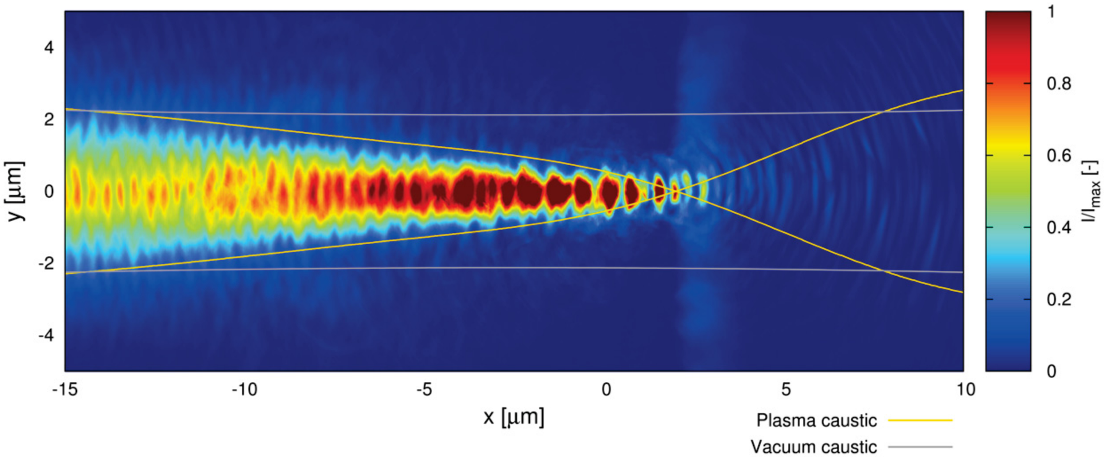

Figure 6.25.: Simulation. In a color map the cycle averaged intensity of the simulation from the previous section, i.e. the magnetic vortex simulation. The light-grey curve shows the gaussian beam caustic as it was defined as initial condition in the simulation. The black curve shows the evaluation of equation 6.29, where the same density profile and a_0 is used as in the simulation. The minimal radius of the plasma caustic, which is zero, is set to the peak of the density profile.

The light-grey curve shows this situation. It is obvious that the beam focuses much stronger. The gold line is the evaluation of equation 6.29 with the density distribution as it is used in the PIC simulation. The curve is in very good agreement with the simulation.

The caustic described by equation 6.29 is valid as long the propagation of the wave is not inside the channel. Therefore the radius of the channel is estimated by calculating the channel length (eq. 6.15) at the position where the radius becomes zero x_0. The radius of the channel is where the channel length fits between the left and right side of x_0 of the caustic. This position is roughly $x_0 \pm d/2$.

Figure 6.26 and 6.27 show the electron density normalized to the critical density at 115 fs and 170 fs. The beam caustic from equation 6.29 and the channel length from equation 6.15 are overlaid. At the intersection of plasma caustic and channel length one reads the radius of the channel, which is roughly 900 nm and basically remains constant, as can be seen in figure 6.26 and 6.27 .

Up to this point the laser in the near critical plasma and in a waveguide is described. As the origin and the size of the electric and magnetic fields is known, the acceleration of the ions is calculated. The force of these fields on a charged particle is given by the Lorentz force

$$\vec{F}_L = e\left[\vec{E} + \vec{v} \times \vec{B}\right] \tag{6.31}$$

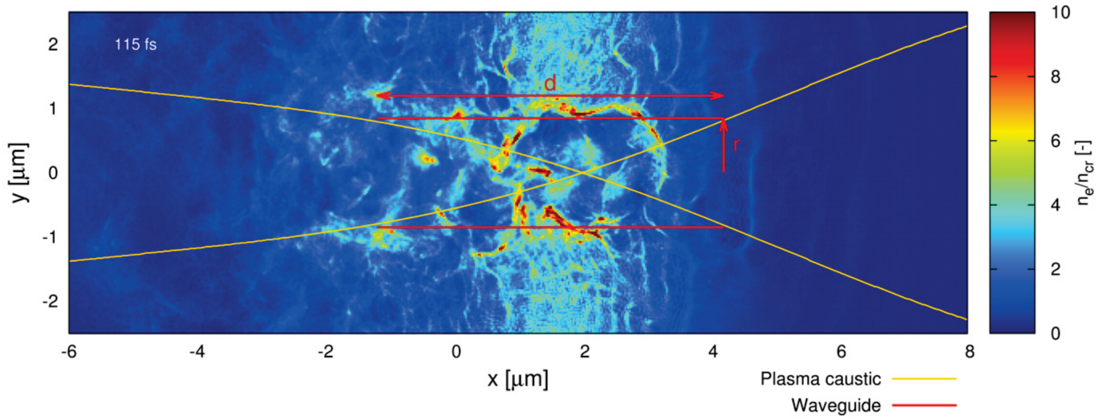

Figure 6.26.: Simulation. In a color map the electron density normalized to the critical density at 115 fs. The light-grey line indicates the plasma caustic. Within the waveguide the plasma caustic breaks down. The freespace TEM wave has to propagate within the boundary conditions of a waveguide and therefore the mode changes. The waveguide length d is known from section A.3.1 which is 5.4 μm. The radius of the waveguide is now defined at $\pm d/2$ of the plasma caustic: $r = 900$nm.

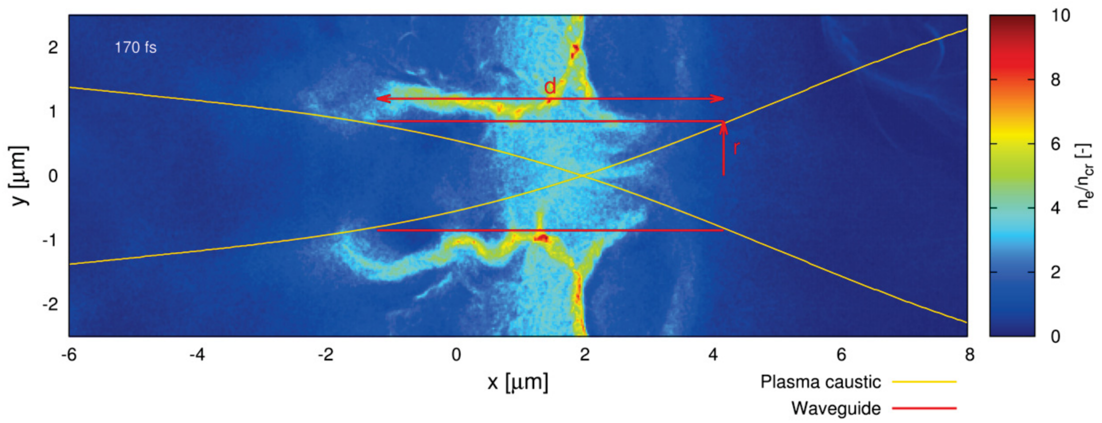

Figure 6.27.: Simulation. The figure shows the same situation as figure 6.26, but at a later time. The laser has completely propagated through the waveguide and therewith the magnetic vortices. In a color map the electron density normalized to the critical density at 170 fs. The light-grey line indicates the plasma caustic.

From the TM_{01} mode follows that $B_x = B_y = 0$ and that $E_z = 0$. In cylindrical coordinates the Lorentz force becomes

$$\begin{aligned}\vec{F}_L &= e\left[\begin{pmatrix}\sqrt{E_x^2+E_y^2}\\ \arctan(E_y/E_x)\\ 0\end{pmatrix} + \begin{pmatrix}\sqrt{v_x^2+v_y^2}\\ \arctan(v_y/v_x)\\ v_z\end{pmatrix} \times \begin{pmatrix}0\\ 0\\ B_z\end{pmatrix}\right]\\ &= e\left[\begin{pmatrix}\sqrt{E_x^2+E_y^2}\\ \arctan(E_y/E_x)\\ 0\end{pmatrix} + \begin{pmatrix}\arctan(v_y/v_x)B_z\\ -\sqrt{v_x^2+v_y^2}B_z\\ 0\end{pmatrix}\right]\end{aligned} \tag{6.32}$$

If now is considered that the motion of the charged particle is on a circle for a brief moment of time, the Lorentz force can be set equal to the centripetal force

$$\vec{F}_C = \frac{m}{r}\vec{v}^2 \tag{6.33}$$

As only the radial component of $\vec{F}_C = \vec{F}_L$ is of interest, the velocity of a charged particle is estimated by

$$v_r = \left(\frac{er}{m}\left[\sqrt{E_x^2+E_y^2} + \arctan(v_y/v_x)B_z\right]\right)^{1/2} \tag{6.34}$$

In the experiment the spectrometer is aligned in the x-direction. Hence, the velocity of the protons in the y-direction is neglected for the comparison of the analytic model with the experiment, so that the second term in the bracket is zero. The channel diameter r was estimated to be roughly 900 nm. Moreover the electric field should have the same strength as the magnetic field times the speed of light. The magnetic field was estimated to be 100 kT (cf. eq. 6.5). Thus, the velocity is

$$v_r = \sqrt{\frac{er}{m}\left[cB_z\right]} = 51 \times 10^6 \text{m/s} \tag{6.35}$$

and with it the maximum kinetic energy of the proton is $\mathcal{E}_{p,max} = 3.55$ MeV, which is in very good agreement with the PIC simulation and most importantly also in very good agreement with the experimental result (cf. figure 6.15b)
Moreover equation 6.35 has a charge to mass dependence as observed in the PIC simulation (cf. figure 6.17).

6.5.5. Conclusion

The aim of this section was the description of the magnetic vortex acceleration from basic principles. The use of transmission line theory was briefly motivated. The theory is used to describe the laser within the self-generated plasma channel a mode of a circular waveguide. From the theory follows the amplitude of the magnetic field. Moreover, the power flow of the waveguide mode is deduced. As the laser pulse has a finite length, the energy in the waveguide is estimated. The acquired energy of a single electron and the total energy acquired of all electrons in the channel lead to the length of the channel.
The last information needed in order to describe the magnetic vortex acceleration is the channel diameter, because the diameter determines the size of a

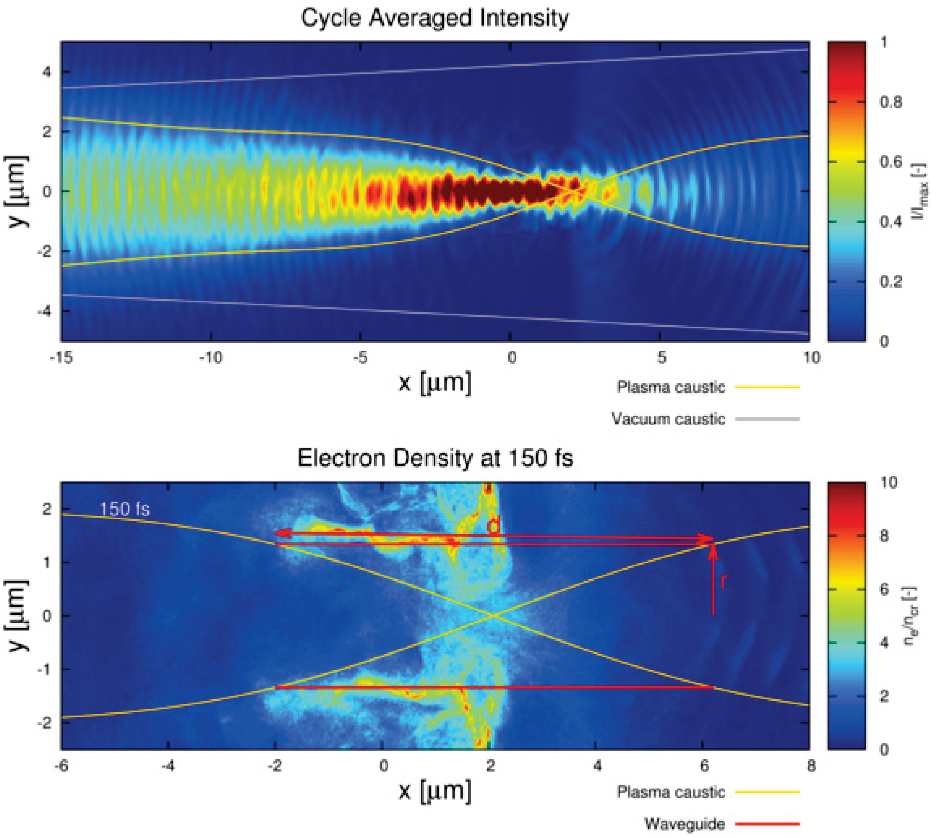

Figure 6.28.: Simulation. The density distribution in this PIC simulation is the same as in the simulation before. The initial laser caustic was chosen to be defocused by -60 μm. a_0 was increased to 12. The simulation evidence that the caustic in plasma calculated with the equation 6.29 is not only valid for one special case.

magnetic vortex. In the PIC simulation a focusing of the laser was observed. Due to the intensity of the laser and the plasma density, relativistic self-focusing in an overdense plasma appeared. The available theories describe relativistic self-focusing only for underdense plasmas. Therefore, the theory is modified in a phenomenological ansatz. In particular the scaling of the focus in plasma frequencies is changed to a scaling in laser wavelengths. This approach prevents the laser to collapse too early in too dense regions. Thus, the caustic and therewith the diameter of the self-generated plasma channel is estimated with this modificated theory.
Finally, the velocity of a proton in the vicinity of a magnetic vortex is calculated with the Lorentz force. The calculated kinetic energy is in very good agreement with the PIC simulation as well as with the experiment.

6.6. Conclusion

The delay between the pulses examined in this chapter was increased from 10s of femtoseconds to 10s of picoseconds compared to the shots examined in the previous chapter. In order to evaluate the experimental shots with PIC simulations, the expansion of the plasma after one main pulse has exploded the target is modeled in 1D PIC simulations. The expansion is simulated until 120 ps and 300ps after the main pulse. The initial conditions for the 1D simulation are the particles' momenta and density distributions, that are taken from a line-out from the last output file of the single beam simulation, i.e. after 750 fs. Two characteristic electron momentum distributions are identified as initial conditions for the 1D simulation: an average electron momentum distribution and a maximum electron momentum distribution. The average momentum distribution leads to an expansion that corresponds to a beam I shot, i.e. the subsequent pulse is beam II. Hence, the maximum momentum distribution leads to an expansion that corresponds to a beam II shot, i.e. the subsequent pulse is beam I.
If the pulse of beam II is delayed in the order of 10s picoseconds, there is no enhancement observed in the proton cut-off energy, but only the proton cut-off energy of beam I is detected. Beam II is strongly refracted in front of the target. Eventually, the beam energy is depleted and the pulse energy locally heats electrons.
If the pulse of beam I is delayed by at least 50ps compared to the pulse of beam II, an enhancement in the proton cut-off energy is observed in the experiment. The subsequent laser pulse cannot enhance the TNSA mechanism, as the quasi-static electric field at the rear side of the target lasts only for a few hundred femtoseconds and the already accelerated ions have moved several centimeters. Thus, a different acceleration mechanism must occur.
In the 2D PIC simulation the laser pulse propagates through the exploded target. The plasma is relativistically transparent to the laser. While the laser propagates through the plasma, a channel - a waveguide - is generated. Within the channel the mode of the electro-magnetic wave changes, i.e. from a TEM_{00} free space wave to a TE_{01} circular waveguide wave, at which the transformation is not complete. As the laser pulse approaches the former rear side of the target, the pulse expands into free space. Due to the interplay between accelerated electrons, waveguide wall and laser pulse, two magnetic vortices are generated

at the tail of the laser pulse. One vortex has a magnetic field, that is positively oriented in the z-direction and the other vortex has a magnetic field, that is negatively oriented in the z-direction. The vortices move next to each other out of the channel and move along the former target surface in different directions. Electrons circulate around the vortices and support with their current the magnetic field. Electric fields are radial arranged around the vortices. Eventually, the electric and magnetic fields accelerate from the TNSA mechanism remaining ions.

Obviously the channel-formation involves hole-boring (cf. sec. 2.6.4). In particular publications by Pukhov and Meyer-te-Vehn [43, 44] are relevant for the here observed phenomenon. In the publications the laser interacts in PIC simulations with a near-critical plasma and generates a channel in the plasma. Strong electron currents cause a magnetic field pattern that is similar to the here made simulations. Pukhov and Meyer-te-Vehn assumed in their simulations an infinite extension of the plasma. Thus, the laser does not break through the plasma into vacuum, but the laser pulse transfer its energy completely to electrons and depletes in the plasma. Hence, no heavy ions are accelerated.

Similar to the here described acceleration mechanism, the break-out afterburner (BOA) mechanism is also found in a regime where the target becomes relativistically transparent to the laser [23]. Beside the difference that BOA is described for target thicknesses of 10s of nanometer, the acceleration relies on the formation of a Bunemann instability [5]. This two stream instability is not found between the electrons and the ions in the PIC simulation. Hence, the BOA mechanism is excluded for the acceleration.

In the last part of the chapter, the observed acceleration mechanism is described in an analytic approach, which supports the exclusion of BOA. The approach adheres to a publication from Bulanov et al. [10], but the results are somewhat different. The modes of the laser within the self-generated channel are described as modes of a a circular waveguide. With this transmission line theory it is possible to determine the field strength within the channel. Moreover, the channel length is estimated from the acquired energy of the electrons in the channel and the power flow in the channel. The second part of the analytic description covers the relativistic focusing in an overdense plasma. The usually applied theory for relativistic self-focusing in underdense plasmas is modified. The width of the laser focus does not scale in plasma frequencies but in laser wavelengths. Moreover relativistic transparency is taken into account. In this way, the early collapse of the beam caustic is prevented.
The size and strength of the magnetic vortices is known. Finally, the kinetic energy is estimated with the Lorentz force. The analytic approach confirms the results from the PIC simulations as well as the results from the experiment.

7. Summary and Outlook

This work presented the first experiment of two ultrashort, high intensity laser pulses, that interact with a solid target. The main objectives of the experiment were to examine the scalability of TNSA with multiple beams and to find the transition beyond TNSA.
The Arcturus laser facility at the Heinrich Heine University in Düsseldorf provides two <30fs laser pulses with an energy of 3J and 6J, respectively. Both pulses were spatially and temporally overlapped on a 5μm thick titanium foil. As an additional parameter in the experiment appears the delay between the two pulses. The delay was varied during the experiment in a range close-to-synchronize, i.e. $\pm$200fs, and on a range of a few 10s of picoseconds.
Three regimes were identified from the different delay ranges

- Defocused, close to synchronized shots
- Focused, close to synchronized shots
- Magnetic vortex acceleration

The three regimes strongly depend on the plasma distribution *seen* by the main pulses. For the first two cases the prepulses of both laser beams drive the initial plasma distribution.
The extension of the preplasma is reduced by defocusing both beams, because the absolute contrast is increased. The remarkable result for synchronized defocused lasers is a reduction of the proton cut-off energy. This behavior is somewhat counter-intuitive. The discrepancy is further enhanced, if one checks the electric field strength from the corresponding PIC simulation. The field strength is the highest for synchronized shots in the PIC simulations and lower for an increased delay. Nevertheless, the simulations also show the drop of proton cut-off energy for synchronized pulses. The solution of the dilemma is found in the prepulses. The enhanced absolute contrast of the laser pulses while defocusing the two beams leads also to a reduced plasma temperature at the time the main pulses approach the target. Thus, the protons and carbon ions

remain relatively close to the target - confined in a small area. The rise and fall of the ambipolar electric field on the rear side of the target driven by the synchronized pulses is too fast for the heavy ions. The temporal appearance of the field is stretched by a delay between the two defocused pulses, so that the ions gain time for their acceleration. This phenomenon is consistent with the effect for TNSA, that long pulses are more advantageous than short pulses with the same intensity for the acceleration of ions.

If both beams are focused and both pulses are synchronized, the proton cut-off energy is higher compared to the delayed pulses. Thus, the behavior is the opposite compared to the defocused shot series. As the intensity of the prepulses is higher, the ions from the contamination layer have expanded more compared to the defocused shot series. In preparation for the 2D PIC simulation it was important to consider the delay also for the prepulses. The prepulse of the subsequent mainpulse is interrupted by the first main pulse that approaches the target. Thus, the largest preplasma appears for synchronized pulses. If the influence of the delay on the prepulses is neglected, the cut-off energies are almost the same for any delay.
In the experiment it was observed, that the first main pulse imprints its characteristics onto the MCP images. Similarly, the behavior was observed in the PIC simulation for the spatial proton energy distribution. The first main pulse creates the electron sheath. The subsequent laser pulse only modifies this electron sheath and finally the so-modified sheath causes a slightly different proton energy distribution. It can be concluded from the PIC simulations, that it is interesting in upcoming experiments to check the ion energies under different angles than only in 0° direction.
Experimental shots showed for synchronized and focused beams an unique MCP result. Only a few ion species appeared and the highest proton cut-off energies of the experiment were detected. In the PIC simulation the proton energy distribution also showed unique characteristics. Proton energies below 0.5MeV do not appear and the protons are accelerated only from a small area. The distribution is explained by a resonantly enhanced $\vec{j} \times \vec{B}$ heating in agreement with a publication from Nuter et al. [38]. In the PIC simulation the proton cut-off energy for synchronized shots is even higher than the sum of the cut-off energies of the single beam interactions. Thus, this regime is highly attractive for further investigations, as the proton energy scales at the least linearly with the intensity instead with the square root of the intensity.

The last regime appeared in the experiment only for shots, where the main beam with a normal angle of incidence is 10s of picosecond behind the beam with an angle of incidence of about 40°. The proton cut-off energy is higher than the single beam interaction for those shots. The ions accelerated by the TNSA mechanism from the first laser pulse are already too far away to be influenced by the subsequent laser pulse. Thus, a different acceleration mechanism must apply. The mechanism is identified with the aid of PIC simulations as magnetic vortex acceleration. The first main pulse explodes the target. This explosion is modeled with a 1D PIC simulation over a time span of 100s of picoseconds. The results of the 1D PIC simulation are used as initial conditions for the 2D PIC simulation of the subsequent laser pulse. The expanded plasma becomes rela-

tivistically transparent to the subsequent laser pulse and experiences relativistic self-focusing while it propagates through the plasma. Moreover, the pulse generates a channel in the plasma and accelerates electrons. Due to the interplay between accelerated electrons, waveguide wall and laser pulse, two magnetic vortices are generated at the tail of the laser pulse. The magnetic fields of the vortices are oriented in opposed z-directions and have a magnitude comparable to the magnetic fields of the laser. The front part of the pulse break-through into less dense plasma regions like a point-source. The vortices also leave the channel and move along the former target rear side in opposite directions. Electrons circulate around the vortices and form with their current a self-sustaining generator. The strong electric and magnetic fields that come along with the vortices are the driving force for the acceleration of the remaining ions.
From the observations of the PIC simulations, an analytic ansatz for the description of the observed phenomena was presented. The length of the channel formed by the laser is derived with the aid of transmission line theory of a circular waveguide. The theory of relativistic self-focusing in an underdense plasma is modified in a phenomenological approach, so that the radius of the channel is predicted. The information allowed it to predict the kinetic energy of a proton, that is accelerated by the Lorentz force. The prediction of the cut-off energy from the model is in agreement with the PIC simulation and more importantly also with the experiment.
The proton cut-off energy is indeed somewhat lower with magnetic vortex acceleration compared to the enhanced TNSA regime, but in the experiment the magnetic vortex acceleration showed a higher level of robustness, in terms of repeatability. Moreover, the PIC simulations indicate that higher proton energies can be found at different angles than it has been done in this experiment.

In future experiments the predictions made in this thesis regarding the angular distribution of the ions have to be validated. Additionally, the contrast of the laser pulses should be varied in order to verify the strong influence of the prepulses onto the final proton cut-off energy. As the Arcturus Laser Facility was upgraded in 2013 with a XPW system for contrast improvements, it is the ideal platform for these experiments. Moreover both beamlines can now provide 6J pulse energy, so that the scalability of the enhanced TNSA regime as well as the magnetic vortex acceleration can be tested.

A. Appendix

A.1. Technical Data of Used Instruments

MCP

Table A.1.: MCP Detector MCP-90-D-R-P43-VF

Parameter	Data	Unit
Diameter	88 ± 0.1	mm
Thickness	1.26 ± 0.05	mm
Pore diameter	21 ± 0.5	μm
Input electrode material	NiCr	-
Output electrode material	NiCr	-
MCP in gain @ 1 kV	$> 1.5 \times 10^3$	-
MCP out gain @ 1 kV	$> 1.5 \times 10^3$	-
Chevron gain	$> 4 \times 10^6$	-
Screen substrate	$BK - 270$	-
Phosphor type	P43	-

A.2. Pulse Shape in Space and Time

A.2.1. Spatial Pulse Shape

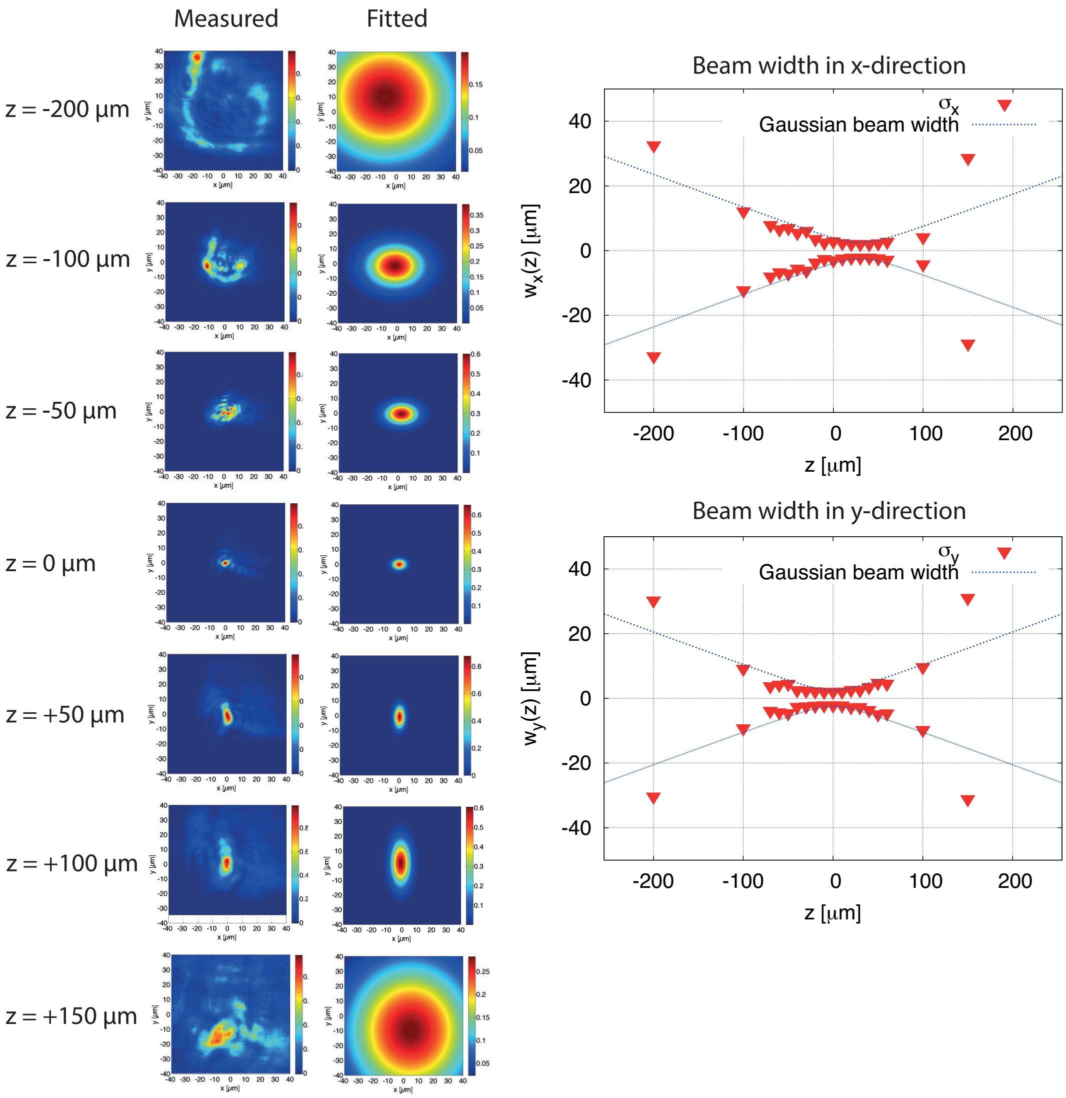

Figure A.1.: Z-scan beam I.

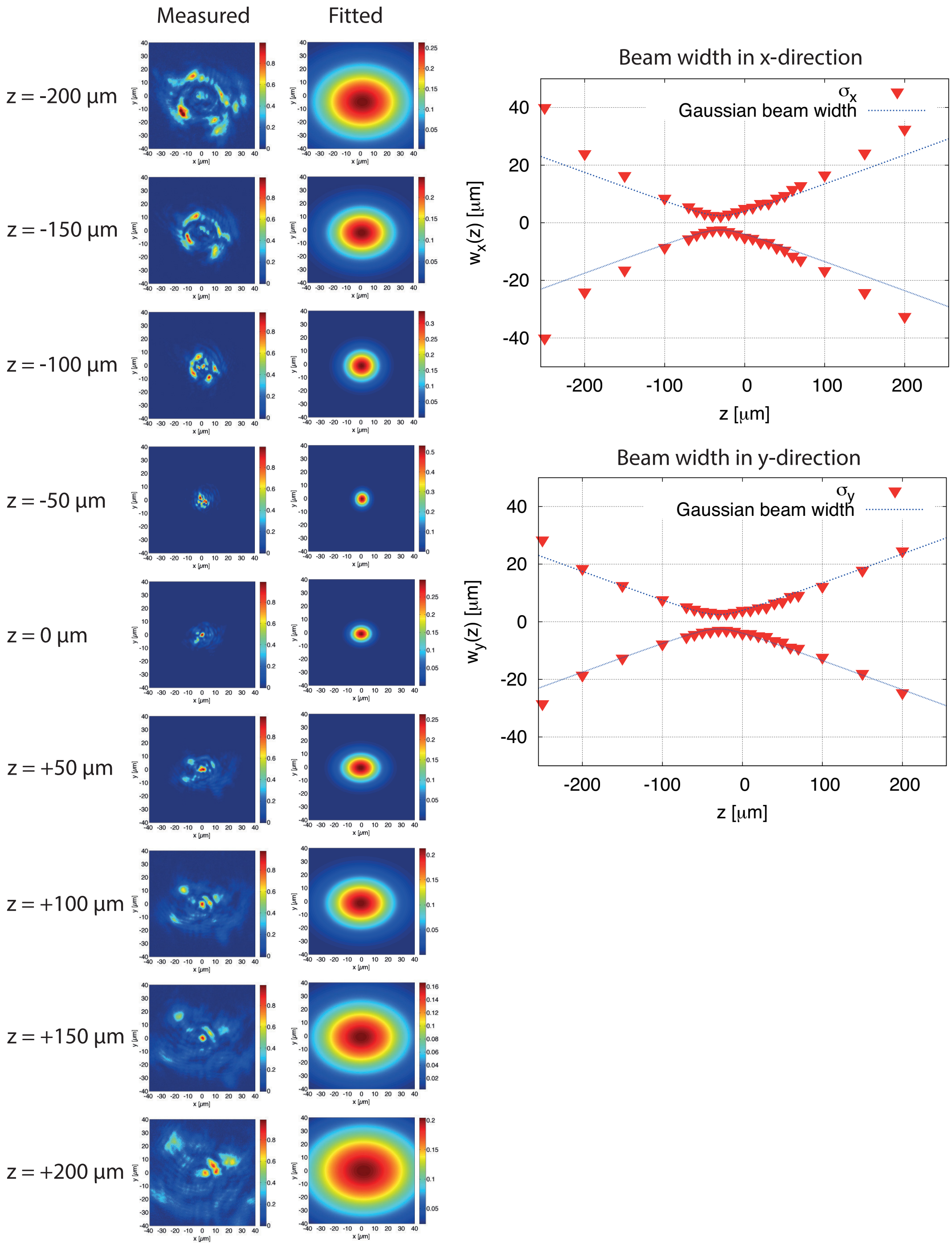

Figure A.2.: Z-scan beam II.

A.2.2. Temporal Pulse Shape and Phase

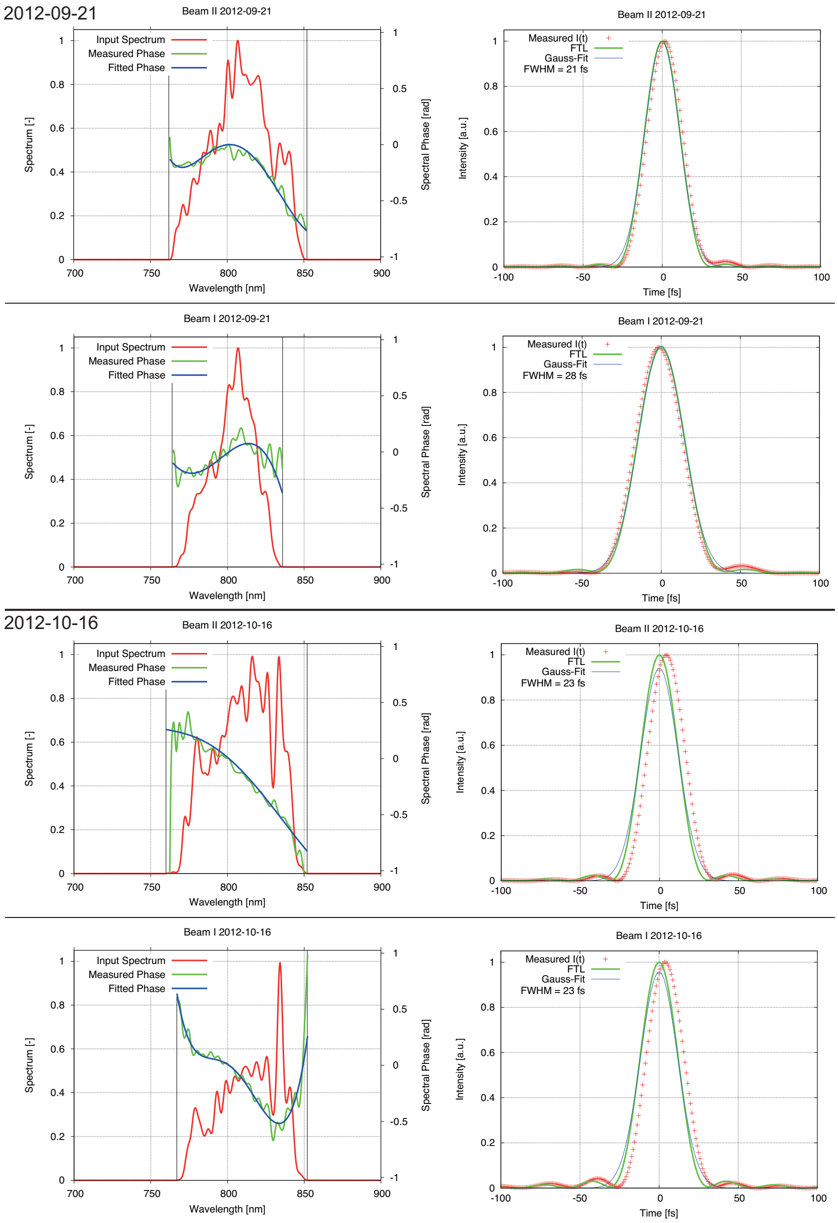

Figure A.3.: Wizzler measurement. Measurement of phase, spectrum and temporal shape of beam II and I on two different days.

A.2.3. CR-39 Cross-Calibration

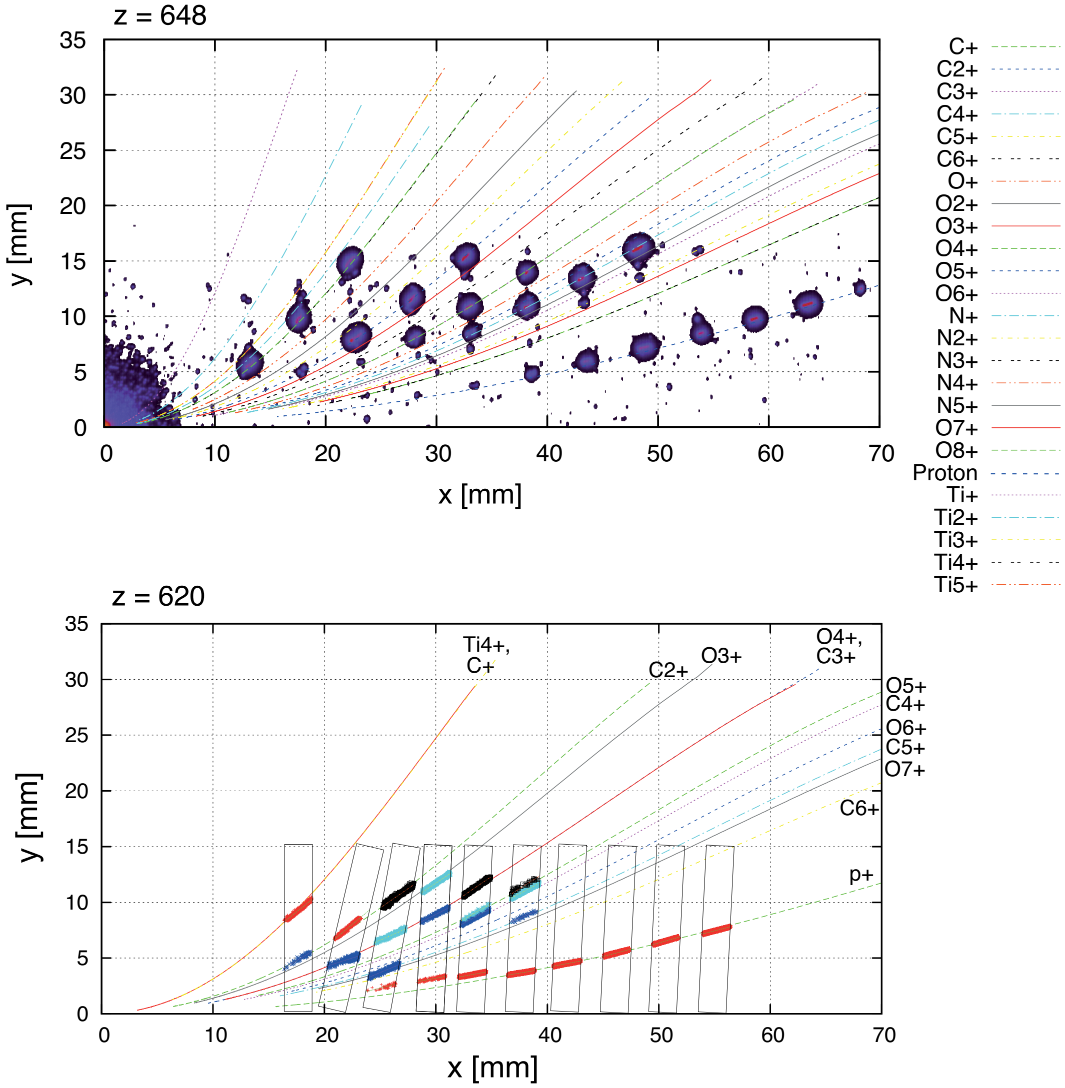

Figure A.4.: Experiment. Second frame CR-39.

A.3. Transmission Line Theory

A.3.1. Circular Waveguide

The here presented derivation of the electric and magnetic fields adheres to the textbook [40]. Again, in general a circular waveguide is a hollow metal tube that supports TE and TM waveguide modes. The geometry suggests itself to choose cylindrical coordinates.

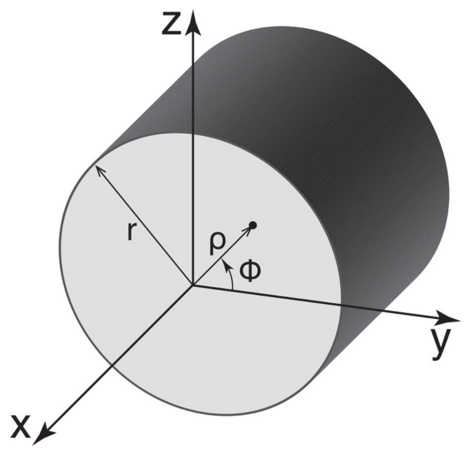

Figure A.5.: Geometry of a circular waveguide.

The waveguide is source free, so that Maxwell's equations can be written as

$$\nabla \times \bar{E} = -j\omega\mu\bar{H} \tag{A.1}$$

$$\nabla \times \bar{H} = j\omega\epsilon\bar{E} \tag{A.2}$$

The electric and magnetic fields depend on $e^{-j\beta x}x$, so that the above vector equations leads to six partial differential equations. These equations can be reduced to

$$E_\rho = \frac{-j}{k_c^2}\left(\beta\frac{\partial E_x}{\partial\rho} + \frac{\omega\mu}{\rho}\frac{\partial H_x}{\partial\phi}\right), \tag{A.3}$$

$$E_\phi = \frac{-j}{k_c^2}\left(\frac{\beta}{\rho}\frac{\partial E_x}{\partial\phi} - \omega\mu\frac{\partial H_x}{\partial\rho}\right), \tag{A.4}$$

$$H_\rho = \frac{j}{k_c^2}\left(\frac{\omega\epsilon}{\rho}\frac{\partial E_x}{\partial\phi} - \beta\frac{\partial H_x}{\partial\rho}\right), \tag{A.5}$$

$$H_\phi = \frac{-j}{k_c^2}\left(\omega\epsilon\frac{\partial E_x}{\partial\phi} + \frac{\beta}{\rho}\frac{\partial H_x}{\partial\rho}\right), \tag{A.6}$$

where $k_c^2 = k^2 - \beta^2$. Although the simulations suggest a TM_{01} mode in the self-generated waveguide, in the following the results of the mode with lowest transverse frequency is presented. This mode is a H-wave, so that $E_x = 0$, and H_x is a solution to the wave equation [40]

$$\nabla^2 H_x + k^2 H_x = 0. \tag{A.7}$$

For the ansatz $H_x(\rho, \phi, x) = h_x(\phi, \rho)e^{-j\beta x}$ equation (A.7) is expressed in cylindrical coordinates

$$\left(\frac{\partial^2}{\partial \rho^2} + \frac{1}{\rho}\frac{\partial}{\partial \rho} + \frac{1}{\rho^2}\frac{\partial^2}{\partial \phi^2} + k_c^2\right) h_x(\rho, \phi) = 0. \tag{A.8}$$

In this equation the variables can be separated on each side of the equation, so that the solution can be derived by the method of separation of variables

$$h_x(\rho, \phi) = R(\rho)P(\phi) \tag{A.9}$$

$$\begin{aligned} \frac{1}{R}\frac{d^2R}{d\rho^2} + \frac{\rho}{R}\frac{dR}{d\rho} + \frac{1}{\rho^2 P}\frac{d^2P}{d\phi^2} + k_c^2 = 0 \\ \frac{\rho^2}{R}\frac{d^2R}{d\rho^2} + \frac{\rho}{R}\frac{dR}{d\rho} + \rho^2 k_c^2 = -\frac{1}{P}\frac{d^2P}{d\phi^2} \end{aligned} \tag{A.10}$$

As the left side of the equation depends only on ρ and the right side depends only on ϕ, each side must be equal to a constant k_ϕ^2. Two separate differential equations are remaining

$$\begin{aligned} -\frac{1}{P}\frac{d^2P}{d\phi^2} = k_\phi^2 \\ \frac{1}{P}\frac{d^2P}{d\phi^2} + k_\phi^2 P = 0 \end{aligned} \tag{A.11}$$

and

$$\rho^2\frac{d^2R}{d\rho^2} + \rho\frac{dR}{d\rho} + (\rho^2 k_c^2 - k_\phi^2)R = 0 \tag{A.12}$$

The general solution for equation (A.11) is

$$P(\phi) = A\sin(k_\phi \phi) + B\cos(k_\phi \phi) \tag{A.13}$$

h_x demands a periodicity in ϕ so that k_ϕ must be an integer n

$$P(\phi) = A\sin(n\phi) + B\cos(n\phi) \tag{A.14}$$

Equation A.12 is identified as Bessel's differential equation, which has the general solution

$$R(\rho) = CJ_n(k_c\rho) + DY_n(k_c\rho) \tag{A.15}$$

$J_n(x)$ is the Bessel function of the first kind and $Y_n(x)$ is the Bessel function of the second kind. For $\rho = 0$, $Y_n(k_c\rho)$ becomes infinite which physically not acceptable for a circular waveguide. Therefore $D = 0$ and the solution for $h_x(\rho, \phi)$ is

$$h_x(\rho, \phi) = (A\sin(n\phi) + B\cos(n\phi))J_n(k_c\rho), \tag{A.16}$$

where the constant C has been merged to the constants A and B. A further simplification is achieved due azimuthal symmetry of the circular waveguide. The coordinate system can be rotated about the x-axis so that either $A = 0$ or $B = 0$. Hence

$$h_x(\rho, \phi) = A \sin(n\phi) J_n(k_c \rho) \tag{A.17}$$

In a circular waveguide the tangential E-field vanishes at the waveguide wall, i.e. at $\rho = r$. From this follows that

$$E_\phi(r, \phi) = 0 \tag{A.18}$$

E_ϕ is found from equation (A.4) and H_x

$$E_\phi(\rho, \phi, x) = \frac{j\omega\mu}{k_c}(A \sin(n\phi) + B \cos(n\phi)) J'_n(k_c \rho) e^{-j\beta x} \tag{A.19}$$

In order E_ϕ to vanish at $\rho = r$ the first derivative of $J'_n(k_c \rho)$ must be

$$J'_n(k_c r) = 0 \tag{A.20}$$

The roots of $J'_n(x)$ are tabulated and defined as p'_{mn}, where p'_{mn} is the mth root of J'_n. Hence k_c is

$$k_{c_{nm}} = \frac{p'_{nm}}{r} \tag{A.21}$$

and the propagation constant is

$$\beta_{nm} = \sqrt{k^2 - k_c^2} = \sqrt{k^2 - \left(\frac{p'_{nm}}{r}\right)^2} \tag{A.22}$$

The smallest root p'_{nm} corresponds to the dominating mode in the circular waveguide which is TE_{11} and $p'_{11} = 1.841$. For this dominating mode the fields can be written as

$$H_x = A \sin\phi J_1(k_c \rho) e^{-j\beta x}, \tag{A.23}$$

$$E_\rho = -\frac{j\omega\mu}{k_c^2 \rho} A \cos\phi J_1(k_c \rho) e^{-j\beta x}, \tag{A.24}$$

$$E_\phi = \frac{j\omega\mu}{k_c} A \sin\phi J'_1(k_c \rho) e^{-j\beta x}, \tag{A.25}$$

$$H_\rho = -\frac{j\beta}{k_c} A \sin\phi J'_1(k_c \rho) e^{-j\beta x}, \tag{A.26}$$

$$H_\phi = -\frac{j\beta}{k_c^2 \rho} A \cos\phi J_1(k_c \rho) e^{-j\beta x}, \tag{A.27}$$

$$E_x = 0 \tag{A.28}$$

The transverse field amplitude inside the waveguide shall be expressed by the dimensionless vector-potential of the laser pulse a

$$E_0 = \frac{m_e c \omega a_0}{e} \tag{A.29}$$

The constants in equation A.24 are set equal to equation (A.29)

$$\frac{\omega \mu}{k_c^2 \rho} A = \frac{m_e c \omega a_0}{e}$$
$$A = \frac{m_e c a_0 k_c^2 \rho}{e \mu} \tag{A.30}$$

A.4. EPOCH Simulations

The following two tables summarize the parameter of the most important PIC simulations. The input data file for the simulation code - the so-called input deck - is divided into several blocks. The tables show some parameters for the control, constant and laser block. The variables in the control and laser block are predefined by the code. The variables in the constant block are freely chosen. More information about the input deck is given in the comprehensive user guide [2].

The first table A.2 has columns regarding the fraction of particles, which are not found in the second table. For the simulations of the second table the density and momentum distributions were taken from the simulation *Titan_159_v4*. The simulation was used for the prepulse analysis. The momentum and density distributions at 6.9ps of *Titan_159_v4* were fitted by functions or value pairs were taken, respectively. Therefore the columns are omitted in the second table.

Table A.2.: EPOCH simulation parameters.

			Titan_147_v4	Titan_148_v4	Titan_149_v4	Titan_150_v4	Titan_151_v4	Titan_151_v4_post50ps	Titan_152_v4	Titan_153_v4	Titan_154_v4	Titan_155_v4	Titan_156_v4	Titan_157_v4	Titan_158_v4	Titan_159_v4
control																
	t_end	fs	740	740	740	740	740	740	740	740	740	740	740	740	740	10000
	x_min	μm	-20	-20	-20	-20	-20	-20	-20	-20	-20	-20	-20	-20	-20	-20
	x_max	μm	20	20	20	20	20	20	20	20	20	20	20	20	20	10
	y_min	μm	-20	-20	-20	-20	-20	-20	-20	-20	-20	-20	-20	-20	-20	-10
	y_max	μm	20	20	20	20	20	20	20	20	20	20	20	20	20	20
	nx		40	40	40	40	40	40	40	40	40	40	40	40	40	40
		nm	25	25	25	25	25	25	25	25	25	25	25	25	25	25
		px	1600	1600	1600	1600	1600	1600	1600	1600	1600	1600	1600	1600	1600	1200
	ny		40	40	40	40	40	40	40	40	40	40	40	40	40	40
		nm	25	25	25	25	25	25	25	25	25	25	25	25	25	25
		px	1600	1600	1600	1600	1600	1600	1600	1600	1600	1600	1600	1600	1600	1200
	npart		40	40	40	40	40	40	40	40	40	40	40	40	40	40/80
constant																
	w0	μm	3	3	3	3	-	3	3	3	3	3	3	3	3	-
	w1	μm	3	3	3	-	3	-	3	3	3	3	3	3	3	see file
	energy_bi	J	0.9	0.9	0.9	0.9	-	1.1	0.9	0.9	0.9	0.9	0.9	0.9	0.9	-
	energy_bii	J	2.8	2.8	2.8	-	2.8	-	2.8	2.8	2.8	2.8	2.8	2.8	2.8	see file
	pulse_length_bi	fs	30	30	30	30	-	30	30	30	30	30	30	30	30	-
	pulse_length_bii	fs	30	30	30	-	30	-	30	30	30	30	30	30	30	see file
	int_bi	W/cm^2	1.06×10^{20}	1.06×10^{20}	1.06×10^{20}	1.06×10^{20}	-	1.30×10^{20}	1.06×10^{20}	1.06×10^{20}	1.06×10^{20}	1.06×10^{20}	1.06×10^{20}	1.06×10^{20}	1.06×10^{20}	-
	int_bii	W/cm^2	3.30×10^{20}	3.30×10^{20}	3.30×10^{20}	-	3.30×10^{20}	-	3.30×10^{20}	3.30×10^{20}	3.30×10^{20}	3.30×10^{20}	3.30×10^{20}	3.30×10^{20}	3.30×10^{20}	see file
	inc	°	325	325	315	325	325	325	325	325	325	325	325	325	325	325
	offset_inc_y	μm	19.5	19.5	19.5	19.5	19.5	see file	19.5	19.5	19.5	19.5	19.5	19.5	22	22
	den_foil	m^{-3}	5.66×10^{28}	5.66×10^{28}	5.66×10^{28}	5.66×10^{28}	5.66×10^{28}	see file	5.66×10^{28}	5.66×10^{28}	5.66×10^{28}	5.66×10^{28}	5.66×10^{28}	5.66×10^{28}	5.66×10^{28}	5.66×10^{28}
	thickness	μm	1.6	1.6	1.6	1.6	1.6	see file	1.6	1.6	1.6	1.6	1.6	1.6	1.6	-
	contamination	nm	150	150	150	150	150	see file	150	150	150	150	150	150	150	-
	scalelength	μm	0.5	0.5	0.5	0.5	0.5	see file	0.5	0.5	0.5	0.5	0.5	0.5	0.5	-
	scalelength_conta	μm	0.5	0.5	0.5	0.5	0.5	see file	0.5	0.5	0.5	0.5	0.5	0.5	0.5	-
	ionization_step	-	4	4	4	4	4	see file	4	4	4	4	4	4	4	0
			0.2	0.2	0.2	0.2	0.2	-	0.2	0.2	0.2	0.2	0.2	0.2	0.2	1
	Fraction_C	-	0.4	0.4	0.4	0.4	0.4	see file	0.4	0.4	0.4	0.4	0.4	0.4	0.4	-
			0.0034	0.0034	0.0034	0.0034	0.0034	see file	0.0034	0.0034	0.0034	0.0034	0.0034	0.0034	0.0034	-
	Fraction_H	-	0.6	0.6	0.6	0.6	0.6	see file	0.6	0.6	0.6	0.6	0.6	0.6	0.6	-
		-	0.01	0.01	0.01	0.01	0.01	see file	0.01	0.01	0.01	0.01	0.01	0.01	0.01	-
	Fraction_Ti	-	0.19	0.19	0.19	0.19	0.19	-	0.19	0.19	0.19	0.19	0.19	0.19	0.19	1
	Fraction_Elec	-	0.79	0.79	0.79	0.79	0.79	-	0.79	0.79	0.79	0.79	0.79	0.79	0.79	-
laser																
id1	t_start	fs	0	0	5	0	-	0	30	60	120	0	0	0	0	-
	t_end	fs	60	60	65	60	-	60	90	120	180	60	60	60	60	-
id2	t_start	fs	0	0	0	-	0	-	0	0	0	120	60	30	0	see file
	t_end	fs	60	60	60	-	60	-	60	60	60	180	120	90	60	see file
	delay	fs	0	0	-5	-	-	-	-30	-60	-120	120	60	30	0	-

Table A.3.: EPOCH simulation parameters. No information about the particles are given, because the momentum and density distribution were taken from simulation *Titan_159_v4* at timestep 6.9ps. The simulation modeled the prepulse and preplasma. The distributions were fitted by functions and value pairs were taken, respectively.

			Titan_161_v4	**Titan_162_v4**	**Titan_163_v4**	**Titan_164_v4**	**Titan_165_v4**	**Titan_166_v4**	**Titan_167_v4**	**Titan_168_v4**	**Titan_169_v4**	**Titan_176_v4**	**Titan_170_v4**
control													
	t_end	fs	740	1500	860	860	740	740	740	550	615	740	740
	x_min	μm	-20	-20	-20	-20	-20	-20	-20	-20	-20	-20	-20
	x_max	μm	20	15	20	20	20	25	25	25	25	25	20
	y_min	μm	-20	-20	-20	-20	-20	-20	-20	-20	-20	-20	-20
	y_max	μm	20	20	20	20	20	20	20	20	20	20	20
	nx		40	80	40	40	40	40	40	40	40	40	40
		nm	25	12.5	25	25	25	25	25	25	25	25	25
		px	1600	2800	1600	1600	1600	1800	1800	1800	1800	1800	0
	ny		40	80	40	40	40	40	40	40	40	40	40
		nm	25	12.5	25	25	25	25	25	25	25	25	25
		px	1600	2400	1600	1600	1600	1600	1600	1600	1600	1600	1600
	npart		60	60	60	60	60	60	60	60	60	60	40
constant													
	w0	μm	3	-	3	3	3	3	3	3	3	3	3
	w1	μm	3	see file	3	3	3	3	3	3	3	3	3
	energy_bi	J	2.75	-	2.75	2.75	2.75	5.5	2.75	2.75	2.75	2.75	2.75
	energy_bii	J	5.5	see file	5.5	5.5	5.5	11	5.5	5.5	5.5	5.5	5.5
	pulse_length_bi	fs	30	-	30	30	30	30	30	30	30	30	30
	pulse_length_bii	fs	30	see file	30	30	30	30	30	30	30	30	30
	int_bi	W/cm^2	3.24×10^{20}	-	3.24×10^{20}	3.24×10^{20}	3.24×10^{20}	6.48×10^{20}	3.24×10^{20}	3.24×10^{20}	3.24×10^{20}	3.24×10^{20}	3.24×10^{20}
	int_bii	W/cm^2	6.48×10^{20}	see file	6.48×10^{20}	6.48×10^{20}	6.48×10^{20}	1.30E+21	6.48×10^{20}	6.48×10^{20}	6.48×10^{20}	6.48×10^{20}	6.48×10^{20}
	inc	°	325	325	325	325	325	325	325	325	325	325	325
	offset_inc_y	μm	22	22	22	22	22	22	22	22	22	22	22
laser													
id1	t_start	fs	0	-	0	120	0	0	0	0	120	0	-
	t_end	fs	60	-	60	180	60	60	60	60	180	60	-
id2	t_start	fs	150	see file	120	0	0	0	120	120	0	-	0
	t_end	fs	75	see file	180	60	60	60	75	180	60	-	60
	delay	fs	150	-	120	-120	0	0	150	120	-120	-30	30

Bibliography

[1] Microchannel plate, desy. http://adweb.desy.de/mdi/documentation/Restgas_at/PETRA/mcp.html.

[2] Epoch:extendable pic open collaboration. http://ccpforge.cse.rl.ac.uk/gf/project/epoch/.

[3] Fastlite, wizzler. http://www.fastlite.com/en/cat465017-460522-Wizzler.html.

[4] *Tunnel ionization of complex atoms and atomic ions in electromagnetic field*, 1986 Quebec Symposium, 1986. URL http://proceedings.spiedigitallibrary.org/proceeding.aspx?articleid=1243407.

[5] B. J. Albright, L. Yin, K. J. Bowers, B. M. Hegelich, K. A. Flippo, T. J. T. Kwan, and J. Fernandez. Relativistic buneman instability in the laser breakout afterburner. *Physics of Plasmas*, 14(9):094502, 2007. ISSN 1070664X. doi: 10.1063/1.2768933. URL http://dx.doi.org/10.1063/1.2768933.

[6] M. V. Ammosov, N. B. Delone, and V. P. Krainov. Tunnel ionization of complex atoms and of atomic ions in an alternating electromagnetic field. *Soviet Physics - JETP*, 64(6):1191–1194, 1986.

[7] A. A. Andreev, K. Y. Platonov, T. Okada, and S. Toraya. Nonlinear absorption of a short intense laser pulse in a nonuniform plasma. *Physics of Plasmas (1994-present)*, 10(1):220–226, 2003. ISSN 1070664X. URL http://scitation.aip.org/content/aip/journal/pop/9/1/10.1063/1.1421369.

[8] H. B. Bebb and A. Gold. Multiphoton ionization of hydrogen and rare-gas atoms. *Physical Review*, 143(1):1, 1966. URL http://prola.aps.org/abstract/PR/v143/i1/p1_1.

[9] A. R. Bell, F. N. Beg, Z. Chang, A. E. Dangor, C. N. Danson, C. B. Edwards, A. P. Fews, M. H. R. Hutchinson, S. Luan, and P. Lee. Observation of plasma confinement in picosecond laser-plasma interactions. *Physical Review E*, 48(3):2087, 1993. URL http://journals.aps.org/pre/abstract/10.1103/PhysRevE.48.2087.

[10] S. S. Bulanov, V. Y. Bychenkov, V. Chvykov, G. Kalinchenko, D. W. Litzenberg, T. Matsuoka, A. G. Thomas, L. Willingale, V. Yanovsky, and K. Krushelnick. Generation of gev protons from 1 pw laser interaction with near critical density targets. *Physics of Plasmas (1994-present)*, 17(4):043105, 2010. ISSN 1070664X. URL http://scitation.aip.org/content/aapm/journal/medphys/35/5/10.1118/1.2900112.

[11] I. W. Choi, C. M. Kim, J. H. Sung, T. J. Yu, S. K. Lee, I. J. Kim, Y.-Y. Jin, T. M. Jeong, N. Hafz, and K. H. Pae. Ion spectrometer composed of time-of-flight and thomson parabola spectrometers for simultaneous characterization of laser-driven ions. *Review of Scientific Instruments*, 80(5): 053302, 2009. ISSN 00346748. URL http://journals.aps.org/rmp/abstract/10.1103/RevModPhys.82.1793.

[12] T. E. Cowan, J. Fuchs, H. Ruhl, Y. Sentoku, A. Kemp, P. Audebert, M. Roth, R. Stephens, I. Barton, and A. Blazevic. Ultra-low emittance, high current proton beams produced with a laser-virtual cathode sheath accelerator. *Nuclear Instruments and Methods in Physics Research Section A: Accelerators, Spectrometers, Detectors and Associated Equipment*, 544(1):277–284, 2005. ISSN 01689002. URL http://scholar.google.com/scholar.ris?q=info:G8VjvtSCtxEJ:scholar.google.com&output=cite&scirp=6&hl=en#pub.

[13] S. R. De Groot, W. A. van Leeuwen, and C. G. van Weert. *Relativistic kinetic theory: principles and applications*. North-Holland Amsterdam, 1980. URL http://www.lavoisier.fr/livre/notice.asp?ouvrage=1333531.

[14] C. Dorrer and M. Joffre. Characterization of the spectral phase of ultrashort light pulses. *Comptes Rendus de l'Académie des Sciences-Series IV-Physics*, 2(10):1415–1426, 2001. ISSN 12962147. URL http://www.opticsinfobase.org/oe/fulltext.cfm?uri=oe-14-24-11892&id=119192.

[15] J. H. Eberly and J. Javanainen. Above-threshold ionisation. *European Journal of Physics*, 9:265–275, oct 1988. doi: 10.1088/0143-0807/9/4/004. URL http://adsabs.harvard.edu//abs/1988EJPh....9..265E.

[16] S. Eliezer. *The interaction of high-power lasers with plasmas*. CRC Press, 2010. URL http://books.google.de/books?hl=en&lr=&id=Hqzjvpu4kEUC&oi=fnd&pg=PA1&dq=the+interaction+of+high+power+lasers+with+plasmas&ots=R3Dtbsxje7&sig=4z2G4b_gZJ1h3aBJMDBCRNeo7NI.

[17] T. Esirkepov, M. Borghesi, S. V. Bulanov, G. Mourou, and T. Tajima. Highly efficient relativistic-ion generation in the laser-piston regime. *Physical review letters*, 92(17):175003, 2004. URL http://journals.aps.org/prl/abstract/10.1103/PhysRevLett.92.175003.

[18] K. G. Estabrook, E. J. Valeo, and W. L. Kruer. Two-dimensional relativistic simulations of resonance absorption. *Physics of Fluids (1958-1988)*, 18 (9), 1975.

[19] P. Gibbon. *Short pulse laser interactions with matter*. Imperial College Press London, 2005. URL http://www.fz-juelich.de/cae/servlet/contentblob/1076020/publicationFile/26069/SPLIM_Lecture01.pdf.

[20] A.-L. Giesecke. *Propagation Dynamics and High Harmonic Generation Using High Contrast Ultrashort Laser Pulses*. PhD thesis, Heinrich-Heine-Universität, Düsseldorf, 2013. URL http://docserv.uni-duesseldorf.de/servlets/DocumentServlet?id=25741.

[21] K. Harres, M. Schollmeier, E. Brambrink, P. Audebert, A. Blažević, K. Flippo, D. C. Gautier, M. Geißel, B. M. Hegelich, and F. Nürnberg. Development and calibration of a thomson parabola with microchannel plate for the detection of laser-accelerated mev ions. *Review of Scientific Instruments*, 79(9):093306, 2008. ISSN 00346748. URL http://scitation.aip.org/content/aip/journal/rsi/79/9/10.1063/1.2987687.

[22] S. P. Hatchett, C. G. Brown, T. E. Cowan, E. A. Henry, J. S. Johnson, M. H. Key, J. A. Koch, A. B. Langdon, B. F. Lasinski, R. W. Lee, A. J. Mackinnon, D. M. Pennington, M. D. Perry, T. W. Phillips, M. Roth, T. C. Sangster, M. S. Singh, R. A. Snavely, M. A. Stoyer, S. C. Wilks, and K. Yasuike. Electron, photon, and ion beams from the relativistic interaction of petawatt laser pulses with solid targets. *Physics of Plasmas*, 7(5):2076, 2000. ISSN 1070664X. doi: 10.1063/1.874030. URL http://dx.doi.org/10.1063/1.874030.

[23] B. M. Hegelich, I. Pomerantz, L. Yin, H. C. Wu, D. Jung, B. J. Albright, D. C. Gautier, S. Letzring, S. Palaniyappan, and R. Shah. Laser-driven ion acceleration from relativistically transparent nanotargets. *New Journal of Physics*, 15(8):085015, 2013. ISSN 13672630. URL http://iopscience.iop.org/1367-2630/15/8/085015.

[24] M. Hegelich, S. Karsch, G. Pretzler, D. Habs, K. Witte, W. Guenther, M. Allen, A. Blazevic, J. Fuchs, and J. C. Gauthier. Mev ion jets from short-pulse-laser interaction with thin foils. *Physical review letters*, 89(8):085002, 2002. URL http://journals.aps.org/prl/abstract/10.1103/PhysRevLett.89.085002.

[25] D. Jung. *Ion acceleration from relativistic laser nano-target interaction.* PhD thesis, LMU, 2012. URL http://edoc.ub.uni-muenchen.de/14074/.

[26] W. H. Kegel. Plasmaphysik. eine einführung. *Plasmaphysik. Eine Einführung., by Kegel, WH. Springer, Berlin (Germany)*, 1, 1998. URL http://adsabs.harvard.edu/abs/1998pee..book.....K.

[27] B. King and H. Ruhl. Trident pair production in a constant crossed field. *Physical Review D*, 88(1):013005, 2013. URL http://journals.aps.org/prd/abstract/10.1103/PhysRevD.88.013005.

[28] B. King, N. Elkina, and H. Ruhl. Photon polarization in electron-seeded pair-creation cascades. *Physical Review A*, 87(4):042117, 2013. URL http://journals.aps.org/pra/abstract/10.1103/PhysRevA.87.042117.

[29] T. A. Klar and S. W. Hell. Subdiffraction resolution in far-field fluorescence microscopy. *Optics letters*, 24(14):954–956, 1999. ISSN 15394794. URL http://www.opticsinfobase.org/abstract.cfm?uri=ol-24-14-954.

[30] W. L. Kruer. *The physics of laser plasma interactions*, volume 70. Addison-Wesley New York, 1988. URL http://www.science.gov/topicpages/l/laser-plasma+interaction+physics.html.

[31] W. L. Kruer and K. Estabrook. J x b heating by very intense laser light. *Physics of Fluids (1958-1988)*, 28(1):430–432, 1985. ISSN 00319171. URL http://scitation.aip.org/content/aip/journal/pof1/28/1/10.1063/1.865171.

[32] P. Lambropoulos and X. Tang. Multiple excitation and ionization of atoms by strong lasers. *JOSA B*, 4(5):821–832, 1987. URL http://www.opticsinfobase.org/abstract.cfm?id=4876.

[33] L. D. Landau and E. M. Lifshitz. Quantum mechanics, non-relativistic theory 1977. *Course of Theoretical Physics*, 1977. URL http://scholar.google.de/scholar.bib?q=info:-RLtADjYf04J:scholar.google.com/&output=citation&hl=en&ct=citation&cd=1.

[34] K. W. D. Ledingham, W. Galster, and R. Sauerbrey. Laser-driven proton oncology—a unique new cancer therapy? *Laser*, 80(959), 2007. URL http://www.sciencedirect.com/science/article/pii/S1350448711001454.

[35] L. Lepetit, G. Cheriaux, and M. Joffre. Linear techniques of phase measurement by femtosecond spectral interferometry for applications in spectroscopy. *JOSA B*, 12(12):2467–2474, 1995. ISSN 15208540. URL http://www.opticsinfobase.org/abstract.cfm?uri=josab-19-5-1019.

[36] A. Macchi, F. Cattani, T. V. Liseykina, and F. Cornolti. Laser acceleration of ion bunches at the front surface of overdense plasmas. *Physical review letters*, 94(16):165003, 2005. URL http://journals.aps.org/prl/abstract/10.1103/PhysRevLett.94.165003.

[37] T. H. Maiman. Stimulated optical radiation in ruby. 1960. URL http://www.joponline.org/doi/abs/10.1902/jop.1985.56.8.492.

[38] R. Nuter, L. Gremillet, P. Combis, M. Drouin, E. Lefebvre, A. Flacco, and V. Malka. Influence of a preplasma on electron heating and proton acceleration in ultraintense laser-foil interaction. *Journal of Applied Physics*, 104(10):103307–103307, 2008. URL http://ieeexplore.ieee.org/xpls/abs_all.jsp?arnumber=4916952.

[39] A. Piel. *Plasma Physics - An Introduction to Laboratory, Space, and Fusion Plasmas*. Springer, 2010. URL http://www.springer.com/physics/atomic,+molecular,+optical+%26+plasma+physics/book/978-3-642-10490-9.

[40] D. M. Pozar. *Microwave engineering*. John Wiley & Sons, 2009. ISBN 8126510498. URL http://ieeexplore.ieee.org/xpls/abs_all.jsp?arnumber=214613.

[41] R. Prasad, D. Doria, S. Ter-Avetisyan, P. S. Foster, K. E. Quinn, L. Romagnani, C. M. Brenner, J. S. Green, P. Gallegos, and M. J. V. Streeter. Calibration of thomson parabola—mcp assembly for multi-mev ion spectroscopy. *Nuclear Instruments and Methods in Physics Research Section A: Accelerators, Spectrometers, Detectors and Associated Equipment*, 623(2):712–715, 2010. ISSN 01689002. URL http://www.clf.rl.ac.uk/resources/PDF/ar09-10_hpls_full_fpp.pdf.

[42] G. Pretzler. Laser-plasma-diagnostik. University Lecture, 2010. Heinrich Heine Universität, Düsseldorf.

[43] A. Pukhov and J. Meyer-ter Vehn. Relativistic magnetic self-channeling of light in near-critical plasma: three-dimensional particle-in-cell simulation. *Physical review letters*, 76(21):3975, 1996. URL http://journals.aps.org/prl/abstract/10.1103/PhysRevLett.76.3975.

[44] A. Pukhov and J. Meyer-ter Vehn. Laser hole boring into overdense plasma and relativistic electron currents for fast ignition of icf targets. *Physical review letters*, 79(14):2686, 1997. URL http://journals.aps.org/prl/abstract/10.1103/PhysRevLett.79.2686.

[45] B. Qiao, M. Zepf, M. Borghesi, B. Dromey, M. Geissler, A. Karmakar, and P. Gibbon. Radiation-pressure acceleration of ion beams from nanofoil targets: The leaky light-sail regime. *Physical review letters*, 105(15):155002, 2010. URL http://journals.aps.org/prl/abstract/10.1103/PhysRevLett.105.155002.

[46] A. P. L. Robinson, M. Zepf, S. Kar, R. G. Evans, and C. Bellei. Radiation pressure acceleration of thin foils with circularly polarized laser pulses. *New Journal of Physics*, 10(1):013021, 2008. ISSN 13672630. URL http://iopscience.iop.org/1367-2630/10/1/013021.

[47] A. P. L. Robinson, P. Gibbon, M. Zepf, S. Kar, R. G. Evans, and C. Bellei. Relativistically correct hole-boring and ion acceleration by circularly polarized laser pulses. *Plasma Physics and Controlled Fusion*, 51(2):024004, 2009. ISSN 07413335. URL http://iopscience.iop.org/0741-3335/51/2/024004.

[48] J. Schreiber, F. Bell, F. Grüner, U. Schramm, M. Geissler, M. Schnürer, S. Ter-Avetisyan, B. M. Hegelich, J. Cobble, and E. Brambrink. Analytical model for ion acceleration by high-intensity laser pulses. *Physical review letters*, 97(4):045005, 2006. URL http://www.nature.com/nature/journal/v439/n7075/abs/nature04400.html.

[49] Y. Sentoku and A. J. Kemp. Numerical methods for particle simulations at extreme densities and temperatures: Weighted particles, relativistic collisions and reduced currents. *Journal of Computational Physics*, 227(14):6846–6861, 2008. ISSN 00219991. URL http://www.sciencedirect.com/science/article/pii/S0021999108001988.

[50] P. Sprangle, E. Esarey, and A. Ting. Nonlinear theory of intense laser-plasma interactions. *Physical review letters*, 64(17):2011, 1990. URL http://journals.aps.org/pre/abstract/10.1103/PhysRevE.48.3003.

[51] D. Strickland and G. Mourou. Compression of amplified chirped optical pulses. *Optics communications*, 55(6):447–449, 1985. ISSN 00304018. URL http://www.opticsinfobase.org/abstract.cfm?uri=ol-21-9-668.

[52] R. N. Sudan. Mechanism for the generation of 10 9 g magnetic fields in the interaction of ultraintense short laser pulse with an overdense plasma target. *Physical review letters*, 70(20):3075, 1993. URL http://journals.aps.org/prl/abstract/10.1103/PhysRevLett.70.3075.

[53] A. Taflove and S. C. Hagness. Computational electrodynamics: the fdtd method. *Artech House Boston, London*, 2000. URL http://scholar.google.com.pk/scholar.ris?q=info:A4v_WKQaIb0J:scholar.google.com&output=cite&scirp=1&hl=en#pub.

[54] T. Toncian. *Ultrafast Laser Driven Micro-Lens to Focus and Energy Select MeV Protons*. PhD thesis, Heinrich-Heine-Universität, Düsseldorf,

2008. URL http://docserv.uni-duesseldorf.de/servlets/DerivateServlet/Derivate-10210.

[55] S. Walz. *Laser-Neutralteilchen-Massenspektrometrie ortsaufgelöste Elementanalytik an Kristallen, Keramiken, Solarzellen, Kunststoffen und archäologischen Funden und Bestimmung von Sättigungsintensitäten ungesättigter Photoionisationsprozesse*. PhD thesis, Universität Freiburg, 2003. URL http://d-nb.info/968460143/about/html.

[56] T. Weiland. A discretization model for the solution of maxwell's equations for six-component fields. *Archiv Elektronik und Uebertragungstechnik*, 31:116–120, 1977. URL http://adsabs.harvard.edu/abs/1977ArElU..31..116W.

[57] T. Weiland. Verfahren und anwendungen der feldsimulation. University Lecture, 2014. TU Darmstadt.

[58] A. Wexler and D. R. Lide. Crc handbook of chemistry and physics. 2009. URL http://scholar.google.de/scholar.bib?q=info:NLjgBmXefEoJ:scholar.google.com/&output=citation&hl=en&ct=citation&cd=4.

[59] S. C. Wilks, W. L. Kruer, M. Tabak, and A. B. Langdon. Absorption of ultra-intense laser pulses. *Physical review letters*, 69(9):1383, 1992. URL http://iopscience.iop.org/0953-4075/26/4/003.

[60] S. C. Wilks, A. B. Langdon, T. E. Cowan, M. Roth, M. Singh, S. Hatchett, M. H. Key, D. Pennington, A. MacKinnon, and R. A. Snavely. Energetic proton generation in ultra-intense laser-solid interactions. *Physics of Plasmas*, 8(2):542, 2001. ISSN 1070664X. doi: 10.1063/1.1333697. URL http://dx.doi.org/10.1063/1.1333697.

[61] L. Willingale, P. M. Nilson, A. G. R. Thomas, S. S. Bulanov, A. Maksimchuk, W. Nazarov, T. C. Sangster, C. Stoeckl, and K. Krushelnick. High-power, kilojoule laser interactions with near-critical density plasmaa). *Physics of Plasmas (1994-present)*, 18(5):056706, 2011. ISSN 1070664X. URL http://scitation.aip.org/content/aip/journal/pofb/4/11/10.1063/1.860333.

[62] L. Yin, B. J. Albright, B. M. Hegelich, and J. C. Fernández. Gev laser ion acceleration from ultrathin targets: The laser break-out afterburner. *Laser and Particle Beams*, 24(02):291–298, 2006. ISSN 1469803X. URL http://journals.cambridge.org/abstract_S0263034606060459.

[63] L. Yin, B. J. Albright, B. M. Hegelich, K. J. Bowers, K. A. Flippo, and T. J. T. Kwan. Monoenergetic and gev ion acceleration from the laser breakout afterburner using ultrathin targets. *Physics of Plasmas*, 14(5):056706, 2007. ISSN 1070664X. doi: 10.1063/1.2436857. URL http://dx.doi.org/10.1063/1.2436857.

[64] L. Yin, B. J. Albright, D. Jung, R. C. Shah, S. Palaniyappan, K. J. Bowers, A. Henig, and B. M. Hegelich. Break-out afterburner ion acceleration in the longer laser pulse length regime. *Physics of Plasmas*, 18(6):063103, 2011. ISSN 1070664X. doi: 10.1063/1.3596555. URL http://dx.doi.org/10.1063/1.3596555.

[65] T.-P. Yu. *Stable laser-driven proton acceleration in ultra-relativistic laser-plasma interaction*. PhD thesis, Heinrich-Heine-Universität, Düsseldorf, 2011.

[66] K. Zeil, S. D. Kraft, S. Bock, M. Bussmann, T. E. Cowan, T. Kluge, J. Metzkes, T. Richter, R. Sauerbrey, and U. Schramm. The scaling of proton energies in ultrashort pulse laser plasma acceleration. *New Journal of Physics*, 12(4):045015, 2010. ISSN 13672630. URL http://iopscience.iop.org/1367-2630/12/4/045015.

[67] J. F. Ziegler, J. P. Biersack, and U. Littmark. *The stopping and range of ions in solids*, volume 1. New York, 1985. URL http://books.google.com/books?hl=de&lr=&id=038n1jKZpq4C&oi=fnd&pg=PA3&dq=The+stopping+and+range+ofions+in+solids&ots=Zolae56JS7&sig=aGb0CXctz0jqill6Xh1fgAKdHqA.

Publications

Scientific publications

1. E. d'Humieres, P. Antici, M. Glesser, **J. Boeker** S. Chen, J. L. Feugeas, F. Filippi, M. Gauthier, A. Levy, P. Nicolai, H. Pepin, L. Romagnani, M. Sciscio, V. T. Tikhonchuk, O. Willi, J. C. Kieffer and J. Fuchs: "Investigation of laser ion acceleration in low-density targets using exploded foils" . *Plasma Physics and Controlled Fusion* 55 (2013) 124025 (7pp)

2. B. Albertazzi, E. d'Humieres, L. Lancia, V. Dervieux, P. Antici, J. Breil, **J. Böcker**, S. N. Chen, J. L. Feugeas, M. Nakatsutsumi, P. Nicolai, L. Romagnani, R. Sheperd, Y. Sentoku, M. Swantusch, V. T. Tikhonchuk, M. Borghesi, O. Willi, H. Pepin, J. Fuchs: "A compact broadband ion beam focusing device based on laser-driven MG thermoelectric magnetic fields" . *Applied Physics Letters* submitted.

Submissions to international conferences

1. **Juergen Boeker**, Marco Swantusch, Toma Toncian, Mirela Cerchez, Monika Toncian, Farzan Hamzehei, Oswald Willi: "Laser-Driven Proton Acceleration with Two Ultrashort Laser Pulses" . *Pulsed Power and Plasma Science Conference*. IEEE, 2013: 5C-3.

2. Marco Swantusch, **Juergen Boeker**, Rajendra Prasad, Mirela Cerchez, Marie Schroer, Stephanie Brauckmann, Sven Spickermann, Thomas Wowra, Toma Toncian, Oswald Willi: "Proton energy enhancement in multiple-beam solid foil interaction" . *56th Annual Meeting of the APS Division of Plasma Physics*. APS, 2014: BO5.9.

Danksagung

Zunächst möchte ich mich bei Herrn Professor Oswald Willi bedanken, der mir die Möglichkeit gegeben hat am Institut für Laser- und Plasmaphysik diese Arbeit anzufertigen und mit seiner Anpacker Mentalität immer wußte das ganze Institut in Schwung zu versetzen. Herrn Professor Carsten Müller gilt meinen besonderen Dank für das Übernehmen des Koreferats dieser Arbeit.

Die langen Tage im Bunker, Labor und Büro wären mir noch viel länger erschienen, wenn Marco nicht da gewesen wäre. Die gefundene Damenunterwäsche wird immer ein Rätsel bleiben. Toma und Monika (+Miriam) danke ich für die freundschaftliche Zusammenarbeit, die mich neben ihrer fachlichen Expertise sehr unterstützt haben - die Kaffeerunde mit euch in der Cafeteria vermisse ich jetzt schon. Eine wesentliche Rolle im Erfolg der Experimente hatten aber auch Mirela, Farzan, Raj und Stefan. Für die stets offene Tür und für (meist) einen freien Node auf Moac, danke ich Götz.

Ganz herzlich bedanken möchte ich mich noch bei Claudia, Katharina und Claudia.

Auch allen anderen Kollegen am Institut für Laser- und Plasmaphysik gilt mein Dank, sowie allen die ich bei verschiedenen Experimenten im Ausland begegnet bin - ihr alle habt mich ein Stück weit geprägt.

Ohne meine Eltern Grete und Heinz-Friedrich Böker mit ihrer immerwährenden Unterstützung und Ermunterung, hätte ich diese Arbeit nicht beginnen und beenden können.

Während meiner Zeit in Düsseldorf habe ich meine Verlobte Annika kennengelernt. Die ganzen Jahre hat sie mich nicht ohne Dissertation gekannt. Ich danke Dir über alles für Deine Hilfe und Geduld und dafür, dass Du mich in den richtigen Momenten vom Schreibtisch gezerrt hast.

Eidesstattliche Versicherung

Ich versichere an Eides Statt, dass die Dissertation von mir selbständig und ohne unzulässige fremde Hilfe unter Beachtung der ”Grundsätze zur Sicherung guter wissenschaftlicher Praxis an der Heinrich-Heine-Universität Düsseldorf” erstellt worden ist.

Die Dissertation wurde in der vorgelegten oder in ähnlicher Form noch bei keiner anderen Institution eingereicht. Ich habe bisher keine erfolglosen Promotionsversuche unternommen.

Köln, 25. Januar 2015 Jürgen Böker